Atomic Layer Deposition in PDMSMicrofluidic Chips forMedical Radionuclide Separation

Santoso, A.

DOI
10.4233/uuid:939fc8b2-6a2e-4be1-bf4c-8fc1badeca07

Publication date
2024

Document Version
Final published version

Citation (APA)
Santoso, A. (2024). *Atomic Layer Deposition in PDMSMicrofluidic Chips forMedical Radionuclide Separation*. [Dissertation (TU Delft), Delft University of Technology]. https://doi.org/10.4233/uuid:939fc8b2-6a2e-4be1-bf4c-8fc1badeca07

Important note
To cite this publication, please use the final published version (if applicable).
Please check the document version above.

Atomic Layer Deposition
in PDMS Microfluidic Chips
for Medical Radionuclide Separation

Albert Santoso

Atomic Layer Deposition in PDMS Microfluidic Chips for Medical Radionuclide Separation

Albert SANTOSO

Printed by: Gildeprint BV
ISBN 978-94-6496-241-3

J.M. Burgerscentrum PhD

Printed in the Netherlands

An electronic copy of this dissertation is available at 0000 repository

For my grandma and grandpa
Who leave in peace while this book is still in piece

Atomic Layer Deposition in PDMS Microfluidic Chips for Medical Radionuclide Separation

Dissertation

for the purpose of obtaining the degree of doctor
at Delft University of Technology
by the authority of the Rector Magnificus Prof. Dr. ir T.H.J.J. van der Hagen
chair of the board for Doctorates
to be defended publicly on Tuesday, 22nd of October 2024 at 10:00 o'clock.

by

Albert SANTOSO

Master of Science in Bioprocess Engineering, Universitas Indonesia, Indonesia
born in Jakarta, Indonesia

This dissertation has been approved by the promotor and copromotors.

Composition of doctoral committee:

Rector Magnificus	Chairperson
Prof.dr.ir. J.R. van Ommen	Delft University of Technology, promotor
Dr.ir. V. van Steijn	Delft University of Technology, promotor

Independent members:

Prof.dr.ir. J.T. Padding	Delft University of Technology
Dr. H.B. Eral	Delft University of Technology
Prof.dr. R.L. Puurunen	Aalto University, Finland
Dr.ir. D.C. Visser	Nuclear Research and Consultancy Group
Dr.ir. R.M. de Kruijff	Delft University of Technology
Prof.dr.ir. C.R. Kleijn	Delft University of Technology, reserve member

The research presented in this thesis was performed at the Product and Process Engineering section of the Department of Chemical Engineering, Faculty of Applied Sciences, Delft University of Technology, the Netherlands.

This research was funded by the Dutch Research Council (NWO) under project number 16913.

Contents

Summary

In the field of cancer diagnostics and targeted therapy, medical radionuclides have gained increasing interest. These nuclides usually have their own unique emission characteristics and reasonably short half-life, and when combined with antibodies/peptides can be used as radiopharmaceuticals. After injection into a patient, the radiopharmaceuticals then interact with specific proteins expressed in a cancer cell. As a result, precise imaging of the cancer cells and/or targeted delivery of therapeutic doses can be performed.

Despite decades of research in medical radionuclides, only a handful manage to be authorized for clinical uses. While their clinical efficacy and safety are still parts of the ongoing research, many radionuclides are also difficult to produce since they are either too short in half-life, complicated to label or limited in availability. Consequently, efforts have been made to also advance the production of medical radionuclides, including the critical separation steps. When it comes to the separation steps, the processes must take place in a relatively short time with high efficiency and reliability. Among many technologies, (liquid-liquid) extraction in microfluidic devices holds the potential to accommodate this by offering a controlled environment with a high surface-to-volume ratio. The large contact area allows the radionuclides to be separated from their respective target materials, from one phase to the other in a fast, continuous and efficient manner.

The commonly used material of choice to fabricate microfluidic chips is polydimethylsiloxane (PDMS). It is easy to replicate, suitable for rapid prototyping, resistant to extreme pH and transparent. Yet, PDMS suffers from being incompatible with organic solvents, commonly used as one of the phases in liquid-liquid extractions. Unfortunately, current solutions involving bulk-, ex-situ surface-, and in-situ liquid phase modifications are limited and practically demanding. To overcome PDMS's main limitation, we develop a new method to deposit metal oxide nano-coatings on the walls of bonded microfluidic chips. These nano-coatings can offer protection without modifying the convenient PDMS bulk properties. Therefore, the central theme of this PhD dissertation is to develop a PDMS microfluidic technology with nano-coatings, able to separate medical radionuclides from their irradiated target materials through continuous flow liquid-liquid extraction.

We started by depositing titanium oxide nano-layers on PDMS flat substrates using atomic layer deposition (ALD). The deposition at atmospheric pressure (AP-ALD) resulted in both surface and subsurface nano-layer growth. These nano-layers were found to increase the organic solvent resistance of PDMS by two orders of magnitude compared to untreated PDMS, even after 24 hours of continuous exposure. We additionally found that the resulting titanium oxide nano-layers also provided surface anchoring groups on PDMS surfaces, indicated by a lower advancing water contact angle when compared with untreated surfaces. When the PDMS was cured at a higher temperature, there was less out-diffusion of PDMS' uncured monomers, resulting in a surface that remained relatively hydrophilic for at least 800 hours. This surface could be further

functionalized by other compounds, such as gold nanoparticles (AuNPs).

We then developed a method to deposit the nano-layers inside bonded PDMS microfluidic channels using AP-ALD. By flowing the ALD reactant gases through the microfluidic channels, full coverage of the walls by a metal oxide nano-layer was found, even with complex channel networks. The treated PDMS chips enabled the wider application of PDMS microfluidics, demonstrated through three case studies.

Hereafter, silicon oxide nano-layers were deposited inside a PDMS microfluidic channel with a guiding phase structure. This structure helped in guiding both aqueous and organic phases used in medical radionuclide extraction, while the nano-layers increased the organic solvent resistance of the PDMS chips. As a result, parallel laminar flows were formed in a relatively wide range of flow rate combinations. Using this system, four radionuclides, including the commercially used ^{90}Y and the emerging ^{225}Ac, were extracted from their respective target materials. Both forward and backward extraction took place in a matter of seconds with efficiencies above 80-98%, depending on the radionuclides, demonstrating a promising system with possible direct recycling of the target materials and fewer post-processing steps. From these, PDMS microfluidic chips treated with atomic layer deposition were demonstrated to separate medical radionuclides in a fast, continuous and efficient manner.

Next to the developed microfluidic approach for radionuclide separation, we revisited the complementary alternative adsorption to separate various medical radionuclides, by developing new column resin beads. Using these beads, we separated the medical radionuclides with high efficiencies (above 98%) and with the contaminant levels within legally permissible limits. The herein developed two separation methods enable the development of a tailored solution for fast and efficient separation of certain medical radionuclides, with possible added benefits such as fewer auxiliary production steps, less radioactive waste and possible automation.

Samenvatting

Op het gebied van kankerdiagnostiek en gerichte therapie hebben medische radionucliden steeds meer belangstelling gekregen. Deze nucliden hebben doorgaans hun eigen unieke emissie-eigenschappen en een redelijk korte halfwaardetijd. In combinatie met antilichamen of peptiden kunnen ze als radiofarmaceutica worden gebruikt. Na injectie in een patiënt gaat het radiofarmaceuticum een interactie aan met specifieke eiwitten die tot expressie worden gebracht in een kankercel. Als gevolg hiervan kunnen nauwkeurige beeldvorming van de kankercellen en/of gerichte afgifte van therapeutische doses worden uitgevoerd.

Ondanks tientallen jaren onderzoek naar medische radionucliden slaagt slechts een handvol erin om toegelaten te worden voor klinisch gebruik. Hoewel hun klinische werkzaamheid en veiligheid nog steeds deel uitmaken van lopende onderzoek, zijn veel radionucliden ook moeilijk te produceren omdat ze een te korte halfwaardetijd hebben, ingewikkeld zijn om te labelen of beperkt beschikbaar zijn. Bijgevolg zijn er pogingen ondernomen om ook de productie van medische radionucliden te bevorderen, inclusief de kritische scheidingsstappen. Als het om de scheidingsstappen gaat, moeten de processen in relatief korte tijd plaatsvinden met een hoge efficiëntie en betrouwbaarheid. Vanuit de vele technologieën heeft vloeistof-vloeistof extractie in microfluidische systemen het potentieel om hieraan tegemoet te komen door een gecontroleerde omgeving te bieden met een hoge oppervlakte-volumeverhouding. Dankzij het grote contactoppervlak kunnen de radionucliden op een snelle, continue en efficiënte manier van de ene fase naar de andere fase gescheiden worden van het materiaal waarvan ze gemaakt worden door extractie.

Het meest gebruikte materiaal bij uitstek om microfluïdische chips te fabriceren is polydimethylsiloxaan (PDMS). Het is gemakkelijk te repliceren, geschikt voor snelle prototyping, bestand tegen extreme pH en transparant. Toch lijdt PDMS eraan dat het incompatibel is met organische oplosmiddelen die doorgaans gebruikt worden bij vloeistof-vloeistof extractie. Helaas zijn de huidige oplossingen die bulk-, ex-situ oppervlakte- en in-situ modificatie in de vloeistoffase omvatten beperkt en praktisch veeleisend. Om dit probleem weg te nemen, ontwikkelen we een nieuwe methode om metaaloxide-nanocoatings op de wanden van gebonden microfluïdische chips aan te brengen. Deze nanocoatings kunnen bescherming bieden zonder de handige bulkeigenschappen van PDMS te wijzigen. Daarom is het centrale thema van dit proefschrift het ontwikkelen van een PDMS-microfluïdische technologie met nanocoatings, die in staat is om medische radionucliden te scheiden van de bestraalde materialen waarmee ze worden geproduceerd.

We zijn begonnen met het afzetten van de titaniumoxide-nanolagen op vlakke PDMS-substraten met behulp van atomaire laagdepositie (ALD). De depositie bij atmosferische druk (AP-ALD) resulteerde in groei van zowel oppervlakte- als ondergrondse nanolagen. Deze nanolagen bleken de weerstand van PDMS tegen organische oplosmiddelen met

twee ordes van grootte te verhogen vergeleken met de onbehandelde PDMS, zelfs na 24 uur continue blootstelling. We ontdekten bovendien dat de resulterende nanolagen van titaniumoxide ook oppervlakteverankerende groepen op PDMS-oppervlakken opleverden, wat blijkt uit een lagere voortschrijdende watercontacthoek in vergelijking met onbehandelde oppervlakken. Wanneer het PDMS bij een hogere temperatuur werd uitgehard, kwamen er minder monomeren uit het PDMS vrij, wat resulteerde in een oppervlak dat gedurende ten minste 800 uur relatief hydrofiel bleef. Dit oppervlak zou verder kunnen worden gefunctionaliseerd door andere verbindingen, zoals gouden nanodeeltjes (AuNP's).

Vervolgens hebben we een methode ontwikkeld om de nanolagen binnenin gebonden PDMS-microfluïdische kanalen te deponeren met behulp van AP-ALD. Door de ALD-reactant-gassen door de microfluïdische kanalen te laten stromen, werd een hoge dekking van nanolaagafzetting gevonden, zelfs in complexe netwerken van microkanalen. De behandelde PDMS-chips maakten de bredere toepassing van PDMS-microfluïdica mogelijk, aangetoond door drie prototypische casestudies uit het toepassingsgebied van microfluidica.

Hierna werden siliciumoxide-nanolagen afgezet in een PDMS-microfluïdisch kanaal met een geleidende fasestructuur. Deze structuur hielp bij het begeleiden van zowel waterige als organische fasen die worden gebruikt bij de extractie van medische radionucliden, terwijl de nanolagen de weerstand tegen organische oplosmiddelen van de PDMS-chips verhoogden. Als gevolg hiervan konden parallelle laminaire stromingen worden gevormd in een relatief groot bereik aan stroomsnelheidscombinaties. Met behulp van dit systeem werden vier radionucliden, waaronder de commercieel gebruikte ^{90}Y en de opkomende ^{225}Ac, uit een oplossing met hun respectieve doelmaterialen geëxtraheerd. Zowel voorwaartse als achterwaartse extractie vond binnen enkele seconden plaats met efficiënties van meer dan 80-98%, afhankelijk van de radionucliden, resulterend in een veelbelovend systeem met mogelijke directe recycling van de doelmaterialen en minder nabewerkingsstappen. Hieruit werd aangetoond dat PDMS-microfluïdische chips behandeld met atomaire laagdepositie gebruikt kon worden om medische radionucliden op een snelle, continue en efficiënte manier te scheiden.

Naast de ontwikkelde microfluidische aanpak voor de scheiding van radionucliden hebben we de complementaire alternatieve adsorptie om een paar medische radionucliden te scheiden opnieuw bekeken, door nieuwe kolomadsorptiedeeltjes te ontwikkelen. Met behulp van deze deeltjes hebben we verschillende medische radionucliden gescheiden met efficiënties van ook boven de 90% en met de verontreinigingsniveaus binnen de wettelijk toegestane grenzen. Met de twee hierin ontwikkelde scheidingsmethoden zou een oplossing op maat voor een snelle en efficiënte scheiding van bepaalde medische radionucliden kunnen worden ontwikkeld, met mogelijke extra voordelen zoals minder aanvullende productiestappen, minder radioactief afval en mogelijke automatisering.

Ikhtisar

Dalam bidang diagnosis kanker dan terapi target, radionuklida medis mendapat atensi yang tinggi. Nuklida ini biasanya memiliki karakteristik emisi yang unik dan waktu paruh yang cukup singkat, dan jika dikombinasikan dengan molekul antibodi/peptida, mereka dapat digunakan sebagai radiofarmasi. Setelah disuntikkan ke pasien, radiofarmasi kemudian berinteraksi dengan protein spesifik yang diekspresikan oleh sel kanker. Sebagai hasilnya, sel kanker dapat dipindai dengan tepat dan/atau dosis medis radioaktif untuk terapi dapat diberikan dengan tepat sasaran.

Meskipun telah dilakukan penelitian selama puluhan tahun di bidang radionuklida medis ini, hanya sedikit nuklida yang berhasil mendapatkan izin penggunaan klinis. Selain dari uji daya guna dan keamanan klinisnya masih menjadi bagian dari penelitian yang sedang berlangsung, banyak radionuklida juga sulit diproduksi karena waktu paruhnya terlalu pendek. Hal ini mengakibatkan radionuklida tersebut rumit untuk diberi label dan dirunut, atau menjadikan ketersediaannya terbatas. Oleh karena itu, berbagai upaya telah dilakukan untuk memajukan produksi radionuklida medis, termasuk langkah-langkah pemisahan (separasi) yang termasuk kritis. Dalam tahap pemisahan, prosesnya juga harus berlangsung dalam waktu yang relatif singkat dengan efisiensi dan keandalan yang tinggi. Di antara banyak teknologi, ekstraksi (cair-cair) pada perangkat mikrofluida memiliki potensi untuk mengakomodasi hal ini dengan menawarkan lingkungan terkendali dengan rasio permukaan-volume yang tinggi. Area kontak yang luas memungkinkan radionuklida dipisahkan dari bahan sasarannya, dari satu fasa ke fasa lainnya secara cepat, kontinyu, dan efisien.

Bahan pilihan yang umum digunakan untuk membuat perangkat mikrofluida adalah poli-dimetilsiloksan (PDMS). Hal ini dikarenakan kemudahannya untuk ditiru, kecocokan untuk pembuatan prototipe cepat, ketahanan terhadap pH yang ekstrem, dan warnanya yang nil. Namun demikian, PDMS tidak kompatibel dengan pelarut organik, yang biasa digunakan sebagai salah satu fase dalam ekstraksi cair-cair. Sayangnya, solusi saat ini untuk meningkatkan kompatibilitas PDMS melibatkan modifikasi bahan pembuat perangkat mikrofluida, mengubah permukaan secara ex situ, dan in situ masih terbatas dan kurang praktis. Untuk mengatasi keterbatasan PDMS tersebut, kami mengembangkan metode baru untuk menyimpan lapisan nano oksida logam pada dinding perangkat mikrofluida yang telah terikat dengan perangkat bawahnya. Lapisan nano ini dapat memberikan perlindungan tanpa mengubah sifat bahan PDMS yang nyaman. Oleh karena itu, tema sentral disertasi S3 ini adalah untuk mengembangkan teknologi mikrofluida PDMS dengan lapisan nano, yang mampu memisahkan radionuklida medis dari bahan target yang diiradiasi melalui ekstraksi cair-cair aliran kontinu.

Kami memulai dengan memberikan lapisan nano oksida titanium pada panel datar PDMS menggunakan deposisi lapisan atom (dalam bahasa inggris, dikenal sebagai ALD). Pelapisan pada tekanan atmosfer (atau disebut juga AP-ALD) menghasilkan pertumbuhan lapisan nano permukaan dan bawah permukaan. Lapisan nano ini ditemuk-

an dapat meningkatkan ketahanan PDMS terhadap larutan organik sebesar seratus kali lipat dibandingkan dengan PDMS yang tidak diberikan perlakuan, bahkan setelah paparan kontinyu selama 24 jam. Kami juga menemukan bahwa lapisan nano oksida titanium yang dihasilkan juga menyediakan gugus fungsi aktif pada permukaan PDMS, yang ditunjukkan oleh sudut kontak air yang lebih rendah jika dibandingkan dengan permukaan yang tidak diberi perlakuan. Ketika PDMS dipolimerisasikan (dikeraskan) pada suhu yang lebih tinggi, molekul PDMS yang tidak terikat berdifusi keluar lebih sedikit, menghasilkan permukaan yang relatif hidrofilik setidaknya selama 800 jam. Permukaan ini dapat difungsikan lebih lanjut oleh lapisan lain, seperti nanopartikel emas (AuNPs).

Kami kemudian mengembangkan metode untuk memberikan lapisan nano di dalam perangkat mikrofluida PDMS yang terikat menggunakan teknik AP-ALD. Dengan mengalirkan gas reaktif dari proses ALD tersebut melalui saluran mikrofluida, ditemukan cakupan penuh dari dinding saluran mikrofluida yang dilapisi oleh lapisan nano oksida logam, bahkan di dalam perangkat dengan jaringan saluran yang kompleks. Perangkat mikrofluida yang terbuat oleh PDMS ini kemudian dapat diolah lebih lanjut untuk memungkinkan penerapan mikrofluida berbasis PDMS yang lebih luas, yang ditunjukkan melalui tiga studi kasus.

Selanjutnya, lapisan nano oksida silikon diberikan di dalam saluran mikrofluida berbasis PDMS dengan struktur fase pemandu pada perangkatnya. Struktur ini membantu memandu fase air dan organik yang digunakan dalam ekstraksi radionuklida medis, sementara lapisan nano meningkatkan ketahanan perangkat mikrofluida berbasis PDMS terhadap pelarut organik. Sebagai hasilnya, aliran laminar paralel terbentuk dengan penggunaan kombinasi laju alir yang relatif luas. Dengan menggunakan sistem ini, empat radionuklida, termasuk ^{90}Y yang digunakan secara komersial dan ^{225}Ac yang sedang banyak diteliti, diekstraksi dari bahan sasaranya. Ekstraksi maju dan mundur terjadi dalam hitungan detik dengan efisiensi di atas 80-98%, tergantung pada radionuklida, dan menunjukkan sistem yang menjanjikan dengan kemungkinan daur ulang langsung bahan sasaran dan langkah paska-pemrosesan yang lebih sedikit. Dari sini, perangkat mikrofluida berbasis PDMS yang diolah dengan proses deposisi lapisan atom terbukti dapat memisahkan radionuklida medis dengan cara yang cepat, berkelanjutan, dan efisien.

Di samping pendekatan mikrofluida yang dikembangkan untuk pemisahan radionuklida, kami meninjau kembali proses alternatif dan komplementer berbasis adsorpsi untuk memisahkan berbagai radionuklida medis, dengan mengembangkan partikel resin baru. Dengan menggunakan partikel resin ini, kami memisahkan radionuklida medis dengan efisiensi tinggi (di atas 98%) dan dengan tingkat kontaminan di bawah ambang batas yang diizinkan secara hukum. Dua metode pemisahan yang dikembangkan di sini memungkinkan pengembangan solusi yang disesuaikan untuk pemisahan radionuklida medis tertentu secara cepat dan efisien, dengan kemungkinan manfaat tambahan seperti langkah produksi tambahan yang lebih sedikit, limbah radioaktif yang lebih sedikit, dan kemungkinan otomatisasi.

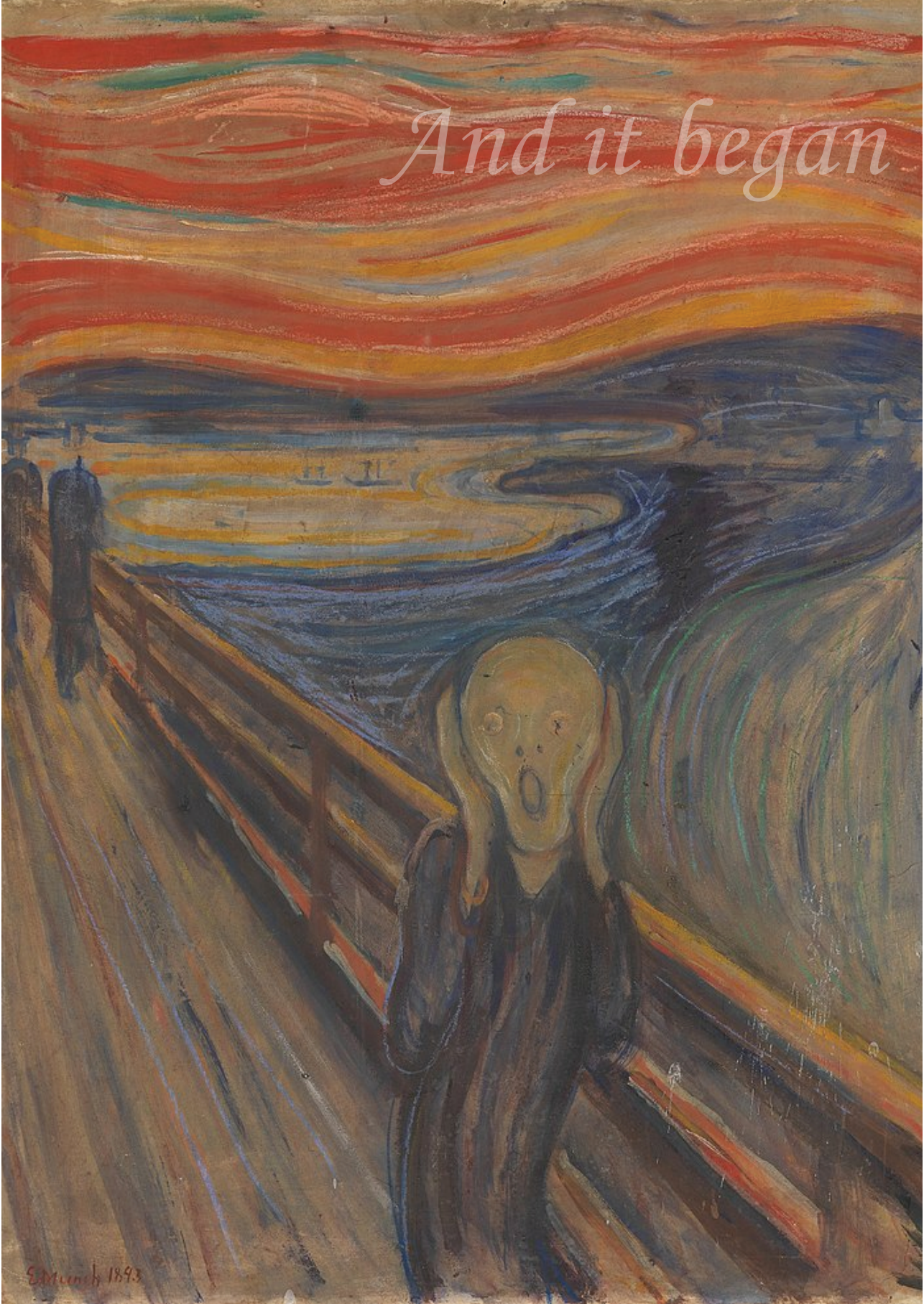
And it began
E. Munch 1893

Skrik
Edvard Munch, 1893

1

Introduction

In this chapter, the background of this dissertation is introduced, summarizing the challenges in medical radionuclide separation and the potential role of microfluidic channel and atomic layer deposition in addressing the challenges. Hereafter, the objectives of this thesis and the corresponding chapters are outlined, followed by the project setup.

1

1.1. Challenges in current medical radionuclide separation

In recent years, radionuclides have gained increasing interest in the field of cancer diagnostics and targeted therapy [1–3]. When combined with certain antibodies or peptides, these radionuclides can be used as a label or as a therapeutic agent [3]. The radiolabelled antibodies or peptides then interact with specific vectors expressed in a malignant cell in a human body, leading to precise imaging or delivery of a therapeutic radiation dose with a minimum dose delivered to the surrounding healthy tissues [4, 5]. To be applicable, these radionuclides should have suitable nuclear decay characteristics, ease of production, and amenable chemistry [6, 7]. While a quick literature study suggests some hundreds of isotopes that fit the requirements, only a handful of them managed to be clinically approved and commercially used in clinics [1, 6, 8]. The most notable commercial radionuclides include gamma-emitting Tc-99m (for single-photon emission computed tomography, SPECT), positron-emitting Ga-68 and F-18 (for positron emission tomography, PET), beta-emitting I-131 (for treatment of thyroid cancer), Sr-89 and Sm-153 (for bone pain palliation), and alpha-emitting Ra-223 (for treatment of metastatic bone cancer) [3, 6]. Aside from their clinical compatibilities, all these radionuclides have two other important qualities: a reasonably short half-life ranging from tens of minutes to a few days and practical convenience to be produced and processed to become radiopharmaceuticals. The half-life defines the imaging/treatment duration, total radiation doses received by the patient and the surrounding personnel, and the treatment efficacy [1, 9, 10]. Hence, only radionuclides with a reasonably short half-life are preferred to limit the superfluous radioactive doses [9]. However, this exact short half-life poses challenges in the second quality, the production steps. As an example, an alternative production route of Ga-68 from Zn takes hours while its half-life ($t_{1/2}$) is only 67.7 minutes [11, 12]. Similar challenges are also encountered in many other potential radionuclides such as theranostic pair Cu-64/Cu-67 [13], beta-emitter Y-90 [14], and alpha-emitter Ac-225 [15]. These radionuclides have a relatively short half-life (12.7 hours for Cu-64, 61.8 hours for Cu-67, 64.1 hours for Y-90, and 9.9 days for Ac-225), yet the production steps could last from a few hours to days. In some cases, the product radionuclides undergo several additional steps to meet the required purity [16–18]. Consequently, a fast and efficient production process, including the critical separation step, is essential in determining the breakthrough and the accessibility of these promising radiopharmaceuticals in the clinic [4, 10, 16, 19–23].

The production process of medical radionuclides generally involves irradiation and separation steps, along with additional post-production labelling and recycling steps (Figure 1.1). A target material (solid, liquid or gas) is usually preprocessed and then irradiated in a nuclear reactor or an accelerator (cyclotron or linear accelerator) resulting in product radionuclides [20]. Furthermore, the choice of the production route depends on target material supply availability, possible nuclear reaction, estimated product yield, and other factors [20, 24, 25]. From the irradiation process, a mixture of target materials, product radionuclides, and various impurities is obtained. This mixture, either initially present in liquid form or dissolved into a solution, should be separated into two or three streams: one containing only the target nuclides, one containing only the product radionuclides, and another possible stream containing the rest of the impurities. The

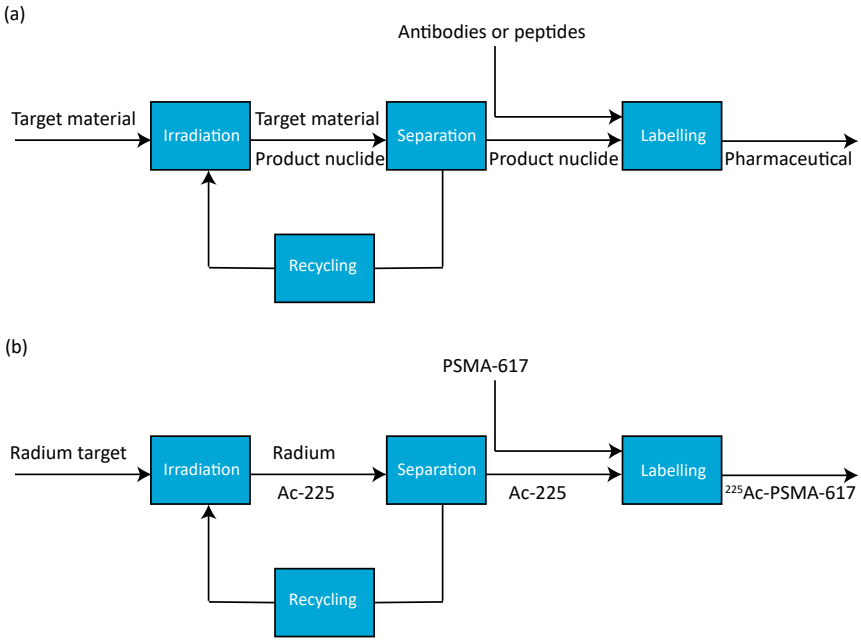

Figure 1.1: (a) Flowchart of a production process of a radiopharmaceutical from a target material and (b) an example of the production of ^{225}Ac-PSMA-617 from radium target.

product radionuclides could then be processed further into radiopharmaceuticals, while the valuable target nuclides could ideally be recycled back. Within this process, this dissertation focuses on the development of the fast and efficient separation step.

Currently, there are two main separation processes used in commercial settings: adsorption and liquid-liquid extraction [26]. In an adsorption-based process such as ion-exchange chromatography, a solution containing both target and product (radio-) nuclides flows into a resin column [20]. Generally, in the column, the product nuclide and its target are both adsorbed on the resin. Afterwards, elution solutions with a different pH are used to take out the product radionuclides and target in the subsequent elution steps. Due to its high selectivity and amenability for automation [16], this separation process has been widely employed [26]. However, there are several issues with the column separation, namely its limited adsorbent capacity, non-continuous process, and in some cases, low radio-stability of the resin [16, 17]. As a result, multiple pre- and post-handling steps and complex fabrication of the resin are required, leading to a time-consuming process or a high amount of radioactive waste [17], disqualifying their implementation for several promising production routes.

In comparison, liquid-liquid extraction does not involve costly resin fabrication and can be straightforward in operation while still offering high selectivity and separation efficiency [26, 27]. Despite the advantages, solvent extraction is not widely used for radionuclide separation. The process requires careful control over the liquid-liquid con-

tact area in a container or a flow channel and the separation of the two liquid phases at its exit. Furthermore, personnel handling in decanting, evaporating, and possibly recovering the solvents is needed, thus the process is difficult to automate, requires high consumption of solvent, and has poor reliability with continuous use [17, 26, 28]. Only recently, with the rise of microfluidics, the solvent extraction method has been revisited [26]. This microfluidics consists of channels typically around 5 to 200 µm in height, 10 to 2000 µm in width and up to a few cm in length, where extraction can take place. As the scale goes down to the micron range, the surface-to-volume ratio increases, improving the separation efficiency while decreasing the amount of solvents needed [26, 29, 30]. Additionally, this downscaling to microscale also leads to possible geometry manipulation, allowing an unsurpassed control of single- and two-phase flows when compared with conventional extractions in a tank or a pipe [31]. This opens the possibility for an automated, continuous separation process using microfluidics [29, 30].

1.2. PDMS microfluidic chip for continuous extraction

Since its rise in the early 2000s, microfluidics has been used in various fields involving fluid manipulation at the micro-scale, including liquid-liquid extraction [32, 33]. In this approach, two or more immiscible fluids are used: typically an aqueous solution and an organic solution. During the extraction, they flow in a micro-scale channel and are brought in contact with each other for a specified length and time before being separated at the outlet junction. Due to the increase in surface-to-volume ratio and the decrease in diffusion length, a high extraction efficiency with short throughput time can be achieved on a single chip even at low concentrations (micromolar to picomolar) [34–38]. These characteristics fit well with the requirements for medical radionuclides separation, that is often done in small volume and low concentration, and within a short processing time. Furthermore, the microfluidics-based approach also offers the possibility to achieve the separation of the medical radionuclides and the recycling of unused, expensive target materials in a single step, along with the possibility of continuous operation and the ease of automation [26, 39]. After the development of the approach, it can be easily numbered up to increase the capacity. Therefore, the concept of using liquid-liquid extraction in microfluidic systems is a potential candidate for fast, efficient, automatable separation of medical radionuclides.

Unfortunately, there are two challenges in using the microfluidic system to separate medical radionuclides. This extraction process involves both an aqueous phase with possibly low/high pH and an organic phase, which are often not compatible with common chip material. Furthermore, both phases should also be separated perfectly at the outlet, as the presence of contaminants is toxic to patients [2, 22]. While there are several approaches to overcome the second challenge, such as modifying the microfluidic channel geometry or surface wettability to guide the two phases through the microfluidic devices in a stable manner [31, 40–42], finding the right material for the microfluidic chip material remains a challenge [34, 43]. Aside from its compatibility with the used solvents, the material should be easy to fabricate and compliant with pharmaceutical production regulations. Especially when it comes to radionuclide processing, the material should also have good tolerance against the radiation doses anticipated during the

contact [44]. Among many fabrication materials for microfluidic chips, polydimethylsiloxane (PDMS) is promising due to its fidelity and high resistance against extreme pH [45]. It has also been used in biomedicine applications due to its biocompatibility and favorable biomechanical behaviour [45]. In comparison to more expensive glass microfluidics, PDMS microfluidic devices could be rapidly prototyped with adjustable designs [32, 43]. When exposed to high doses of radiation damage, the crosslinking reaction between PDMS molecules dominates over the chain scission, leading to less leaching out issues [44, 46, 47]. Furthermore, PDMS can also be used for disposable purposes, catering to Good Manufacturing Practices (GMP) [48]. Thus, this dissertation focuses on the use of PDMS microfluidic devices for the development of liquid-liquid extraction of radionuclides.

1.3. Microfluidic channel coating: atomic layer deposition

While PDMS ticks almost all the important requirements in medical radionuclide separations, it does have one glaring challenge: its poor chemical resistance against organic solvents [49]. When exposed to organic solvents, PDMS swells and deforms, rendering it useless for further use [34, 49]. Unfortunately, most extraction-based radionuclide separations involve the use of water-immiscible organic solvents [50]. To increase the chemical resistance of PDMS, there are two approaches: bulk modification and surface coating. Bulk modification includes optimizing the PDMS curing parameters [51, 52] and blending/doping PDMS with other chemicals [43, 53, 54]. This approach, however, reduces the overall benefits of PDMS such as its flexibility, transparency, and fidelity [43]. On the contrary, surface coating offers a protective layer, acting as a barrier towards organic solvent diffusion without sacrificing the convenient PDMS bulk properties [53]. Therefore, this dissertation explores the use of surface modification in addressing the issue of chemical resistance.

Surface modification of a PDMS microfluidic channel can be done ex-situ and in-situ. In an ex-situ approach, the modification is conducted on the surface of one or more PDMS slabs before the bonding step. Despite the simplicity, the modified PDMS slabs are often difficult to bond [55]. Due to different surface properties and chemical groups, the widely used oxygen plasma bonding [56] is not applicable [55]. Other bonding techniques such as hot press, clamping, partial curing and adhesion can be intrusive to the small channel geometry and/or result in a non-leak-tight channel [57].

In an in-situ approach, the modification is conducted internally, after bonding. This approach does not reduce the leak-tightness of the channels, leading to modified and ready-to-use PDMS microfluidic chips. There are two ways to deposit inert coatings on PDMS microfluidic channels in-situ: liquid-phase and gas-phase processing. Current methods mostly focus on liquid-phase processing, such as the use of glass-like materials and fluoro-based coatings [58, 59]. Yet, these methods are difficult, costly or time-consuming [34, 60]. The removal of the remaining liquid with gas is also challenging due to the high viscosity difference, especially in networks of microchannels in which the liquid can get trapped in part of the network [59]. Moreover, the resulting coatings are relatively thick and not conformal with respect to the features of the microchannels [61].

Gas-phase processing, on the other hand, allows the deposition of thin conformal

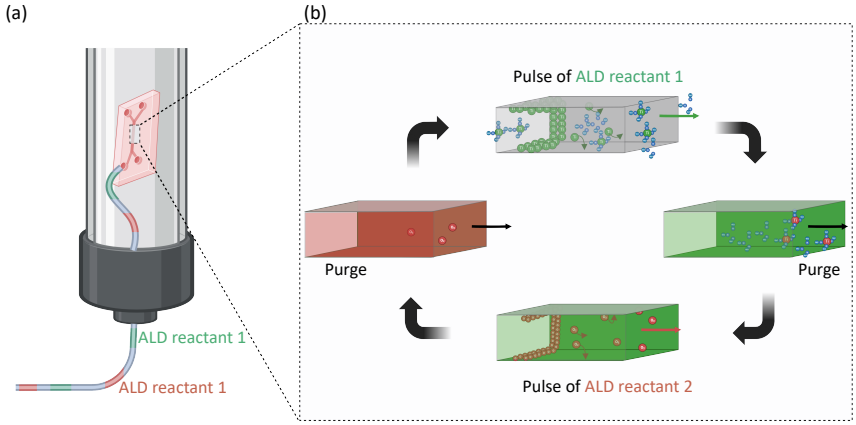

Figure 1.2: Illustration of in-channel coating of bonded PDMS microfluidic chips by alternatingly flowing two ALD reactants through the channel. The microfluidic chip is placed in a tubular glass column to contain excess ALD reactants. (b) Schematic figure of an atmospheric pressure atomic layer deposition in a microfluidic chip

coating. Among the gas-phase processes, atomic layer deposition (ALD) stands out due to its high uniformity, even when coating complex structures [62]. By introducing gas reactants to the surface alternatingly, self-limiting reactions can take place and thin, conformal nano-layers can be deposited. Furthermore, the thickness of the coating, and subsequently its performance, can be controlled by determining the number of the alternating reactions (cycles) [62]. The choice of the coating types can also be tuned by changing the reactants, resulting in a wide variety of options [62, 63]. In the case of modifying the surface of PDMS channels in-situ to increase the organic chemical resistance, ALD can be used to deposit conformal metal oxide nano-layers. These metal oxide nano-layers have been explored as a gas barrier layer [64]. In our case, they can act as a barrier layer to reduce or even omit direct contact between PDMS and organic solvents. Even more, these metal oxides also have the potential to increase the radiation damage tolerance of PDMS [65, 66].

However, to the author's best knowledge, the potential of ALD to coat the PDMS microfluidic channels in-situ has never been realized. The typical ALD processes are conducted in vacuum. As a result, the transport of the gas reactants from the chamber of the ALD reactor to the surface relies mostly on diffusion and other transport phenomena in a vacuum. When placing a bonded microfluidic channel in the chamber, the resulting pressure drop between the inlet(s) and the outlet(s) of the channel is considerably low. Consequently, it might take an impractically long time for the reactants from the chamber to diffuse into the channels and coat the walls over their entire length [67]. To overcome this issue, atmospheric pressure atomic layer deposition (AP-ALD) is a good alternative. By making use of flow driven by certain pressure drops, the reactants get transported through the channel faster while reducing the diffusion lengths needed to reach the PDMS microfluidic channel surface. Figure 1.2 illustrates the introduction of the gas and the AP-ALD process taking place inside the channel. Moreover, conducting ALD at atmospheric pressure eliminates the need for expensive vacuum technologies,

bringing this approach closer to commercial applications. Therefore, in this dissertation, AP-ALD for PDMS microchannels is explored, so that the deposited metal oxide nano-layers allow the introduction of organic solvents into the microchannels, enabling a fast and efficient medical radionuclide separation.

1.4. Thesis objective

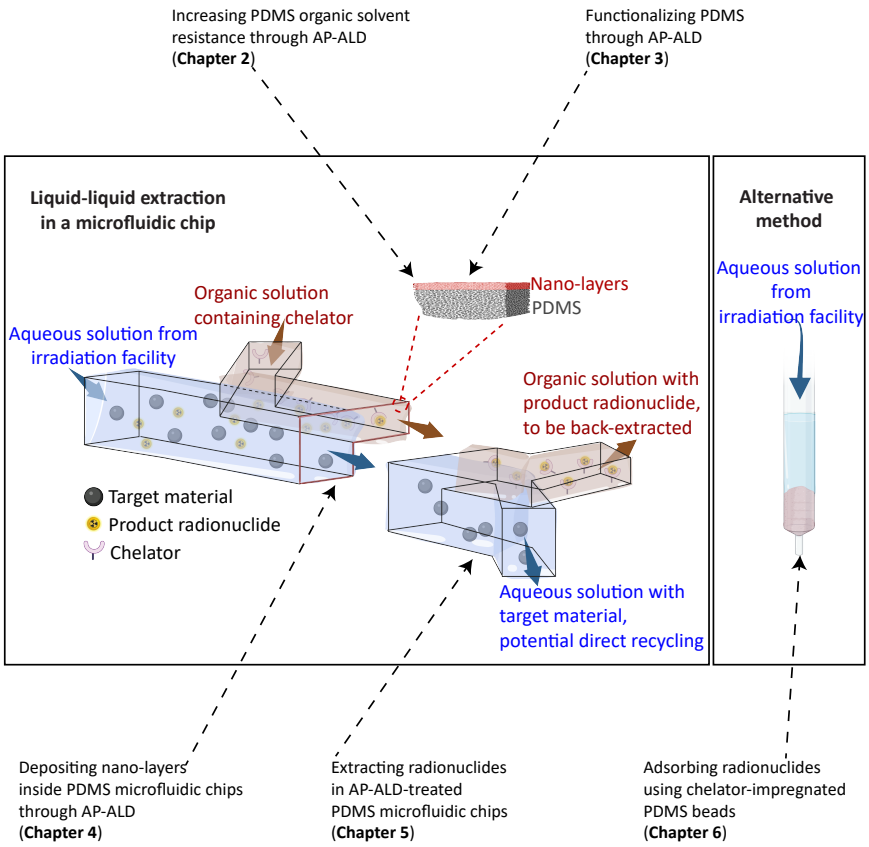

Figure 1.3: Illustration of the concept of the microfluidic chip and the corresponding 5 research objectives to develop the chip aimed in this dissertation .

This dissertation aims to develop a PDMS microfluidic chip with a conformal metal oxide nano-layer coating to accommodate liquid-liquid extraction of medical radionuclides. Figure 1.3 illustrates the concept of the microfluidic chip aimed in this dissertation. In the chip, two immiscible liquids flow parallel to each other for radionuclide separation. One of the liquids is typically an acidic solution coming out from the irradiation facility, containing both the target and product (radio-) nuclide. This aqueous solution is brought into contact with an organic solvent containing an extracting agent, called a

chelator. This chelator can have a high selectivity towards the product radionuclide over its target materials, forming stable coordination bonds [50]. During phase contact, the product radionuclide diffuses and is selectively chelated. As a result, the aqueous solution containing only the target nuclide and the organic solution containing only the chelated product nuclide are obtained. The target nuclide solution is ideally recycled back to the irradiation facility while the organic solution containing chelated product nuclide flows into another similar microfluidic chip to be back-extracted. In this step, the organic solution is brought in contact with a new aqueous solution with a specific pH, breaking the chelation such that the product radionuclide gets extracted into the aqueous solution [50]. The aqueous solution, typically HCl, can then be processed further to radiopharmaceuticals. The organic solution containing only the chelating agent is ideally re-used for the next extraction process. To accommodate the stable parallel flow and perfect fluid disengagement during the extraction process, a microchannel with a difference in height is used, allowing pinning of the interface between the two liquids [31, 40, 41, 68].

The overall aim of this thesis can be divided into five objectives, each described in a separate chapter, as illustrated in Figure 1.3. We first have to understand the formation of nano-layers on PDMS substrates. While conventional vacuum ALD on PDMS has been explored for modifying the surface wettability, biocompatibility, and gas barrier property [69–73], there is limited literature on the use of AP-ALD and their resulting layers. Therefore, the first two objectives of this PhD thesis are:

- Exploring the use of atmospheric pressure atomic layer deposition (AP-ALD) in increasing the organic solvent resistance of polydimethylsiloxane flat substrates **(Chapter 2)**.
- Evaluating the use of atmospheric pressure atomic layer deposition (AP-ALD) in functionalizing the surface of polydimethylsiloxane flat substrates **(Chapter 3)**.

After studying the deposition of nano-layers on PDMS flat substrates, the third objective of this thesis is:

- Developing a method for the use of atmospheric pressure atomic layer deposition (AP-ALD) for in-situ coating of polydimethylsiloxane (PDMS) microfluidic chips **(Chapter 4)**.

Once we understood how to treat PDMS with atomic layer deposition and developed a method for in situ coating of the microfluidic channels, the fourth objective of the thesis is:

- Using the AP-ALD-treated PDMS microfluidic chips to explore the use of microfluidic liquid-liquid extraction for the separation of medical radionuclides from their target materials **(Chapter 5)**.

While developing all methods for the microfluidic liquid-liquid extraction of medical radionuclide using PDMS, including the ALD methods to protect PDMS from swelling upon contact with organic solvents, we realised that we could also take advantage of the

swelling of PDMS. This idea, not in the original plan for the project, led to the unexpected journey to using PDMS as a resin in a chromatography column and exploring its use for radionuclide separation as an alternative to the developed microfluidic liquid-liquid separation method. The fifth objective of this thesis, which led to a patent (No. 2037212 [74]), is:

- Developing chelator-impregnated PDMS beads and exploring their use in a chromatography column for the separation of medical radionuclides from their target materials **(Chapter 6)**.

1.5. Project Setup

This dissertation is conducted within the framework of Open Technology Programme (with project number 16913) financed by the Dutch Research Council (NWO). The project, titled "Fast and Efficient Purification of Medical Isotopes by Microfluidic Extraction", is carried out by three PhD candidates along with collaborations with NRG (NL), Urenco (NL), TRIUMF (CA), Fluidominica (PT) and University Medical Center of Groningen (NL). The main aims of my PhD partners were to optimize the geometry of microfluidic channels and to develop a chemical method in liquid-liquid extractions. The synergy between our projects led to a set of joint publications, residing in Chapter 5, Chapter 6 and some other publications-in-preparations.

1

References

[1] T. Haddad, A. Fard-Esfahani, and R. Vali, *A review of pediatric neuroendocrine tumors, their detection, and treatment by radioisotopes,* Nuclear Medicine Communications **42**, 21 (2021).

[2] F. B. Payolla, A. C. Massabni, and C. Orvig, *Radiopharmaceuticals for diagnosis in nuclear medicine: A short review,* Eclética Química **44**, 11 (2019).

[3] G. Crișan, N. S. Moldovean-Cioroianu, D.-G. Timaru, G. Andrieș, C. Căinap, and V. Chiș, *Radiopharmaceuticals for pet and spect imaging: A literature review over the last decade,* International Journal of Molecular Sciences **23**, 5023 (2022).

[4] W. A. Weber, J. Czernin, C. J. Anderson, R. D. Badawi, H. Barthel, F. Bengel, L. Bodei, I. Buvat, M. DiCarli, M. M. Graham, J. Grimm, K. Herrmann, L. Kostakoglu, J. S. Lewis, D. A. Mankoff, T. E. Peterson, H. Schelbert, H. Schöder, B. A. Siegel, and H. W. Strauss, *The future of nuclear medicine, molecular imaging, and theranostics,* Journal of Nuclear Medicine **61**, 263S (2020).

[5] J. Pellico, P. J. Gawne, and R. T. de Rosales, *Radiolabelling of nanomaterials for medical imaging and therapy,* Chemical Society Reviews **50**, 3355 (2021).

[6] T. Das and M. Pillai, *Options to meet the future global demand of radionuclides for radionuclide therapy,* Nuclear Medicine and Biology **40**, 23 (2013).

[7] P. J. Blower, *A nuclear chocolate box: the periodic table of nuclear medicine,* Dalton Transactions **44**, 4819 (2015).

[8] C. Decristoforo, O. Neels, and M. Patt, *Emerging radionuclides in a regulatory framework for medicinal products–how do they fit?* Frontiers in Medicine **8**, 678452 (2021).

[9] C.-H. Yeong, M.-h. Cheng, and K.-H. Ng, *Therapeutic radionuclides in nuclear medicine: current and future prospects,* Journal of Zhejiang University. Science. B **15**, 845 (2014).

[10] S. M. Qaim, I. Spahn, B. Scholten, S. Spellerberg, and B. Neumaier, *The role of chemistry in accelerator-based production and separation of radionuclides as basis for radiolabelled compounds for medical applications,* Radiochimica Acta **110**, 707 (2022).

[11] M. K. Pandey, J. F. Byrne, K. N. Schlasner, N. R. Schmit, and T. R. DeGrado, *Cyclotron production of ^{68}Ga in a liquid target: effects of solution composition and irradiation parameters,* Nuclear Medicine and Biology **74**, 49 (2019).

[12] P. J. Blower, R. Cusnir, A. Darwesh, N. J. Long, M. T. Ma, B. E. Osborne, T. W. Price, J. Pellico, G. Reid, R. Southworth, *et al.*, *Gallium: New developments and applications in radiopharmaceutics,* Advances in Inorganic Chemistry **78**, 1 (2021).

[13] M. Hussain, S. M. Qaim, I. Spahn, M. N. Aslam, and B. Neumaier, *Copper radionuclides for theranostic applications: Towards standardisation of their nuclear data. a mini-review,* Frontiers in Chemistry **11**, 1270351 (2023).

[14] B. J. Tickner, G. J. Stasiuk, S. B. Duckett, and G. Angelovski, *The use of yttrium in medical imaging and therapy: Historical background and future perspectives,* Chemical Society Reviews **49**, 6169 (2020).

[15] D. A Scheinberg and M. R McDevitt, *Actinium-225 in targeted alpha-particle therapeutic applications,* Current radiopharmaceuticals **4**, 306 (2011).

[16] A. Dash and R. Chakravarty, *Pivotal role of separation chemistry in the development of radionuclide generators to meet clinical demands,* RSC Advances **4**, 42779 (2014).

[17] M. F. Alam, Z. A. Begum, Y. Furusho, H. Hasegawa, and I. M. Rahman, *Selective separation of radionuclides from environmental matrices using proprietary solid-phase extraction systems: A review,* Microchemical Journal **181**, 107637 (2022).

[18] J. Kim, H. Park, and K. Chun, *Effective separation method of ^{64}Cu from ^{67}Ga waste product with a solvent extraction and chromatography,* Applied Radiation and Isotopes **68**, 1623 (2010).

[19] J. Notni and H.-J. Wester, *Re-thinking the role of radiometal isotopes: Towards a future concept for theranostic radiopharmaceuticals,* Journal of Labelled Compounds and Radiopharmaceuticals **61**, 141 (2018).

[20] J.-V. Kratz and K. H. Lieser, *Nuclear and Radiochemistry* (Wiley Online Library, 2013).

[21] P. Schmor, *Review of cyclotrons for the production of radioactive isotopes for medical and industrial applications,* Reviews of Accelerator Science and Technology **4**, 103 (2011).

[22] E. A. Perini, M. Skopchenko, T. T. Hong, R. Harianto, A. Maître, M. R. R. Rodríguez, N. de Oliveira Santos, Y. Guo, X. Qin, C. A. Zeituni, *et al.*, *Pre-feasibility study for establishing radioisotope and radiopharmaceutical production facilities in developing countries,* Current Radiopharmaceuticals **12**, 187 (2019).

[23] S. M. Qaim, *Theranostic radionuclides: recent advances in production methodologies,* Journal of Radioanalytical and Nuclear Chemistry **322**, 1257 (2019).

[24] C. Hoehr, F. Bénard, K. Buckley, J. Crawford, A. Gottberg, V. Hanemaayer, P. Kunz, K. Ladouceur, V. Radchenko, C. Ramogida, *et al.*, *Medical isotope production at TRIUMF–from imaging to treatment,* Physics Procedia **90**, 200 (2017).

[25] A. Azzam, S. Said, and M. Al-Abyad, *Evaluation of different production routes for the radio medical isotope ^{203}Pb using TALYS 1.4 and EMPIRE 3.1 code calculations,* Applied Radiation and Isotopes **91**, 109 (2014).

[26] P. Martini, A. Adamo, N. Syna, A. Boschi, L. Uccelli, N. Weeranoppanant, J. Markham, and G. Pascali, *Perspectives on the use of liquid extraction for radioisotope purification,* Molecules **24**, 334 (2019).

[27] A. Dash, F. R. Knapp Jr, and M. Pillai, *^{99}Mo/^{99m}Tc separation: An assessment of technology options,* Nuclear Medicine and Biology **40**, 167 (2013).

[28] S. J. do Carmo, P. J. Scott, and F. Alves, *Production of radiometals in liquid targets,* EJNMMI Radiopharmacy and Chemistry **5**, 1 (2020).

[29] K. Wang and G. Luo, *Microflow extraction: A review of recent development,* Chemical Engineering Science **169**, 18 (2017).

[30] D. Ciceri, J. M. Perera, and G. W. Stevens, *The use of microfluidic devices in solvent extraction,* Journal of Chemical Technology & Biotechnology **89**, 771 (2014).

[31] P. Vulto, S. Podszun, P. Meyer, C. Hermann, A. Manz, and G. A. Urban, *Phaseguides: a paradigm shift in microfluidic priming and emptying,* Lab on a Chip **11**, 1596 (2011).

[32] G. M. Whitesides, *The origins and the future of microfluidics,* Nature **442**, 368 (2006).

[33] N. Convery and N. Gadegaard, *30 years of microfluidics,* Micro and Nano Engineering **2**, 76 (2019).

[34] S. Goyal, A. V. Desai, R. W. Lewis, D. R. Ranganathan, H. Li, D. Zeng, D. E. Reichert, and P. J. Kenis, *Thiolene and SIFEL-based microfluidic platforms for liquid–liquid extraction,* Sensors and Actuators B: Chemical **190**, 634 (2014).

[35] C. Priest, J. Zhou, R. Sedev, J. Ralston, A. Aota, K. Mawatari, and T. Kitamori, *Microfluidic extraction of copper from particle-laden solutions,* International Journal of Mineral Processing **98**, 168 (2011).

[36] C. Priest, J. Zhou, S. Klink, R. Sedev, and J. Ralston, *Microfluidic solvent extraction of metal ions and complexes from leach solutions containing nanoparticles,* Chemical Engineering & Technology **35**, 1312 (2012).

[37] S. Marsousi, J. Karimi-Sabet, M. A. Moosavian, and Y. Amini, *Liquid-liquid extraction of calcium using ionic liquids in spiral microfluidics,* Chemical Engineering Journal **356**, 492 (2019).

[38] P. Martini, L. Uccelli, A. Duatti, L. Marvelli, J. Esposito, and A. Boschi, *Highly efficient micro-scale liquid-liquid in-flow extraction of 99mtc from molybdenum,* Molecules **26**, 5699 (2021).

[39] J. G. Kralj, H. R. Sahoo, and K. F. Jensen, *Integrated continuous microfluidic liquid–liquid extraction,* Lab on a Chip **7**, 256 (2007).

[40] A. Hibara, S. Iwayama, S. Matsuoka, M. Ueno, Y. Kikutani, M. Tokeshi, and T. Kitamori, *Surface modification method of microchannels for gas–liquid two-phase flow in microchips,* Analytical Chemistry **77**, 943 (2005).

[41] A. Hibara, M. Fukuyama, M. Chung, C. Priest, and M. A. Proskurnin, *Interfacial phenomena and fluid control in micro/nanofluidics,* Analytical Sciences **32**, 11 (2016).

[42] A. Aota, K. Mawatari, S. Takahashi, T. Matsumoto, K. Kanda, R. Anraku, A. Hibara, M. Tokeshi, and T. Kitamori, *Phase separation of gas–liquid and liquid–liquid microflows in microchips,* Microchimica Acta **164**, 249 (2009).

[43] K. S. Elvira, F. Gielen, S. S. Tsai, and A. M. Nightingale, *Materials and methods for droplet microfluidic device fabrication,* Lab on a Chip **22**, 859 (2022).

[44] K. Lee, D. Lee, S. Baek, J. Kim, J. Park, S. J. Lee, S. Park, J. Kim, J.-L. Lee, W. K. Chung, *et al.*, *Radiation damage of polydimethylsiloxane and polyimide by X-ray free-electron laser,* Applied Sciences **12**, 8431 (2022).

[45] A. Victor, J. Ribeiro, and F. F. Araújo, *Study of PDMS characterization and its applications in biomedicine: A review,* Journal of Mechanical Engineering and Biomechanics **4**, 1 (2019).

[46] J. Davenas, I. Stevenson, N. Celette, S. Cambon, J. Gardette, A. Rivaton, and L. Vignoud, *Stability of polymers under ionising radiation: the many faces of radiation interactions with polymers,* Nuclear Instruments and Methods in Physics Research Section B: Beam Interactions with Materials and Atoms **191**, 653 (2002).

[47] Q. Liu, W. Huang, B. Liu, P.-C. Wang, and H.-B. Chen, *Gamma radiation chemistry of polydimethylsiloxane foam in radiation-thermal environments: experiments and simulations,* ACS Applied Materials & Interfaces **13**, 41287 (2021).

[48] K. Raj M and S. Chakraborty, *PDMS microfluidics: A mini review,* Journal of Applied Polymer Science **137**, 48958 (2020).

[49] R. Dangla, F. Gallaire, and C. N. Baroud, *Microchannel deformations due to solvent-induced PDMS swelling,* Lab on a Chip **10**, 2972 (2010).

[50] H. Itabashi and T. Nakahara, *Chelation solvent extraction for separation of metal ions, Comprehensive Analytical Chemistry Volume 41* (2003).

[51] J. Lee, J. Kim, H. Kim, Y. M. Bae, K.-H. Lee, and H. J. Cho, *Effect of thermal treatment on the chemical resistance of polydimethylsiloxane for microfluidic devices,* Journal of Micromechanics and Microengineering **23**, 035007 (2013).

[52] Y. Huang, K. Choi, and C. H. Hidrovo, *The improved resistance of PDMS to pressure-induced deformation and chemical solvent swelling for microfluidic devices,* Microelectronic Engineering **124**, 66 (2014).

[53] J. Liu, Y. Yao, X. Li, and Z. Zhang, *Fabrication of advanced polydimethylsiloxane-based functional materials: Bulk modifications and surface functionalizations,* Chemical Engineering Journal **408**, 127262 (2021).

[54] M. P. Wolf, G. B. Salieb-Beugelaar, and P. Hunziker, *PDMS with designer functionalities—properties, modifications strategies, and applications,* Progress in Polymer Science **83**, 97 (2018).

[55] M. A. Eddings, M. A. Johnson, and B. K. Gale, *Determining the optimal PDMS–PDMS bonding technique for microfluidic devices,* Journal of Micromechanics and Microengineering **18**, 067001 (2008).

[56] M. J. Owen and P. J. Smith, *Plasma treatment of polydimethylsiloxane,* Journal of Adhesion Science and Technology **8**, 1063 (1994).

[57] A. Borók, K. Laboda, and A. Bonyár, *PDMS bonding technologies for microfluidic applications: A review,* Biosensors **11**, 292 (2021).

[58] B.-Y. Kim, L.-Y. Hong, Y.-M. Chung, D.-P. Kim, and C.-S. Lee, *Solvent-resistant PDMS microfluidic devices with hybrid inorganic/organic polymer coatings,* Advanced Functional Materials **19**, 3796 (2009).

[59] A. Shakeri, S. Khan, and T. F. Didar, *Conventional and emerging strategies for the fabrication and functionalization of PDMS-based microfluidic devices,* Lab on a Chip **21**, 3053 (2021).

[60] F. Kotz, P. Risch, D. Helmer, and B. E. Rapp, *Highly fluorinated methacrylates for optical 3D printing of microfluidic devices,* Micromachines **9**, 115 (2018).

[61] A. R. Abate, D. Lee, T. Do, C. Holtze, and D. A. Weitz, *Glass coating for PDMS microfluidic channels by sol–gel methods,* Lab on a Chip **8**, 516 (2008).

[62] H. Van Bui, F. Grillo, and J. R. van Ommen, *Atomic and molecular layer deposition: off the beaten track,* Chemical Communications **53**, 45 (2017).

[63] J. R. van Ommen, A. Goulas, and R. L. Puurunen, *Atomic layer deposition,* Kirk-Othmer Encyclopedia of Chemical Technology (2021).

[64] M. Groner, S. George, R. McLean, and P. Carcia, *Gas diffusion barriers on polymers using al2o3 atomic layer deposition,* Applied Physics Letters **88** (2006).

[65] A. Lushchik, C. Lushchik, V. Nagirnyi, S. Pazylbek, O. Sidletskiy, K. Schwartz, E. Shablonin, A. Shugai, and E. Vasil'chenko, *On the mechanisms of radiation damage and prospects of their suppression in complex metal oxides,* Physica Status Solidi (B) **250**, 261 (2013).

[66] K. Arshak and O. Korostynska, *Response of metal oxide thin film structures to radiation,* Materials Science and Engineering: B **133**, 1 (2006).

[67] M. Ylilammi, O. M. Ylivaara, and R. L. Puurunen, *Modeling growth kinetics of thin films made by atomic layer deposition in lateral high-aspect-ratio structures,* Journal of Applied Physics **123** (2018).

[68] P. Desir, T.-Y. Chen, M. Bracconi, B. Saha, M. Maestri, and D. G. Vlachos, *Experiments and computations of microfluidic liquid–liquid flow patterns,* Reaction Chemistry & Engineering **5**, 39 (2020).

[69] B. Gong, J. C. Spagnola, and G. N. Parsons, *Hydrophilic mechanical buffer layers and stable hydrophilic finishes on polydimethylsiloxane using combined sequential vapor infiltration and atomic/molecular layer deposition,* Journal of Vacuum Science & Technology A **30** (2012).

[70] S. H. Astaneh, G. Jursich, C. Sukotjo, and C. G. Takoudis, *Surface and subsurface film growth of titanium dioxide on polydimethylsiloxane by atomic layer deposition,* Applied Surface Science **493**, 779 (2019).

[71] E. Y. Choi, J.-H. Kim, B.-J. Kim, J. H. Jang, J. Kim, and N. Park, *Development of moisture-proof polydimethylsiloxane/aluminum oxide film and stability improvement of perovskite solar cells using the film,* RSC advances **9**, 11737 (2019).

[72] J. C. Spagnola, B. Gong, and G. N. Parsons, *Surface texture and wetting stability of polydimethylsiloxane coated with aluminum oxide at low temperature by atomic layer deposition,* Journal of Vacuum Science & Technology A **28**, 1330 (2010).

[73] R. Pessoa, V. dos Santos, S. Cardoso, A. Doria, F. Figueira, B. Rodrigues, G. Testoni, M. Fraga, F. Marciano, A. Lobo, and H. Maciel, *TiO_2 coatings via atomic layer deposition on polyurethane and polydimethylsiloxane substrates: Properties and effects on C. albicans growth and inactivation process,* Applied Surface Science **422**, 73 (2017).

[74] A. Santoso, S. Trapp, V. van Steijn, R. de Kruijff, and J. R. van Ommen, *Method for preparing silicon elastomer beads loaded with chelating agents and their use for the separation of radionuclides,* Netherlands **Number: 2037212** (2024).

Resist! Again, resist!

De bedreigde zwaan
Jan Asselijn, 1650

2

AP-ALD to increase organic solvent resistance of PDMS

In this study, we explore three variants of atomic layer deposition (ALD) to deposit titanium oxide on the soft polymer Polydimethylsiloxane (PDMS). We show that the organic solvent resistance of PDMS is increased by two orders of magnitude compared to uncoated PDMS for ALD performed at atmospheric pressure, which results in a unique surface-subsurface coating of PDMS.

This chapter has been published in Chemical Communication **58**, 10805 (2022) [1].

2.1. Introduction

Since its introduction as a material for microfluidics in 1998 [2], the rise of polydimethylsiloxane (PDMS) has revolutionized research in the fields of medicine, biology, and chemistry.[3] While PDMS is easy to micro-mold, cheap, and amicable in rapid prototyping, it has one major drawback: its poor chemical resistance against common organic solvents.[2–6] Upon contact, PDMS swells and deforms, rendering it useless in many applications such as solvent-based extraction, production of liposomes, and flow chemistry for organic synthesis. Currently, most approaches focus on the use of inert coatings such as glass-like materials and fluoro-based polymers.[7–10] The coating processes, however, involve difficult, costly or time-consuming steps.[11–13] Furthermore, the resulting coatings are typically relatively thick with respect to the features of the microchannels, such that the properties of the channel walls do not stem from the soft and pliant bulk properties of PDMS, but from the hard and brittle surface properties of the coating.[8]

To overcome inherent disadvantages of existing PDMS coatings, metal oxide nanofilms present a promising class of materials due to their ability to withstand organic solvents[14, 15] while being nanoscopically thin and faithfully following the structures of the PDMS. Among many surface deposition techniques, atomic layer deposition (ALD) stands out for its high uniformity, even when coating complex structures.[16] This uniformity stems from the successive build up of the coating by exposing a surface to alternating, self-limiting reactions. [16] It is hence interesting to explore the coating of PDMS with metal oxide nano-films through ALD in order to achieve organic solvent resistance of PDMS.

A general challenge in coating polymers with a thin layer of metal oxide through ALD arises from the difference in thermal expansion coefficient of the metal oxide coating and the polymer. Thermal expansion or contraction leads to cracks in the coating, [17–21] compromising its performance. [17–24] Adding intermediate layers may solve this problem, at the expense of a more complex process.[21] While there is significant advancement on ALD coating of hard-set polymers such as polyethylene, polypropylene, polyethylene terephthalate (PET), and polylactic acid (PLA), [25–27] examples of successful ALD coatings on PDMS are scarce. The additional complexity arises from the non-reactive porous nature of PDMS, [17] such that the reactions are not only confined to the surface, but also take place in the subsurface of the PDMS. This turns ALD coating of PDMS into a complex reaction-diffusion problem, in which reactivity, reactant residence time, operating conditions and substrate pre-treatment all play a role in the resulting morphology. [28–31] Even when moderate temperature, time-consuming steps or rigorous sample preparations are employed, studies so far reported metal oxide layers on PDMS with varying degree of conformality and robustness.[17, 29, 30] An outstanding challenge hence is the development of a simple ALD process for metal oxides on PDMS to significantly expand the use of PDMS in practical applications involving the use of organic solvents.

In this paper, we explore three variants of ALD to coat titanium oxide on PDMS. Aside from its resistance against organic solvents, titanium oxide is chosen over other metal oxides for its relatively mild ALD precursors.[14, 15] We show that these three variants lead to three different types of treatments: a surface treatment, a subsurface treatment,

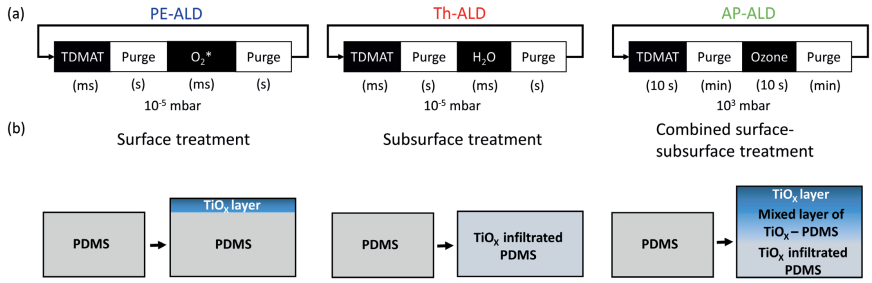

Figure 2.1: (a) Illustration of three different variants of ALD and (b) simplified representations of the resulting deposition profiles (details in Figure 2.2).

and a combined surface-subsurface treatment. We tested the resistance of the resulting coatings against a variety of common solvents and found the surface-subsurface treatment to be the most successful, with an increase in chemical resistance over two orders of magnitude as compared to untreated PDMS.

2.2. Result and discussion

We fabricated PDMS samples by mixing Sylgard 184 elastomer (Dow-Corning) and its curing agent in a 10 to 1 weight ratio and subsequent curing of the mixture at 200°C for at least 10 hours. PDMS samples were treated with ALD using a Ti precursor (tetrakis-(dimethylamino)titanium, TDMAT) and an oxidizing agent. Reactants were sequentially introduced into the ALD reactor chamber. In between, the reactor was purged with an inert gas. Unless stated otherwise, we repeated this sequence, known as an ALD cycle, 100 times and carried out the ALD process at 100°C. The difference between the three explored ALD variants stems from the used oxidizing agent, the used pressure, and the used reactant pulse and purge times, see Fig. 2.1a. We used a strong and a mild oxidizing agent. As demonstrated later, the former led to a nanoscopically thin TiO_x coating on the PDMS surface, while the latter led to infiltration of TiO_x inside the PDMS, see the left and middle panel in Fig. 2.1b. As strong oxidizing agent, we used oxygen plasma and refer to this first variant as plasma enhanced ALD (PE-ALD). As mild oxidizing agent, we used water vapour and refer to this second variant as thermal ALD (Th-ALD). Besides these two variants carried out under vacuum, we also performed ALD at atmospheric pressure, requiring comparatively longer times for the pulse and purge steps. As demonstrated later, this led to a combined surface-subsurface layer of TiO_x, see the right panel in Fig. 2.1b. Here, we used ozone as the oxidizing agent and refer this third variant as atmospheric pressure ALD (AP-ALD). Further details are given in Supporting Information.

We analysed the surface and subsurface of the ALD coated PDMS samples using X-Ray photoelectron spectroscopy (XPS). To obtain the elemental analysis of the surface and subsurface, we sequentially etched the surface for 5-50 seconds with an ion-beam etching unit and then performed an XPS reading. To convert the etch time into an etch depth, we placed a silicon wafer next to the PDMS samples during the ALD process, to coat them with TiO_x, and subsequently performed comparative etching measurements,

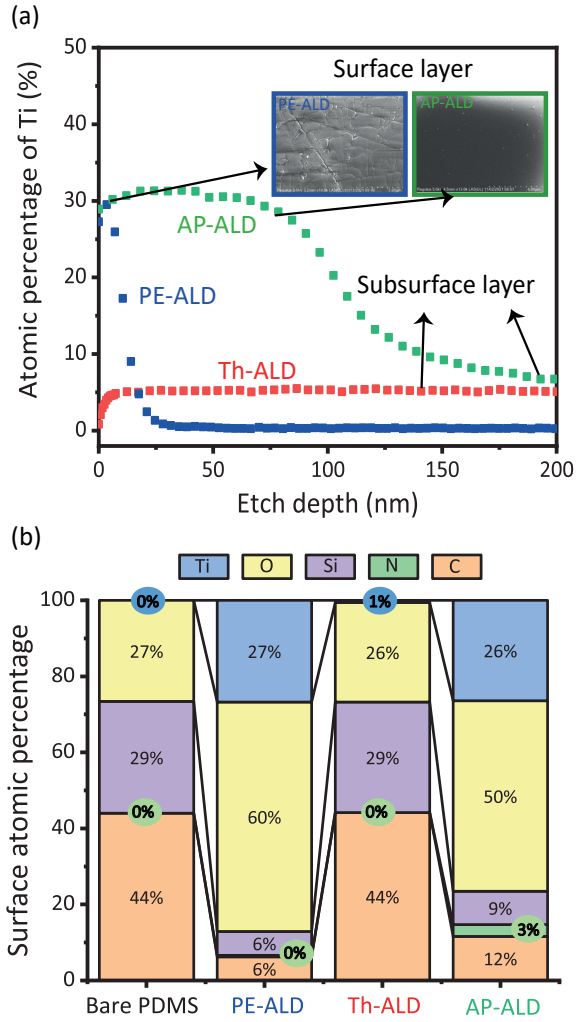

Figure 2.2: (a) XPS depth profiling showing the atomic percentage of titanium in the surface and subsurface of various PDMS samples and (b) XPS elemental analysis of the surface. All depositions were conducted at 100°C for 100 cycles, and the TiO_x layer thickness is estimated to be 7 and 78 nm for the PE-ALD and AP-ALD treated samples respectively.

see Section S1 and Fig.2.10 for details. We note that ALD on soft materials such as PDMS where infiltration may occur is more ambiguous to characterize than ALD on hard materials without infiltration. We therefore choose to omit the commonly used concept of growth per cycle.

Fig. 2.2a shows how the atomic percentage of titanium changes along the depth of the PDMS samples coated with the three ALD variants. The PE-ALD treated PDMS shows a significant atomic percentage of titanium at the surface (before etching). After 7 nm,

the percentage rapidly drops to zero. A closer look at the XPS surface spectra confirms the dominance of titanium and oxygen atoms, with an atomic ratio of about 1 to 2, indicating TiO_2 deposition on the surface (Fig. 2.2b). PE-ALD hence leads to a layer of TiO_x at the surface of the PDMS. In sharp contrast, PDMS treated with Th-ALD shows hardly any titanium on the surface itself (Figure 2.2a). In fact, the surface composition is comparable to bare PDMS, as evident from Fig. 2.2b. Interestingly, a meaningful percentage of titanium (~5%) is found in the subsurface of the PDMS, over an etch depth of ~200 nm, see Fig. 2.2a. Th-ALD hence leads to a TiO_x infiltrated PDMS layer. From the above findings, we infer that the high reactivity of the oxygen plasma leads to nucleation only at the surface of the PDMS, while the lower reactivity of water vapour allows for the diffusion of both reactants into the PDMS pores, in line with earlier work.[17, 28–30]

Unique to this work is AP-ALD coating of PDMS. Elemental analysis shows an atomic percentage of titanium at the surface comparable to PE-ALD, indicating the presence of a surface layer. Strikingly different from PE-ALD, the atomic percentage decreases more gradual with etch depth and does not drop to zero over a depth of ~5200 nm, but approaches the value for Th-ALD. While a higher TiO_x loading of AP-ALD with respect to the two vacuum-based variants (PE-ALD and Th-ALD) is understood from higher partial pressures of the reactants, the formation of a surface-subsurface layer is understood from the balance between the reactivity of the ozone as oxidizing agent on the one hand, and the diffusion properties of the reactants on the other hand, allowing for simultaneous infiltration and surface reaction. AP-ALD treatment of PDMS hence results in a unique surface-subsurface coating. We note that an additional XPS test shows that the ratio of Ti:O on the surface remains the same with 20 and 250 cycles for all three ALD variants.

With three distinctly different TiO_x coatings on PDMS obtained, we now continue testing the coatings for their resistance against organic solvents. Organic resistance of ALD coated and bare PDMS was tested by immersing the samples in a beaker with organic solvent for a given exposure time and measuring the mass of the samples before and after immersion, as illustrated in Fig. 2.3a. To remove solvent adhering to the samples, samples were briefly blown dry using compressed nitrogen. As a model organic solvent, we used cyclohexane (Sigma-Aldrich). As well known, the uptake of cyclohexane by bare PDMS is significant.[5] This is confirmed in our experiments, see the increase in mass relative to the initial mass plotted in Fig. 2.3b. Th-ALD treated PDMS, with an infiltrated TiO_x subsurface, but no TiO_x surface, shows a similar trend. The slightly reduced uptake indicates that the TiO_x infiltrated subsurface layer has potential to decrease the organic solvent uptake, yet to a small extent. PE-ALD treated PDMS, with a TiO_x surface, but no TiO_x subsurface, shows a much stronger reduction in uptake. AP-ALD treated PDMS, with a TiO_x surface as well as a TiO_x subsurface, shows virtually no uptake, with a fractional mass increase of 0.0035 g/g after 24 h of immersion. Even after 240 h, there is only a slight increase, hence the coating is considered durable. Compared to 0.15 g/g for bare PDMS after 24 h, the reduction in uptake is two orders of magnitude for AP-ALD treated PDMS. To test whether it is the thickness of the surface layer or the presence of a subsurface layer that explains the reduced uptake for AP-ALD treated PDMS (0.0035 g/g after 24 h) in reference to PE-ALD treated PDMS (0.037 g/g after 24 h), we performed additional PE-ALD experiments by using 20, 300 and 700 ALD cycles. While the result-

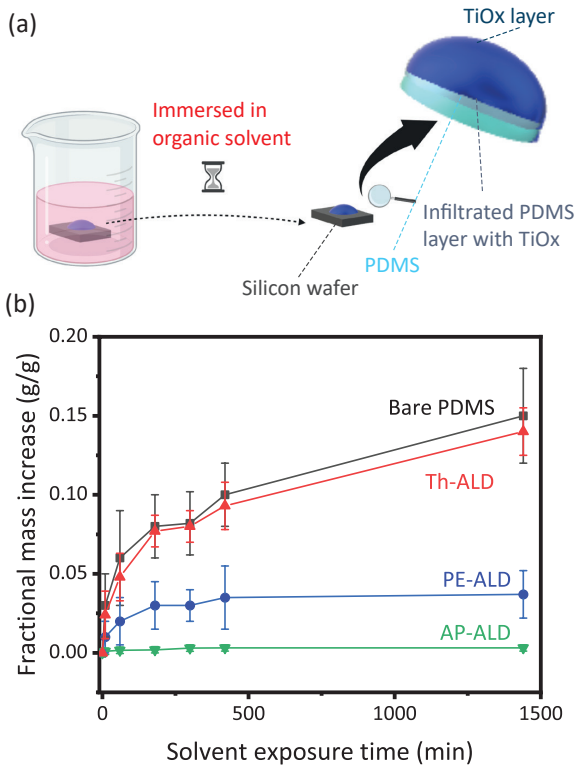

Figure 2.3: (a) Measurement of organic solvent resistance performance of the samples (made with biorender.com), (b) Fractional mass increase of bare and ALD-treated PDMS, cured at 200°C. Error bars of bare PDMS were calculated as the standard deviation of 20 samples per time point, while error bars of the ALD treated PDMS were based on 3 samples.

ing TiO_x surface layer was 1 nm, 22 nm and 54 nm respectively, we did not observe significant reduction of the uptake after 24 h (0.14, 0.035 and 0.034 g/g). Additionally, we performed an AP-ALD experiment with 50 cycles and found a fractional mass increase of 0.0031 g/g after 24 h of immersion. These experiments indicate that the organic solvent resistance is not attributed to the surface layer thickness, but to the combined surface-subsurface structure. To gain further insight, we pretreated a PDMS sample with oxygen plasma before treating it with Th-ALD; we also pretreated a PDMS sample with Th-ALD before treating it with PE-ALD. On both samples, we observed the organic resistance performance was comparable with PE-ALD treated samples, due to absence of a unique surface-subsurface layer. This further supports the finding that atmospheric pressure is key.

Before examining the ALD coated samples in more detail, we point out the importance of the temperature used to cure PDMS. Fig. 2.4 (Supporting Information) is equivalent to Fig. 2.3, but for a curing temperature of 70°C instead of 200°C. Rather than a monotonic increase in uptake over time, all curves show a rapid initial uptake, to

much higher values than for 200°C, followed by a decrease. This decrease is explained by leaching of monomers from the PDMS, a well reported phenomena.[32] The mass and internal structure of PDMS hence changes during immersion. For bare and Th-ALD treated PDMS, with no or little TiO_x barrier, the final value (after 24 h) is comparable to PDMS cured at 200°C. However, for PE-ALD and AP-ALD treated samples, with a significant TiO_x barrier, restructuring of the PDMS due to leaching compromises the barrier, such that the final values (after 24 h) are significantly larger for PDMS cured at 70°C than at 200°C. These comparative experiments illustrate the importance to cure the PDMS at a sufficiently high temperature to minimize leaching of monomers, because leaching compromises the surface and subsurface coating due to restructuring of PDMS upon contact with organic solvents. Besides cyclohexane as model organic solvent, we also tested the solvent resistance of AP-ALD coated PDMS for other common solvents. These experiments shows a comparable resistance, see Fig. 2.5 (Supporting Information). While a TiO_x layer is relatively stable against various organic solvents and alkaline solution, it should be noted that it dissolves in acids such as 0.1 M HNO_3. For applications involving acids, other metal oxides should be considered such as SiO_x.

To investigate why AP-ALD samples performed better than the PE-ALD ones, we examined the surface morphology using field emission scanning electron microscopy (FE-SEM, Hitachi Regulus SU8230). While all samples appear visually transparent and are comparable with bare PDMS (refer to Fig. 2.9(Supporting Information)), Fig. 2.6 shows that cracks are visible on the PE-ALD samples, and not on the AP-ALD samples. While no cracks are visible on the Th-ALD samples, the SEM images confirm that there is virtually no TiO_x layer present, explaining its poor solvent resistance. To approximate the crack depth of the PE-ALD samples, we conducted atomic force microscopy. The average crack depth is up to 100 nm (Figure 2.8). With an estimated TiO_x layer thickness of 7 nm on PE-ALD surfaces, cracks hence extend deep into the PDMS layer, allowing direct contact between organic solvent and PDMS. Whether cracks were formed during the ALD process due to thermal expansion of PDMS[19] or afterwards due to a difference between strains on sharply divided layers[33] remains a question, which is beyond the scope of this study. Cracks were not observed in the AP-ALD samples. We hence expect that the unique and gradual surface-subsurface layer formed by AP-ALD (Fig. 2.2a) prevents crack formation due to thermal expansion and undistributed residual strain loads, explaining limited swelling upon contact with organic solvents. In follow-up experiments, we explored the operating parameters of AP-ALD on the solvent resistance, highlighting a lower limit for the number of cycles and an upper limit for the deposition temperature (Fig. 2.7).

2.3. Conclusion

In conclusion, we found that the deposition of TiO_x on the soft polymer PDMS using AP-ALD results in a combined surface-subsurface coating. We demonstrated that this coating acts as a barrier against organic solvents, limiting the issue of swelling that is often a challenge in the application of PDMS. By using simpler atmospheric operation instead of vacuum technologies, this proof-of-principle brings the application of ALD on polymers closer to commercial realizations. This publication is part of the Open Technology programme financed by the Dutch Research Council (NWO). We thank Mojgan

Talebi and Bart Boshuizen for their technical support. There are no conflicts to declare.

2.4. Supporting information

PDMS sample preparation: The samples used for the organic resistance testing were prepared by depositing a droplet of degassed PDMS (elastomer and curing agent in a 10:1 weight ratio) on top of the surface of a silicon wafer, which was diced in pieces of 2 cm × 2 cm. The resulting spherical cap had a diameter of 1.5 cm and a thickness of 1 mm. The reason to deposit PDMS on top of a silicon wafer is that the full surface of PDMS is then treated in the ALD reactor. This is not the case when simply treating a slab of PDMS in the ALD reactor as the bottom is then left untreated. PDMS was cured at 200°C and 70°C for at least 10 hours for samples reported in Figures 2.3 and 2.4, respectively.

Thermal and plasma-enhanced atomic layer deposition: Th-ALD and PE-ALD experiments were carried out in a commercial ALD reactor (Veeco Fiji G2) at 10^{-5} mbar and 100°C. The Ti precursor (tetrakis(dimethylamino)titanium, TDMAT) was stored in a stainless-steel bubbler and kept at 70°C. For Th-ALD, water was used as the co-reactant and kept in a stainless-steel bubbler at room temperature. For PE-ALD, oxygen was flown through a plasma coil. Both reactants were introduced into the ALD chamber at 20 sccm for 60 ms alternately, with a purging step with argon introduced in the ALD chamber at 60 sccm for 5 s (PE-ALD) and 45 s (Th-ALD). The pulse and purge time of the PE-ALD and Th-ALD have been established by the previous researchers and the suppliers.

Atmospheric pressure atomic layer deposition: AP-ALD experiments were carried out in a custom-built tubular flat-substrate reactor, equipped with a reaction chamber consisting of a metal cylinder (100 mm in internal diameter and 300 mm in length) with a substrate holder (70 mm × 100 mm). Experiments were carried out at atmospheric pressure and 100°C. The gas flowed parallel to the surface of the substrate. A heating cable with isolation bands was wrapped on the reactor, with feedback control to maintain constant temperature during AP-ALD. The Ti precursor (TDMAT) was stored in a stainless-steel bubbler and kept at 70°C. The Ti precursor was carried to the reactor column with nitrogen gas flow of 0.5 L min^{-1}. The other reactant, ozone, was produced by flowing in oxygen at flowrate of 0.5 L min^{-1} into an ozoniser (Sander Certizon). One ALD process cycle consisted of exposures of the PDMS substrate to 10 s of Ti precursor and 10 s of ozone, with 150 s of nitrogen purging step (1.7 L min^{-1}). We note that at higher flow rate of purging, and/or longer purge time, the obtained layer thickness at similar number of cycles was comparable.

Sample storage: To prevent contamination of the ALD treated PDMS samples prior to XPS analysis, the samples were transferred to a closed and clean container directly after ALD treatment.

Organic solvent resistance evaluation: Bare and treated PDMS samples were weighed before fully immersing in a beaker glass containing cyclohexane. At certain period of time (10, 60, 180, 300, 420, 1440, and 14400 minutes), the sample was taken out, blown dry and weighed directly. The sample was then put back to the beaker glass to continue the exposure. The mass at the measuring time and the mass difference were noted down. The fractional mass increase was calculated by comparing the mass difference with the initial mass. In Figures 2.5 and 2.7, the fractional mass increase was measured after 24

hours of immersion. After this time, the system was considered in equilibrium and we use the commonly used symbol Q (equilibrium swelling ratio).

X-Ray Photoelectron Spectroscopy: The XPS machine (ThermoFisher Scientific Nexsa) is equipped with a monochromatic Al Kα radiation source (pass energy of 100 eV) and a flood gun to compensate for the positive charge. The etching was conducted with Ar^+ ions of 2 keV and then performed an XPS reading. This sequence was repeated, with a buffer time of 2 s between each sequence to allow the temporary excited electrons to come back to their ground state. The XPS spectra were post-processed using CASA-XPS software, which included a charge-correction of the carbon peak at 284.8 eV.

Remarks on determination of film thickness: We approximated the etch rate of TiO_x layer on PDMS by placing a Si wafer next to the PDMS sample during the ALD process, and calculated the etch rate of TiO_x layer on silicon wafer. The etch rate was then fixed although it depends on the material etched; a harder or denser material would etch slower than a softer one. Despite the etch depth measured from XPS cannot be considered as the conclusive film thickness, we can still use these values to compare the depth profiles between the different PDMS samples.

Transmittance test: The transmittance test is conducted using UV-Vis spectrophotometer VWR®using glass cuvette holder as reference for 100% transmittance. The measurement is conducted from 200 to 1000 nm, with increment of 1 nm, and repeated 3 times.

Spectroscopy ellipsometry Woolam: The thickness of metal oxide layer on silicon wafer is approximated using spectroscopy ellipsometry Woolam M-2000 at 50°,60°, and 70° inspection angle. Cauchy is used as a model to approximate the psi and delta, with mean square error (MSE) lower than 1.

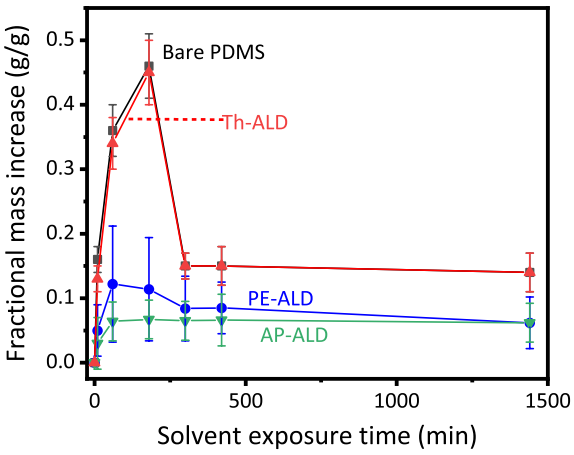

Figure 2.4: Fractional mass increase of bare and ALD-treated PDMS, cured at 70°C. Error bars of bare PDMS were calculated as the standard deviation of 20 samples per time point, while error bars of ALD-treated PDMS were based on 3 samples.

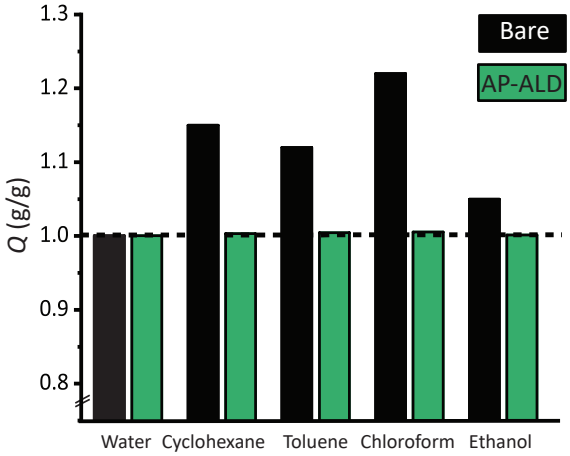

Figure 2.5: Equilibrium solvent coefficient (Q, in g/g) of bare and AP-ALD treated PDMS (cured at 200°C) after 24 h of immersion in different common solvents.

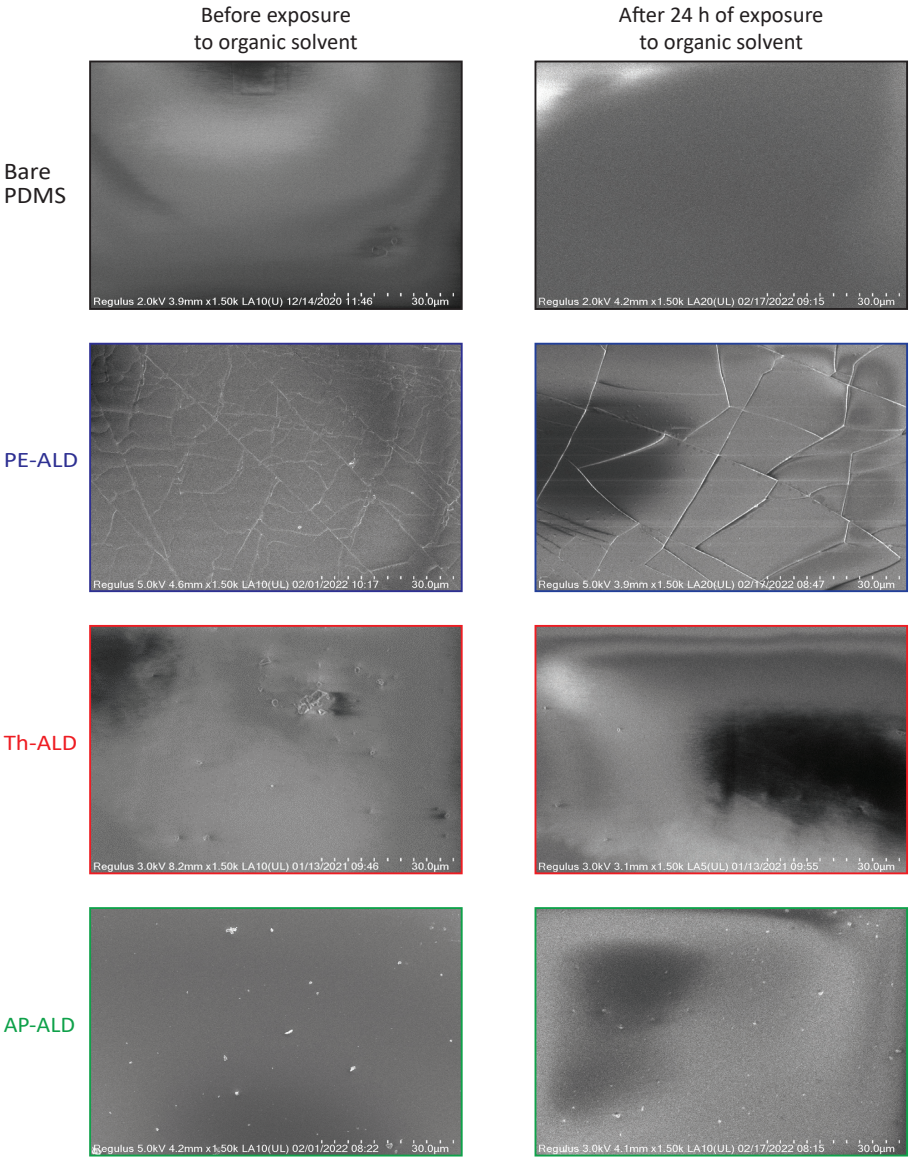

Figure 2.6: Scanning electron microscopy pictures of bare and ALD-treated PDMS samples (cured at 200°C) before and after being immersed in cyclohexane for 24 hours.

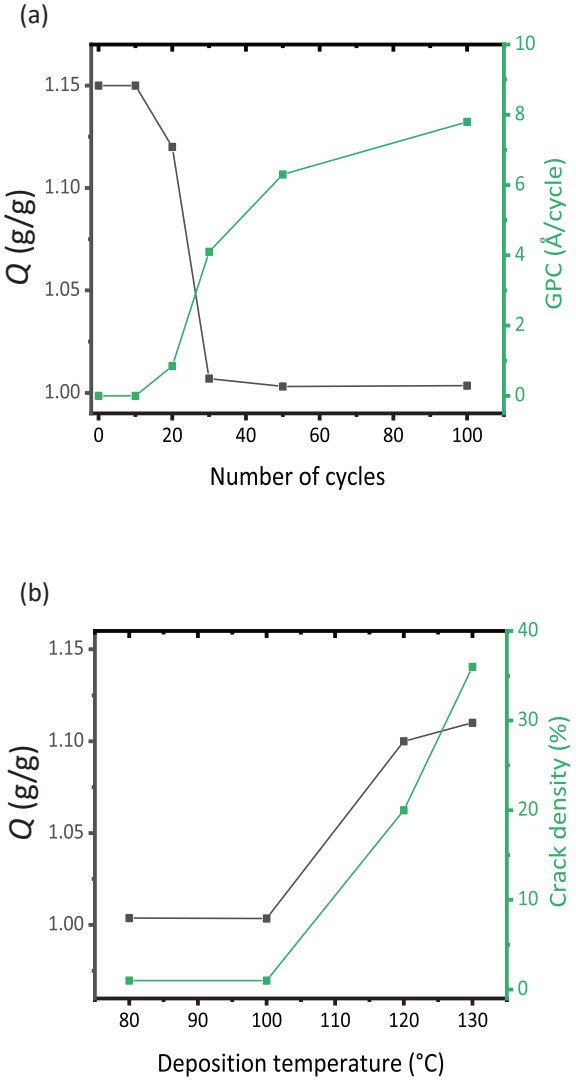

Figure 2.7: Equilibrium solvent coefficient (Q) of AP-ALD treated PDMS (cured at 200°C) after 24 hours of exposure to cyclohexane for (a) different numbers of ALD cycles at 100°C and (b) different deposition temperatures at 100 cycle. These graphs show range of operating parameter where comparable low swelling is found.

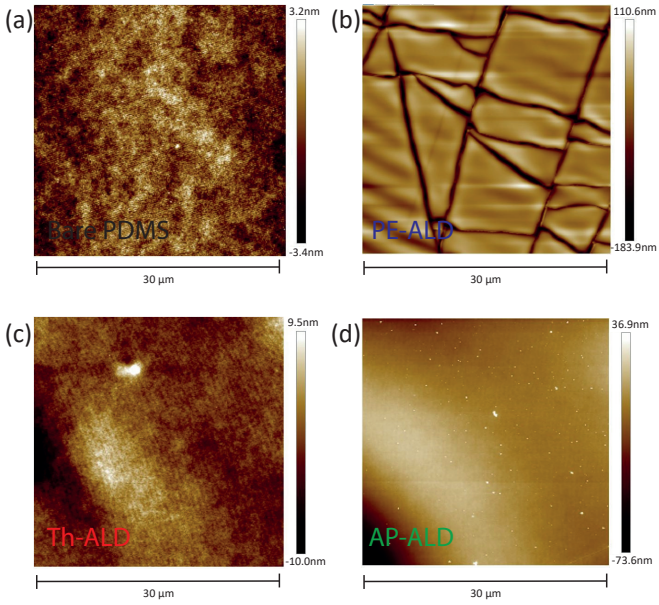

Figure 2.8: Atomic force microscopy surface height profile of (a) bare PDMS, (b) PE-ALD treated sample, (c) Th-ALD treated sample and (d) AP-ALD treated sample. All samples are treated at 100°C for 100 cycles. Cracks on PE-ALD sample extends up to hundreds of nm, deeper than the expected metal oxide thickness in the range of tens of nm

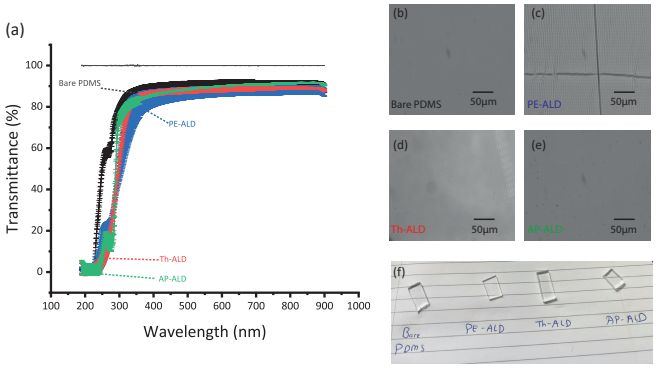

Figure 2.9: (a)Transmittance spectra of bare PDMS and ALD treated samples from 100nm to 1000nm range obtained using UV-Vis spectrophotometer; (b-e) Surface profile obtained by optical microscopy of bare PDMS and treated PDMS; and (f) comparative visual photo of bare PDMS and treated samples. All samples are cured at 200°C, and treated at 100°C for 100 cycles

a. Bare silicon wafer

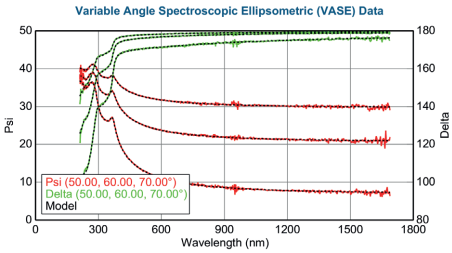

c. Silicon with Th-ALD TiOx

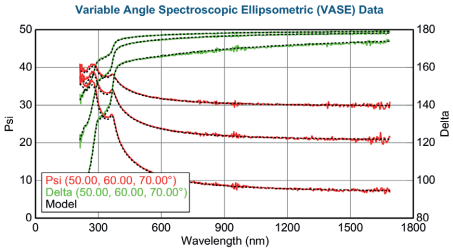

b. Silicon with PE-ALD TiOx

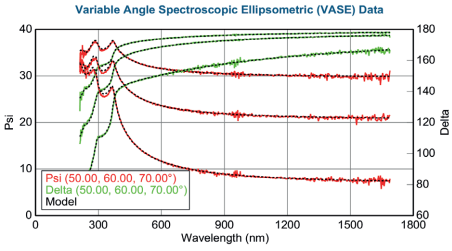

d. Silicon with AP-ALD TiOx

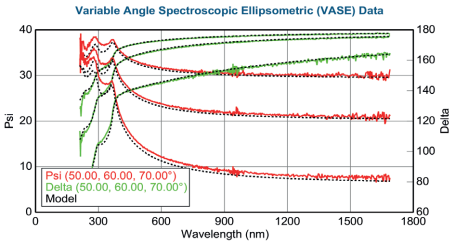

e. Table containing ellipsometry results and estimated XPS etch rate

Sample	Ellipsometry			XPS	Estimated etch rate (nm/s)
	Thickness (nm)	Error bar	MSE	Etch time (s)	
Bare silicon	0	0.007	0.330	0	0
PE-ALD treated Si	6.21	0.016	0.478	36	0.173
Th-ALD treated Si	1.53	0.011	0.436	9	0.171
AP-ALD treated Si	6.82	0.033	0.980	34	0.200

Figure 2.10: (a-d) Psi and delta spectroscopy ellipsometric profile of bare and treated silicon wafer. The measurement is conducted at 50°, 60°, and 70° with Cauchy model to approximate the thickness and mean squared error lower than 1. (e) Table showing the approximated thickness obtained from spectroscopy ellipsometry fitted with Cauchy, the XPS etch time where the plateau of Titanium atom starts going down, and the estimated XPS etch rate.

References

[1] A. Santoso, A. Damen, J. R. van Ommen, and V. van Steijn, *Atmospheric pressure atomic layer deposition to increase organic solvent resistance of PDMS,* Chemical Communications **58**, 10805 (2022).

[2] J. C. McDonald, D. C. Duffy, J. R. Anderson, D. T. Chiu, H. Wu, O. J. Schueller, and G. M. Whitesides, *Fabrication of microfluidic systems in poly (dimethylsiloxane),* Electrophoresis **21**, 27 (2000).

[3] K. Raj M and S. Chakraborty, *Pdms microfluidics: A mini review,* Journal of Applied Polymer Science **137**, 48958 (2020).

[4] Y. Hwang and R. N. Candler, *Non-planar pdms microfluidic channels and actuators: a review,* Lab on a Chip **17**, 3948 (2017).

[5] J. N. Lee, C. Park, and G. M. Whitesides, *Solvent compatibility of poly (dimethylsiloxane)-based microfluidic devices,* Analytical Chemistry **75**, 6544 (2003).

[6] R. Dangla, F. Gallaire, and C. N. Baroud, *Microchannel deformations due to solvent-induced pdms swelling,* Lab on a Chip **10**, 2972 (2010).

[7] B.-Y. Kim, L.-Y. Hong, Y.-M. Chung, D.-P. Kim, and C.-S. Lee, *Solvent-resistant pdms microfluidic devices with hybrid inorganic/organic polymer coatings,* Advanced Functional Materials **19**, 3796 (2009).

[8] A. R. Abate, D. Lee, T. Do, C. Holtze, and D. A. Weitz, *Glass coating for pdms microfluidic channels by sol–gel methods,* Lab on a Chip **8**, 516 (2008).

[9] T. J. Renckens, D. Janeliunas, H. van Vliet, J. H. van Esch, G. Mul, and M. T. Kreutzer, *Micromolding of solvent resistant microfluidic devices,* Lab on a Chip **11**, 2035 (2011).

[10] T. Yang, J. Choo, S. Stavrakis, and A. de Mello, *Fluoropolymer-coated PDMS microfluidic devices for application in organic synthesis,* Chemistry-A European Journal **24**, 12078 (2018).

[11] S. Goyal, A. V. Desai, R. W. Lewis, D. R. Ranganathan, H. Li, D. Zeng, D. E. Reichert, and P. J. Kenis, *Thiolene and SIFEL-based microfluidic platforms for liquid–liquid extraction,* Sensors and Actuators B: Chemical **190**, 634 (2014).

[12] A. Vitale, M. Quaglio, S. L. Marasso, A. Chiodoni, M. Cocuzza, and R. Bongiovanni, *Direct photolithography of perfluoropolyethers for solvent-resistant microfluidics,* Langmuir **29**, 15711 (2013).

[13] F. Kotz, P. Risch, D. Helmer, and B. E. Rapp, *Highly fluorinated methacrylates for optical 3D printing of microfluidic devices,* Micromachines **9**, 115 (2018).

[14] J. P. Niemelä, G. Marin, and M. Karppinen, *Titanium dioxide thin films by atomic layer deposition: A review,* Semiconductor Science and Technology **32**, 093005 (2017).

[15] K. Liu, M. Cao, A. Fujishima, and L. Jiang, *Bio-inspired titanium dioxide materials with special wettability and their applications,* Chemical Reviews **114**, 10044 (2014).

[16] H. Van Bui, F. Grillo, and J. R. van Ommen, *Atomic and molecular layer deposition: off the beaten track,* Chemical Communications **53**, 45 (2017).

[17] J. C. Spagnola, B. Gong, and G. N. Parsons, *Surface texture and wetting stability of polydimethylsiloxane coated with aluminum oxide at low temperature by atomic layer deposition,* Journal of Vacuum Science & Technology A: Vacuum, Surfaces, and Films **28**, 1330 (2010).

[18] H. C. Guo, E. Ye, Z. Li, M.-Y. Han, and X. J. Loh, *Recent progress of atomic layer deposition on polymeric materials,* Materials Science and Engineering: C **70**, 1182 (2017).

[19] G. N. Parsons, S. E. Atanasov, E. C. Dandley, C. K. Devine, B. Gong, J. S. Jur, K. Lee, C. J. Oldham, Q. Peng, J. C. Spagnola, *et al.*, *Mechanisms and reactions during atomic layer deposition on polymers,* Coordination Chemistry Reviews **257**, 3323 (2013).

[20] A. Bulusu, S. Graham, H. Bahre, H. Behm, M. Böke, R. Dahlmann, C. Hopmann, and J. Winter, *The mechanical behavior of ALD-polymer hybrid films under tensile strain,* Advanced Engineering Materials **17**, 1057 (2015).

[21] A. Behrendt, J. Meyer, P. van de Weijer, T. Gahlmann, R. Heiderhoff, and T. Riedl, *Stress management in thin-film gas-permeation barriers,* ACS Applied Materials & Interfaces **8**, 4056 (2016).

[22] K. L. Jarvis and P. J. Evans, *Growth of thin barrier films on flexible polymer substrates by atomic layer deposition,* Thin Solid Films **624**, 111 (2017).

[23] S.-H. Jen, J. A. Bertrand, and S. M. George, *Critical tensile and compressive strains for cracking of Al_2O_3 films grown by atomic layer deposition,* Journal of Applied Physics **109**, 084305 (2011).

[24] F. Nehm, H. Klumbies, C. Richter, A. Singh, U. Schroeder, T. Mikolajick, T. Monch, C. Hoßbach, M. Albert, J. W. Bartha, *et al.*, *Breakdown and protection of ALD moisture barrier thin films,* ACS Applied Materials & Interfaces **7**, 22121 (2015).

[25] J. H. Jang, N. Kim, X. Li, T. K. An, J. Kim, and S. H. Kim, *Advanced thin gas barriers film incorporating alternating structure of PEALD-based Al_2O_3/organic-inorganic nanohybrid layers,* Applied Surface Science **475**, 926 (2019).

[26] T. O. Kääriäinen, P. Maydannik, D. C. Cameron, K. Lahtinen, P. Johansson, and J. Kuusipalo, *Atomic layer deposition on polymer based flexible packaging materials: Growth characteristics and diffusion barrier properties,* Thin Solid Films **519**, 3146 (2011).

[27] K. Lahtinen, P. Maydannik, P. Johansson, T. Kääriäinen, D. C. Cameron, and J. Kuusipalo, *Utilisation of continuous atomic layer deposition process for barrier enhancement of extrusion-coated paper,* Surface and Coatings Technology **205**, 3916 (2011).

[28] E. Y. Choi, J.-H. Kim, B.-J. Kim, J. H. Jang, J. Kim, and N. Park, *Development of moisture-proof polydimethylsiloxane/aluminum oxide film and stability improvement of perovskite solar cells using the film,* RSC Advances **9**, 11737 (2019).

[29] S. H. Astaneh, G. Jursich, C. Sukotjo, and C. G. Takoudis, *Surface and subsurface film growth of titanium dioxide on polydimethylsiloxane by atomic layer deposition,* Applied Surface Science **493**, 779 (2019).

[30] B. Gong, J. C. Spagnola, and G. N. Parsons, *Hydrophilic mechanical buffer layers and stable hydrophilic finishes on polydimethylsiloxane using combined sequential vapor infiltration and atomic/molecular layer deposition,* Journal of Vacuum Science & Technology A: Vacuum, Surfaces, and Films **30**, 01A156 (2012).

[31] S.-M. Lee, E. Pippel, U. Gösele, C. Dresbach, Y. Qin, C. V. Chandran, T. Bräuniger, G. Hause, and M. Knez, *Greatly increased toughness of infiltrated spider silk,* Science **324**, 488 (2009).

[32] K. J. Regehr, M. Domenech, J. T. Koepsel, K. C. Carver, S. J. Ellison-Zelski, W. L. Murphy, L. A. Schuler, E. T. Alarid, and D. J. Beebe, *Biological implications of polydimethylsiloxane-based microfluidic cell culture,* Lab on a Chip **9**, 2132 (2009).

[33] Y. Li, Y. Xiong, H. Yang, K. Cao, and R. Chen, *Thin film encapsulation for the organic light-emitting diodes display via atomic layer deposition,* Journal of Materials Research **35**, 681 (2020).


Functional, I say...

Meisje met de parel
Johannes Vermeer, 1665

3

Robust surface functionalization of PDMS through AP-ALD

Polydimethylsiloxane (PDMS) has been widely employed as a material for microreactors and lab-on-a-chip devices. However, in its applications, PDMS suffers from two major problems: its weak resistance against common organic solvents and its chemically non-functional surface. To overcome both issues, atmospheric pressure atomic layer deposition (AP-ALD) can be used to deposit an inorganic nano layer (TiO_x) on PDMS that in turn can be further functionalized. The inorganic nano layer is previously communicated to durably increase the organic solvent resistance of PDMS. In this study, we investigate the possibility of this TiO_x nano layer in providing surface anchoring groups on PDMS surfaces, enabling further functionalization. We treat PDMS samples cured at three different temperatures with AP-ALD and measure the hydrophilicity of the treated samples as an indicator of the presence of surface anchoring groups. We find that all the treated PDMS samples become hydrophilic right after the AP-ALD treatment. We further find that the AP-ALD-treated PDMS samples cured at 150 °C and 200 °C maintain their hydrophilicity, while the samples cured at 70 °C become less hydrophilic over time. The presence of surface anchoring groups through TiO_x nano layer deposition on PDMS is further demonstrated and utilized by depositing gold nanoparticles (AuNPs) on the AP-ALD-treated samples. The samples exhibit visible light absorbance at 530 nm, a typical absorbance peak for AuNPs. In conclusion, this study demonstrates the use of nano layers grown by AP-ALD to solve the two major problems of PDMS simultaneously, widening its applicability, especially for use in high-end applications such as catalysis and bio-sensing.

This chapter has been published in Atomic Layer Deposition **1**, 1-13 (2023) [1].

3.1. Introduction

In the fields of medicine, biology, and chemistry, there is a rising trend of using polydimethylsiloxane (PDMS) as a material for microfluidics and protective coatings [2, 3]. The high transparency, excellent biocompatibility, ease of rapid prototyping, and tunable bulk properties of PDMS make it an attractive substrate, enabling wide selections of optical-based micro-(bio)processing [2, 4, 5]. However, PDMS has two major issues: its weak resistance against organic solvents and its chemically non-functional surface. When it comes in contact with common organic solvents such as chloroform and acetone, PDMS swells and deforms. Furthermore, the PDMS surface is naturally hydrophobic and mostly dominated by methyl groups, making it difficult to introduce functional groups such as hydroxyl, thiol, amine, carboxylic, epoxy rings, and many others [6, 7]. As a result, the use of PDMS is limited, especially in applications where the presence of functional groups or the use of organic solvents is vital [4, 5, 8, 9].

To overcome the limitations of PDMS, researchers explored two main directions: bulk modification and surface treatment [6, 10]. Since bulk modification leads to undesirable changes in PDMS bulk properties (e.g. softer/stiffer, lower transparency), wet and dry surface treatments have been explored [2, 5, 6, 11, 12]. A common dry surface treatment is the use of oxygen plasma to introduce hydroxyl groups on PDMS. While it renders the surface hydrophilic, the surface recovers to its initial hydrophobic state within hours known as hydrophobic recovery [13, 14]. Furthermore, this treatment does not render the surface inert such that oxygen-treated PDMS samples cannot be used for systems involving organic solvents. As such, numerous modifications involving liquid chemistry and sol-gel methods have been developed [15–20]. While using (hydroxyethyl)methacrylate (HEMA), polyethylene glycol (PEG), polyvinylpyrollidone (PVP), or polyvinyl alcohol (PVA) solutions to coat the PDMS surface does make the surface more hydrophilic [15–18], the introduced functional group could be desorbed and washed away by many solvents [16]. Furthermore, the PDMS is still susceptible to organic solvents. As an alternative, researchers looked into depositing non-organic layers. Roman and Culbertson used transition metal sol-gel precursors to introduce metal oxide groups [17], while the group of Weitz used tetraethyl orthosilicate (TEOS) and methyltrimethoxysilane (MTES) to deposit a glass-like substance on the PDMS surface [20]. While both offer a more robust layer to both protect the PDMS from direct organic solvent exposure and provide hydrophilic surface groups, the sol-gel method cannot be used to coat complex structures uniformly because the removal of the thick sol-gel solution using gas leaves unwanted residues. Apart from being uneven, the microscopically thick coating may compromise the bulk properties [21]. Therefore, vapor deposition of inorganic nanoscopically thin layers on PDMS becomes promising due to the use of a single phase in its whole deposition process while solving both issues of PDMS simultaneously [7, 22–27].

Among all vapor deposition methods, atomic layer deposition is renowned as it faithfully coats complex nanostructures with a wide variety of coating materials [28]. Using alternating reactions, the thickness of the coating layer, and its corresponding properties [28], can be controlled in a straightforward manner. When it comes to polymeric

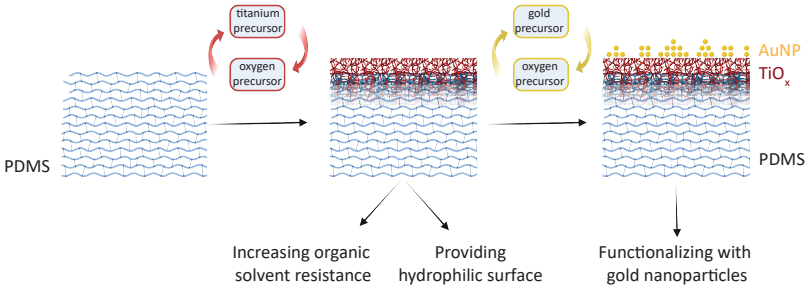

Figure 3.1: Illustration of modification of PDMS through deposition of a TiO_x nano layer and further functionalization through the deposition of gold nanoparticles (AuNPs). The deposition of a TiO_x nano layer both increases the organic solvent resistance of PDMS and renders the surface hydrophilic through hydroxyl groups. These groups act as anchoring points for further functionalization, here shown for AuNPs.

substrates including the elastomer PDMS, substrate infiltration could occur [27, 29, 30]. Therefore, numerous terms have been coined to better represent the process, such as multiple pulsed infiltration, vapor phase infiltration, sequential infiltration synthesis, atomic layer deposition, or atomic layer infiltration [31]. The group of Parsons made use of this by exposing PDMS to a metal precursor pulse, then a water precursor pulse, for several hours before conducting a sequential atomic layer deposition, and a sequential molecular layer deposition resulting in a significantly lowered hydrophobic recovery rate for 200 h. In their work, the surface growth and the subsurface growth were achieved in several process steps, and the samples' surface terminated with an organic-inorganic molecular layer (alucone) [7]. By contrast, our previous study communicated that both surface growth and subsurface infiltration of metal oxide occurs during atmospheric pressure deposition [32]. There, we showed that this unique surface-subsurface deposition contributes positively to increasing PDMS organic solvent resistance through a coating of titanium oxide [32]. Due to more than one phenomenon taking place in our previous and current work, we opt to use the more general term atomic layer deposition (ALD).

In this study, we follow up on our previous work by extending the use of the atmospheric pressure ALD (AP-ALD) of titanium oxide (TiO_x) to functionalize the PDMS substrate. While TiO_x has been demonstrated to provide a protective layer against organic solvents [32], it also has potential in providing hydroxyl groups that act as anchoring points for other molecules or particles [18, 33, 34]. In this study, we measure the hydrophilicity of the treated samples as an indicator for the functionality. We further demonstrate the presence of surface anchoring groups by functionalizing the treated PDMS surface by depositing gold nanoparticles (AuNPs) on top of the TiO_x layer, as illustrated in Figure 3.1. The presented results show a promising use of AP-ALD to tackle both weaknesses of PDMS in one go by increasing the organic solvent resistance and functionalizing the surface robustly while eliminating the need for expensive vacuum technology in its fabrication.

3.2. Methods and Materials

3.2.1. Substrate preparation

PDMS samples were fabricated by mixing the elastomer and curing agent (Sylgard 184 Elastomer Kit, Dow Corning) in a ratio of 10:1. After manual stirring of the mixture for 2 min, trapped air bubbles were removed using a vacuum desiccator for 30 min. The degassed mixture was poured into a Petri dish and placed in the vacuum desiccator again for another 30 min. PDMS was then cured in an oven at 70 °C, 150 °C, or 200 °C for at least 10 hours. Samples of 25 mm × 30 mm (0.5 mm thick) were cut from the cured PDMS and bonded on a glass slide after plasma treatment (oxygen in air, Harrick, PDC-002) at 0.2 - 0.4 mbar for 140 s.

3.2.2. Atomic layer deposition of TiO_x layers

TiO_x was deposited using a home-built atmospheric-pressure setup with a tubular flat-substrate reactor, where the precursor was delivered parallel to the substrate, as described previously [32]. Tetrakis-dimethylamino titanium (IV) (TDMAT, >99.99% Merck Sigma) and ozone-enriched air (Sander Certizon) were used as titanium and oxygen precursor respectively, while nitrogen (N_2 99.999%, Linde) was used as carrier gas. The carrier gas flowed through a bubbler for the metal precursor (kept at 70 °C) at 0.5 L/min for 10 s, while the ozone-enriched air flowed at 0.7 L/min for 30 s. In between, the nitrogen purging was done at 2 L/min for 100 s. Unless otherwise stated, we performed 100 cycles and kept the chamber at 100 °C. The ALD temperature was chosen to avoid condensation of ALD precursors at too low a temperature and possible cracks due to thermal expansion and contraction of PDMS at too high a temperature during the deposition process. As a comparison to AP-ALD treatment, we also conducted TiO_x deposition through thermal atomic layer deposition (Th-ALD) and plasma enhanced atomic layer deposition (PE-ALD) in a commercial atomic layer deposition reactor (Veeco Fiji G2) at 10^{-5} mbar and 100 °C. While TDMAT was used as the Ti precursor, water and oxygen plasma were used for the oxygen precursor in Th-ALD and PE-ALD, respectively. Both precursors were introduced into the chamber at 0.02 L/min for 60 ms alternatingly with 45 s (Th-ALD) or 5 s (PE-ALD) of nitrogen purging done in between. To ensure a fair comparison, we performed 100 cycles at 100 °C.

3.2.3. Atomic layer deposition of gold nanoparticles on TiO_x layers

To demonstrate the ability to functionalize the TiO_x-treated PDMS surface, we performed a second AP-ALD treatment in which we deposited gold nanoparticles (AuNPs) on TiO_x-treated PDMS samples cured at 150 °C. AuNPs were deposited using trimethylphosphino-trimethyl gold(III) (6-Me, prepared according to literature procedure [35, 36]) and ozone-enriched air as a precursor for 5 cycles at 100 °C using the same ALD set-up. The nitrogen carrier gas flowed through a bubbler for the metal precursor (kept at 75 °C) at 0.5 L/min for 15 s, while the ozone-enriched air flowed at 0.7 L/min for 30 s. In between, the purging was done at 2 L/min for 100 s. As a control, we also deposited AuNPs on bare PDMS samples with similar operating parameters.

3.2.4. Surface characterization of AP-ALD-treated PDMS samples

In order to characterize the surface morphology, field emission scanning electron microscopy (FESEM, Hitachi Regulus SU8230) at a beam current of 1-5 μA and electron energy of 1-10 keV was conducted. To obtain the surface elemental information, X-ray photoelectron spectroscopy (XPS) (ThermoFisher Scientific Nexsa) equipped with a monochromatic Al Kα radiation source and a pass energy of 30 and 100 eV for the survey scan and ion-beam etching unit was used. Depth profiling was conducted by etching the surface using Ar^+ ions (2 keV with a raster size of 2 mm) while a flood gun was used to compensate for the differential charging. Thermo Avantage 5.913 and CASA-XPS software were used to post-process the XPS peak profile, where the spectra were charge-corrected with the adventitious carbon peak at 284.8 eV. The thickness of the TiO_x layer was approximated using an etch rate obtained in our previous study [32]. This thickness was used to calibrate the etch rate of the TiO_x layer on PDMS during XPS measurements, indicating an approximated elemental depth profile.

3.2.5. Particle size distribution of the deposited AuNPs

To obtain the particle size distribution of AuNPs, ALD-coated PDMS samples were sonicated in HNO_3 1 M (Merck Sigma) for 15 min and left immersed for 48 h to dissolve the TiO_x layer under the AuNPs and disperse them into the solution. The solution was then centrifuged (MicroCL 21/21R, Thermoscientific) at 14800 rpm for 10 min and the supernatant was decanted as much as possible prior to being washed three times with ethanol (96%) and transferred onto Quantifoil copper TEM grids (coated with carbon). Transmission electron microscopy (TEM) images of the AuNPs were acquired using a JEOL JEM1400 microscope operating at a voltage of 120 kV working in bright-field mode. The average particle size and particle size distribution curves were obtained using the diameter of more than 350 individual particles analyzed using ImageJ.

3.2.6. Wettability study of TiO_x-coated PDMS samples

To quantify the surface wetting property, the dynamic contact angles were measured using a Krüss drop shape analyzer (Figure S1) at ambient conditions. An automated dispensing system was used to form the droplet and to increase and decrease the volume of the droplet. After forming a droplet of milliQ-water at a needle and bringing it in close contact with the surface of a PDMS sample, the droplet formed a contact line with the surface. As the droplet's volume increased gradually, the droplet inflated while the contact line remained pinned, resulting in an increase in the contact angle. The maximum contact angle before the droplet unpinned and started advancing is referred to as the advancing contact angle (θ_{adv}, Figure 3.5a), After that, the volume of the droplet was decreased, resulting in again pinning of the contact line and a decrease in contact angle. The minimum contact angle before the droplet unpinned and started receding is referred to as the receding contact angle (θ_{rec}, Figure 3.5b). Contact angle measurements were done a few minutes, 24 h, 48 h, 200 h, 400 h, and 800 h after the samples were taken out of the ALD reactors, with samples being stored in a glove box to reduce random air contamination during storage. Drop shape analysis software was used to measure contact angles from camera images. Average values were reported from 10 measurements via the typical uncertainty (2 s.d.).

3.2.7. Washing of the PDMS samples and ATR-FTIR characterization

To examine our hypothesis about the presence of uncured monomer in PDMS that diffuses out and compromises the AP-ALD coating, we pre-washed the PDMS samples to remove non-crosslinked molecules from the PDMS [37]. The PDMS samples were soaked in 70 mL cyclohexane (99% vol, Merck Sigma) for 72 h. Hereafter, the washing solvent was taken out and kept for infrared spectroscopy measurement, and a second soaking step of the PDMS samples was conducted for 24 h. After measuring the weight of the swollen PDMS samples, the samples were dried at room temperature for at least 8 h. The dried PDMS samples were weighed again to calculate the weight loss during the washing. The ATR-FTIR (attenuated total reflectance Fourier-transform infra-red spectroscopy) measurements on the washing solvents were performed on a Thermo Nicolet NEXUS instrument equipped with a liquid nitrogen cooled MCT detector with a wavelength range of 4000 to 500 cm^{-1}.

3.2.8. UV-Vis spectrophotometry study

To measure the photonic effect of the TiO_x-treated PDMS surface functionalized with AuNPs, light absorption was measured with a wide scan reading (300 - 800 nm) using a NanoDrop™ 2000/2000c spectrophotometer. The reported value was an average of 3 measurements via the typical uncertainty (2 s.d.).

3.3. Result and Discussion

3.3.1. Simultaneous surface and subsurface growth in AP-ALD

Before examining the treated samples, we point out that deposition of TiO_x on PDMS may result in both surface and subsurface growth, and therefore is more ambiguous to characterize [32]. Figure 3.2a shows the relative atomic percentage of titanium changes along the depth of the PDMS samples obtained using XPS depth profiling, while Figure 3.2b shows the corresponding XPS surface composition. On all samples, a significant percentage of Ti is observed on the surface, even to an etch depth of about 70-80 nm, indicating the formation of the TiO_x layer. A closer look at Figure 3.2b confirms that the atomic ratio of titanium to oxygen is about 1 to 2, indicating TiO_2 deposition. The titanium atomic percentage of all samples gradually declines in a comparable manner along the etch depth, before dropping to a percentage of ~5% at the depth of 200 nm. This gradual decline indicates the formation of an infiltrated layer. This result is in good agreement with previous results [32]. For all three AP-ALD samples, we observe similar profiles, indicating that the curing temperature has no effect on the resulting surface-subsurface structure. This is expected because the average size of the pores in PDMS is in the range of a few tens of nm to a few µm [38], much larger than the size of the precursor molecules. Thus, irrespective of the relative difference between the pore sizes due to differences in crosslinking densities, the penetration behavior of the precursor is the same in all three samples. Additionally, we study the effect of the number of cycles on the depth profile. We find that the Ti2p signal is not detected on the samples deposited with 10 cycles, while an appreciable signal is detected after 20 cycles (Figure 3.6a), indicating the presence of nucleation delay, which is typical for non-reactive substrates such as PDMS [25, 27, 32].

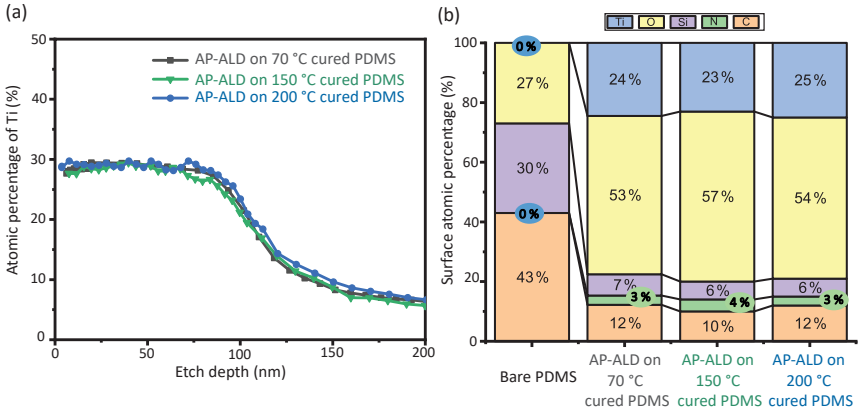

Figure 3.2: (a) XPS depth profiling showing the relative atomic percentage of titanium in the surface and subsurface of AP-ALD-coated PDMS samples cured at 70 °C, 150 °C, 200 °C, and (b) XPS elemental analysis of the surface.

Of note, XPS milling may influence the XPS reading. In case this artifact is significant, we expect it to influence the profiles obtained for different numbers of cycles in a similar way. Yet, when inspecting for example the profiles obtained with 50 and 100 cycles in Figure 3.6b, we see that the minimum and maximum percentage is the same, while the gradient of the slope of these profiles differs significantly. We suspect that at the given number of cycles, the diffusion coefficient of the ALD precursors is not much reduced due to the wide range of PDMS pore sizes and that the fresh PDMS surface group at the end of the coated area reacts with the ALD precursors as well. We hence conclude that a higher number of ALD cycles leads to both a thicker TiOx layer and a more moderate, deeper infiltration. We also note that this growth profile differs from commonly reported growth in vacuum ALD. Besides the XPS analysis of the surface and subsurface, an analysis of the surface by FE-SEM shows that the coating is visually smooth without nano cracks, even after 800 h, indicating a stable TiO_x layer (Figure 3.7).

3.3.2. Hydrophilicity as indicator of functional surface

We use hydrophilicity as an indicator for the presence of surface anchoring groups (in this case hydroxyl groups) on the ALD-coated PDMS surfaces. More specifically, we use the contact angle of a droplet of water brought into contact with the coated surfaces. Although the observed angle depends on the way of contacting, it is bounded by the contact angle hysteresis range, with an upper and lower bound intrinsic to the surface. The upper bound, called the advancing contact angle, is taken as the relevant characteristic in this work. While the range is known to depend on the roughness of the surfaces, we confirm the roughness of the samples' surfaces to be similar [32]. The advancing contact angle (θ_{adv}) measurement of bare PDMS and AP-ALD-coated PDMS samples cured at different temperatures are presented in Figure 3.3a. Directly after coating ($t = 0$), the (three) bare PDMS samples show a similar advancing contact angle at 118°±1°, in accordance with reported values [39, 40]. The AP-ALD-coated PDMS samples exhibit a

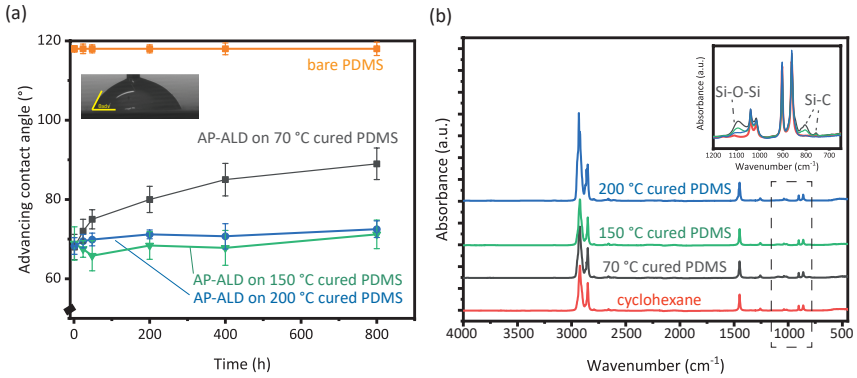

Figure 3.3: (a) Advancing contact angle measurement on bare and AP-ALD-coated PDMS samples cured at three different temperatures and (b) ATR-FTIR spectra of the solvent (cyclohexane) used to wash PDMS samples cured at different temperatures together with a control (pure cyclohexane).

significantly lower θ_{adv}, around 68°±4° at $t = 0$. A closer look at the XPS surface composition of these samples shows a high TiO_x coverage (Figure 3.2b), indicating that the hydrophilicity of the samples depends on the composition and possibly on the structure of the TiO_x coating. To confirm, we conducted two additional types of ALD treatment on PDMS samples, plasma enhanced ALD (PE-ALD) and thermal ALD (Th-ALD), that are known to yield notably different TiO_x layers [32]: PE-ALD leads to a TiO_x layer on top of the PDMS surface, while Th-ALD leads to a TiO_x layer inside the PDMS (infilling). As expected, the PE-ALD-coated PDMS samples exhibit a θ_{adv} of 69°±1° that is comparable to the AP-ALD-coated PDMS samples (Figure 3.8a). This result is in line with the previous finding by Pessoa [24]. By contrast, the Th-ALD-coated PDMS samples exhibit a θ_{adv} of 111°±2° that is comparable to bare PDMS samples (Figure 3.8a). When looking at the surface elemental composition (Figure 3.8b), the XPS surface spectra of PE-ALD-, Th-ALD-, and AP-ALD-coated PDMS samples show the expected profile of the TiO_x layers [32]. Both PE-ALD- and AP-ALD-coated samples show a dominance of Ti2p peak with little C1s and Si2p peaks, indicating a high coverage of TiO_x layers. By contrast, the Th-ALD-coated samples show a dominance of C1s and Si2p peaks with little Ti2p peaks, typical elements found in PDMS molecular chains. These XPS results are in line with previously reported SEM photos and XPS profiles [32]. These observations underline the importance of the type of TiO_x layer, and the type of ALD treatment used, on the hydrophilicity of the coated PDMS samples.

A well-known phenomenon in the coating of PDMS samples is the gradual temporal change in surface composition leading to the recovery of the hydrophobicity [23]. To test the robustness of the AP-ALD treatment, we measured the advancing contact angle on the same samples over prolonged periods of time. While the hydrophobicity of the bare PDMS samples is constant in time, we find that θ_{adv} of AP-ALD-coated PDMS samples cured at 70 °C increases along the duration of the measurement, reaching 89°±4° after 800 h (Figure 3.3a). This increase is significantly lower when compared to PE-ALD-coated PDMS samples cured at 70 °C (reaching 103°±1° after 800 h, see Figure 3.8a). We

argue that the combined surface-subsurface TiO_x layer obtained through AP-ALD acts as a barrier for the out-diffusion of uncured monomers, slowing down the hydrophobic recovery as compared to the surface-only TiO_x layer obtained through PE-ALD. This is in line with the observation that the surface-subsurface TiO_x layer obtained through AP-ALD shows no visual cracks (Figure 3.7), while nano cracks have been reported in the surface-only TiO_x layer obtained through PE-ALD [32]. While these nano cracks do not affect the hydrophilicity of the PE-ALD-coated samples at $t = 0$ (Figure 3.8a), it becomes a route for the uncured monomers to out diffuse, leading to hydrophobic recovery after 800 h.

The AP-ALD coating on PDMS samples cured at 70 °C renders the surface hydrophilic over prolonged times, yet it is subject to change due to the out-diffusion of uncured monomers. Earlier studies have suggested that curing of PDMS at higher temperatures changes the internal crosslinking of PDMS, leading to a tighter network [41] and fewer low-molecular-weight molecules [42]. For the AP-ALD-coated PDMS samples cured at

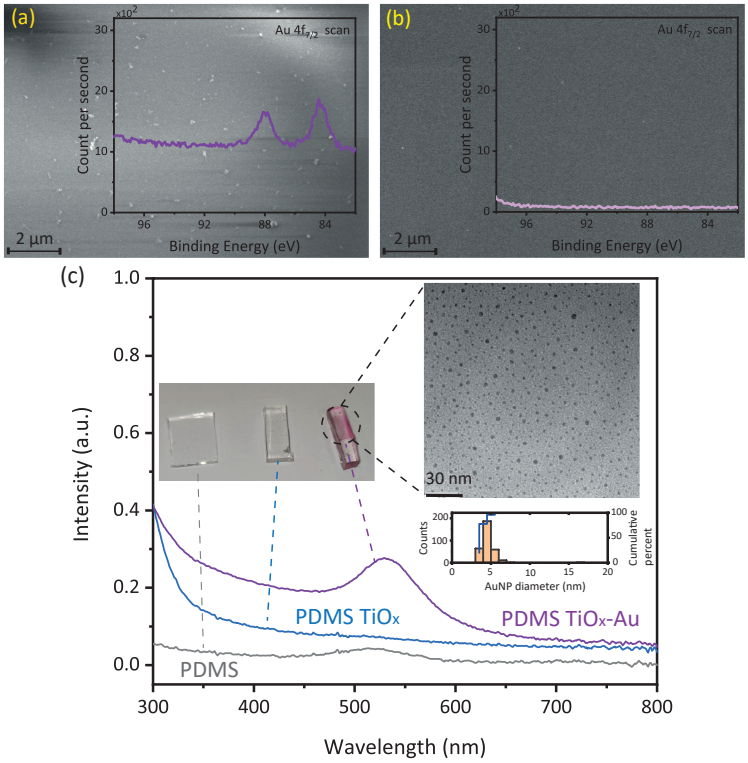

Figure 3.4: Scanning electron microscopy image of PDMS samples coated with 5 cycles of Au precursors preceded by (a) 100 cycles and (b) 0 cycles of Ti precursors on PDMS samples cured at 150 °C. Both AP-ALD processes were conducted at 100 °C. The insets show the corresponding XPS spectra at the typical Au4f binding energy range. (c) UV-Vis spectra of PDMS, PDMS coated with TiO_x, and PDMS coated with TiO_x and AuNPs. The insets show a photograph of the three samples, a TEM image of the TiO_x-AuNPs-coated PDMS sample, and the corresponding particle size distribution of the AuNPs.

150 °C and 200 °C, we indeed observe a negligible increase of advancing contact angle, from 69°±4° after coating to 71°±4° after 800 h for 150 °C, and from 68°±2° after coating to 73°±2° after 800 h for 200 °C (Figure 3.3a). Another way to reduce the amount of uncured monomer present in PDMS samples is to wash the cured PDMS samples using a solvent. The ATR-FTIR spectra of the solvent used to wash PDMS samples cured at 70 °C, 150 °C, and 200 °C show elevated peaks associated with the Si-O-Si and Si-C bonds in reference to the spectrum of the pure solvent [7, 23, 43], with the amount of uncured monomer decreasing with increasing curing temperature (Figure 3.3b). As expected, the advancing contact angle of the AP-ALD-coated PDMS samples cured at 70 °C and washed prior to ALD show a reduction in hydrophobic recovery, reaching 80°±4° after 800 h. Given that the surface of the AP-ALD-coated PDMS samples cured at 150 °C and 200 °C remains stable, washing with solvent is expected to have a little gain. Indeed, the advancing contact angle after 800 h is 70°±3° and 70°±3°, respectively, similar to the non-washed samples. To confirm that this gain is exclusive to only AP-ALD-coated samples, we carried out an additional experiment by coating the PDMS samples cured at 150 °C with PE-ALD. The advancing contact angle after 800 h is 94°±4°, with the hydrophobic recovery attributed to cracks in the TiO_x coating [32].

Since treated PDMS surfaces may usually not be stored in a nitrogen environment in a glove box, we performed an additional experiment where AP-ALD-coated samples (cured at 70 °C, 150 °C, and 200 °C) were kept in the air at ambient conditions in clean storage. The advancing contact angle after 800 h is 83°±4°, 72°±2°, and 71°±2° respectively, comparable to the samples stored in the nitrogen environment in the glove box. This also shows that both curing at temperature 150 °C and 200 °C and deposition of an (intact) surface-subsurface layer through AP-ALD are essential in obtaining a stable hydrophilic TiO_x coating on PDMS. This stable hydrophilicity, along with a significant percentage of TiO_x on the surface, also indicates a high surface coverage of hydroxyl groups (estimated to be in the order of 10^{14} molecules per cm^2, [44–46]). These hydroxyl groups are of importance for further functionalization.

3.3.3. Demonstration of functional surface

To demonstrate the ability to functionalize the PDMS surface, we deposit gold nanoparticles (AuNPs) on AP-ALD-coated PDMS samples. Figure 3.4a shows the presence of AuNPs on the PDMS samples sequentially coated with the Ti and Au precursors (indicated by Au4f signal in Figure 3.4a, inset), while no appreciable Au4f signal is found on the control PDMS sample coated with only Au precursor that shows no AuNPs (Figure 3.4b), indicating the importance of hydroxyl groups on the surface of AP-ALD treated layers, in comparison with methyl-dominated bare PDMS [47]. The post-processing of the signal (Figure 3.9a, calibrated with C1s peak at 248.8eV) shows the presence of mostly Au (0) at the peaks of 84.4eV and 88.1eV, a well-separated spin-orbit component of 3.7eV. From the comparison, the presence of a (stable) TiO_x layer on the PDMS is critical in providing reactive groups for initiating gold-based ALD. Furthermore, to check the purity of the formed AuNPs, an extra scan is conducted on P2p binding energy range as phosphorus is an identifiable element in the ALD Au precursor ligand. Figure 3.9b shows that the P2p signal is below the detection limit, suggesting the absence of AP-ALD by-products or remaining ligands. We examine the photonic performance of the AuNP-coated sam-

ple by measuring the diffuse surface reflectance with UV-Vis. A clear peak of 530 nm is observed (Figure 3.4c), corresponding to a typical local surface plasmon resonance of AuNPs [48]. We confirm that this peak is not seen in bare PDMS samples and TiO_x-coated PDMS samples. To characterize the particle size distribution, the AuNPs are dispersed by dissolving the underlying TiO_x layer first using HNO_3 1 M, before being washed with ethanol and placed on a TEM grit. The processed image (Figure 3.4c, inset) shows an average diameter of 4.6 nm and a standard deviation of 0.7 nm accordingly. This AuNPs size with a relatively narrow size distribution is of interest in many applications including photocatalysis and biosensing [49, 50].

3.4. Conclusion

In conclusion, we show that a nano layer of metal oxide can be deposited on the transparent soft elastomer PDMS, providing it with the necessary hydroxyl groups to allow further functionalization of the surface. We find that the surface-subsurface TiO_x layer obtained through atmospheric pressure ALD is critical in providing a surface that remains hydrophilic and stable over prolonged periods of time, with reduced out-diffusion of uncured monomer. For stable hydrophilic TiO_x layers that do not display hydrophobic recovery, curing of PDMS at a temperature of at least 150 °C is found to be of key importance. In comparison with PE-ALD and Th-ALD, AP-ALD offers a robust nano layer that can be further functionalized. We illustrate the further functionalization of the TiO_x-coated PDMS surfaces by depositing gold nanoparticles, also through ALD, opening the opportunity window to high-end applications.

3.5. Acknowledgment and conflict of interest

This publication is part of the Open Technology programme (with project number 16913) financed by the Dutch Research Council (NWO). We thank Mojgan Talebi, Joost Middelkoop, and Bart Boshuizen for their technical support. We acknowledge that Figure 3.1 was partially made using Biorender. There are no conflicts of interest to declare.

3.6. Supplementary Information

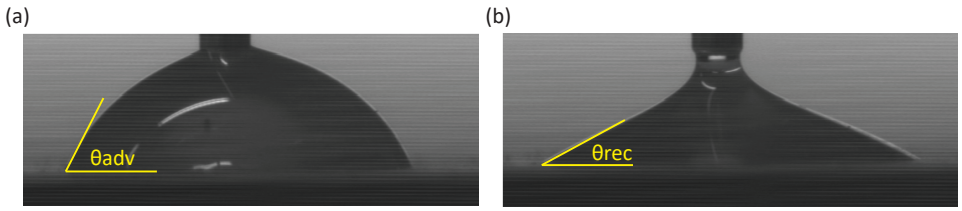

Figure 3.5: Measurement of the advancing (left) and receding contact angle (right) on AP-ALD-treated PDMS samples. In the main manuscript, we report the advancing contact angles.

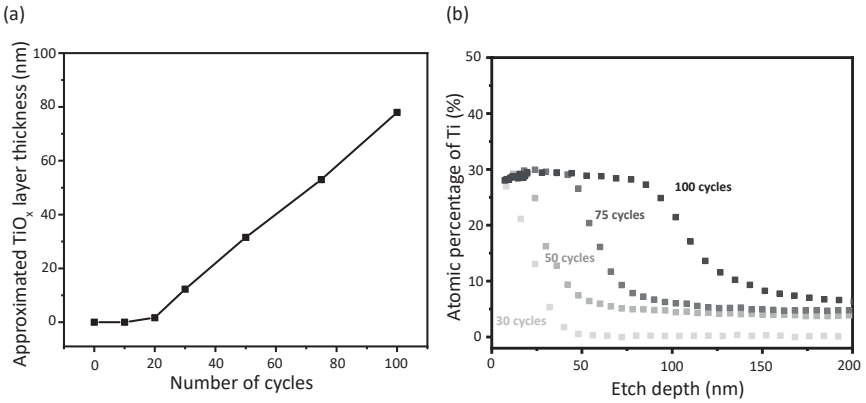

Figure 3.6: (a) Approximated TiO_x layer thickness obtained from XPS depth profiling with the etch rate determined using a TiO_x layer on a silicon wafer as described previously [32]. (b) XPS depth profiling of AP-ALD coated PDMS samples for 30, 50, 75, and 100 cycles. All PDMS samples are cured at 150 °C.

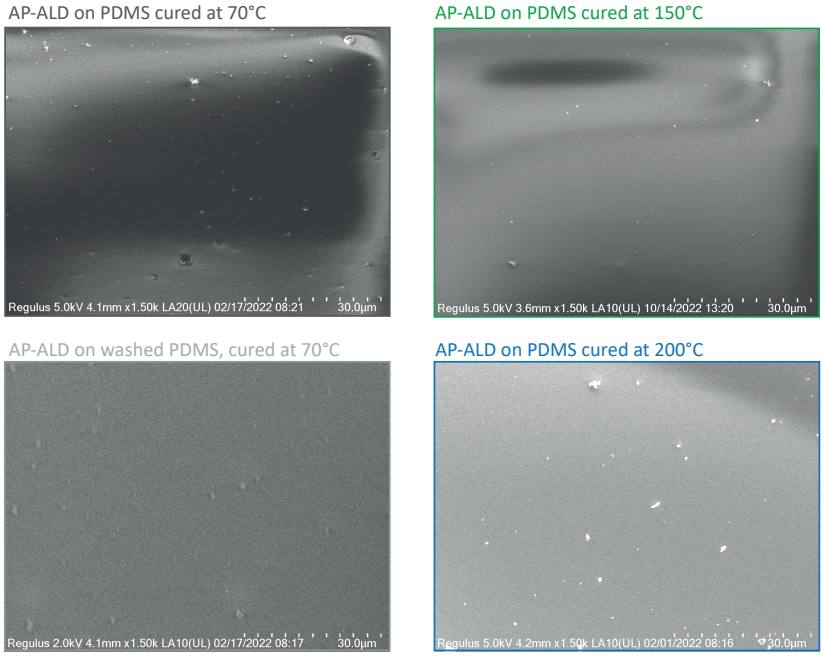

Figure 3.7: Scanning electron microscopy images of AP-ALD treated PDMS samples after 800 h. Both of the left images were cured at 70 °C (the bottom image was washed in cyclohexane before AP-ALD treatment), and the right images were cured at 150 °C (top), and 200 °C (bottom).

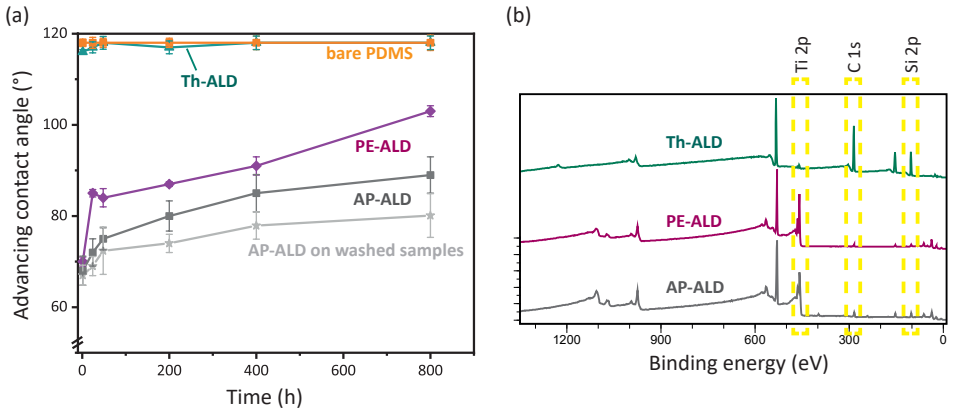

Figure 3.8: (a) Advancing contact angle measurement on bare PDMS and PDMS coated with PE-ALD, Th-ALD, and AP-ALD. AP-ALD is also performed on washed samples. All PDMS samples were cured at 70 °C. (b) Corresponding XPS surface spectra of the ALD-coated PDMS samples. The XPS spectra show a high presence of Si2p peak and a low presence of Ti2p peak on Th-ALD samples, indicating minimum TiO_x surface coverage. The PE-ALD and AP-ALD samples show the opposite, indicating high TiO_x surface coverage.

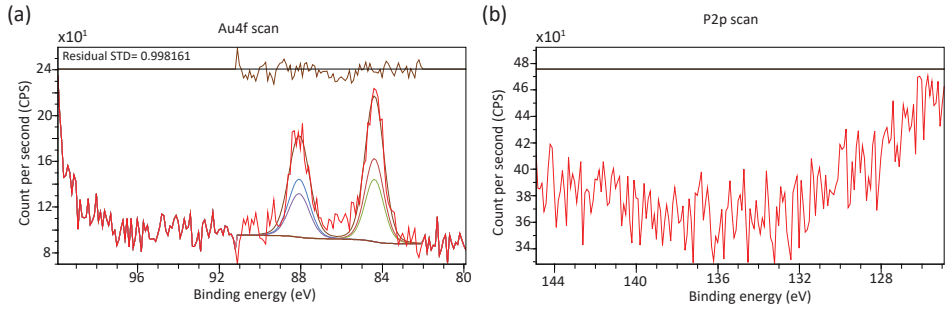

Figure 3.9: XPS spectrum of (a) Au4f, (b) P2p of coated PDMS samples. The samples were coated with 100 cycles of Ti precursors and 5 cycles of Au precursors. The horizontal line gives the baseline for the background signal. No clear peak of P2p was observed at the measured binding energy range.

References

[1] A. Santoso, B. J. van den Berg, S. Saedy, E. Goodwin, V. van Steijn, and J. R. van Ommen, *Robust surface functionalization of pdms through atmospheric pressure atomic layer deposition,* Atomic Layer Deposition **1**, 1 (2023).

[2] K. Raj M and S. Chakraborty, *PDMS microfluidics: A mini review,* Journal of Applied Polymer Science **137**, 48958 (2020).

[3] U. Eduok, O. Faye, and J. Szpunar, *Recent developments and applications of protective silicone coatings: A review of PDMS functional materials,* Progress in Organic Coatings **111**, 124 (2017).

[4] I. Miranda, A. Souza, P. Sousa, J. Ribeiro, E. M. Castanheira, R. Lima, and G. Minas, *Properties and applications of PDMS for biomedical engineering: A review,* Journal of Functional Biomaterials **13**, 2 (2021).

[5] M. P. Wolf, G. B. Salieb-Beugelaar, and P. Hunziker, *PDMS with designer functionalities—properties, modifications strategies, and applications,* Progress in Polymer Science **83**, 97 (2018).

[6] A. Shakeri, S. Khan, and T. F. Didar, *Conventional and emerging strategies for the fabrication and functionalization of PDMS-based microfluidic devices,* Lab on a Chip **21**, 3053 (2021).

[7] B. Gong, J. C. Spagnola, and G. N. Parsons, *Hydrophilic mechanical buffer layers and stable hydrophilic finishes on polydimethylsiloxane using combined sequential vapor infiltration and atomic/molecular layer deposition,* Journal of Vacuum Science & Technology A: Vacuum, Surfaces, and Films **30**, 01A156 (2012).

[8] C. Wang, M. Liu, Z. Wang, S. Li, Y. Deng, and N. He, *Point-of-care diagnostics for infectious diseases: From methods to devices,* Nano Today **37**, 101092 (2021).

[9] F. Akther, S. B. Yakob, N.-T. Nguyen, and H. T. Ta, *Surface modification techniques for endothelial cell seeding in PDMS microfluidic devices,* Biosensors **10**, 182 (2020).

[10] J. Liu, Y. Yao, X. Li, and Z. Zhang, *Fabrication of advanced polydimethylsiloxane-based functional materials: Bulk modifications and surface functionalizations,* Chemical Engineering Journal **408**, 127262 (2021).

[11] J. Zhou, D. A. Khodakov, A. V. Ellis, and N. H. Voelcker, *Surface modification for PDMS-based microfluidic devices,* Electrophoresis **33**, 89 (2012).

[12] Z. Almutairi, C. L. Ren, and L. Simon, *Evaluation of polydimethylsiloxane (PDMS) surface modification approaches for microfluidic applications,* Colloids and Surfaces A: Physicochemical and Engineering Aspects **415**, 406 (2012).

[13] D. Bodas and C. Khan-Malek, *Hydrophilization and hydrophobic recovery of PDMS by oxygen plasma and chemical treatment—an SEM investigation,* Sensors and Actuators B: Chemical **123**, 368 (2007).

[14] M. Amerian, M. Amerian, M. Sameti, and E. Seyedjafari, *Improvement of PDMS surface biocompatibility is limited by the duration of oxygen plasma treatment,* Journal of Biomedical Materials Research Part A **107**, 2806 (2019).

[15] S. Hemmilä, J. V. Cauich-Rodríguez, J. Kreutzer, and P. Kallio, *Rapid, simple, and cost-effective treatments to achieve long-term hydrophilic PDMS surfaces,* Applied Surface Science **258**, 9864 (2012).

[16] T. Trantidou, Y. Elani, E. Parsons, and O. Ces, *Hydrophilic surface modification of PDMS for droplet microfluidics using a simple, quick, and robust method via PVA deposition,* Microsystems & Nanoengineering **3**, 1 (2017).

[17] G. T. Roman, T. Hlaus, K. J. Bass, T. G. Seelhammer, and C. T. Culbertson, *Sol-gel modified poly (dimethylsiloxane) microfluidic devices with high electroosmotic mobilities and hydrophilic channel wall characteristics,* Analytical Chemistry **77**, 1414 (2005).

[18] J.-B. Orhan, V. Parashar, J. Flueckiger, and M. Gijs, *Internal modification of poly (dimethylsiloxane) microchannels with a borosilicate glass coating,* Langmuir **24**, 9154 (2008).

[19] G. T. Roman and C. T. Culbertson, *Surface engineering of poly (dimethylsiloxane) microfluidic devices using transition metal sol-gel chemistry,* Langmuir **22**, 4445 (2006).

[20] A. R. Abate, D. Lee, T. Do, C. Holtze, and D. A. Weitz, *Glass coating for PDMS microfluidic channels by sol–gel methods,* Lab on a Chip **8**, 516 (2008).

[21] H. Fallahi, J. Zhang, H.-P. Phan, and N.-T. Nguyen, *Flexible microfluidics: Fundamentals, recent developments, and applications,* Micromachines **10**, 830 (2019).

[22] H.-Y. Chen, Y. Elkasabi, and J. Lahann, *Surface modification of confined microgeometries via vapor-deposited polymer coatings,* Journal of the American Chemical Society **128**, 374 (2006).

[23] J. C. Spagnola, B. Gong, and G. N. Parsons, *Surface texture and wetting stability of polydimethylsiloxane coated with aluminum oxide at low temperature by atomic layer deposition,* Journal of Vacuum Science & Technology A: Vacuum, Surfaces, and Films **28**, 1330 (2010).

[24] R. Pessoa, V. dos Santos, S. Cardoso, A. Doria, F. Figueira, B. Rodrigues, G. Testoni, M. Fraga, F. Marciano, A. Lobo, *et al.*, *TiO_2 coatings via atomic layer deposition on polyurethane and polydimethylsiloxane substrates: Properties and effects on C. albicans growth and inactivation process,* Applied Surface Science **422**, 73 (2017).

[25] E. Y. Choi, J.-H. Kim, B.-J. Kim, J. H. Jang, J. Kim, and N. Park, *Development of moisture-proof polydimethylsiloxane/aluminum oxide film and stability improvement of perovskite solar cells using the film,* RSC Advances **9**, 11737 (2019).

[26] S. Hoshian, V. Jokinen, and S. Franssila, *Robust hybrid elastomer/metal-oxide superhydrophobic surfaces,* Soft Matter **12**, 6526 (2016).

[27] S. H. Astaneh, G. Jursich, C. Sukotjo, and C. G. Takoudis, *Surface and subsurface film growth of titanium dioxide on polydimethylsiloxane by atomic layer deposition,* Applied Surface Science **493**, 779 (2019).

[28] H. Van Bui, F. Grillo, and J. Van Ommen, *Atomic and molecular layer deposition: off the beaten track,* Chemical Communications **53**, 45 (2017).

[29] I. Weisbord, N. Shomrat, R. Azoulay, A. Kaushansky, and T. Segal-Peretz, *Understanding and controlling polymer–organometallic precursor interactions in sequential infiltration synthesis,* Chemistry of Materials **32**, 4499 (2020).

[30] E. K. McGuinness, F. Zhang, Y. Ma, R. P. Lively, and M. D. Losego, *Vapor phase infiltration of metal oxides into nanoporous polymers for organic solvent separation membranes,* Chemistry of Materials **31**, 5509 (2019).

[31] J. Pinson and D. Thiry, *Surface modification of polymers - methods and applications,* (John Wiley & Sons, 2020) Chap. 5 Atomic Layer Deposition and Vapor Phase Infiltration, pp. 135–157.

[32] A. Santoso, A. Damen, J. R. van Ommen, and V. van Steijn, *Atmospheric pressure atomic layer deposition to increase organic solvent resistance of PDMS,* Chemical Communications **58**, 10805 (2022).

[33] X. Kang, S. Liu, Z. Dai, Y. He, X. Song, and Z. Tan, *Titanium dioxide: from engineering to applications,* Catalysts **9**, 191 (2019).

[34] X. Liu, P. K. Chu, and C. Ding, *Surface modification of titanium, titanium alloys, and related materials for biomedical applications,* Materials Science and Engineering: R: Reports **47**, 49 (2004).

[35] M. B. Griffiths, P. J. Pallister, D. J. Mandia, and S. T. Barry, *Atomic layer deposition of gold metal,* Chemistry of Materials **28**, 44 (2016).

[36] F. S. Hashemi, F. Grillo, V. R. Ravikumar, D. Benz, A. Shekhar, M. B. Griffiths, S. T. Barry, and J. R. Van Ommen, *Thermal atomic layer deposition of gold nanoparticles: controlled growth and size selection for photocatalysis,* Nanoscale **12**, 9005 (2020).

[37] J. González-Rivera, R. Iglio, G. Barillaro, C. Duce, and M. R. Tinè, *Structural and thermoanalytical characterization of 3D porous PDMS foam materials: the effect of impurities derived from a sugar templating process,* Polymers **10**, 616 (2018).

[38] D. Zhu, S. Handschuh-Wang, and X. Zhou, *Recent progress in fabrication and application of polydimethylsiloxane sponges,* Journal of Materials Chemistry A **5**, 16467 (2017).

[39] A. Mata, A. J. Fleischman, and S. Roy, *Characterization of polydimethylsiloxane (PDMS) properties for biomedical micro/nanosystems,* Biomedical microdevices **7**, 281 (2005).

[40] R. Seghir and S. Arscott, *Extended PDMS stiffness range for flexible systems,* Sensors and Actuators A: Physical **230**, 33 (2015).

[41] K. Berean, J. Z. Ou, M. Nour, K. Latham, C. McSweeney, D. Paull, A. Halim, S. Kentish, C. M. Doherty, A. J. Hill, *et al.*, *The effect of crosslinking temperature on the permeability of PDMS membranes: Evidence of extraordinary CO_2 and CH_4 gas permeation,* Separation and Purification Technology **122**, 96 (2014).

[42] D. T. Eddington, J. P. Puccinelli, and D. J. Beebe, *Thermal aging and reduced hydrophobic recovery of polydimethylsiloxane,* Sensors and Actuators B: Chemical **114**, 170 (2006).

[43] K. J. Regehr, M. Domenech, J. T. Koepsel, K. C. Carver, S. J. Ellison-Zelski, W. L. Murphy, L. A. Schuler, E. T. Alarid, and D. J. Beebe, *Biological implications of polydimethylsiloxane-based microfluidic cell culture,* Lab on a Chip **9**, 2132 (2009).

[44] A. Boonstra and C. Mutsaers, *Relation between the photoadsorption of oxygen and the number of hydroxyl groups on a titanium dioxide surface,* The Journal of Physical Chemistry **79**, 1694 (1975).

[45] K. Liu, M. Cao, A. Fujishima, and L. Jiang, *Bio-inspired titanium dioxide materials with special wettability and their applications,* Chemical Reviews **114**, 10044 (2014).

[46] E. Hyde and M. Beck, *Comprehensive dft study of hydroxyl coverage on titania surfaces,* Applied Surface Science **498**, 143893 (2019).

[47] A. Gökaltun, Y. B. Kang, M. L. Yarmush, O. B. Usta, and A. Asatekin, *Simple surface modification of poly (dimethylsiloxane) via surface segregating smart polymers for biomicrofluidics,* Scientific Reports **9**, 7377 (2019).

[48] S. Y. Lee, D. Kang, S. Jeong, H. T. Do, and J. H. Kim, *Photocatalytic degradation of rhodamine b dye by TiO_2 and gold nanoparticles supported on a floating porous polydimethylsiloxane sponge under ultraviolet and visible light irradiation,* ACS Omega **5**, 4233 (2020).

[49] S. Witzel, A. S. K. Hashmi, and J. Xie, *Light in gold catalysis,* Chemical Reviews **121**, 8868 (2021).

[50] P. Si, N. Razmi, O. Nur, S. Solanki, C. M. Pandey, R. K. Gupta, B. D. Malhotra, M. Willander, and A. de la Zerda, *Gold nanomaterials for optical biosensing and bioimaging,* Nanoscale Advances **3**, 2679 (2021).


A whole new world

Oude vrouw en jongen met kaarsen
Peter Paul Rubens, 1617

4

AP-ALD for in-channel surface modification of PDMS microfluidic chips

Polydimethylsiloxane (PDMS) is one of the materials of choice for the fabrication of microfluidic chips. However, its broad application is constrained by its incompatibility with common organic solvents and the absence of surface anchoring groups for surface functionalization. Current solutions involving bulk-, ex-situ surface-, and in-situ liquid phase modifications are limited and practically demanding. In this work, we present a simple, novel strategy to deposit a metal oxide nano-layer on the inside of bonded PDMS microfluidic channels using atmospheric pressure atomic layer deposition (AP-ALD). Using three important classes of microfluidic experiments, i.e., (i) the production of micron-sized particles, (ii) the cultivation of biological cells, and (iii) the photocatalytic degradation in continuous flow chemistry, we demonstrate that the metal oxide nano-layer offers a higher resistance against organic solvent swelling, higher hydrophilicity, and a higher degree of further functionalization of the wall. We demonstrate the versatility of the approach by not only depositing SiO_x nano-layers, but also TiO_x nano-layers, which in the case of the flow chemistry experiment were further functionalized with gold nanoparticles through the use of AP-ALD. This study demonstrates AP-ALD as a tool to broaden the applicability of PDMS devices.

This chapter has been published in Chemical Engineering Journal **498**, 155269 (2024) [1].

4.1. Introduction

For the past two decades, polydimethylsiloxane (PDMS) is the choice material for the development of micro analysis systems [2, 3], lab-on-a-chips [4, 5], micro-reactors [5, 6], and organ-on-a-chips [7]. Despite the unique material properties and especially the ease of replication and rapid prototyping, bare PDMS does not resist common organic solvents, absorbs various (bio)molecules, and is difficult to functionalize robustly [8, 9]. Current solutions involve bulk or surface modification of PDMS prior to bonding the microfluidic channels. Yet, doping the PDMS can reduce the optical transparency [10], while depositing a ceramic coating before bonding results in less leak-tight microchannels [11]. Hence, various methods for the in-channel modification of the surface of bonded PDMS microfluidic have been developed, to render the walls inert or provide them with the required functionality, without sacrificing the advantageous properties of PDMS [12–15].

In-channel surface modification methods can be classified into liquid [16, 17] and gas phase methods [18]. Most in-channel surface modification methods make use of liquids flown through bonded microchannels to deposit either organic molecules and/or an inorganic layer [14]. However, the introduced layer may be relatively thick with respect to the dimensions of the microchannels [14, 17], and conformal coating of a network of channels poses a challenge due to the entrapment of air and/or coating solution during filling and/or emptying of a channel network [19].

Gas phase methods, on the contrary, are known to be able to coat a surface with

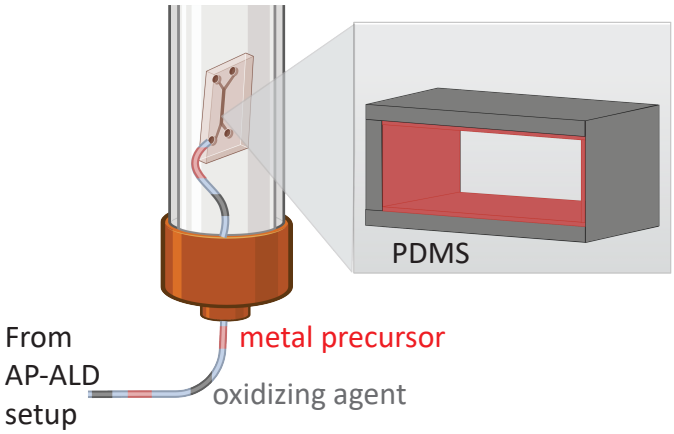

Figure 4.1: Illustration of in-channel coating of bonded PDMS microfluidic chips by alternatingly flowing a metal precursor and an oxidizing agent through the channels of a microfluidic chip for the atomic layer deposition of a nano-layer of metal oxide on the inside of the microfluidic channels. For safety reasons, the microfluidic chip is placed in the tubular glass column of a home-built atmospheric pressure atomic layer deposition (AP-ALD) setup. The two metal-oxides deposited in this work to allow the use of organic solvents and the functionalization of the channel walls are silicon oxide (SiO_x) and titanium oxide (TiO_x).

high resolution [20]. In particular, atomic layer deposition (ALD) offers exceptional conformality and tunable film composition [21, 22]. By exposing the surface to alternating, self-limiting reactions, one can grow nano-layers and control the thickness at the Angstrom level [23]. These deposited nano-layers offer attractive surface functionality, for example in terms of their catalytic-, barrier-, wetting-, and other properties, interesting for many applications [21–23]. Despite the potential, to the authors' best knowledge, conventional ALD has never been used for in-channel modification of bonded PDMS microfluidic channels. Typically, ALD, like many other established gas (plasma) treatments, is carried out in a vacuum chamber with a surface directly exposed to the gases in the chamber [24]. Consequently, in-channel coating of bonded PDMS microchannels would require impractically long exposure times for the ALD precursors to react over the full length of the channels in case their transport is solely based on diffusion. The diffusion distance can however be minimized if the ALD precursors are flown through the channels. This requires a reasonable pressure drop along the microchannels, which is possible when carrying out ALD at atmospheric pressure. Furthermore, in earlier work we have shown that the obtained coatings on flat PDMS surfaces are superior with AP-ALD as compared to vacuum-based ALD process [8, 9]. Therefore, forcing the ALD precursors through the microchannels using convective flow offers an attractive route to address the challenge to coat long microchannels, akin to deep trenches and benefits from all advantages of gas phase ALD.

In this study, we explore the use of convective flow via atmospheric pressure ALD (AP-ALD) for in-channel functionalization of bonded PDMS microfluidic channels through a layer of metal oxide. The concept is illustrated in Figure 4.1, which shows that we alternatingly flow ALD precursors through a bonded microfluidic chip, which is enclosed in a tubular glass reactor connected to a home-built AP-ALD setup. In this way, we deposit a nano-layer of metal oxide on all walls of the microfluidic channels (silicon oxide as well as titanium oxide), rendering them inert against organic solvents, and providing surface functionality in terms of their wetting and photocatalytic properties and, at the same time, rendering them inert against organic solvents. These metal oxide layers hence offer additional benefits over commonly used organic layers that effectively functionalize the surface, but do not render it inert[17, 25]. We demonstrate the beneficial properties for three important classes of applications in the field of microfluidics: the production of microparticles, the cultivation of biological cells, and the photocatalytic degradation of a pollutant. The presented results show the potential use of AP-ALD to modify the walls of bonded microfluidic channels, broadening the application window of PDMS chips [15, 26].

4.2. Methods and Materials

4.2.1. Fabrication of PDMS microfluidic chips

We fabricated PDMS microfluidic chips using soft lithography. In short, a negative photoresist (SU-8 2050, micro resist technology GmbH) was spin-coated on top of a 4 inch silicon wafer following the recipe of the manufacturer before baked at 100°C for 15 minutes to obtain a 50 µm thick layer. The coated wafer was then loaded onto a Laser-Writer (Heidelberg, 1 µm laser beam at 365 nm), where the two-dimensional layout of

the microchannels (Autocad 2019, Autodesk, see Figure 4.9) was written on the wafer. After laser writing, we soft-baked the wafer at 100°C for 5 minutes, developed the patterned photoresist coating using propylene glycol methyl ether acetate (PGMEA, >99.5%, Merck Sigma) for 10 minutes, and post-baked the thus obtained master mold at 200°C for 30 minutes.

To fabricate PDMS microfluidic chips from the master mold, we mixed the elastomer and curing agent (Sylgard 184 Elastomer Kit, Dow Corning Comp.) in a mass ratio of 10:1. After degassing, we poured the mixture over the master mold placed in a 5 inch Petri dish. We cured the PDMS at 70°C for at least 8 hours. The PDMS slab was then gently removed from the wafer and cut to size. PDMS chips were obtained by punching inlets and outlets into the pieces of PDMS using a 1.5 mm biopsy puncher, washing them with ethanol to remove debris, and bonding them on glass slides spin-coated with a 20 μm thick PDMS layer (2000 rpm for 2 minutes, Laurell WS-650-23B) using an oxygen plasma treatment (Harrick PDC-002) at 0.2-0.4 mbar for 140 seconds. The bonded chips were stored in the oven at 70°C before use.

4.2.2. In-channel coating of bonded microfluidic chips using AP-ALD

To coat the inner walls of the bonded PDMS microfluidic chips with a thin layer of metal oxide, we used a home-built atmospheric-pressure ALD (AP-ALD) setup with a tubular glass column. One microfluidic chip was placed inside the column and one of the inlets of the chip was directly connected to the inlet of the column through a polytetrafluorethylene (PTFE) tube (outer diameter 1.6 mm, inner diameter 0.5 mm, Diba, 008T16-050-200). In this way, the gases entering the column flowed entirely through the microchannels. The role of the column was to safely contain the excess reactants and byproducts. The metal oxide nano-layer was grown on the walls of the microchannels by subsequently flowing a metal precursor and an oxidizing agent through the chip, both in the gas phase, separated by a purge with nitrogen gas in order to remove excess reactants and byproducts. The thickness of the nano-layer was controlled by the number of such sequences, commonly referred to as ALD cycles.

The simplified process flow diagram of the setup is shown in Figure 4.10. Nitrogen gas (N_2 99.999%, Linde) was used to carry the metal precursor as well as to purge the chip through the use of three gate valves, two connected to a dip-tube bubbler that contains the metal precursor, and one to the tubular glass column, as shown in Figure 4.10. When the two valves connected to the dip-tube bubbler opened and the middle (by-pass) valve closed, nitrogen gas first flowed into the dip-tube bubbler, and then into the column and the microchannels. When both valves connected to the dip-tube bubbler closed, and the by-pass valve opened, nitrogen gas bypassed the dip-tube bubbler, purging the microchannels and the column. From the column, the gases flowed through a series of two trapping bottles, and subsequently through a carbon filter, before being released in a fume hood.

Two types of metal oxides were used in this work: silicon oxide and titanium oxide. All development and characterization studies were done using silicon oxide, while two complementary case studies, showing the versatility of the ALD approach, were done with titanium oxide. The deposition of the SiO_x nano-coating was conducted using silicon tetrachloride ($SiCl_4$, Alfa Aesar) as the metal precursor and ozone-treated humidi-

fied air as the oxidizing agent. The stream of the oxidizing agent was made by flowing compressed air through metallic tubing to an ozonator (Sander Certizon), and then to a dip-tube bubbler containing water at room temperature. Unless stated otherwise, the silicon precursor, kept in the bubbler at room temperature, flowed at 0.2 L/min for an exposure time of 10 seconds, while the oxidizing agent flowed at 0.2 L/min for an exposure time of 30 seconds. In between, nitrogen purging was done at 0.2 L/min for 100 seconds. The AP-ALD treatment was carried at 50°C for different numbers of ALD cycles (5, 20, 50, and 100 cycles). The gas flow leaving the glass column was neutralized by flowing it through a series of two trapping bottles, both containing a solution of 10% (w/v) sodium hydroxide (Merck Sigma).

The deposition of the TiO_x nano-coating was conducted using Tetrakis-dimethylamino titanium (IV) (TDMAT, >99.99% Merck Sigma) as the metal precursor and ozone-treated air as the oxidizing agent. The stream of the oxidizing agent was made by flowing compressed air through metallic tubing to an ozonator, and then directly into the column. The titanium precursor, kept in the bubbler covered with a heating mantle at 70°C, flowed at 0.2 L/min for an exposure time of 10 seconds, while the oxidizing agent flowed at 0.2 L/min for an exposure time of 30 seconds. In between, nitrogen purging was done at 0.2 L/min for 100 seconds. The AP-ALD treatment was carried at 100°C for different numbers of ALD cycles (3, 25, and 100 cycles). The gas flow leaving the glass column was neutralized by flowing it through a series of two trapping bottles, both containing a mineral oil (Kaydol).

To accommodate the reaction temperature, we covered the tubing with heating cables. We furthermore heated the tubular glass column with an infrared heating lamp, see Figure 4.10.

4.2.3. Characterization of metal oxide coating on microchannel walls

To characterize the metal oxide coating deposited on the inner walls of the bonded microfluidic channels, we made a cross-sectional cut of the ALD-treated channels using a scalpel. We analyzed the channel cross sections with field emission scanning electron microscopy (FE-SEM, Hitachi Regulus SU8230, with a beam current of 1-5 μA, electron energy of 1-10 keV, and a tilt angle of 0° to 15°). The surface morphology and the surface chemical composition were studied in more detail by conducting ALD experiments with the same operation parameters on flat samples (PDMS spin-coated on a silicon wafer) as described elsewhere [9]. The surface morphology was studied using atomic force microscopy (AFM, Bruker Dimension Icon with an amplitude of 80-150 nV, a feedback gain of 0.05-0.5, and scan rates of 0.6-0.9 Hz). The surface chemical composition was measured using X-ray photoelectron spectroscopy (XPS, ThermoFisher Scientific Nexsa, equipped with a monochromatic Al Kα radiation source and a pass energy of 30 and 100 eV for the survey scan and ion-beam etching unit). Depth profiling was conducted by etching the surface using Ar^+ ions (2 keV with a raster size of 2 mm) while a flood gun was used to compensate for the positive charge. Thermo Avantage 5.913 and CASA-XPS software packages were used to post-process and deconvolute the XPS peak profile, where the spectra were charge-corrected with the adventitious carbon peak at 284.8 eV.

On top of the above characterization of the metal oxide coating obtained for a fixed set of ALD operating parameters, we studied the influence of the temperature on the

surface morphology. More specifically, we obtained FE-SEM images of the cross sections of microfluidic chips treated at 30°C, 50°C, and 100°C, for a fixed number of 20 ALD cycles. Given the observed differences in morphology and the differences in possible detachment of the coating from the PDMS walls under flow, we checked the attachment of the coating to the PDMS by flowing water through the treated chips at 50 µL/min for 10 minutes. We studied the solution collected from the outlet of the chips using inductively coupled plasma optical emission spectroscopy (ICP-OES, PerkinElmer Optima 8000), with argon gas as a carrier.

4.2.4. Evaluation of AP-ALD coating in microfluidic experiments

To evaluate the performance of the metal oxide coating, we conducted two studies with coated microfluidic chips: (1) a channel wall deformation study and (2) a channel wall absorption study. Bare PDMS channel walls are known to swell and deform when exposed to organic solvents as well as to absorb small hydrophobic molecules in a liquid solvent [16, 17, 27]. We then performed these two studies to evaluate to what extent the metal oxide coating prevents direct contact between the PDMS and the solvent, mitigating both issues.

The channel deformation study was conducted as follows. We fabricated microfluidic chips featuring a simple long straight microchannel (length: 11.6 mm, width: 500 µm, height: 50 µm), see Figure 4.9(a) for the two-dimensional layout. We coated the inner walls of the chips with a SiO_x nano-layer using 5, 20, and 100 ALD cycles. To evaluate the deformation of the channel walls when flowing an organic solvent through the channel, we used a confocal laser scanning microscope (CLSM 710, AxioObserverZ.1, Fluar 2.5x/0.12, 543 nm laser source (20%) and PMT detector). To this end, rhodamine B (Merck Sigma), a known fluorescent agent, was added to the organic solvent. More specifically, we prepared a solution of 1 µM rhodamine B in chloroform (99%, Merck Sigma). We loaded the rhodamine B solution into a 5 mL syringe (Beckton-Dickinson, Discardit II) with a non-rubber plunger, connected the syringe with PTFE tubing to the inlet of the microfluidic chip, and drove the solution through the microchannel using a syringe pump (Harvard Apparatus Pump 11 Pico Elite Plus) at a flow rate of 40 µL/min, while taking confocal (z-stack) images of the channel at 10-15 different planes across the height of the channel. From these images, we reconstructed the 3-D shape of the lumen of the microchannel using Zen 3.8 software (Zeiss), normalized to its maximum intensity (1). For reference, we first performed the same type of measurements in the same channel with a solution of 1 µM rhodamine B in demi water, since no swelling of the PDMS, and hence no deformation of the channel walls is expected for water.

The wall absorption study was conducted as follows. After fabrication and coating of the chips with a nano-layer of SiO_x through 20 ALD cycles, we injected a rhodamine B solution (30 µM, in demi water) inside bare and AP-ALD-treated PDMS microfluidic chips using a 5 mL syringe mounted on a syringe pump. After filling the channels, we left the chips (with the outlets open to air) to dry for 3 days in a dark environment, where the solutions dried through the inlets and outlets. After three days, we measured the intensity of the fluorescent agent inside the walls of the PDMS using a confocal laser scanning microscope (CLSM 980, Zeiss Axio-ObserverZ.1/7) with EC Plan-Neofluar 5×/NA 0.16 and 10×/NA 0.30 air objectives, a 543 nm laser source (0.2%, emitted 565 nm), and

a GaAsP-PMT detector. Background fluorescence was reduced using the Zen autofocus strategy with the best contrast method. The intensity profile was processed using Zen 3.8 software to visualize the penetration of rhodamine B into the channel walls.

An advantage of forcing the precursor through the microfluidic channels instead of letting the precursors in the ALD tubular reactor enter the microchip through the inlets and outlets by diffusion is the ability to coat long channels and even channel networks. Rather than using the long channel used to assess the deformability of the (coated) wall, we, therefore, used the channel network as shown in Figure 4.9(b) to assess the coating based on the absorption of the wall. To study to what extent the walls of the channels perpendicular to the ALD precursor flow direction were exposed to the precursors and covered by a layer of SiO_x, we performed the experiment for various pulse times of the ALD precursors (1, 10, 30, and 100 seconds). We kept the purge time fixed to 100 seconds. To confirm the location of the channel wall, we additionally took brightfield images of the bare PDMS chip (EC Plan-Neofluar 5×/NA 0.16 objective and Multialkali-PMT detector).

4.2.5. Case study 1: microparticle production using organic solvents

A first important class of applications in the field of microfluidics is to utilize the unsurpassed control over minute amounts of fluids to produce single, double, and even higher order emulsions, foams, and particles [28, 29]. Yet, the use of organic solvents, for example, necessary to produce synthetic cells through the use of lipids that are typically dissolved in chloroform, does not permit the use of PDMS chips. In this first case study, we show the ability to use ALD-coated microfluidic chips for the production of polylactic acid microparticles using chloroform as the organic solvent.

We fabricated a microfluidic chip featuring a flow-focusing junction commonly used for the generation of droplets, see the two-dimensional layout in Figure 4.9(c). We coated the walls with a nano-layer of SiO_x using 20 ALD cycles. To produce polylactic acid (PLA) microparticles, a solution of 5% (w/v) poly(D,L-lactide) (PLA, 10–18 kDa, Resomer R 202H, ester terminated, Sigma Aldrich) in chloroform was injected in the chip at a flow rate of 0.5 µL/min and broken up into droplets in a solution of 1% (w/v) poly(vinyl alcohol) (99%, hydrolyzed, Merck Sigma) in MilliQ water injected at a flow rate of 40 µL/min. The formation of the PLA droplets was observed using a camera (ImagingSource DFK33-UX273, 600 frames per second) through an LWD plan phase 40X objective lens on a light microscope (Euromex Oxion Inverso PLPH). The polymerized PLA microparticles were collected at the outlet using a glass slide after 0, 1, and 3 hours of continuous production. Their photos were taken using the same camera. A minimum of 100 particles was analyzed using ImageJ to determine the particle size distribution.

4.2.6. Case study 2: biological cell culture on PDMS walls functionalized with titanium oxide

A second important class of applications in the field of microfluidics is to utilize control over micro environments for the study of biological cells, tissue, and organoids [12]. Yet, it is well known that cells do not adhere to bare PDMS surfaces. On top, cytotoxic uncured monomers in the PDMS matrix may leach out during cell culture, compromising the cell culture [30]. In this second case study, we show the ability to use ALD-coated

microfluidic chips for the culture of biological cells using titanium oxide as a nano-layer on top of the PDMS, as this metal oxide is known to promote cell adhesion [31, 32].

We fabricated a microfluidic chip featuring a growth chamber, see the two-dimensional layout in Figure 4.9(d). We then coated the walls with a nano-layer of TiO_x using 3 and 25 ALD cycles. Before seeding the cell (A549-Vim-RFP, from a human lung adenocarcinoma cell line, the vimentin being tagged with a red fluorescent protein), in bare and TiO_x-coated chambers, the chips were rinsed with 70% ethanol and washed three times with complete media (see details below). The cells were seeded into the microfluidic chips at a density of approximately 3.75×10^3 cells/mL and the chips were incubated at 37°C with 5% CO_2 in a dark environment. The cells in the chips were imaged every 24 hours for 72 hours using a confocal laser scanning microscope (AxioObserverZ.1/7, Plan-Apochromat 10x/0.45). We obtained red fluorescent images of cells using LED-module 567 nm laser source (50%) filtered so that the excitation wavelength was at 543-568 nm, and the emission wavelength was measured at 581-679 nm, with exposure time of 150 ms and a 56 HE GFP/DsRed reflector and an Orca Flash 4.0 V2 Hamamatsu camera. To reduce the background noise, the autofocus function of the Zen 3.8 software was used. The images were analyzed using ImageJ to derive the number of cells. The cell adhesion response on the microfluidic channel surface was studied by analyzing the sphericity of the cells after 24 hours of incubation. Detached cells were indicated with the sphericity and shape factor near 1 (0.99-1.00), while the adhered cells were indicated with the sphericity and shape factor less than 1 (0.00-0.98) [33]. The experiment was repeated three times in three independent microfluidic chips. A paired comparison method with the Bonferroni post-test (OriginPro 2022) at a significance level of p=0.05 was used to study the statistical significance between the results.

To check the viability of the cells, we stained the cells with calcein AM (1 μM in serum-free culture media, ITK) after 72 hours of incubation. Green fluorescence images were obtained using a LED-module 475 nm laser source (2%) filtered so that the excitation wavelength was at 450-490 nm and the emission wavelength was at 500-550 nm, with a 38 HE Green Fluorescent Prot reflector and an Orca Flash 4.0 V2 Hamamatsu camera.

Preparation of the cell solution used for seeding of the PDMS chips was done as follows: cells from cell line A549-Vim-RFP (generously gifted by Peter Ten Dijk, Leiden University Medical Centre) were grown on T25 flasks (Sarstedt) using a 'complete medium'. The medium consists of Dulbecco's Modified Eagle's media (DMEM, Thermofisher), supplemented with 5% of Fetal Bovine Serum (FBS, Thermofisher), and 1% of antibiotic-antimycotic (Merck Sigma). After reaching 80% confluency, the cells were detached from the flask using trypsin (0.25% EDTA, Thermo Fisher Scientific) and counted with trypan blue (Thermo Fisher Scientific) using an automated counter (TC20, Bio-rad). The obtained cell solution was then diluted using complete media to a cell concentration of 3.75×10^3 cells/mL.

To better understand the observed behavior on the titanium-oxide coated PDMS walls, we additionally characterized the surface properties (wetting and surface chemical composition) of the TiO_x nano-layer. To be able to perform water contact angle measurements, we turned to flat samples (PDMS spin-coated on a silicon wafer) and performed the AP-ALD with the same operational parameters. Both bare and AP-ALD-treated PDMS samples were kept in water and dried before the dynamic water contact

angle measurements were performed using a Krüss drop shape analyzer as described elsewhere [8]. The average advancing contact angle was reported from 10 measurements via the typical uncertainty (1 s.d.). To obtain the surface chemical composition, XPS survey scans were performed on the flat samples.

4.2.7. Case study 3: continuous flow chemistry at PDMS walls functionalized with a titanium oxide nano-layer and gold nanoparticles

A third important class of applications in the field of microfluidics is to perform chemical reactions under continuous flow, thereby making use of the well-known advantages of microreactor technology, including the high surface-to-volume ratio, etc. [34]. While heterogeneous catalytic reactions with a catalyst coated on the wall are interesting for a wide range of applications, including electrochemical conversions, direct functionalization of bare PDMS walls is a challenge [8, 14]. In this third case study, we show the ability to use ALD-coated microfluidic chips to functionalize the PDMS walls with gold nanoparticles used for the photocatalytic degradation of a pollutant in water.

We fabricated a microfluidic chip featuring the same chamber as used for the cell study, see the two-dimensional layout in Figure 4.9(d). We coated the walls with a nano-layer of TiO_x using 100 ALD cycles. We then further functionalized the TiO_x nano-layer through the deposition of gold nanoparticles (AuNPs) using trimethylphosphino-trimethyl gold(III) (6-Me, prepared as described in [35]) and ozone as the ALD precursors [36]. This AP-ALD process was carried out using nitrogen as the carrier gas flowing at 0.2 L/min at 100°C for 5 cycles, with a pulse time for the 6-Me of 10 seconds and for the ozonated air of 30 seconds, with 100 seconds of nitrogen purge in between. After the deposition of the gold nanoparticles, we performed 5 additional TiO_x AP-ALD cycles. As a pollutant in the photocatalytic degradation study, we use rhodamine B. We prepared an aqueous solution of rhodamine B (17 μM, or 7.2 mg/L, in demi-water) and injected it into the coated chip using a syringe pump at a wide range of flow rates leading to a wide range of residence times in the chip (0.02, 0.04, 0.1, 0.2, 0.4, 1, 2, and 4 minutes). The photocatalytic conversion was done by top-exposing the chip to a visible light source (Dotlux LED-Einbaupanel, 225 mm x 225 mm, 25 W, 4000 K, 2375 lm, distanced 5 cm from the top of the chip). The inlet and outlet concentrations were measured using UV-Vis NanoDrop™ 2000/2000c Spectrophotometer (wide scan reading, with wavelengths in the range 300 -800 nm). For reference, the same measurements were performed in bare PDMS microchips. For each experiment, three samples were collected from the outlet and the averages are reported.

To characterize the AuNPs inside the chip, we conducted a similar deposition and cut the chip into pieces of cross-sections. The pieces were sonicated in 1 M HNO_3 solution (65%, Merck Sigma) for 15 minutes, before being left immersed for 48 hours to dissolve the underneath TiO_x layers and disperse the AuNPs. The immersing liquid was then centrifuged (MicroCL 21/21R, Thermoscientific) at 14800 rpm for 10 min, decanted, washed with ethanol, and transferred onto a Quantifoil copper TEM grids. Transmission electron microscopy (TEM, JEOL JEM1400) was performed with a voltage of 120 kV and the particle size was analyzed using ImageJ.

4.3. Results and discussion

4.3.1. Characterization of the metal oxide coating on the inner walls of the microchannels

Figure 4.2(a) shows FE-SEM images of the cross-section of bare and AP-ALD-treated PDMS microfluidic channels. The wall of a bare PDMS channel is relatively smooth, as shown in Figure 4.2(a). In comparison, after 5 ALD cycles, patches are seen on the channel wall. These patches appear smaller in size after 20 cycles and more packed after 50 cycles. After 100 cycles, individual patches are no longer observed and the wall appears as fully covered by a sheet of SiO_x. Since the angle of the SEM beams and detectors may affect our perception of the morphology, we supplemented the surface morphology study by conducting the same depositions on a flat 20 µm thick layer of PDMS spin-coated on a silicon wafer. AFM measurements performed on bare and ALD-treated samples confirm a smooth surface for bare PDMS and a relatively rough surface after 5 ALD cycles, which gets smoother with an increasing number of ALD cycles as shown in Figure 4.2(b).

In addition to the surface morphology, we characterized the chemical composition of the surface of bare and ALD-treated flat PDMS samples. Figure 3.2 shows the Si2p spectra obtained at different etch depths for a PDMS sample treated with 20 ALD cycles. At the surface (depth ~0.4 nm), two peaks in the Si2p spectrum are found at 99.95 eV and 103.5 eV. When etched deeper to ~10 nm, the peak at 103.5 eV starts decreasing and the two peaks become less distinctive. At the largest etch depth of ~132 nm, we observe only one peak at 99.95 eV. While the observed peaks point to the presence of silicon, the shape and position of the peaks indicate different oxidation states of the silicon element.

To confirm the presence of a SiO_x nano-layer on the surface, we deconvolute the XPS spectra at the etch depth of ~0.4 nm. The first peak at 99.95 eV has a peak split of 0.51 eV, that easily ends up as one broad peak or an asymmetric one [37, 38]. This peak, unfortunately, corresponds to all possible oxidation states of the silicon element (from Si^0 to

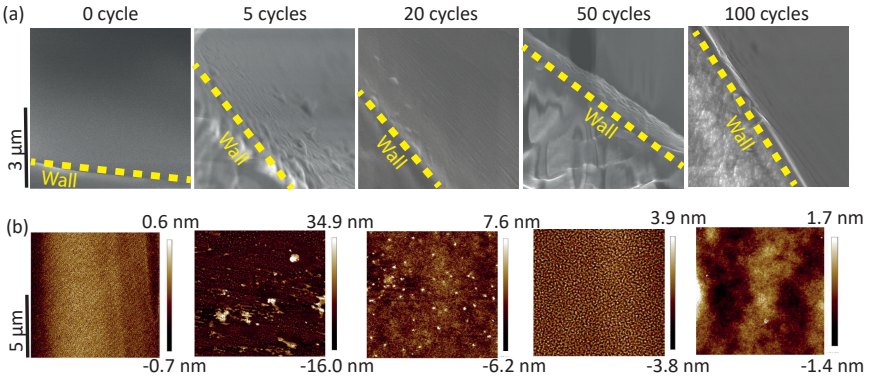

Figure 4.2: (a) FE-SEM images of bare and SiO_x-coated PDMS chips obtained after making cross-sectional cuts of the chips that feature a straight 11.6 mm long, 500 µm wide, and 50 µm high microchannel. SiO_x AP-ALD treatment: 5, 20, 50, and 100 ALD cycles at 50°C. (b) AFM surface profiles on a flat PDMS layer treated the same as in the corresponding images in (a).

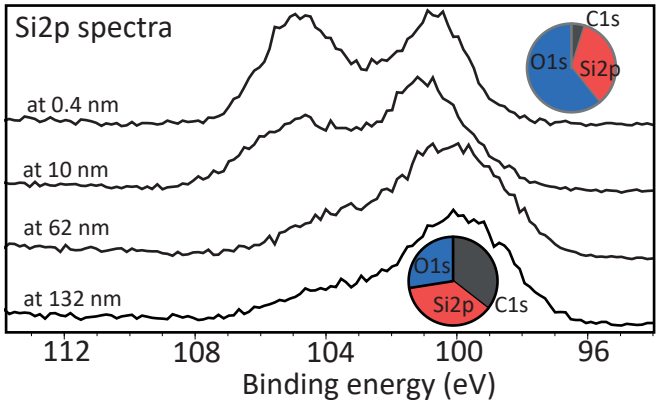

Figure 4.3: Surface chemical composition of a flat PDMS layer treated with 20 ALD cycles at 50°C (corresponding to the panels in the middle of Figure 4.2) studied using XPS, showing XPS Si2p spectra obtained at different etch depths. The top graph shows the Si2p spectrum at an etch depth <1 nm and the top inset shows the corresponding atomic composition. The bottom graph shows the Si2p spectrum at an etch depth >100 nm and the bottom inset shows the corresponding atomic composition. The etch depth was approximated using the etch rate determined in our earlier work [9].

.

Si^{4+}) that could be found in a silicon wafer, in a silicon oxide layer, and a PDMS sample [37, 38]. However, the second peak (at 103.5 eV) corresponds exclusively to a higher Si oxidation state (e.g., Si^{3+} and Si^{4+}), typically found in a silicon oxide layer and not in a PDMS sample [39]. Therefore this peak suggests the presence of a SiO_x nano-layer at the etch depth of ~0.4 nm. We then further confirm it by conducting an XPS survey scan at a similar etch depth, shown in the corresponding pie chart (see Figure 3.2, top inset). It shows that the surface is dominated by silicon and oxygen elements, with a low presence of carbon, confirming the presence of SiO_x. Of note, the low carbon presence is acceptable and can be explained by possible adventitious carbon contamination and the out-diffusion of uncured PDMS oligomers into the surface [9, 40]. Looking closer at the surface composition, the atomic ratio of Si to O is found to be around 1:1.7, lower than the expected stoichiometric ratio of SiO_2. A comparable value, however, is reported by other researchers when the SiO_x is deposited at lower temperature [41], attributed to the incomplete reaction between surface-adsorbed chemical species [42].

Going deeper into the layers underneath, the decrease and shift of the distinctive peak at 103.5 eV points to the declining Si presence at a higher oxidation state (e.g. Si^{3+} and Si^{4+}). This indicates the possible formation of a mixed layer of SiO_x and PDMS, as suggested by our previous study [9]. As the layers are etched deeper (~132 nm), the disappearance of the peak at 103.5 eV suggests the absence of SiO_x. An additional XPS survey scan (see Figure 3.2, bottom inset) shows the typical atomic percentage distribution of a PDMS layer as found in earlier work [9]), confirming the absence of SiO_x. While the unique surface-subsurface metal oxide growth on PDMS through AP-ALD is in agreement with the reported phenomena in our previous study [9], we point out that the depth profile of the deposited layers depends on various factors, including the operating

temperature [21–23].

After confirming the presence of the SiO_x nano-layer, we performed an additional study to gain insight into the effect of the AP-ALD operating temperature for a fixed number of 20 ALD cycles. When AP-ALD was carried out at 30°C, a rugged and rough-textured surface was observed (Figure 4.11(b)), that became less rough as the operating temperature increased to 50°C (Figure 4.11(c)), and even smoother at 100°C (Figure 4.11(d)). We then compared our results with the reported phenomena in the literature [43]. The rugged surface and patches obtained when we conducted the AP-ALD at lower temperatures (30°C) are comparable with the results reported by others as they deposited SiO_x at a lower temperature, without the presence of a catalyst, and on less reactive substrates [44–46]. There, they argue the presence of non-ideal ALD growth, such as condensation of ALD precursors (especially water) and hydrolysis [44, 47, 48], as commonly found in conventional chemical vapor deposition (CVD) of SiO_x [48]. As the operating temperature increases to 50°C, then to 100°C, where water molecules are expected to condense less, we obtain a smoother surface, consistent with the results reported by other groups [44].

Given that the observed differences in morphology may have an impact on how strongly the patches or layer is bound to the PDMS surface under flow, we flowed water into the channels treated with different AP-ALD operating temperatures at a relatively high flow rate (50 µL/min) for 10 minutes. We measured the silicon concentration in the solution collected at the channel outlet. The ICP-OES result shows that silicon (20.15 ± 0.20 mg/L) is detected for the liquid flowing in the microfluidic channel coated at 30°C, indicating the expected weak physical bond between the deposited silicon oxide and PDMS channel wall, and indirectly corroborates the dominance of condensation (physisorption) during the deposition process. Conversely, no silicon is detected when flowing water through untreated channels and channels treated at 50°C and 100°C (0.10 mg/L and 0.06 mg/L respectively, lower than the reliable ICP-OES detection limit), indicating a strong bond between the metal oxide layer and the PDMS wall.

4.3.2. Evaluation of metal oxide coating performance in microchannel experiments

Bare PDMS microfluidic channels are known to be compatible with aqueous solutions such as water. However, when exposed to common organic solvents, PDMS swells, such that the channel walls deform and the lumen of the microchannels gets (partly) occluded [9, 25]. We, therefore, evaluated to what degree the metal oxide nano-layer prevents direct contact between PDMS and the organic solvent by visualizing the extent to which the cross-section of untreated and treated microchannels deforms when flowing chloroform through the channels. We hereby note that the relatively thin layer of metal oxide provides optical access to the treated channels such that they can be studied using optical microscopy as commonly done in the field. We use the deformation study to get an indication of the coverage of the nano-layers inside the chips, given that measuring the coverage directly inside the chips is a challenging task due to uneven morphology and the non-conductive nature of PDMS channels.

In the untreated (bare) PDMS chip, a serious channel deformation is seen, as evident from the intensity profile in Figure 4.4(a), where the low intensities in the middle

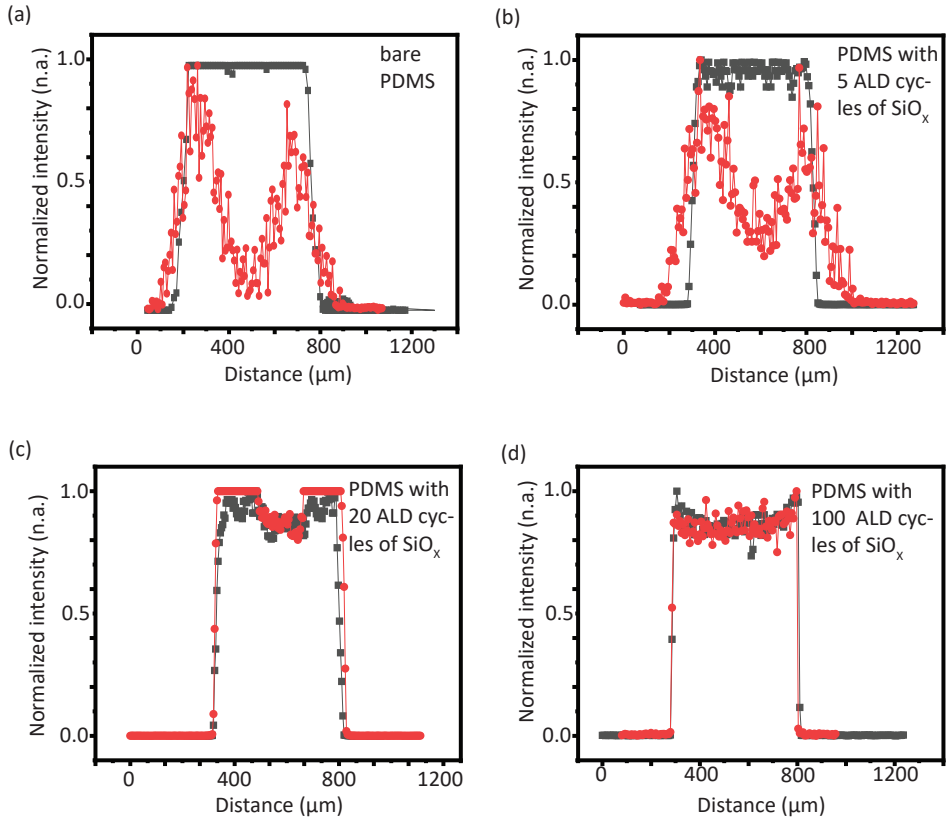

Figure 4.4: Fluorescence intensity across the 500 µm wide channel, averaged of the height of 50 µm, illustrating the deformation of the cross-sectional shape of a bare PDMS chip (a) and PDMS chips treated with 5 (b), 20 (c), and 100 ALD cycles. The dark gray lines show the intensity profiles for 1 µM rhodamine B in water, while the red lines show the intensity profiles for 1 µM rhodamine B. For comparison, each intensity profile was normalized by its maximum intensity.

of the 500 µm wide channel indicate that the top wall of the channel almost collapsed onto the bottom wall. The intensity of the red line increases first and declines later, indicating a larger, deformed base of the channel. While deformations are seen along the length of the channel, we note that the exact shape differs from place to place. We further note that the experiments with untreated PDMS devices are cumbersome, as some chips leaked when the chloroform solution was introduced into the channels. As expected, no deformation is observed for reference measurements with water, as evident from the well-defined, intensity profile, resembling the rectangular-shaped cross-section.

For the microchannels treated with 5 ALD cycles, we also observe channel deformation, albeit less pronounced compared to the untreated channel, see Figure 4.4(b). This indicates that 5 ALD cycles result in a non-conformal coverage of the PDMS. The observation is in agreement with the previous characterization in Figure 4.2, where after 5 cycles, the PDMS surface is covered only with patches of SiO_x. On the contrary, for

the microchannels treated with 20 and 100 ALD cycles, we observe overlapping intensity profiles for chloroform and water (no significant difference, as determined through a paired t-test, showing a p-value larger than 0.05), see Figure 4.4(c) and Figure 4.4(d), indicating complete SiO_x coverage of the PDMS channel walls even after repeated usage. The SiO_x layer hence prevents direct contact between PDMS and the organic solvent, demonstrating AP-ALD as a suitable approach to expand the use of PDMS microfluidic devices from aqueous solutions to organic solutions as well.

A strength of the developed approach in which ALD precursors are alternating flown through the microfluidic device is the ability to coat long microchannels as well as complete networks of microchannels. To study over what extent channels perpendicular to the direction of the flow of the ALD precursors can be coated, we treated the channel network illustrated in Figure 4.5(a). The ALD precursors were flown into the chip using the inlet at the top, while the three outlets were open. We visualized the coating coverage along the channel by conducting a wall absorption study. To this end, we exposed the channels to a rhodamine B in water solution, introduced at the inlet on the left in order to fill all channels without the entrapment of air. When the PDMS microfluidic channel walls are not covered by SiO_x nano-layers, rhodamine B molecules are expected to penetrate slowly into the PDMS matrix [17, 27]. Contrarily, when SiO_x nano-layers are present, the rhodamine B molecules are expected to be retained in the solution [16, 17], which over the course of the experiment evaporates from the chip, leaving the rhodamine B concentrate near one of the outlets.

As expected, the fluorescent signal of rhodamine B is observed inside the walls of the untreated PDMS microfluidic chip, extending up to millimeter into the walls, see Figure 4.5(b), in line with earlier work [17, 27]. In contrast, the rhodamine B molecules are relatively retained at the walls in the AP-ALD-treated microfluidic channels, see Figure 4.5(c). This retainment is shown over the length of the 20 mm long channel. A closer look at the fluorescence intensity near the walls shows that the fluorescent signal is found only at the edge of the walls, which drops to a non-detectable level inside the walls, see Figure 4.5(c). For the shortest ALD pulse exposure time of 1 s, this drop occurs over a distance of 120 µm into the wall. For an ALD pulse exposure time of 10 s, the penetration distance into the walls is reduced, while the chips treated with pulse exposure times of 30 s and 100 s show comparable behavior with minimal penetration of rhodamine B into the wall. We note that the saturation conditions in a PDMS chip are difficult to determine due to differences in the channel width (distance for the ALD precursors to reach the channel wall) and the simultaneous surface-subsurface growth occurring on PDMS. While this study shows a possible effect of a very short pulse exposure time (e.g. way lower than 1 s), it also indicates the dependence of the conformality of the coating on the flow rate. Therefore, the conformality is limited by the pressure drop achievable in the microchannel. Furthermore, this study also proves the presence of SiO_x nano-layers inside the microfluidic channels, as the nano-layers have 2-3 orders of magnitude lower relative permeability against hydrophobic molecules than bare PDMS [9], offering a barrier against rhodamine B.

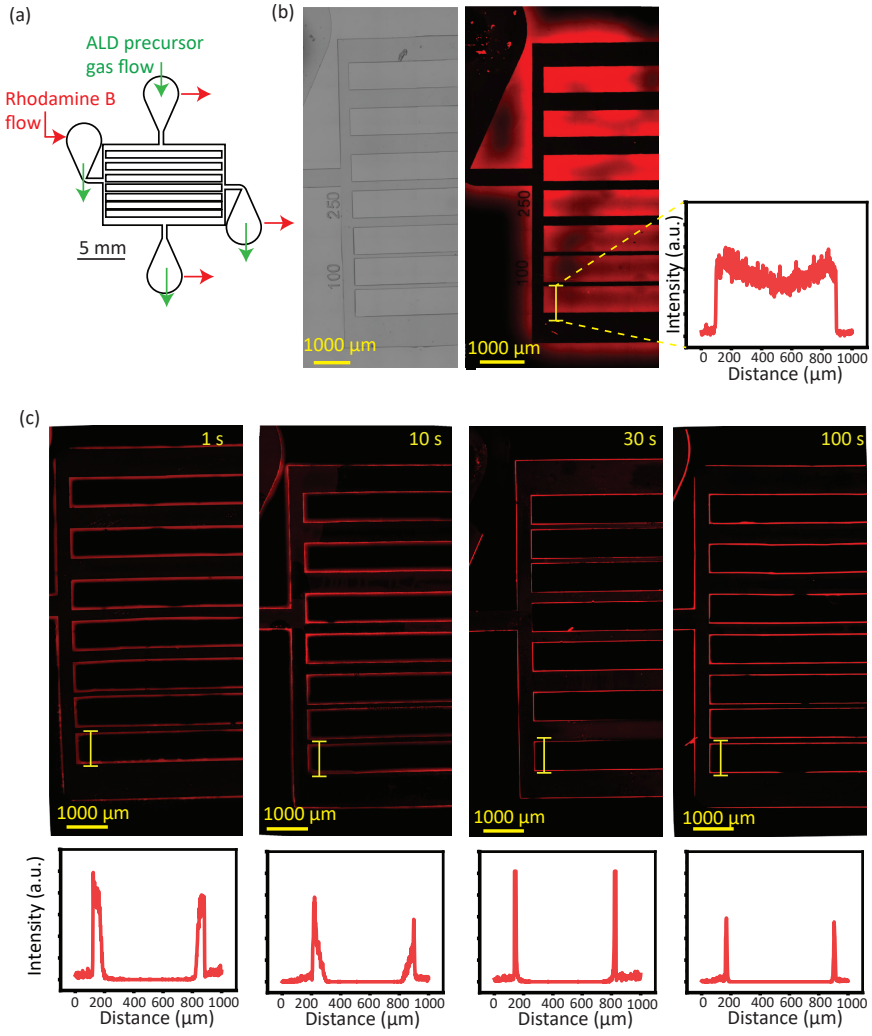

Figure 4.5: (a) Microfluidic channel network featuring channels of various widths (100, 250, and 500 µm) perpendicular to the direction of flow of the ALD precursors, to visualize how far inwards these channels can be coated. The green arrows indicate the flow direction of ALD gas precursors during AP-ALD, while the red arrows show the flow of the rhodamine B solution during the wall absorption study. (b) Brightfield image of a bare PDMS microfluidic chip and fluorescence image showing the absorption of rhodamine B into the PDMS walls. (c) Fluorescence images of PDMS microfluidic chips exposed to the ALD precursors for different pulse exposure times of 1 s, 10 s, 30 s and 100 s, with the intensity profiles taken along the yellow line in the corresponding images at the bottom. SiO_x AP-ALD treatment: 20 ALD cycles at 50°C.

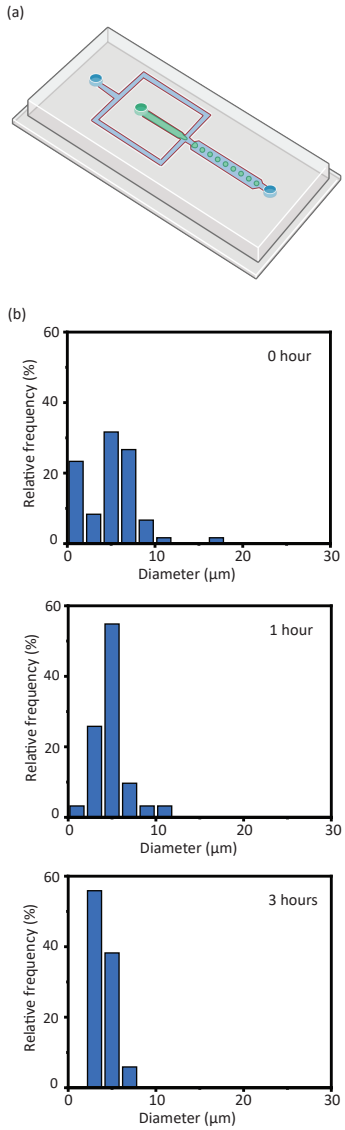

Figure 4.6: (a) Illustration of the microfluidic chip featuring a 25 μm wide flow focusing junction as used for the continuous production of polylactic acid (PLA) microparticles using chloroform as an organic solvent for the PLA.(b) Distribution of the diameter of the microparticles collected off chip after 0, 1, and 3 hours of continuous operations. A minimum of 100 particles was analyzed.

4.3.3. Case study 1: microparticle production using organic solvents

In the first case study, we demonstrate the use of ALD-coated microfluidic chips for the production of particles using chloroform as one of the solvents. Using the chip with a flow-focusing junction illustrated in Figure 4.6(a), a stream of 5% PLA in chloroform is broken up into droplets by a stream of 1% PVA in water. A few minutes after the start of the flows, a significant spread is observed in the diameter of the polymerized particles collected at the outlet, see the top panel in Figure 4.6(b). More specifically, the average diameter of the particles is 4.85 μm and the coefficient of variation (CoV) is 0.63. We attribute the relatively large CoV to the formation of satellite droplets as well as to the coalescence of droplets during the stabilization of the flow. After 1 hour of production, the average diameter of the droplets is about the same, 4.99 μm, and the CoV has reduced to 0.35. After 3 hours of production, the average diameter is 4.98 μm and the CoV has further reduced to 0.21. For reference, we attempted to perform the same experiments in bare PDMS chips. Upon introducing chloroform in bare chips, we observe swelling of channels and narrowing of the junction, in cases followed by leakage near the inlets due to the build-up of pressure in the chips. These experiments confirm the importance of the SiO_x coating. While further optimization of the experiments to produce particles with narrower particle size distribution is certainly possible, we conclude the discussion on the case study by emphasizing a second possible advantage of the SiO_x coating, next to mitigating the problem of swelling of the PDMS. PDMS is hydrophobic in nature, which generally limits the production of emulsions in uncoated PDMS chips to water-in-oil emulsions. The SiO_x coating renders the PDMS walls hydrophilic, providing a route to produce oil-in-water emulsions.

4.3.4. Case study 2: biological cell culture on PDMS walls functionalized with titanium oxide

In the second case study, we demonstrate the use of ALD-coated microfluidic chips for the cultivation of biological cells at functionalized PDMS walls, hereby using TiO_x instead of SiO_x in order to illustrate the versatility of the AP-ALD approach. We functionalized the walls of a microfluidic chip featuring a circular 10 mm wide and 50 μm high chamber, see Figure 4.7(a) and Figure 4.9(d) and seeded epithelial, non-migratory, lung adenocarcinoma cells in the chamber. We measured the number of cells per square millimeter adhering to the bottom wall of the chamber after 24 hours of incubation in bare PDMS chips and chips treated with 3 and 25 ALD cycles. The cell density is significantly higher in the AP-ALD-treated PDMS chips, as evident from Figure 4.7(b) and Table 4.1. Especially the density of cells with a sphericity less than one, a proxy for the ease with which the cells adhere to a surface, is significantly higher in treated PDMS chips. In bare PDMS chips, ~62 % of the cells are observed with sphericity less than 1, comparable to reported values in literature [33]. In treated PDMS chips, this percentage is significantly larger, i.e., ~91 % and ~80 % for 3 and 25 ALD cycles, respectively. This observation is in line with the notion that a more hydrophilic surface generally offers a better adherence for cells [33]. The treated surfaces are indeed considerably more hydrophilic, see Figure 4.12(a), consistent with our previous work [9]. While the surface chemical composition of the chips treated with 3 and 25 cycles is slightly different (Figure 4.12(b)), we attribute the larger percentage for 3 cycles to its rougher surface [8], which is known to

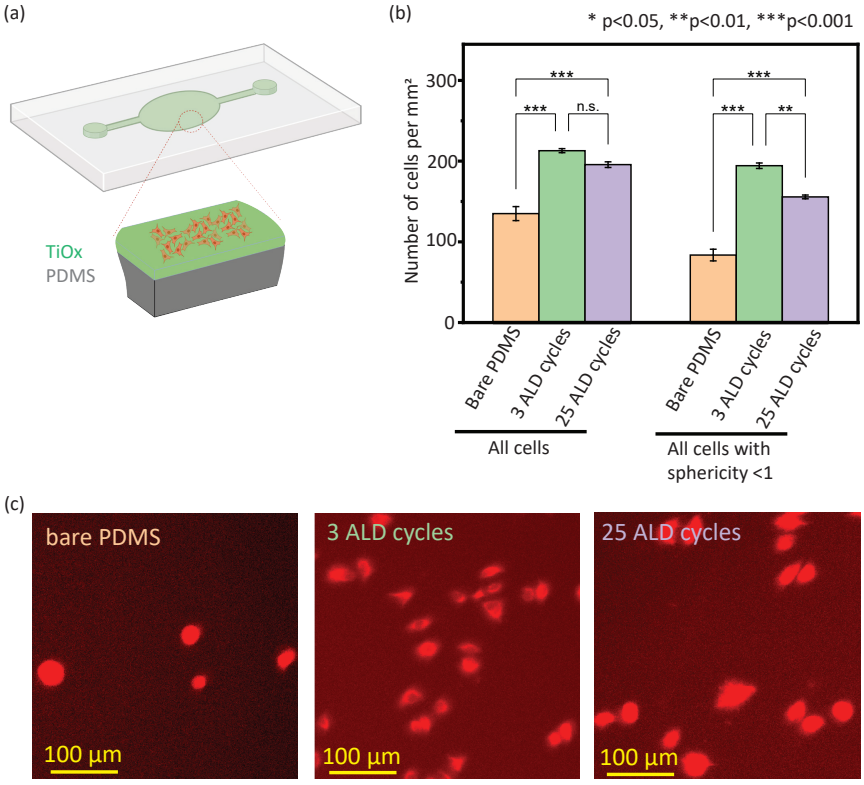

Figure 4.7: (a) Illustration of the microfluidic chip featuring a circular chamber (10 mm wide and 50 µm high) as used for the case study of the attachment of cells to the walls of bare and TiO_x-coated PDMS walls. (b) Number of A549 cells per mm^2 measured after 24 hours of on-chip incubation, including the number of cells with a sphericity of less than 1. Values are presented as mean ± standard error (n=3) and the corresponding numbers are provided in Table 4.1. (c) Representative images of cells attached to bare and TiO_x-coated PDMS walls taken after 24 hours of on-chip incubation.

promote cell adhesion [49].

To study the viability of the cells, we extended the culture up to 72 hours. The cell density steadily increased as shown in Figure 4.12(c) and Table 4.2. On top, we performed a live-dead assay with calcein AM after 72 hours of culture, confirming a viability of nearly ~100% in all experiments. We additionally tested the adherence of the cells after 72 hours of culture, by flowing culture media inside the chips at flow rates of 0, 1, 5, 20, and 50 mL/min, confirming no meaningful differences were observed in cell density during this test, indicating strong adherence of the cells inside both the bare and treated PDMS microfluidic chips. While this case study oriented on the cultivation of cells highlights the ability to functionalize PDMS walls with a metal oxide nano-layer, the next case study highlights the ability to use the metal oxide nano-layer as a base to further functionalize the walls.

4.3.5. Case study 3: continuous flow chemistry at PDMS walls functionalized with a titanium oxide nano-layer and gold nanoparticles

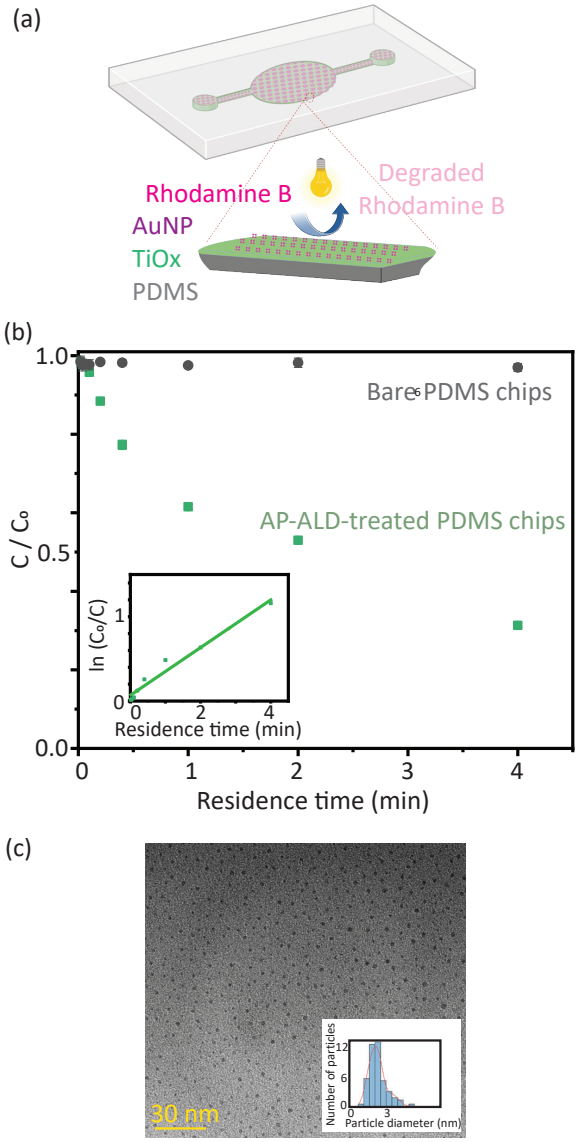

Figure 4.8: (a) Illustration of the microfluidic chip featuring a circular chamber (10 mm wide and 50 µm high) as used for the case study of the photocatalytic degradation of rhodamine B at TiO_x-coated PDMS walls further functionalized with gold nanoparticles. (b) Concentration of rhodamine B at the outlet of bare and ALD-treated chips relative to the initial concentration. The inset shows a linear fit to $\ln C_0/C$ of the ALD-treated chips over the residence time. (c) TEM image of gold nanoparticles and their corresponding particle size distribution.

In the third case study, we demonstrate the use of ALD-coated microfluidic chips for the photocatalytic degradation of rhodamine B dye at TiO_x-coated PDMS walls further functionalized with gold nanoparticles. Gold nanoparticles in conjunction with titanium oxide have been shown to have an increased photocatalytic activity towards various reactions, including oxidation of organic compounds [36, 50]. This is explained by an enhanced absorption in the visible range due to plasmon resonance [36]. Previously, we showed that TiO_x nano-layers and AuNPs can be deposited on PDMS substrates, allowing the PDMS surface to be functionalized robustly [8]. We functionalized the walls of a microfluidic chip featuring a circular 10 mm wide and 50 µm high chamber, see Figure 4.8(a) and Figure 4.9(d). We flowed a rhodamine B in water solution through the chip, while exposing the chip to visible light. Figure 4.8(b) shows the concentration of rhodamine B measured at the outlet of the chip relative to the initial concentration. For the shortest residence times, little to no degradation of rhodamine B is observed. As the residence time increases, the rhodamine B concentration at the outlet decreases, indicating photocatalytic reduction. The kinetics hereof is known to depend on the properties of the titanium oxide and gold nanoparticle coating [36]. The TEM indicated an average AuNP size of ~2.7 nm (Figure 4.8(c)). To compare the results with earlier work, we determine an apparent kinetic constant of 0.29 min^{-1} based on the logarithmic representation of the data in the inset of Figure 4.8(b), which is of the same order of magnitude as previously reported kinetic constants [36, 51–53]. For reference, we performed the same experiment in a bare PDMS microfluidic chip. We observed the concentration of rhodamine B at the outlet to be comparable to the initial concentration, irrespective of the residence time, indicating no photocatalytic reaction takes place without functionalizing the PDMS walls with a TiO_x-AuNP nano-layer. While these three case studies demonstrate the benefit of the deposited nano-layers inside the channel, the approach can be extended to other metal oxides (e.g. AlO_x, ZnO_x, PtO_x, IrO_x, AgO_x), other metals (e.g. platinum, iridium, silver), or even other metal forms (sulfides, nitrides). The introduced layers can also be functionalized with other groups, such as functionalizing metal oxide with amine-containing groups [54, 55], functionalizing AuNPs with thiol-containing groups [56], or using them in combination with other gas processing [57]. This versatility, along with the possible scalability due to cost reduction from the absence of low-pressure (vacuum) technologies/auxiliaries needed to operate the processes, makes AP-ALD an attractive process to coat bonded microfluidic chips.

4.4. Conclusion

In conclusion, we find that AP-ALD is useful for modifying the surface of bonded PDMS microfluidic channels in a simple and controlled manner. By depositing various metal oxide nano-layers, i.e., SiO_x and TiO_x, two weak points of PDMS are simultaneously solved: the weak resistance against common organic solvents and the lack of surface anchoring groups for surface functionalization. After studying how the morphology of the metal oxide nano-layers depends on important ALD operating parameters such as the temperature and the number of cycles we alternatingly flow a metal precursor followed by an oxidizing agent, we illustrate the use of the coated PDMS microfluidic devices in three classes of microfluidic applications. The developed approach for the in-channel treatment enables various applications, that are otherwise unattainable with untreated

PDMS chips.

4.5. Acknowledgment and Conflicts of interest

This publication is part of the Open Technology Programme (with project number 16913) financed by the Dutch Research Council (NWO). We thank Mojgan Talebi, Cas Veenhoven, Duco Bosma, Hozanna Miro and Stefan ten Hagen for their technical support during the ALD experiments. We also thank Eden Goodwin and Sean Barry for the synthesis of the ALD gold precursor. We furthermore thank Jan-Willem Hurkmans for fruitful discussions and extend our gratitude to Runjie Zheng and Nick Wijers. We acknowledge the use of Biorender in making some figures.

We extend our heartfelt gratitude to Professor Guy Marin for his leadership in the field of Chemical Reaction Engineering over the past several decades. Under his guidance, significant advancements have been made in research, including CO_2 utilization and the tailoring of catalysts through atomic layer deposition. Beyond his research contributions, Professor Marin has played numerous pivotal roles within the community. He has chaired evaluation panels and served as an editor for the Chemical Engineering Journal, among other positions. We are deeply appreciative of the exemplary standard he has set for the community.

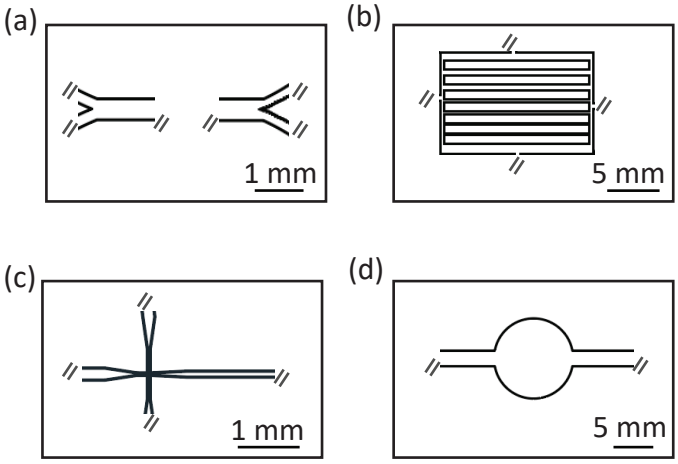

Figure 4.9: Two-dimensional layouts of the microfluidics chips used in this work: (a) Y-Y junction chip used in the characterization study (Section 4.2.3 and 4.2.4), (b) pillar chip used in the study of coating coverage (Section 4.2.4), (c) flow focus junction chip used in the case study of PLA microparticles production (Section 4.2.5), and (d) chamber chip used in the case study of A549 cells' interaction with nano-layers (Section 4.2.6) and in the case study of photocatalytic reduction of water pollutant model (Section 4.2.7). The height of the channels of all chips produced by printing these two-dimensional layouts onto a layer of photoresists is determined by the thickness of the photoresist layer, which was 50 µm. The inlets and outlets of the chips are not shown.

Table 4.1: Number of cells per mm^2 and the number of cells per mm^2 with sphericity less than 1 in bare and TiO_x-coated PDMS chips, measured 24 hours (day 1) after incubation. Values are given as mean ± standard error (n=3).

Sample	Number of cells per mm^2	Number of cells per mm^2 with sphericity <1
Bare PDMS	135 ± 9	84 ± 7
3 ALD cycles	213 ± 3	194 ± 4
25 ALD cycles	196 ± 4	156 ± 2

4.6. Supplementary information

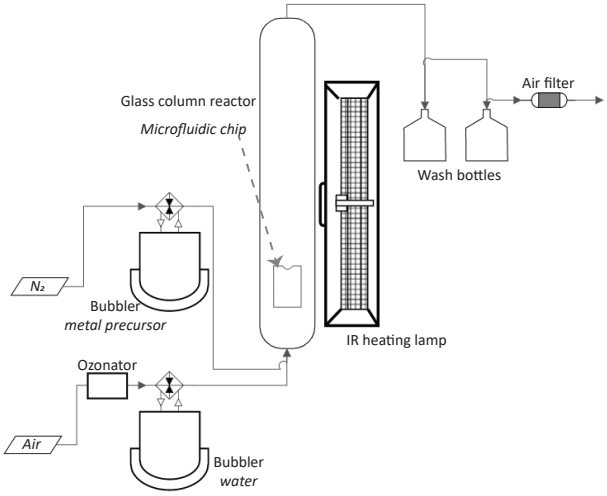

Figure 4.10: Simplified process flow diagram of the home-built atmospheric-pressure ALD (AP-ALD) setup.

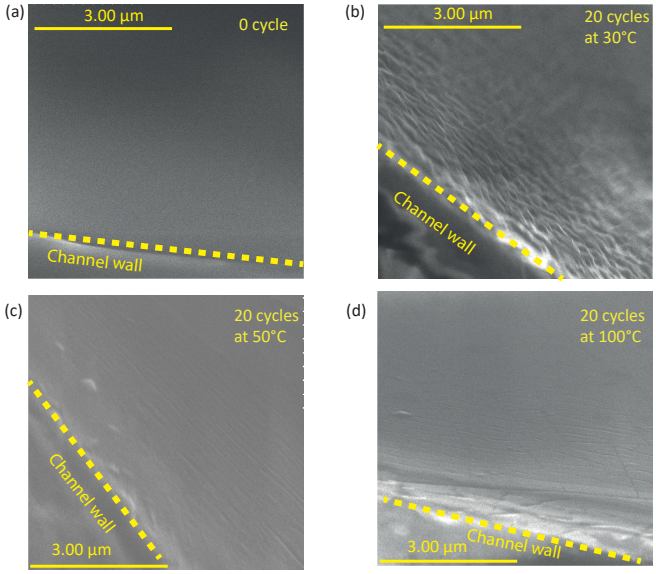

Figure 4.11: FE-SEM images of bare and SiO_x-coated PDMS chips obtained after making cross-sectional cuts of the chips that feature a straight 11.6 mm long, 500 µm wide, and 50 µm high microchannel. SiO_x AP-ALD treatment: 20 ALD cycles at 30°C, 50°C, and 100°C.

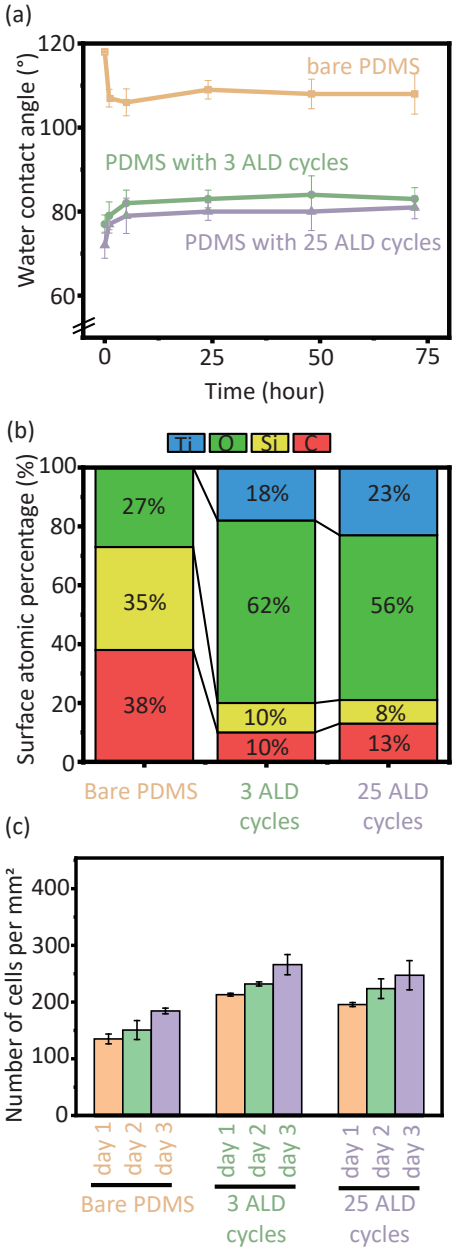

Figure 4.12: (a-b) Characterization of the surface properties of the TiO_x nano-layer on flat samples, with the advancing water contact angle in (a) and the surface chemical composition in (b). (c) Density of the cells grown on bare and AP-ALD-treated PDMS microfluidic chambers for 24 to 72 hours. TiO_x AP-ALD treatment: 3 and 25 ALD cycles at 100°C.

Table 4.2: Number of cells per mm^2 in bare and TiO_x-coated PDMS chips, measured 24 hours (day 1), 48 hours (day 2), and 72 hours (day 3) after incubation (n=3). Values are given as mean ± standard error (n=3).

Sample	Incubation time	Number of cells per mm^2
Bare PDMS	day 1	135 ± 9
	day 2	151 ± 17
	day 3	184 ± 5
3 ALD cycles	day 1	213 ± 3
	day 2	232 ± 4
	day 3	266 ± 18
25 ALD cycles	day 1	196 ± 4
	day 2	224 ± 17
	day 3	247 ± 26

References

[1] A. Santoso, M. K. David, P. E. Boukany, V. van Steijn, and J. R. van Ommen, *Atmospheric pressure atomic layer deposition for in-channel surface modification of PDMS microfluidic chips,* Chemical Engineering Journal , 155269 (2024).

[2] W.-R. Shin, G. Ahn, J.-P. Lee, I.-H. Oh, J.-Y. Ahn, Y.-H. Kim, and S. Chae, *Recent advances in engineering aptamer-based sensing and recovery of heavy metals and rare earth elements for environmental sustainability,* Chemical Engineering Journal , 144742 (2023).

[3] N. Chu, Q. Liang, W. Hao, Y. Jiang, P. Liang, and R. J. Zeng, *Microbial electrochemical sensor for water biotoxicity monitoring,* Chemical Engineering Journal **404**, 127053 (2021).

[4] H. Shi, K. Nie, B. Dong, M. Long, H. Xu, and Z. Liu, *Recent progress of microfluidic reactors for biomedical applications,* Chemical Engineering Journal **361**, 635 (2019).

[5] P. Martinez-Bulit, A. Sorrenti, D. R. San Miguel, M. Mattera, Y. Belce, Y. Xia, S. Ma, M.-H. Huang, S. Pané, and J. Puigmartí-Luis, *In flow-based technologies: A new paradigm for the synthesis and processing of covalent-organic frameworks,* Chemical Engineering Journal **435**, 135117 (2022).

[6] C.-Y. Lee, W.-T. Wang, C.-C. Liu, and L.-M. Fu, *Passive mixers in microfluidic systems: A review,* Chemical Engineering Journal **288**, 146 (2016).

[7] Q. Wu, J. Liu, X. Wang, L. Feng, J. Wu, X. Zhu, W. Wen, and X. Gong, *Organ-on-a-chip: Recent breakthroughs and future prospects,* Biomedical Engineering Online **19**, 1 (2020).

[8] A. Santoso, B. J. van den Berg, S. Saedy, E. Goodwin, V. van Steijn, and J. R. van Ommen, *Robust surface functionalization of PDMS through atmospheric pressure atomic layer deposition,* Atomic Layer Deposition **1**, 1 (2023).

[9] A. Santoso, A. Damen, J. R. van Ommen, and V. van Steijn, *Atmospheric pressure atomic layer deposition to increase organic solvent resistance of PDMS,* Chemical Communications **58**, 10805 (2022).

[10] J. Liu, Y. Yao, X. Li, and Z. Zhang, *Fabrication of advanced polydimethylsiloxane-based functional materials: Bulk modifications and surface functionalizations,* Chemical Engineering Journal **408**, 127262 (2021).

[11] M. A. Eddings, M. A. Johnson, and B. K. Gale, *Determining the optimal PDMS–PDMS bonding technique for microfluidic devices,* Journal of Micromechanics and Microengineering **18**, 067001 (2008).

[12] S. Torino, B. Corrado, M. Iodice, and G. Coppola, *PDMS-based microfluidic devices for cell culture,* Inventions **3**, 65 (2018).

[13] A.-G. Niculescu, C. Chircov, A. C. Bîrcă, and A. M. Grumezescu, *Fabrication and applications of microfluidic devices: A review,* International Journal of Molecular Sciences **22**, 2011 (2021).

[14] A. Shakeri, S. Khan, and T. F. Didar, *Conventional and emerging strategies for the fabrication and functionalization of PDMS-based microfluidic devices,* Lab on a Chip **21**, 3053 (2021).

[15] D. Cambie, C. Bottecchia, N. J. Straathof, V. Hessel, and T. Noel, *Applications of continuous-flow photochemistry in organic synthesis, material science, and water treatment,* Chemical Reviews **116**, 10276 (2016).

[16] G. T. Roman and C. T. Culbertson, *Surface engineering of poly (dimethylsiloxane) microfluidic devices using transition metal sol–gel chemistry,* Langmuir **22**, 4445 (2006).

[17] A. R. Abate, D. Lee, T. Do, C. Holtze, and D. A. Weitz, *Glass coating for PDMS microfluidic channels by sol–gel methods,* Lab on a Chip **8**, 516 (2008).

[18] J. Zhou, A. V. Ellis, and N. H. Voelcker, *Recent developments in PDMS surface modification for microfluidic devices,* Electrophoresis **31**, 2 (2010).

[19] H. Becker and C. Gärtner, *Polymer microfabrication technologies for microfluidic systems,* Analytical and Bioanalytical Chemistry **390**, 89 (2008).

[20] H.-Y. Chen, Y. Elkasabi, and J. Lahann, *Surface modification of confined microgeometries via vapor-deposited polymer coatings,* Journal of the American Chemical Society **128**, 374 (2006).

[21] R. W. Johnson, A. Hultqvist, and S. F. Bent, *A brief review of atomic layer deposition: from fundamentals to applications,* Materials Today **17**, 236 (2014).

[22] H. Van Bui, F. Grillo, and J. R. van Ommen, *Atomic and molecular layer deposition: off the beaten track,* Chemical Communications **53**, 45 (2017).

[23] J. R. van Ommen, A. Goulas, and R. L. Puurunen, *Atomic layer deposition,* in *Kirk-Othmer Encyclopedia of Chemical Technology* (John Wiley & Sons, Ltd, 2021) pp. 1–42.

[24] J. Yim, E. Verkama, J. A. Velasco, K. Arts, and R. L. Puurunen, *Conformality of atomic layer deposition in microchannels: impact of process parameters on the simulated thickness profile,* Physical Chemistry Chemical Physics **24**, 8645 (2022).

[25] R. Geczy, D. Sticker, N. Bovet, U. O. Häfeli, and J. P. Kutter, *Chloroform compatible, thiol-ene based replica molded micro chemical devices as an alternative to glass microfluidic chips,* Lab on a Chip **19**, 798 (2019).

[26] K. S. Elvira, R. C. Wootton, A. J. deMello, *et al.*, *The past, present and potential for microfluidic reactor technology in chemical synthesis,* Nature Chemistry **5**, 905 (2013).

[27] M. A. Iyer and D. Eddington, *Storing and releasing rhodamine as a model hydrophobic compound in polydimethylsiloxane microfluidic devices,* Lab on a Chip **19**, 574 (2019).

[28] L. Chen, C. Yang, Y. Xiao, X. Yan, L. Hu, M. Eggersdorfer, D. Chen, D. Weitz, and F. Ye, *Millifluidics, microfluidics, and nanofluidics: manipulating fluids at varying length scales,* Materials Today Nano **16**, 100136 (2021).

[29] R. Geczy, M. Agnoletti, M. F. Hansen, J. P. Kutter, K. Saatchi, and U. O. Häfeli, *Microfluidic approaches for the production of monodisperse, superparamagnetic microspheres in the low micrometer size range,* Journal of Magnetism and Magnetic Materials **471**, 286 (2019).

[30] K. J. Regehr, M. Domenech, J. T. Koepsel, K. C. Carver, S. J. Ellison-Zelski, W. L. Murphy, L. A. Schuler, E. T. Alarid, and D. J. Beebe, *Biological implications of polydimethylsiloxane-based microfluidic cell culture,* Lab on a Chip **9**, 2132 (2009).

[31] M. Motola, J. Capek, R. Zazpe, J. Bacova, L. Hromadko, L. Bruckova, S. Ng, J. Handl, Z. Spotz, P. Knotek, K. Baishya, P. Majtnerova, J. Prikryl, H. Sopha, T. Rousar, and J. M. Macak, *Thin TiO_2 coatings by ALD enhance the cell growth on TiO_2 nanotubular and flat substrates,* ACS Applied Bio Materials **3**, 6447 (2020).

[32] J. Capek, M. Sepúlveda, J. Bacova, J. Rodriguez-Pereira, R. Zazpe, V. Cicmancova, P. Nyvltova, J. Handl, P. Knotek, K. Baishya, H. Sopha, L. Smid, T. Rousar, and J. M. Macak, *Ultrathin TiO_2 coatings via atomic layer deposition strongly improve cellular interactions on planar and nanotubular biomedical Ti substrates,* ACS Applied Materials & Interfaces (2024).

[33] A. Zuchowska, P. Kwiatkowski, E. Jastrzebska, M. Chudy, A. Dybko, and Z. Brzozka, *Adhesion of MRC-5 and A549 cells on poly (dimethylsiloxane) surface modified by proteins,* Electrophoresis **37**, 536 (2016).

[34] A. Günther and K. F. Jensen, *Multiphase microfluidics: from flow characteristics to chemical and materials synthesis,* Lab on a Chip **6**, 1487 (2006).

[35] M. B. Griffiths, P. J. Pallister, D. J. Mandia, and S. T. Barry, *Atomic layer deposition of gold metal,* Chemistry of Materials **28**, 44 (2016).

[36] F. S. Hashemi, F. Grillo, V. R. Ravikumar, D. Benz, A. Shekhar, M. B. Griffiths, S. T. Barry, and J. R. van Ommen, *Thermal atomic layer deposition of gold nanoparticles: controlled growth and size selection for photocatalysis,* Nanoscale **12**, 9005 (2020).

[37] G. Beamson, *High-resolution XPS of organic polymers,* The Scienta ESCA 300 Database (1992).

[38] P. Louette, F. Bodino, and J.-J. Pireaux, *Poly (dimethyl siloxane) (PDMS) XPS reference core level and energy loss spectra,* Surface Science Spectra **12**, 38 (2005).

[39] D. Mitchell, K. Clark, J. Bardwell, W. Lennard, G. Massoumi, and I. Mitchell, *Film thickness measurements of SiO_2 by XPS,* Surface and Interface Analysis **21**, 44 (1994).

[40] B. Gong, J. C. Spagnola, and G. N. Parsons, *Hydrophilic mechanical buffer layers and stable hydrophilic finishes on polydimethylsiloxane using combined sequential vapor infiltration and atomic/molecular layer deposition,* Journal of Vacuum Science & Technology A: Vacuum, Surfaces, and Films **30**, 01A156 (2012).

[41] T. Nam, H. Lee, T. Choi, S. Seo, C. M. Yoon, Y. Choi, H. Jeong, H. K. Lingam, V. R. Chitturi, A. Korolev, *et al.*, *Low-temperature, high-growth-rate ALD of SiO_2 using aminodisilane precursor,* Applied Surface Science **485**, 381 (2019).

[42] G. Dingemans, C. Van Helvoirt, D. Pierreux, W. Keuning, and W. Kessels, *Plasma-assisted ALD for the conformal deposition of SiO_2: process, material and electronic properties,* Journal of the Electrochemical Society **159**, H277 (2012).

[43] J. W. Klaus, O. Sneh, and S. M. George, *Growth of SiO_2 at room temperature with the use of catalyzed sequential half-reactions,* Science **278**, 1934 (1997).

[44] D. Arl, V. Rogé, N. Adjeroud, B. Pistillo, M. Sarr, N. Bahlawane, and D. Lenoble, *SiO_2 thin film growth through a pure atomic layer deposition technique at room temperature,* RSC Advances **10**, 18073 (2020).

[45] G.-Y. Fang, L.-N. Xu, Y.-Q. Cao, L.-G. Wang, D. Wu, and A.-D. Li, *Self-catalysis by aminosilanes and strong surface oxidation by O_2 plasma in plasma-enhanced atomic layer deposition of high-quality SiO_2,* Chemical Communications **51**, 1341 (2015).

[46] M. Putkonen, M. Bosund, O. M. Ylivaara, R. L. Puurunen, L. Kilpi, H. Ronkainen, S. Sintonen, S. Ali, H. Lipsanen, X. Liu, *et al.*, *Thermal and plasma enhanced atomic layer deposition of SiO_2 using commercial silicon precursors,* Thin Solid Films **558**, 93 (2014).

[47] N. E. Richey, C. De Paula, and S. F. Bent, *Understanding chemical and physical mechanisms in atomic layer deposition,* The Journal of Chemical Physics **152**, 040902 (2020).

[48] G. Fang, L. Xu, J. Ma, and A. Li, *Theoretical understanding of the reaction mechanism of SiO_2 atomic layer deposition,* Chemistry of Materials **28**, 1247 (2016).

[49] M. Nouri-Goushki, L. Angeloni, K. Modaresifar, M. Minneboo, P. E. Boukany, M. J. Mirzaali, M. K. Ghatkesar, L. E. Fratila-Apachitei, and A. A. Zadpoor, *3D-printed submicron patterns reveal the interrelation between cell adhesion, cell mechanics, and osteogenesis,* ACS Applied Materials & Interfaces **13**, 33767 (2021).

[50] Z. Long, Q. Li, T. Wei, G. Zhang, and Z. Ren, *Historical development and prospects of photocatalysts for pollutant removal in water,* Journal of Hazardous Materials **395**, 122599 (2020).

[51] A.-L. Liu, Z.-Q. Li, Z.-Q. Wu, and X.-H. Xia, *Study on the photocatalytic reaction kinetics in a TiO_2 nanoparticles coated microreactor integrated microfluidics device,* Talanta **182**, 544 (2018).

[52] S. Witzel, A. S. K. Hashmi, and J. Xie, *Light in gold catalysis,* Chemical Reviews **121**, 8868 (2021).

[53] S. Y. Lee, D. Kang, S. Jeong, H. T. Do, and J. H. Kim, *Photocatalytic degradation of rhodamine B dye by TiO_2 and gold nanoparticles supported on a floating porous polydimethylsiloxane sponge under ultraviolet and visible light irradiation,* ACS Omega **5**, 4233 (2020).

[54] D. Meroni, L. Lo Presti, G. Di Liberto, M. Ceotto, R. G. Acres, K. C. Prince, R. Bellani, G. Soliveri, and S. Ardizzone, *A close look at the structure of the TiO_2-APTES interface in hybrid nanomaterials and its degradation pathway: An experimental and theoretical study,* The Journal of Physical Chemistry C **121**, 430 (2017).

[55] M. Hu, S. Noda, T. Okubo, Y. Yamaguchi, and H. Komiyama, *Structure and morphology of self-assembled 3-mercaptopropyltrimethoxysilane layers on silicon oxide,* Applied surface science **181**, 307 (2001).

[56] P. D. Jadzinsky, G. Calero, C. J. Ackerson, D. A. Bushnell, and R. D. Kornberg, *Structure of a thiol monolayer-protected gold nanoparticle at 1.1 A resolution,* science **318**, 430 (2007).

[57] D. La Zara, F. Zhang, F. Sun, M. R. Bailey, M. J. Quayle, G. Petersson, S. Folestad, and J. R. van Ommen, *Drug powders with tunable wettability by atomic and molecular layer deposition: From highly hydrophilic to superhydrophobic,* Applied Materials Today **22**, 100945 (2021).


Let them flow

De sterrennacht
Vincent van Gogh, 1889

5

Solvent extraction of Ac-225 in nano-layer coated, solvent resistant PDMS microfluidic chips

Separating medical radionuclides from their targets is one of the most critical steps in radiopharmaceutical production. Among many separation methods, solvent extraction has a lot of potential due to its simplicity, high selectivity, and high efficiency. Especially with the rise of polydimethylsiloxane (PDMS) microfluidic chips, this extraction process can take place in a simple and reproducible chip platform continuously and automatically. Furthermore, the microfluidic chips can be coated with metal-oxide nano-layers, increasing their resistance against the employed organic solvents. We fabricated such chips and demonstrated a parallel flow at a considerably large range of flow rates using the aqueous and organic solutions commonly used in medical radionuclide extraction. In our following case study for the separation of Ac-225 from radium with the chelator di(2-ethylhexyl)phosphoric acid (D2EHPA), a remarkable extraction efficiency of 97.1 % ± 1.5 % was reached within 1.8 seconds of contact time, while maintaining a near perfect phase separation of the aqueous and organic solutions. This method will enable the automation of solvent extraction and faster target recycling, and serves, therefore, as a proof-of-concept for the applicability of microfluidic chip solvent extraction of (medical) radionuclides.

This chapter has been submitted to Scientific Reports.
This chapter is co-authored with Svenja Trapp

5.1. Introduction

In nuclear medicine, radionuclides are utilized for imaging and treatment of various diseases [1]. Despite numerous existing potential radionuclides, only a handful reach clinical use, partly due to their limited availability [2, 3]. Increasing the global supply requires a production system that is not only fast and efficient, but also continuous and automatable, incorporating the necessary steps to separate the produced radionuclide from its initial target material [2, 4]. Solvent extraction, among other methods, offers a simple, selective, and efficient means of separation [5]. By bringing an aqueous solution that contains the product radionuclide as well as its target material in contact with an immiscible organic solution that contains a chelator, the chelator selectively binds to the product radionuclide [5, 6]. As a result, the product radionuclide gets extracted into the organic solution, while the valuable target material stays in the aqueous solution, potentially ready to be recycled. To prepare the product radionuclide for further use, it needs to be transferred to a fresh aqueous solution, which is possible through a simple second (back-) extraction step. Microfluidic devices offer precise control over two-phase flows and their interfaces, enabling the design of a continuous and potentially automatable extraction system [7–12]. With short diffusion paths, these devices consistently achieve high extraction efficiencies for many radionuclides [9].

Polydimethylsiloxane (PDMS), among the most used materials for microfluidic devices stands out as it (1) allows rapid prototyping through a simple molding technique [13], (2) has a high radiation resistance as opposed to commercial membranes used for radionuclide separation [14], and (3) resists solution with extreme pH used in the (back-) extraction step for the separation of medical radionuclides [15–17]. Furthermore, PDMS has also been used in medical industries, easily complying with regulatory demands [15]. The only downside is that it swells and deforms when it comes in contact with organic solutions commonly used for extraction [18]. To overcome this issue, direct contact between the organic solution and the PDMS microfluidic chip must be prevented. Recently, we developed a simple approach to coat the channels of PDMS chips with metal oxide nano-layers using atomic layer deposition (ALD) [17]. These nano-layers are grown by alternatingly flowing the two gaseous ALD reactants through the chips, a metal precursor and an oxidizing agent, with a purge of inert gas in between. The number of repeats allows high control over the layer thickness and its properties due to the self-limiting nature of the ALD reactions [19]. This invention now opens the door to develop a PDMS-based microfluidic system for radionuclide solvent extraction.

In this study, we present a PDMS-based microfluidic radionuclide extraction system, in which the PDMS is rendered inert against the use of organic solutions through a silicon oxide nano-layer deposited by means of ALD. Besides the nano-layer, a second important feature of the microfluidic chip is the difference in height between the channels for the organic phase containing the chelator and the aqueous phase containing the product radionuclide and its target material, see Figure 5.1. The height difference ensures pinning of the interface [20], securing stable parallel flow, even at the lowest flow rates. A third important feature is the wavy-wall near the exit, securing that the interface remains pinned, achieving perfect phase separation. As a proof of concept, we present a case study for the separation of Ac-225 from radium, using di-2-ethylhexylphosphoric acid (D2EHPA) as the chelator, after initial experiments on the separation of La-140 from

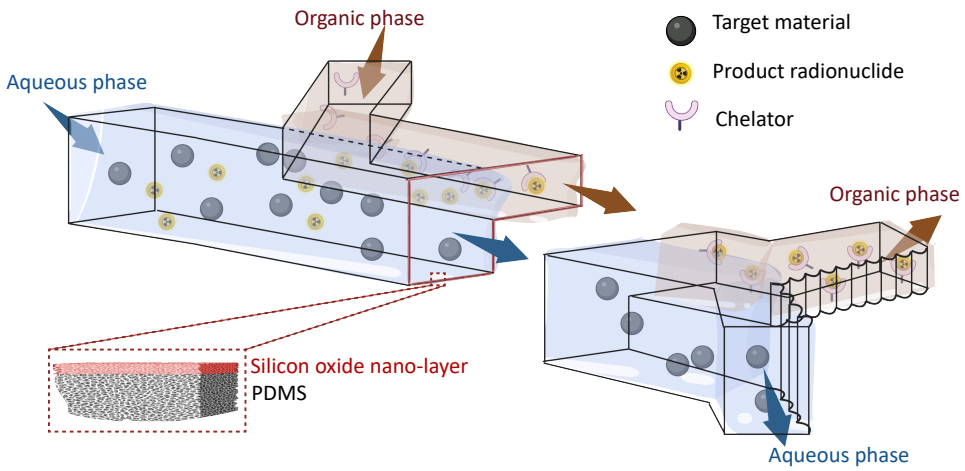

Figure 5.1: Illustration of continuous two-phase liquid-liquid extraction of radionuclides in a PDMS-based microfluidic chip, with the product radionuclide and its target supplied in the aqueous phase and the chelator in the organic phase. The silicon oxide nano-layer coated on the walls using atomic layer deposition renders the wall inert against the organic phase. The difference in height between the side where aqueous phase and the organic phase flow ensures pinning of the interface, ensuring stable parallel flow. The wavy wall near the exit pins the interface as well, ensuring perfect phase separation.

barium as substitutes. Ac-225 is a medical radionuclide, currently researched for targeted alpha therapy, showing very promising clinical results [21–23]. However, so far, the global supply of Ac-225 is severely limited and does not meet the predicted clinical demand [3]. Therefore, many efforts are made to produce Ac-225 via a plethora of different production routes [24], including the irradiation of Ra [3, 25–27]. The presented case study showcases a fast, continuous, and efficient process using microfluidic solvent extraction, with the potential for establishing an automated purification system for medical radionuclides.

5.2. Methods and Materials

5.2.1. Microfluidic device

Working principle of the microfluidic device design

Two key requirements for continuous two-phase flow extraction are that the two phases (1) flow stably side by side through the main channel, without breaking up into slugs, and (2) leave the device separately via the two dedicated outlet channels. To accommodate these requirements, we adapted the geometry often used in solvent extraction [5], namely a simple straight channel (500 µm wide and 11.6 mm long in our work) with a Y-junction for the introduction of the two phases and another Y-junction for their exit. Two important geometries were added to pin the interface throughout the device: a vertical guiding structure in the form of a step height [20, 28] and a lateral guiding structure in the form of a wavy wall at the outlet junction, see Figure 5.1. The position of the step height in the main channel is determined by the estimated interface position of the two

fluids. Assuming two-dimensional flow and considering continuity of velocity and shear stress, the interface position is a function of the viscosity ratio and the flow rate ratio [29–31]. In this study, the viscosities of the fluids used for the radionuclide separations are of a comparable order of magnitude. Additionally, extraction is done at comparable flow rates. Therefore, the step height is placed in the middle of the main channel to account for most of the used operating conditions. The channel for the aqueous phase was 100 µm deep, while the channel for the organic phase was 50 µm deep. This difference was based on preliminary experiments, in which we found that this step height was enough to guide the two phases without compromising the contact area too much.

Ideally, pinning of the interface near the outlet occurs at the outlet junction point. In case of unpinning, the wavy wall at the end provides a new pinning point, similar to the pinning in pillar-based or array-based microfluidic devices [32, 33]. This wavy wall comprises of half-circles (diameter of 5 µm) pattern starting from the outlet junction point and extends for 1 cm into each outlet channel. The joining points between two half-circles facilitate the new pinning of the interface, lowering the risk of phase contamination from one side of the channel to the other.

Microfluidic device fabrication

We fabricated our microfluidic devices using soft lithography [34]. In short, a 4-inch silicon wafer was spin-coated at 2000 rpm for 30 seconds with a negative photoresist (SU8-2050, Kayaku Advanced Materials, Inc.) and soft-baked at 100°C for 15 minutes. The thickness of this first layer of photoresist was 50 µm as determined by a profilometer (DektakXT 2, Bruker, Billerica, US). Instead of transferring the two-dimensional channel design to the coated wafer by exposing it through a patterned mask as commonly done in soft lithography, the design made in AutoCAD 2023 (Autodesk) was directly written on the coated wafer with a tabletop LaserWriter (µmLA, Heidelberg Instruments, Germany; raster scan with 1 µm laser beam at 365 nm), using an exposure dose of 300 mJ/cm^2. The patterned wafer was then post-exposure-baked at 100°C for 5 minutes. To obtain the step height, a second 50 µm thick layer of SU8-2050 photoresist was spin-coated on top of the post-exposure-baked wafer. After aligning the design of the second layer to the design of the first layer using the embedded inspection camera of the LaserWriter, the second layer was written. The wafer was then post-exposure-baked at 100°C for 5 minutes. After this second post-exposure-bake, the fully patterned wafer was developed using propylene glycol monomethyl ether acetate (Sigma-Aldrich, 99.5 %), washed with isopropyl alcohol (Sigma-Aldrich, 70 %), and hard-baked at 200°C for 20 minutes. Before its first use, the patterned wafer was silanized by exposing it to 1H,1H,2H,2H-perfluorooctyltrichlorosilane (Sigma-Aldrich, 95 %) vapour in a vacuum desiccator for one hour to prevent polydimethylsiloxane (PDMS) from sticking to the wafer.

The microfluidic devices were made from PDMS. They were prepared by mixing polymer elastomer and curing agent (Sylgard 184 Elastomer Kit, Dow Corning Comp.) in a mass ratio of 5:1. After degassing the mixture in a vacuum desiccator, it was poured over the patterned wafer in a glass 5-inch Petri dish and cured at 150°C for at least 2 hours [17]. The cured PDMS was then gently removed from the patterned wafer and cut to size. The inlets and outlets were subsequently punched using a 1.5 mm biopsy puncher. The chips were cleaned with ethanol (Sigma-Aldrich, 70 %) and dried using compressed air, before being bonded on a glass slide spin-coated with a 20 µm thick layer of PDMS

(2000 rpm for 2 minutes, Laurell WS-650Mz-23NPPB) after oxygen plasma treatment for 140 seconds at 0.2-0.4 mbar (Harrick, PDC-002). The microfluidic devices were stored at 70°C for at least 12 hours before further modification to allow the PDMS to recover to its hydrophobic state.

Atmospheric pressure atomic layer deposition in microfluidic devices

To coat a thin layer of silicon oxide on the inner walls of the microfluidic channels in order to render the walls inert against the solvents used in the extraction experiments, a home-built atomic layer deposition setup was used [17, 35, 36]. In-channel growth of a layer of silicon oxide was achieved by sequentially flowing gas phase ALD precursors through the microchannels as described in our recent work [37]. In short, silicon tetrachloride (Alfa Aesar) was used as the metal precursor, while ozonated air (Sander Certizon) combined with deionized water was used as the oxygen precursor. A gas flow rate of 0.2 L/min was used, with the metal precursor flowing for 10 seconds and the oxygen precursor for 30 seconds, with nitrogen purges for 100 seconds in between. Each microfluidic channel was coated with 25 of such ALD cycles (i.e., the described sequence was repeated 25 times), carried out at 60°C.

Stability of parallel two-phase flow in bare and ALD-treated PDMS microfluidic devices

We studied the stability of the two-phase flow over a wide range of flow rates (0.1-150 µL/min) of the aqueous and organic solutions. As model liquids, we used a 1 M nitric acid (HNO_3, 65 %, Merck Sigma) solution as the aqueous phase and chloroform ($CHCl_3$, Merck Sigma) as the organic phase. The viscosity of 1 M HNO_3 at 20°C is estimated to be 0.99 mPa.s (measured using a VWR falling ball viscometer, comparable with reported values in the literature[38]). The viscosity of chloroform at 20°C as provided by the supplier is 0.57 mPa.s. To estimate the interfacial tension between 1 M HNO_3 and chloroform, we conducted pendant drop tensiometry (Kruss easydrop) by forming a 10 µL chloroform droplet (Worthington number was ~1[39]) in a cuvette filled with 1 M HNO_3. Using the Young-Laplace equation, the interfacial tension was calculated to be 31.6 mN/m, comparable to reported values in the literature[40].

The liquids were loaded in separate 5 mL syringes (Beckton-Dickinson, Discardit II) with a plastic plunger. The syringes were connected to the inlets of the microfluidic device with polytetrafluorethylene (PTFE) tubing (outer diameter 1.6 mm, inner diameter 0.5 mm, length 300 mm, Diba, 008T16-050-200) and the liquids were driven into the device using individual syringe pumps (Harvard Apparatus Pump 11 Pico Elite Plus). The aqueous phase was injected at the inlet leading to the deeper part of the main channel, while the organic phase was injected at the inlet leading to the shallower part. Snapshots of the flow were taken using a camera (ImagingSource DFK33UX273) through an LWD plan phase 10X lens on a microscope (Euromex Oxion Inverso PLPH).

To rationalize the flow stability experiments, we compared the outcome against an available simple theoretical model [41]. In short, the transition between stable and unstable parallel flow is expected when the difference in organic and aqueous phase pressure drop over the length of the main channel due to viscous flow exceeds the difference in organic and aqueous phase pressure due to interfacial forces, known as the Laplace

pressure jump. At the onset of this transition, small perturbations in the flow, for example due to the step motor of a syringe pump [42–44] lead to unpinning of the interface at the step height.

The Laplace pressure jump ($\Delta P_{Laplace}$) can be estimated using the following expression [28]

$$\Delta P_{Laplace} = \frac{2\gamma \sin(\theta - 90^{\circ})}{d}, \tag{5.1}$$

where γ represents the interfacial tension between two liquids, θ represents the solid-liquid-liquid contact angle, and d represents the height between the ceiling of the main channel and the step (i.e., 50 μm in our work). A simple estimate of the pressure drop over the channel (ΔP_F) in both the aqueous and the organic phase is obtained through the pressure drop of a single phase flow in a rectangular channel [28, 30, 45], i.e.,

$$\Delta P_F = \frac{12Q\eta L}{\left(1 - 0.630\frac{d}{w}\right) d^3 w}, \tag{5.2}$$

where Q represents the flow rate of the considered phase, η represents the dynamic viscosity of the considered phase, L represents the length of the main channel, and d and w represent the height and width of considered phase (approximated as 100 μm × 250 μm for the aqueous phase and 50 μm × 250 μm for the organic phase. The transitions between stable and unstable parallel flow is estimated as

$$\left|\Delta P_{F,aqueous} - \Delta P_{F,organic}\right| = \Delta P_{Laplace}. \tag{5.3}$$

5.2.2. Radionuclide separation experiments

Radiotracer production and radioactivity measurements

Initial experiments were focused on the separation of La-140 from $Ba(NO_3)_2$ in Milli-Q. The radiotracers Ba-139 and La-140 were produced by neutron irradiation of BaO and La_2O_3 (Merck Sigma), respectively, at the Hoge Onderwijs Reactor (HOR) of the TU Delft Reactor Institute (the Netherlands) with a thermal neutron flux of $4.69 \cdot 10^{16}$ $s^{-1}m^{-2}$ for 3 hours. They were subsequently dissolved in 1 M HNO_3, dried down, and redissolved in ultrapure water (Milli-Q; Merck Milli-Q Advantage A10). Ac-225 was supplied in 0.05 M HCl by Eckert & Ziegler, and Ra-223 was supplied as $^{223}RaCl_2$ (Xofigo) by GE Healthcare (Leiderdorp, the Netherlands). Ba-139, La-140, and Ra-223 were measured directly with the Wallac Wizard2 3" 2480 Automatic Gamma Counter (Perkin Elmer). Ac-225 was measured indirectly at equilibrium (> 30 minutes after experiments) through its daughter Fr-221, emitting 218 keV γ-rays. Additional experiments for the separation of Sc-46 from $Ca(NO_3)_2$ and Y-90 from $Sr(NO_3)_2$ are presented as Supplementary Information.

Solution preparation

The aqueous solutions used in the solvent extraction experiments were prepared by dissolution of different amounts of $Ba(NO_3)_2$ (Merck Sigma) in Milli-Q water and subsequent addition of radiotracers. Note that for the separation of Ac-225 from Ra-223, rather than using 0.1 M $Ra(NO_3)_2$ as the (target) solution, we used 0.1 M $Ba(NO_3)_2$. This is justified by the chemical similarities of Ra and Ba, making it an often used substitute [46, 47]. The organic solution used in the solvent extraction experiments contains the chelator

di-2-ethylhexylphosphoric acid (D2EHPA, reagent grade < 98 %; Merck Sigma) and was prepared as a 10 %v/v D2EHPA in chloroform (Merck Sigma) solution.

Batch solvent extraction experiments

Batch extraction experiments were performed to determine the equilibrium extraction efficiency, which is the highest possible extraction efficiency that can be obtained in the continuous-flow microfluidic experiments for a given combination of solutions and chelator. Next to these (forward) extraction experiments, also back-extraction experiments were performed to determine the optimal conditions, i.e., the lowest HCl concentration required for maximum back-extraction.

The batch forward extraction experiments were done in Eppendorf vials at a 1:1 volumetric ratio, with 0.5 mL of the aqueous and 0.5 mL of the organic solution. The vials containing both solutions were shaken on a Vortex-Genie 2 mixer (Scientific Industries, Inc.) for 1 minute at the highest speed setting, to reach equilibrium. Afterwards, the solutions were separated by pipetting and the radioactivity of both solutions was measured in order to determine the extraction efficiency. The extraction efficiency of the batch experiments ($EE\%_{batch}$) was defined as the radioactivity of the organic solution after extraction ($A_{org,out}$) relative to the radioactivity of the aqueous solution before extraction ($A_{aq,in}$), i.e.,

$$EE\%_{batch} = \frac{A_{org,out}}{A_{aq,in}} \times 100\%. \tag{5.4}$$

The extraction efficiency was determined for the 'produced' radionuclide as well as for the target material.

The batch back-extraction experiments were performed in a similar manner, to release the 'produced' radionuclide from the organic solutions into an aqueous solution for further use in radiopharmaceutical production. The organic solution obtained after forward extraction containing the complexed radionuclide was brought into contact with an aqueous HCl (Merck Sigma) solution. The organic and aqueous solution were pipetted into a vial at equal volumes, shaken on the Vortex mixer for 5 minutes, and subsequently separated by pipetting. Different HCl concentrations were tested to determine the lowest HCl concentration necessary. The back-extraction efficiency ($BEE\%_{batch}$) was defined as the radioactivity in the resulting aqueous HCl solution ($A_{HCl,out}$) relative to the total radioactivity of the HCl and the organic solution ($A_{HCl,out} + A_{org,out}$), i.e.,

$$BEE\%_{batch} = \frac{A_{HCl,out}}{A_{HCl,out} + A_{org,out}} \times 100\%. \tag{5.5}$$

All batch experiments were done in triplicate and errors in the obtained values of the extraction and back-extraction efficiency were given as one standard deviation of the mean.

Microfluidic continuous-flow solvent extraction experiments

Microfluidic extraction experiments were performed in ALD-treated PDMS microfluidic chips. The aqueous, radionuclide-containing $Ba(NO_3)_2$ solution and the D2EHPA/$CHCl_3$

organic solution were loaded into 2.5 mL syringes, which were loaded on two separate syringe pumps (AL-1000 Programmable Syringe pumps 941-371-1003, World Precision Instruments, Inc.) and connected to the chips using PTFE tubing (outer diameter 1.6 mm, inner diameter 0.5 mm, length 200 mm). The extraction efficiency was studied for different contact times between the two phases in the microfluidic chips. The contact times were adjusted by varying the total volumetric flow rate of the two solutions, while keeping the ratio of flow rates at 1:1. The contact time t was calculated as $t = L/v$, with the length L of the main channel being equal to 11.63 mm and the average velocity v estimated from the sum of the volumetric flow rates ($Q_{aq} + Q_{org}$) over the cross-sectional channel area (S), i.e., $v = (Q_{aq} + Q_{org})/S$, with S equal to the sum area of both rectangular channel parts (deeper and shallower). At the outlet of the chip the organic solution, enriched in the 'produced' radionuclide with radioactivity $A_{org,out}$, and the aqueous solution, depleted in the 'produced' radionuclide with radioactivity $A_{aq,out}$, were collected separately and measured for their radioactivity to determine the extraction efficiency ($EE\%_{continuous}$) determined as

$$EE\%_{continuous} = \frac{A_{org,out}}{A_{aq,out} + A_{org,out}} \times 100\%. \tag{5.6}$$

Microfluidic back-extraction experiments were performed by injecting the organic solutions containing the 'produced' radionuclide and different aqueous HCl solutions through microfluidic chips for varying contact times. The aqueous solution with radioactivity $A_{HCl,out}$ and the organic solution with radioactivity $A_{org,out}$ were collected at the outlets and the continuous back-extraction efficiency ($BEE\%_{continuous}$) was determined as

$$BEE\%_{continous} = \frac{A_{HCl,out}}{A_{org,out} + A_{HCl,out}} \times 100\%. \tag{5.7}$$

All microfluidic experiments were done in triplicate and errors in the obtained extraction and back-extraction efficiency were given as one standard deviation of the mean.

5.3. Results and discussion

5.3.1. Stability of parallel two-phase flow in bare and ALD-treated PDMS microfluidic devices

Figure 5.2(a) shows the three possible flow profiles taking place in the ALD-treated PDMS microfluidic chip when using 1 M HNO_3 as the aqueous phase and $CHCl_3$ as the organic phase: stable parallel flow with the interface pinned at the step height, unstable parallel with the interface not pinned at the step height, and break-up of the parallel flow into slugs. A map of these flow profiles shows that stable parallel flow with a pinned interface (filled squares) is obtained for a relatively wide range of flow rate combinations, see Figure 5.2(b). This window of stable operation is much larger than in microfluidic chips without the guiding structure [29–31], especially at a low flow rate, indicating the importance of the guiding structure. For the larger flow rates studied in this work, parallel flow is still observed, but with the interface not pinned to the step height over the full length of the microchannel (open squares). For this flow profile, we observe occasional break-up of the unpinned interface into slugs. For the highest flow rate ratios, the

unpinned interface breaks-up downstream the Y-junction and slug flow (red circles) is observed. The transition between parallel flow with (partly) pinned interface (squares) and slug flow, represented by the solid lines, is reasonably well captured by the simple model (Equations 5.1 - 5.3).

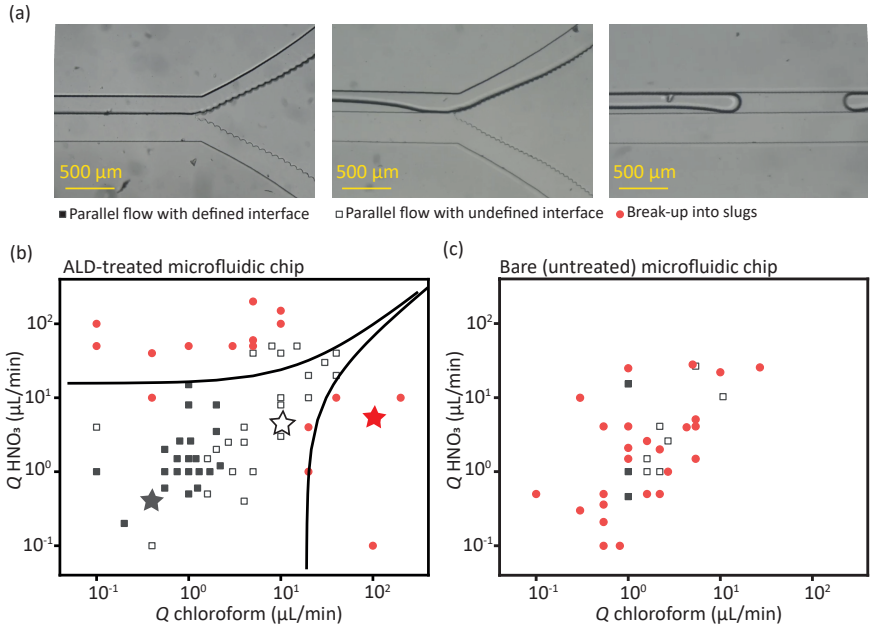

Figure 5.2: (a) Optical microscopy photos taken in an ALD-treated PDMS microfluidic chip, illustrating the three types of two-phase flow observed at different combinations of the flow rate of the aqueous and organic solution. The solution in the upper and lower half of the channel is 1 M HNO_3 and $CHCl_3$, respectively. (b) Flow map of 1 M HNO_3 and $CHCl_3$ inside ALD-treated PDMS microfluidic chips (n=3). The stars correspond to the photos shown in (a). The lines represent the calculated transition between stable and unstable parallel flow using Equations 5.1 - 5.3. (c) Flow map of 1 M HNO_3 and $CHCl_3$ inside a bare (untreated) microfluidic chip (n=1).

For reference, we attempted to perform the same measurements in a bare (untreated) microfluidic chip. As expected, during these experiments, many chips leaked due to the swelling and deformation of PDMS under exposure to organic solvents [48]. The employed $CHCl_3$ induces matrix swelling inside the microfluidic channel, estimated at around 1.39 (length swelling ratio [18]). Swelling also reduces the channel space, leading to an undefined flow profile. While the experiments in ALD-treated chips were reproducible, we observed strong variations from experiment to experiment in untreated chips. An example experiment in a single untreated chip is shown in Figure 5.2(c), illustrating the importance of the silicon oxide nano-layer of the ALD-treated chip to increases the organic solvent resistance of PDMS by preventing direct contact between the organic solvent and PDMS, as further detailed in our earlier work [17, 37].

Batch solvent extraction

Batch extraction of La-140 (simulated 'produced' radionuclide) from Ba (simulated target material) and of Ac-225 from Ra-223 (in 0.1 M $Ba(NO_3)_2$) showed high extraction efficiencies (> 98 %) for all tested solutions, see Figure 5.3(a). With a mixing time of (less than) 1 minute, the complexation of D2EHPA is considered very fast. Simultaneously, co-extraction of the target material into the organic phase remained low in all solutions: below 2 % for Ba-139 and below 0.3 % for Ra-223. However, it should be noted that the aqueous solution did not consist purely of Ra, but a Ra-223 tracer dissolved in a 0.1 M $Ba(NO_3)_2$ solution (commonly written as $[^{223}Ra]Ba(NO_3)_2$). Because of the chemical similarities of group 2 and 3 elements, we additionally conducted extraction experiments for the separation of Y from Sr and Sc from Ca, which can be found in the Supplementary Information. All the extractions also show considerably high efficiency (> 80 %), as expected.

Back-extraction experiments show back-extraction efficiencies over 98 % for both La-140 and Ac-225 (as well as for Ba-139 and Ra-223) when using 0.1 M HCl, see Figure 5.3(b). These efficiencies decrease with decreasing HCl concentration. When using 0.01 M HCl as back-extraction solution, the back-extraction efficiency is significantly higher for Ac-225 compared to La-140. These results indicate a higher complex stability of ^{140}La-D2EHPA over ^{225}Ac-D2EHPA. The complex stability is dependent on the electronegativity and the ionic size and therefore, on the charge density, resulting in a lower complex stability for the larger Ac. This trend of decreasing complex stability with decreasing charge density is often found in chelate complexation [49] and was shown for La and Ac before [50]. Our back-extraction results, including the results shown in the Supplementary Information for the separation of Y from Sr and Sc from Ca, are in line with this trend.

5.3.2. Microfluidic continuous-flow solvent extraction

The batch experiments were instrumental in determining the maximum achievable extraction efficiency with the continuous-flow microfluidic experiments. We used the insights from the batch experiments to design and perform the microfluidic (forward) extraction experiments with (target) solution concentrations of 0.1 M $Ba(NO_3)_2$ and 1 µM $Ba(NO_3)_2$ in Milli-Q for La-140 and 0.1 M $Ba(NO_3)_2$ for Ac-225. Additionally, the back-extraction experiments were designed and performed with HCl solutions with concentrations higher than 0.1 M. For La-140 extraction from the 0.1 M and 1 μM $Ba(NO_3)_2$ solutions, the extraction efficiency for the longest contact time (1.7 seconds) was 97.44 % ± 0.71 % and 99.01 % ± 0.22 %, respectively, see Figure 5.3(c). For Ac-225 extraction from the 0.1 M $Ba(NO_3)_2$ solution, a comparable extraction efficiency of 97.2 % ± 1.5 % was obtained for the same contact time, see Figure 5.3(e).

The speed of extraction is slightly influenced by the target concentration, as seen from the two curves in Figure 5.3(c), which are different in target concentration by 5 orders of magnitude. The salting-out-effect, usually increasing extraction efficiency and separation because of a higher ionic strength of the solution, only has a minor influence on the results. A comparison of the curves in Figure 5.3(c) and Figure 5.3(e) suggests that the speed of extraction is insensitive to the radionuclide concentration, which is six orders of magnitude higher for La-140 than for Ac-225. Usually, the metal concentration

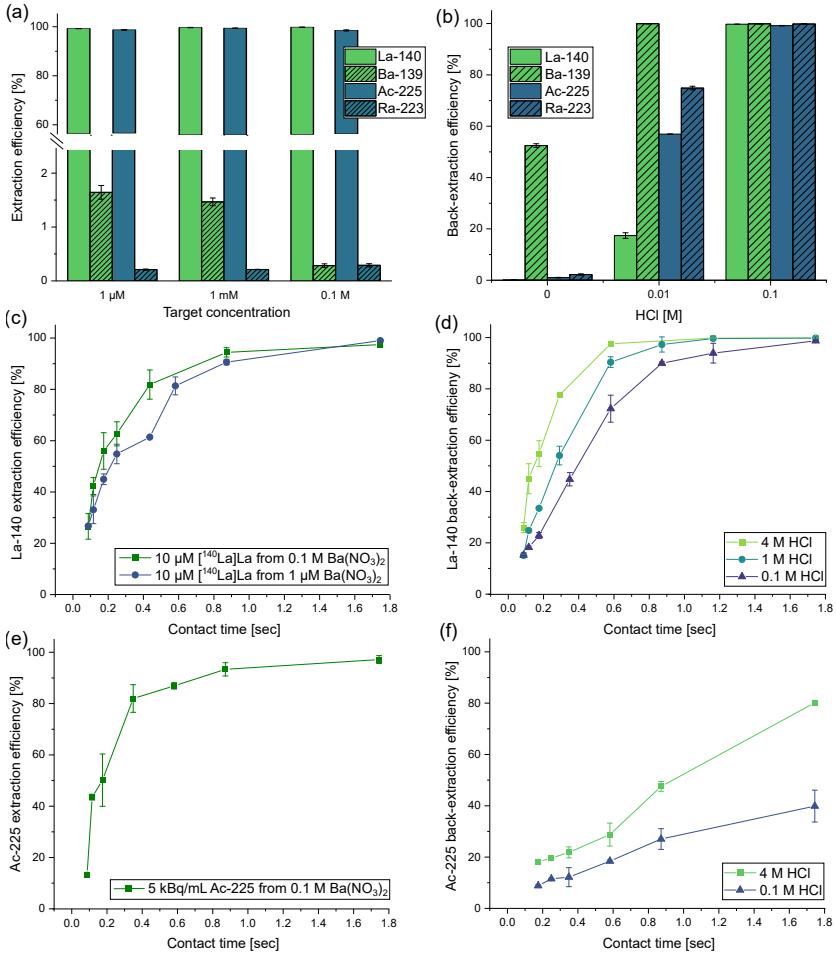

Figure 5.3: (a) Batch extraction of Ba-139, La-140, Ac-225, and Ra-223 for varying target concentrations. (b) Batch back-extraction of Ba-139, La-140, Ac-225, and Ra-223 for varying HCl concentrations. (c) Microfluidic extraction of La-140 from two different $Ba(NO_3)_2$ solutions for varying contact times. (d) Microfluidic back-extraction of La-140 into different HCl solutions for varying contact times. (e) Microfluidic extraction of Ac-225 from 0.1 M $Ba(NO_3)_2$ solutions for varying contact times. (f) Microfluidic back-extraction of Ac-225 into different HCl solutions for varying contact times. All experiments were done in triplicate and error bars represent the standard deviation of the mean.

(both radionuclide and target) plays a major role during the extraction in a microfluidic device because the concentration drives the diffusive flux [51]. Our results indicate that the concentration of the radiometal that is to be extracted does not have a large influence on the extraction when using D2EHPA. Others have shown before that the D2EHPA concentration and its reaction kinetics have the highest influence on the extraction speed [52, 53]. Based on the molecular structure of D2EHPA illustrated in Figure 5.4(a), Sun et al. (2021) [54] proposed that D2EHPA first transfers into the aqueous phase where it forms a complex with the product radionuclide, which subsequently transfers into the organic phase, see Figure 5.4(b), shortening the diffusion distance of the radiometal. These steps, including the electrostatic pull of D2EHPA towards the metal ions[55], influence the extraction speed. While the full set of Ac-225 extraction experiments was performed with fixed radionuclide and target concentrations, we expect based on the aforementioned reasons that the Ba (or Ra) target concentration and the Ac-225 concentration have no major influence on Ac-225 extraction.

The back-extraction efficiency of La-140 into 0.1 M, 1 M, and 4 M HCl solutions exceeded 99 % within 1.7 seconds of contact time, see Figure 5.3(d). The back-extraction efficiency of Ac-225 with the same contact time is considerably lower, i.e., 80.16 % ± 0.77 % and 39.9 % ± 6.2 % for extraction into 4 M and 0.1 M HCl solutions, respectively, see Figure 5.3(f). While the speed of back-extraction depends on the used HCl concentration, the extraction efficiency plateaus within 1.7 seconds for all three used HCl concentrations for La-140. For Ac-225, the plateau is not visible within 1.7 seconds. A comparison of the La-140 and Ac-225 back-extraction experiments for the same HCl concentrations suggests that the concentration of the radionuclide/D2EHPA complex has a higher influence on the back-extraction speed compared to the speed of the (forward) extraction. This implies that diffusion plays a more prominent role in back-extraction. Additionally, the now-neutral charge of the complex does not offer the ability of electrostatic pull of the complex near the interface. Therefore, the movement to the interface is slower. An increase in the back-extraction efficiency of Ac-225 could likely be accomplished by increasing the HCl concentration or increasing the contact time.

Overall, excellent extraction and back-extraction efficiencies can be achieved with the developed microfluidic solvent extraction method for both La-140 (97.44 % ± 0.71 % and 99.86 % ± 0.12 %, respectively) and Ac-225 (97.2 % ± 1.5 % and 80.16 % ± 0.77 %, respectively). Ac-225 currently receives enormous attention for its potential in targeted alpha therapy. Other commonly used methods for the separation of Ac-225 include the use of ion-exchange column chromatography [3, 56, 57], microfluidic ion-exchange [58], or solvent impregnated resins [59]. While achieving comparable results for the total recovery (the combination of extraction and back-extraction efficiency) of Ac-225, the developed microfluidic solvent extraction method exceeds the above-mentioned methods in terms of minimizing chemical volumes [56, 57, 59], reducing the acidity of the final solution [56, 58, 59], or lowering processing time [58, 59]. Thus, the developed microfluidic solvent extraction of Ac-225 presents a promising alternative to conventional separation methods. The newly developed nano-layer coated PDMS microfluidic chip with a step-height and wavy outlet geometry solves the issue of insufficient phase separation and unstable parallel flow in microfluidic chips, and enables the future use and automation of solvent extraction for the separation of medical radionuclides.

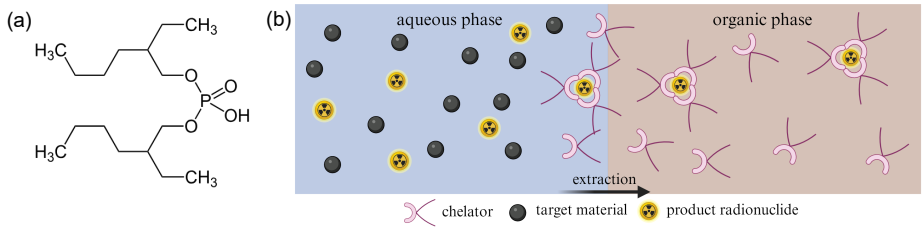

Figure 5.4: (a) Structure of D2EHPA. (b) Illustration of the extraction mechanism proposed by Sun et al.[54] showing that D2EHPA transfers into the aqueous phase where it forms a complex with the product radionuclide, which subsequently transfers into the organic phase.

5.4. Conclusion

We developed a microfluidic PDMS-based chip for fast, continuous, and efficient solvent extraction of radionuclides. To overcome the general issue that PDMS is incompatible with common organic solvents used in solvent extraction experiments, we used our recently developed atomic layer deposition method to deposit a layer of silicon oxide on the inside of the microchannels, rendering them inert. Two key features incorporated in the microfluidic chip, a difference in height in the channel for the organic and aqueous phase and a wavy wall near the exit, proved essential to obtain a stable parallel flow and a near-perfect separation of the phases at the exit. With the newly designed microfluidic chip and using the chelator D2EHPA in chloroform as the organic solution, a high extraction efficiency of 97.2 % ± 1.5 % of Ac-225 was accomplished in less than 1.8 seconds of contact time, while only co-extracting a maximum of 0.293 % ± 0.034 % of Ra, according to batch experiments. Back-extraction can be achieved in 0.1 M HCl, where increasing the contact time or the HCl concentration was found to speed up the back-extraction process. The presented proof-of-concept showcases the potential of microfluidic chips, for fast, continuous, and potentially automatable liquid-liquid extraction for the separation of medical radionuclides.

5.5. Acknowledgment and conflict of interest

This publication is part of the Open Technology Programme (with project number 16913) financed by the Dutch Research Council (NWO). We thank Astrid van der Meer and Baukje Terpstra for their help with the irradiation at HOR. We extend our gratitude to Mojgan Tahlebi, Stefan ten Hagen, Duco Bosma, Cas Veenhoven, and M. Kristen David for their technical assistance. We acknowledge the use of Biorender.com in making some figures. The authors declare no competing interests.

5.6. Supplementary information

Because of the chemical similarities of group 2 and group 3 elements, additional extraction experiments were conducted for the separation of Sc-46 from $Ca(NO_3)_2$ and Y-90 from $Sr(NO_3)_2$ solutions. The radionuclides Ca-45, Sc-46, Sr-85, and Y-90 were produced by neutron irradiation of [^{44}Ca]CaO (Neonest AB, Sweden), Sc_2O_3 (ACROS ORGANICS; VWR, Amsterdam, the Netherlands), SrO, and Y_2O_3, respectively, at the Hoger Onder-

wijs Reactor (HOR) of the TU Delft | Reactor Institute (the Netherlands). [^{44}Ca]CaO and SrO were irradiated with a thermal neutron flux of 4.24 $\cdot 10^{17}$ $s^{-1}m^{-2}$ for 10 days and 1 day, respectively. Sc_2O_3 was irradiated with a thermal neutron flux of 4.69 $\cdot 10^{16}$ $s^{-1}m^{-2}$ for 5 hours, and Y_2O_3 was irradiated with a thermal neutron flux of 4.69 $\cdot 10^{16}$ $s^{-1}m^{-2}$ for 3 hours. The irradiated [^{44}Ca]CaO and Sr were subsequently dissolved in dilute HNO_3, dried down, and redissolved in ultrapure water. Ca-45 and Y-90 were measured with a Liquid Scintillation Counter (tri-carb 2750TR/LL, Packard). Sc-46 and Sr-85 were measured directly with the Wallac Wizard2 3" 2480 Automatic Gamma Counter (Perkin Elmer).

The aqueous solutions used in the solvent extraction experiments were prepared by dissolution of different amounts of $Ca(NO_3)_2$ and $Sr(NO_3)_2$ (Merck Sigma, Zwijndrecht, the Netherlands) in ultrapure water and subsequent addition of above mentioned radiotracers. Both batch and microfluidic extraction were performed as described in the main manuscript. The results off all batch and microfluidic extration experiments are shown in Fig. 5.5. The batch extraction of Sc-46 from 1 M $Ca(NO_3)_2$ resulted in a very good separation, with over 99 % extraction of Sc-46 and below 1 % of Ca-45 co-extraction. However, results differed tremendously for the 1 mM and 1 µM $Ca(NO_3)_2$ solution. Here, the Ca co-extraction increased up to 80 %, while the Sc-46 extraction decreased to 70 %. Back-extraction of Sc-46 was unsuccessful into every tested HCl solution, and therefore no microfluidic back-extraction of Sc-46 was done. The extraction of Y-90 from $Sr(NO_3)_2$ yielded successful efficiencies of over 95 % for all three $Sr(NO_3)_2$ solutions while the Sr-89 co-extraction remained below 2 %. Back-extraction of Y-90 could be achieved with efficiencies over 99 % into HCl concentrations over 0.1 M HCl. Microfluidic extraction of 10 µM [^{46}Sc]Sc was achieved with maximum efficiencies as shown during batch extraction in 1.8 seconds of contact time. Microfluidic extraction of 100 µM [^{90}Y]Y resulted in efficiencies of 99 % in approximately 1 second of contact time from 1 µM $Sr(NO_3)_2$ and in around 0.3 seconds from 1 M $Sr(NO_3)_2$. Microfluidic back-extraction of Y-90 however was slower and resulted in around 90 % back-extraction efficiency into 4 M HCl within 1.2 seconds and only 60 % into 1 M HCl within 1.8 seconds of contact time.

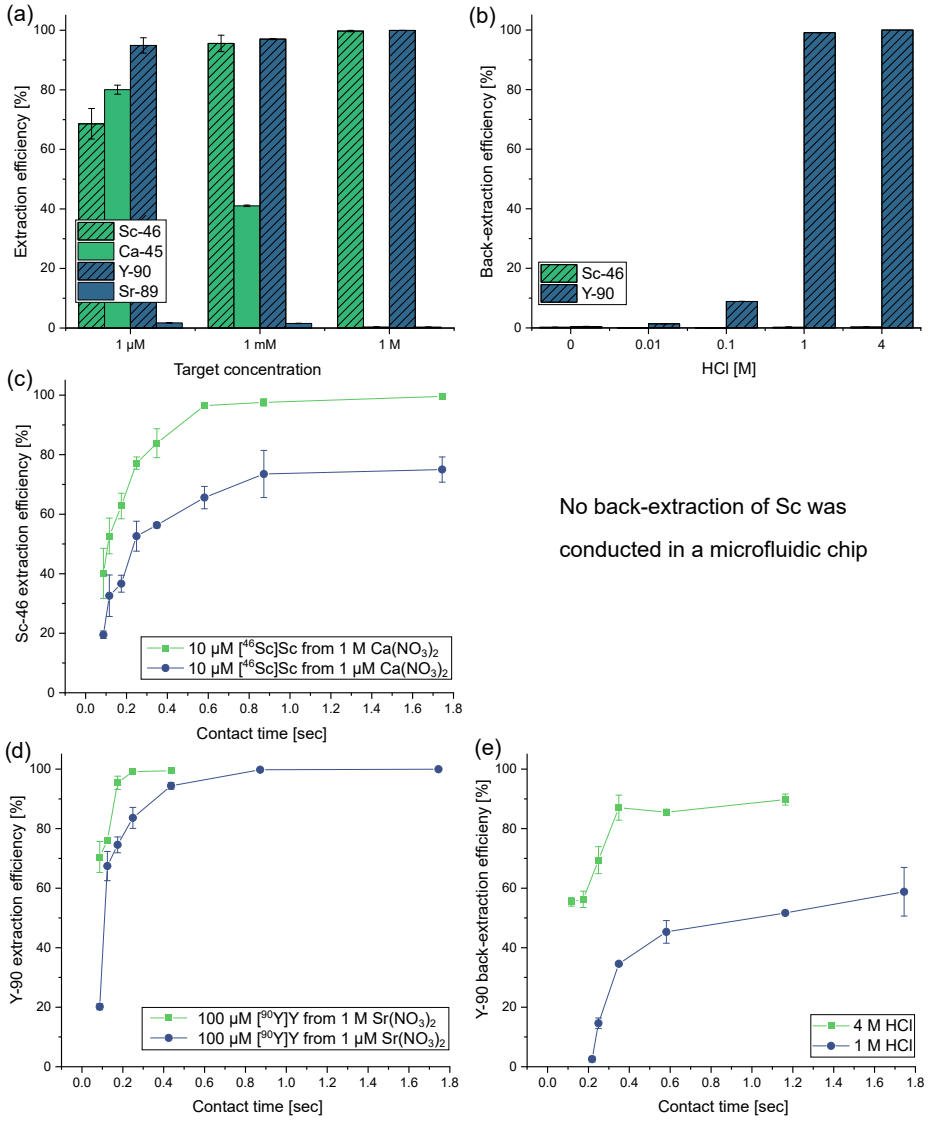

Figure 5.5: (a) Batch extraction of Ca-45, Sc-46, Sr-89, and Y-90 for varying target concentrations. (b) Batch back-extraction of Sc-46 and Y-90 for varying HCl concentrations. (c) Microfluidic extraction of Sc-46 from two different $Ca(NO_3)_2$ in MQ solutions for varying contact times. (d) Microfluidic extraction of Y-90 from two different $Sr(NO_3)_2$ in MQ solutions for varying contact times. (e) Microfluidic back-extraction of Y-90 into different HCl solutions for varying contact times. All experiments were done in triplicate and error bars represent the standard deviation of the mean.

References

[1] https://world nuclear.org, *Radioisotopes in medicine,* (last updated April 2024, accessed April 2024) .

[2] S. M. Qaim and I. Spahn, *Development of novel radionuclides for medical applications,* Journal of Labelled Compounds and Radiopharmaceuticals **61**, 126 (2018).

[3] A. K. H. Robertson, C. F. Ramogida, P. Schaffer, and V. Radchenko, *Development of ^{225}Ac radiopharmaceuticals: Triumf perspectives and experiences,* Current Radiopharmaceuticals **11**, 156 (2018).

[4] H. H. Boersma, *GMP in radiopharmacy: The current situation in its context. in: Nuclear medicine and molecular imaging: Basic concepts, radiopharmacy and instrumentation,* (Elsevier, 2022) pp. 243–249.

[5] P. Martini, A. Adamo, N. Syna, A. Boschi, L. Uccelli, N. Weeranoppanant, J. Markham, and G. Pascali, *Perspectives on the use of liquid extraction for radioisotope purification,* Molecules **24**, 334 (2019).

[6] C. F. Ramogida, A. K. Robertson, U. Jermilova, C. Zhang, H. Yang, P. Kunz, J. Lassen, I. Bratanovic, V. Brown, L. Southcott, C. Rodríguez-Rodríguez, V. Radchenko, F. Bénard, C. Orvig, and P. Schaffer, *Evaluation of polydentate picolinic acid chelating ligands and an alpha-melanocyte-stimulating hormone derivative for targeted alpha therapy using ISOL-produced ^{225}Ac,* EJNMMI Radiopharmacy and Chemistry **4** (2019), 10.1186/s41181-019-0072-5.

[7] K. S. Pedersen, K. M. Nielsen, J. Fonslet, M. Jensen, and F. Zhuravlev, *Separation of radiogallium from zinc using membrane-based liquid-liquid extraction in flow: Experimental and cosmo-rs studies,* Solvent Extraction and Ion Exchange **37**, 376 (2019).

[8] S. Trapp, T. Lammers, G. Engudar, C. Hoehr, A. G. Denkova, E. Paulssen, and R. M. de Kruijff, *Membrane-based microfluidic solvent extraction of Ga-68 from aqueous zn solutions: towards an automated cyclotron production loop,* EJNMMI Radiopharmacy and Chemistry **8**, 9 (2023).

[9] R. Chakravarty, N. Sen, S. Patra, A. Rajeswari, P. Shetty, K. K. Singh, and S. Chakraborty, *Microfluidic solvent extraction of no-carrier-added ^{64}Cu from irradiated Zn target for radiopharmaceutical preparation,* Chemical Engineering Journal Advances **13**, 100433 (2023).

[10] G. Helle, C. Mariet, and G. Cote, *Microfluidic tools for the liquid-liquid extraction of radionuclides in analytical procedures,* Procedia Chemistry **7**, 679 (2012).

[11] C. Mariet, A. Vansteene, M. Losno, J. Pelle, J.-P. Jasmin, A. Bruchet, and G. Helle, *Microfluidics devices applied to radionuclides separation in acidic media for the nuclear fuel cycle,* Micro and Nano Engineering **3**, 7 (2019).

[12] P. Abdollahi, J. Karimi-Sabet, M. A. Moosavian, and Y. Amini, *Microfluidic solvent extraction of calcium: Modeling and optimization of the process variables,* Separation and Purification Technology **231**, 115875 (2020).

[13] G. M. Whitesides, *The origins and the future of microfluidics,* Nature **442**, 368 (2006).

[14] Q. Liu, W. Huang, B. Liu, P.-C. Wang, and H.-B. Chen, *Gamma radiation chemistry of polydimethylsiloxane foam in radiation-thermal environments: experiments and simulations,* ACS Applied Materials & Interfaces **13**, 41287 (2021).

[15] A. Victor, J. Ribeiro, and F. F. Araújo, *Study of PDMS characterization and its applications in biomedicine: A review,* Journal of Mechanical Engineering and Biomechanics **4**, 1 (2019).

[16] K. Ren, J. Zhou, and H. Wu, *Materials for microfluidic chip fabrication,* Accounts of Chemical Research **46**, 2396 (2013).

[17] A. Santoso, A. Damen, J. R. van Ommen, and V. van Steijn, *Atmospheric pressure atomic layer deposition to increase organic solvent resistance of PDMS,* Chemical Communications **58**, 10805 (2022).

[18] J. N. Lee, C. Park, and G. M. Whitesides, *Solvent compatibility of poly (dimethylsiloxane)-based microfluidic devices,* Analytical Chemistry **75**, 6544 (2003).

[19] H. Van Bui, F. Grillo, and J. Van Ommen, *Atomic and molecular layer deposition: off the beaten track,* Chemical Communications **53**, 45 (2017).

[20] P. Vulto, S. Podszun, P. Meyer, C. Hermann, A. Manz, and G. A. Urban, *Phaseguides: a paradigm shift in microfluidic priming and emptying,* Lab on a Chip **11**, 1596 (2011).

[21] C. Kratochwil, F. Bruchertseifer, F. L. Giesel, M. Weis, F. A. Verburg, F. Mottaghy, K. Kopka, C. Apostolidis, U. Haberkorn, and A. Morgenstern, *^{225}Ac-PSMA-617 for psma-targeted a-radiation therapy of metastatic castration-resistant prostate cancer,* Journal of Nuclear Medicine **57**, 1941 (2016).

[22] P. M. Anderson, V. Subbiah, and M. M. Trucco, *Current and future targeted alpha particle therapies for osteosarcoma: Radium-223, actinium-225, and thorium-227,* Frontiers in Medicine **9**, 1030094 (2022).

[23] T. Mastren, V. Radchenko, A. Owens, R. Copping, R. Boll, J. R. Griswold, S. Mirzadeh, L. E. Wyant, M. Brugh, J. W. Engle, *et al.*, *Simultaneous separation of actinium and radium isotopes from a proton irradiated thorium matrix,* Scientific Reports **7**, 8216 (2017).

[24] J. W. Engle, *The production of Ac-225,* Current Radiopharmaceuticals **11**, 173 (2018).

[25] C. Apostolidis, R. Molinet, J. McGinley, K. Abbas, J. Möllenbeck, and A. Morgenstern, *Cyclotron production of Ac-225 for targeted alpha therapy.* Applied Radiation and Isotopes **62**, 383 (2005).

[26] K. Nagatsu, H. Suzuki, M. Fukada, T. Ito, J. Ichinose, Y. Honda, K. Minegishi, T. Higashi, and M.-R. Zhang, *Cyclotron production of ^{225}Ac from an electroplated ^{226}Ra target,* European Journal of Nuclear Medicine and Molecular Imaging **49**, 279 (2021).

[27] G. Melville and B. J. Allen, *Cyclotron and linac production of Ac-225,* Applied Radiation and Isotopes **67**, 549 (2009).

[28] A. Hibara, S. Iwayama, S. Matsuoka, M. Ueno, Y. Kikutani, M. Tokeshi, and T. Kitamori, *Surface modification method of microchannels for gas- liquid two-phase flow in microchips,* Analytical Chemistry **77**, 943 (2005).

[29] A. Pohar, M. Lakner, and I. Plazl, *Parallel flow of immiscible liquids in a microreactor: modeling and experimental study,* Microfluidics and Nanofluidics **12**, 307 (2012).

[30] H. Bruus, *Theoretical microfluidics*, Vol. 18 (Oxford university press, 2007).

[31] A. Hibara, M. Fukuyama, M. Chung, C. Priest, and M. A. Proskurnin, *Interfacial phenomena and fluid control in micro/nanofluidics,* Analytical Sciences **32**, 11 (2016).

[32] A. A. Saha and S. K. Mitra, *Effect of dynamic contact angle in a volume of fluid (VOF) model for a microfluidic capillary flow,* Journal of Colloid and Interface Science **339**, 461 (2009).

[33] B. Gumuscu, J. G. Bomer, A. van den Berg, and J. C. Eijkel, *Large scale patterning of hydrogel microarrays using capillary pinning,* Lab on a Chip **15**, 664 (2015).

[34] D. C. Duffy, J. C. McDonald, O. J. Schueller, and G. M. Whitesides, *Rapid prototyping of microfluidic systems in poly (dimethylsiloxane),* Analytical Chemistry **70**, 4974 (1998).

[35] A. Santoso, B. J. van den Berg, S. Saedy, E. Goodwin, V. van Steijn, and J. R. van Ommen, *Robust surface functionalization of PDMS through atmospheric pressure atomic layer deposition,* Atomic Layer Deposition **1**, 1 (2023).

[36] A. Goulas and J. R. Van Ommen, *Atomic layer deposition of platinum clusters on titania nanoparticles at atmospheric pressure,* Journal of Materials Chemistry A **1**, 4647 (2013).

[37] A. Santoso, M. K. David, P. E. Boukany, V. van Steijn, and J. R. van Ommen, *Atmospheric pressure atomic layer deposition for in-channel surface modification of pdms microfluidic chips,* Chemical Engineering Journal , 155269 (2024).

[38] O. Sohnel and P. Novotny, *Densities of aqueous solutions of inorganic substances* (Elsevier, 1985).

[39] J. D. Berry, M. J. Neeson, R. R. Dagastine, D. Y. Chan, and R. F. Tabor, *Measurement of surface and interfacial tension using pendant drop tensiometry,* Journal of Colloid and Interface Science **454**, 226 (2015).

[40] A. H. Demond and A. S. Lindner, *Estimation of interfacial tension between organic liquids and water,* Environmental Science & Technology **27**, 2318 (1993).

[41] J. G. Kralj, H. R. Sahoo, and K. F. Jensen, *Integrated continuous microfluidic liquid–liquid extraction,* Lab on a Chip **7**, 256 (2007).

[42] M. Baeckert, M. Batliner, B. Grass, P. K. Buehler, M. S. Daners, M. Meboldt, and M. Weiss, *Performance of modern syringe infusion pump assemblies at low infusion rates in the perioperative setting,* British Journal of Anaesthesia **124**, 173 (2020).

[43] Z. Li, S. Y. Mak, A. Sauret, and H. C. Shum, *Syringe-pump-induced fluctuation in all-aqueous microfluidic system implications for flow rate accuracy,* Lab on a Chip **14**, 744 (2014).

[44] P. M. Korczyk, O. Cybulski, S. Makulska, and P. Garstecki, *Effects of unsteadiness of the rates of flow on the dynamics of formation of droplets in microfluidic systems,* Lab on a Chip **11**, 173 (2011).

[45] Y. Amini, V. Ghazanfari, M. Heydari, M. M. Shadman, A. G. Khamseh, M. H. Khani, and A. Hassanvand, *Computational fluid dynamics simulation of two-phase flow patterns in a serpentine microfluidic device,* Scientific Reports **13**, 9483 (2023).

[46] M. A. Brown, *Metal oxide sorbents for the separation of radium and actinium,* Industrial & Engineering Chemistry Research **59**, 20472 (2020).

[47] M. Toro-González, A. N. Dame, S. Mirzadeh, and J. V. Rojas, *Encapsulation and retention of 225ac, 223ra, 227th, and decay daughters in zircon-type gadolinium vanadate nanoparticles,* Radiochimica Acta **108**, 967 (2020).

[48] R. Dangla, F. Gallaire, and C. N. Baroud, *Microchannel deformations due to solvent-induced PDMS swelling,* Lab on a Chip **10**, 2972 (2010).

[49] D. Chapman, *Electronegativity and the stability of metal complexes,* Nature **174**, 887–888 (1954).

[50] A. Mishustin, *Estimate of the stability constants of trivalent actinide and lanthanide complexes with o-donor ligands in aqueous solutions.* Russ. J. Inorg. Chem. **55**, 746–752 (2010).

[51] M. A. Holden, S. Kumar, E. T. Castellana, A. Beskok, and P. S. Cremer, *Generating fixed concentration arrays in a microfluidic device,* Sensors and Actuators B: Chemical **92**, 199 (2003).

[52] Suyanti and R. A. Amiliana, *Extraction of Yttrium from Nd Hydroxide concentrate by using D2EHPA,* Journal of Physics: Conference Series **1436**, 012002 (2020).

[53] J. STARÝ, *The Solvent Extraction of Metal Chelates* (Pergamon, 1964).

[54] P. Sun, E. A. Binter, Z. Liang, M. A. Brown, A. V. Gelis, I. Benjamin, M. K. Bera, B. Lin, W. Bu, and M. L. Schlossman, *Antagonistic role of aqueous complexation in the solvent extraction and separation of rare earth ions,* ACS Central Science **7**, 1908 (2021).

[55] Y. Jing, J. Chen, W. Su, L. Chen, Y. Liu, and D. Li, *Deep insights into the solution and interface behaviors in heavy rare earth extraction: A molecular dynamics study,* Journal of Molecular Liquids **296**, 111790 (2019).

[56] J. Fitzsimmons, B. Foley, B. Torre, M. Wilken, C. S. Cutler, L. Mausner, and D. Medvedev, *Optimization of cation exchange for the separation of actinium-225 from radioactive thorium, radium-223 and other metals,* Molecules **24**, 1921 (2019).

[57] B. Zielinska, C. Apostolidis, F. Bruchertseifer, and A. Morgenstern, *An improved method for the production of Ac-225/Bi-213 from Th-229 for targeted alpha therapy,* Solvent Extraction and Ion Exchange **25**, 339 (2007).

[58] S. Davern, D. O'Neil, H. Hallikainen, K. O'Neil, S. Allman, L. Millet, S. Retterer, M. Doktycz, R. Standaert, R. Boll, S. V. Cleve, D. DePaoli, and S. Mirzadeh, *Microfluidics-based separation of actinium-225 from radium-225 for medical applications,* Separation Science and Technology **54**, 1994 (2019).

[59] M. T. Friend, T. G. Parker, T. Mastren, V. Mocko, M. Brugh, E. R. Birnbaum, and M. E. Fassbender, *Extraction chromatography of ^{225}Ac and lanthanides on n, n-dioctyldiglycolamic acid/1-butyl-3-methylimidazolium bis (trifluoromethylsulfonyl) imide solvent impregnated resin,* Journal of Chromatography A **1624**, 461219 (2020).

Come closer, my dear

Sebuah banjir di Jawa
Raden Saleh Sjarif Boestaman, 1875

6

Chelator-impregnated PDMS beads for the separation of medical radionuclides

Chelator-impregnated resins have been studied earlier for the chemical separation of elements in aqueous solutions, but issues with their chemical stability have limited their use in the separation of (medical) radionuclides from their respective irradiated targets. We developed a polydimethylsiloxane (PDMS)-based chelator-impregnated resin that showed a high chemical stability against leaching. Several different chelators were tested in this study. After impregnation of PDMS beads with the di-2-ethylhexylphosphoric acid (D2EHPA) chelator, an in-flow separation study with various radionuclides (Y-90, La-140, and Ac-225) was conducted. These three radionuclides have potential use in nuclear medicine and a production route through irradiation of Sr-, Ba-, and Ra-targets respectively, necessitating their chemical separation. The D2EHPA-impregnated beads achieved high adsorption efficiencies of 99.89 % ± 0.14 %, 99.50 % ± 0.10 %, and 98.51 % ± 0.25 %, for Y-90, La-140, and Ac-225, respectively, while co-adsorption of minor amounts (< 3 %) of the targets were reported. These results, together with the high chemical stability of the PDMS-based resin, highlight the potential of chelator-impregnated resins in the rapidly growing field of (medical) radionuclide production.

Parts of this chapter have been filed as a patent (2037212) [1]
This chapter has been published in Separation and Purification Technology **354**, 128865 (2025) [2].
This chapter is co-authored with Svenja Trapp

In the field of nuclear medicine, antibodies, peptides, or small molecules labelled with radionuclides are used for nuclear imaging of a malignancy, or for the delivery of a therapeutic radiation dose to a specific tumor site while minimizing the dose to surrounding healthy tissue [3, 4]. For decades, just a few radionuclides have been used in clinical settings, including the positron (β^+) emitters Ga-68 and F-18 for positron emission tomography (PET) [5, 6], the gamma (γ) emitter Tc-99m for single-photon emission computed tomography (SPECT) [6], and the alpha (α) emitter Ra-223 for the treatment of bone metastases [7]. With technological advancements in targetry and irradiation facilities, increasing numbers of radionuclides are researched for their potential use in nuclear medicine to maximize worldwide capacity and availability of medical radionuclides [3, 4, 8]. Yet, few make it to clinical applications [3, 4, 8, 9].

One of the biggest challenges in realizing the full potential of these radionuclides lies in the production steps and the availability of the enriched target material needed for the production [9]. Most medical radionuclides are produced by irradiation of costly, enriched target materials, either as solid or liquid targets. After irradiation, the produced radionuclide is separated from its respective target and the target material is recovered to be re-used. This separation should be performed quickly, especially in the case of short-lived radionuclides (e.g., Ga-68 with a half-life of $t_{1/2}$ = 67.71 minutes). The separation should also result in a high chemical and radio chemical purity [10] for further use in radiopharmaceutical production. Moreover, concerns about good manufacturing practices (GMP), radiation safety, and cost necessitate a simple, automatable separation process [11, 12].

The most common method for the chemical separation of a product radionuclide from its target is ion-exchange chromatography [13]. In ion-exchange chromatography, the separation of the radionuclide from its target material is commonly done by flowing an aqueous solution containing the product radionuclide and target material through a resin-packed column. The resin consists of a solid support with covalently bound functional (charged) groups. The functional groups act as a binding site, often adsorbing both the radionuclide and the target material. Hereafter, selective elution of the radionuclide, the target, and possible contaminants from the resin is done by subsequently flowing aqueous solutions with a different pH through the column. This also necessitates multiple processing steps to recycle the expensive enriched target material [14–18].

As an alternative to traditional ion-exchange resins, chelator-impregnated resins have been studied. In this approach, a chelator or extracting agent is impregnated onto polymer-based resin beads that act as the solid support [19]. Chelators can have a high selectivity towards the product radionuclide over its target material, forming stable coordination bonds [20]. Due to this high selectivity, a lower amount of resin, and, subsequently, lower volumes of chemicals are needed [21]. Additionally, chelator-impregnated resins possibly allow for direct recycling of the target when a liquid target is used [21], because the target is not adsorbed on the resin. Despite the potential advantages of chelator-impregnated resins, the chemical stability of the resins remains an issue. When in contact with acidic solutions, the chelator can be leached [22]. Consequently, the resins are no longer usable, the expensive target solution can no longer be recycled directly, and the chemical purity of the radionuclide solution decreases, posing issues with GMP pro-

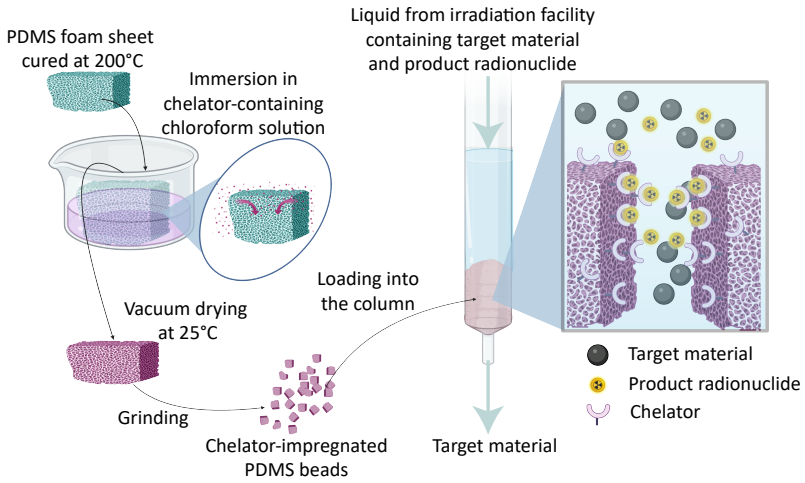

Figure 6.1: **Illustration of the fabrication of chelator-impregnated PDMS beads (left) and their use in separating a product radionuclide of interest from its target material (right).** Cured PDMS foam sheets are immersed in a chelator-containing chloroform solution before being vacuum-dried and mechanically ground into beads. The chelator-impregnated PDMS beads are loaded into a flow column, through which liquid containing the product radionuclide of interest and its target is flown. The radionuclide selectively binds to the chelator on the beads, resulting in a separated target solution leaving the column. The radionuclide is subsequently collected by flowing an eluting solution with a specific pH through the column.

duction. To overcome this, a highly stable combination of support material, chelator, and impregnating method with selective adsorption towards the product radionuclide needs to be found [23].

In this study, we present the synthesis and application of chelator-impregnated polydimethylsiloxane (PDMS) beads with high selectivity towards the radionuclide of interest and a high chemical stability against leaching, for the separation of selected medical radionuclides, as illustrated in Figure 6.1 and detailed in Patent No. 2037212 [1]. Unique when compared with other supporting materials used for chelator-impregnated resins, PDMS has a high resistance against acids, but swells upon contact with common organic solvents in which most chelators can be dissolved [24]. This allows the incorporation of a chelator inside the PDMS, before the PDMS shrinks back upon removal of the organic solvent [25], both physically trapping the chelator and hydrophobically binding it to the surface. This improves the chemical stability of the chelator-impregnated resin and subsequently prevents leaching of the chelator, a known problem in the applications of chelator-impregnated resins [23, 26]. Making use of this feature of PDMS, we demonstrate the fabrication of chelator-impregnated PDMS beads for three different types of chelators: N-benzoyl-N-phenylhydroxylamine (BPHA), di-2-ethylhexylphosphoric acid (D2EHPA), and dithizone (DTZ), all dissolved in chloroform. The selection of the chelators was made due to their demonstrated applicability for the separation of the medical radionuclides Ac-225, Cu-64 [27, 28], and Ga-68 [29], respectively. We subsequently demonstrate our concept with a case study using D2EHPA-impregnated PDMS beads for the separation of Yttrium and Lanthanum (both possessing medically interesting ra-

dionuclides such as the β^+ emitting Y-86 and La-132 [30, 31]) from their respective Strontium and Barium targets, as well as Actinium from Radium, motivated by the increasing attention for the use of Ac-225 in targeted alpha therapy [32, 33].

6.1. Methods and Materials

6.1.1. Fabrication of chelator-impregnated PDMS beads

PDMS beads were fabricated by suspending the PDMS elastomer (dime-thylsiloxane, Sylgard 184 Elastomer Kit, Dow Corning) in water with a mass ratio of 1:5. The suspension was then mixed with a vortex mixer (Vortex Genie 2, Scientific Industries) for 10 minutes before a PDMS curing agent (methyl hydrosilane, Dow Corning) was added with a mass ratio of 1:2 to the elastomer. The mixture was then remixed with the vortex mixer for another 2 minutes before slowly being poured into a beaker containing 10 times as much water by weight at 100 °C. After pouring, an opaque solid foam-like sheet formed on the surface of the boiling water. This PDMS foam sheet was taken out and cured in an oven at 200 °C for at least 10 hours.

Impregnation of the cured PDMS foam sheet with a chelator was done by immersing the sheet in a chloroform solution containing the dissolved chelator at a concentration ranging from 0.01 M to 0.75 M, depending on the solubility of the chelator used and its common practice [34–36]. Three different chelators were studied: N-benzoyl-N-phenylhydroxylamine (BPHA, > 98%, VWR), di-2-ethylhexylphosphoric acid (D2EHPA, > 98%, Merck Sigma), and 1-anilino-3-phenyliminothiourea (dithizone, DTZ, > 98%, Merck Sigma). After immersion for 10 hours at 25 °C and atmospheric pressure in a container open to the atmosphere of a fume hood, the remaining chloroform was removed by placing the container in a vacuum desiccator ($\sim 10^{-2}$ mbar) for 30 minutes.

Chelator-impregnated PDMS beads were obtained by grinding the chelator-impregnated PDMS foam sheets in an electric coffee mill grinder (PCKSW 1021 N) for 5 minutes. Initial tests on bare PDMS beads were performed to determine the influence of the operating parameters of the grinder on the diameter of the beads, see Figure 6.9. With the chosen operating parameters, the median diameter of the chelator-impregnated beads was 0.4 ± 0.1 mm.

6.1.2. Characterization of the PDMS beads

To characterize the diameter of the PDMS beads, brightfield images of the beads were recorded using a camera (ImagingSource DFK33UX273) mounted on an optical microscope (Oxion Inverso) through a 4x Plan Phase LWD Infinity Corrected IOS objective. The obtained images were processed using ImageJ software [37]. From the two-dimensional images, the median diameter of the beads was determined using Martin's diameter. Martin's diameter is defined as the maximum measured distance between opposite sides of the non-spherical beads and was measured transverse to the beads on a line that bisects the projected area [38]. The median diameter of the beads was obtained by measuring Martin's diameter of 100 beads. The PDMS bead diameter was used to obtain a conservative estimate of the available surface area of the PDMS beads.

The impregnation of the chelators was characterized using attenuated total reflection Fourier-transform infrared spectroscopy (ATR-FTIR, Thermo Nicolet NEXUS) with

a wavelength range of 4000 to 500 cm^{-1}. To observe the surface structure of the chelator-impregnated PDMS beads, we conducted field emission scanning electron microscopy (FE-SEM, Hitachi Regulus SU8230) at a beam current of 1 μA and electron energy of 3-5 keV. To approximate the mass of the impregnated chelators in the PDMS beads, a thermogravimetric analysis (TGA, METTLER TOLEDO SF/1100) was performed by heating the beads to 800 °C at a rate of 10 °C min^{-1} under nitrogen (100 mL min^{-1}). Since PDMS starts degrading at temperature above 320 °C [39], while the chelators degrade at lower temperatures (200 °C to 300 °C for BPHA [40], 120 °C to 270 °C for D2EHPA [36, 41], and 150 °C to 250 °C for DTZ [42]), the weight difference at 310 °C was used to approximate the chelator mass [41, 43]. To gain insights on the impregnation mechanism, X-ray photoelectron spectroscopy (XPS, ThermoFisher Scientific Nexsa) was performed using an XPS spectrometer equipped with a monochromatic Al Kα radiation source and a pass energy of 30 eV for the survey scan. Since the XPS beam source and detector are placed at an angle, the XPS reading on particles with random shapes and relatively large sizes can be less reliable. We therefore performed the XPS measurements on a flat layer of PDMS, spin-coated on a silicon wafer [44], and immersed in the chelator-containing chloroform solution, following the method described before. A depth profiling was then conducted by etching the surface using Ar^+ ions (2 keV with a raster size of 1 mm) while the differential charging was compensated using a flood gun. CASA-XPS software was used to post-process the XPS peak profiles, where the spectra were charge-corrected with the adventitious carbon peak at 284.8 eV.

6.1.3. Chemical stability test of chelator-impregnated PDMS beads

We tested the stability of the impregnated beads in pure Milli-Q water and the following acidic solutions: 1 M HCl, 12 M HCl (ACS reagent 37%, Merck Sigma), and 1 M HNO_3 (65%, Merck Sigma). To this end, we immersed 0.5 g of the chelator-impregnated PDMS beads in 5 mL of the acidic solution in a 15 mL Falcon tube, which was continuously shaken (IKA Vibrax VX-2) for short (5 minutes) and long (8 hours) immersion times. The beads were subsequently washed with pure Milli-Q water before being characterized using XPS. In addition, all immersion solutions were characterized using an ultraviolet-visible spectrophotometer (UV-Vis, NanoDrop 2000/2000c) with a wide scan reading (300 - 800 nm).

As a reference, we also tested the stability of chelator-impregnated silicon (IV) oxide powder (Silica, 99.5%, Millipore, 0.063 -0.200 mm), where the powder was impregnated with the chelators following a similar methodology to the impregnation of PDMS beads. The chelator-impregnated silica powder was subsequently immersed in the same acidic solutions. Once the powder was separated, the immersion liquid was characterized using UV-Vis. Since the concentration of the chelators leached from the silica powder was higher than the concentration from the PDMS beads, the immersion liquid was diluted 1000 times before being measured with UV-Vis. Please note that the concentration of the leached BPHA and DTZ from silica powder after dilution was within the detection limit of the UV-Vis. However, the leached D2EHPA was in the liquid phase at room temperature. Due to its relatively high concentration, the leached D2EHPA from silica powder was highly dispersed in the immersion liquid, resulting in an opaque liquid. This high opacity reduced the reliability of UV-Vis measurement, even after being diluted 10^9

times. Therefore, to quantify the leached D2EHPA from the chelator-impregnated silica powder reliably, the opaque D2EHPA immersion liquid was left in the fume hood for 24 hours to partition. After 24 hours, two liquid phases separated and a clear boundary between the two phases was observed. The top liquid was decanted and the bottom liquid was weighed, indicating the mass of the leached D2EHPA.

To evaluate the interaction between the chelator and the PDMS responsible for the chemical stability (i.e., minimal leaching), the extended Derjaguin-Landau-Verwey-Overbeek theory (EDLVO) was used [45–52]. More specifically, we determined the Gibbs free energy, which is an indicator of the interaction strength between the chelator and the PDMS. The details of the calculation can be found in Supplementary Information.

6.1.4. Radiotracer production and radioactivity measurements

The radiotracers Y-90, La-140, and Cu-64 were produced by neutron irradiation of Y_2O_3, La_2O_3 (Merck Sigma), and Zn-foil, respectively, at the Hoger Onderwijs Reactor (HOR) of the TU Delft Reactor Institute, the Netherlands. The Zn-foil was irradiated at a thermal neutron flux of $4.24 \cdot 10^{17}$ $m^{-2}s^{-1}$ for 6 hours, and subsequently, dissolved in 8 M nitric acid (HNO_3), slowly dried down on a heating plate, and redissolved in Milli-Q water. Y_2O_3, and La_2O_3 were irradiated at a thermal neutron flux of $4.69 \cdot 10^{16}$ $m^{-2}s^{-1}$ for 3 hours and subsequently, dissolved in 1 M HNO_3 solution, slowly dried down on a heating plate, and redissolved in Milli-Q water. The radiotracer Ga-68 was eluted from an Eckert & Ziegler IGG100 GMP Ge-68/Ga-68 generator (generously supplied by Erasmus MC, the Netherlands) in 0.1 M HCl. The radiotracer Ac-225 was supplied by Eckert & Ziegler and Ra-223 was supplied by GE Healthcare.

Radioactivity measurements of the radiotracers were performed as follows: The Wallac Wizard2 3" 2480 Automatic Gamma Counter from Perkin Elmer (Groningen, the Netherlands) was used for gamma-radiation measurements of La-140, Cu-64, Ga-68, and Ra-223, while the beta-emitting Y-90 was measured with a Liquid Scintillation Counter (tricarb 2750TR/LL, Packard). Ac-225 was measured indirectly at equilibrium (> 30 minutes after experiments) with its γ-emitting daughter Fr-221 ($t_{1/2}$ = 4.9 minutes).

6.1.5. Separation of radionuclides with chelator-impregnated PDMS beads

Sorption capacity

To measure the sorption capacity of chelator-impregnated PDMS beads for different radionuclide-chelator combinations, 10 mg of the impregnated beads was submerged in 1 mL aqueous solutions with known concentration of Y (1 μM), La (1 μM), Cu (1 nM), or Ga (1 nM). The corresponding radioactive tracers Y-90, La-140, Cu-64, and Ga-68 were added to their respective solutions at concentrations between 1 - 10 kBq/mL. For Y and La, PDMS beads impregnated with the chelator D2EHPA were selected. For Cu and Ga, DTZ and BPHA were chosen, respectively, due to their use in prior studies on microfluidic solvent extraction of Cu-64 [27, 28] and Ga-68 [29]. The solutions containing Y and La had a pH of 6, the Cu solution had a pH of 0, and the Ga solution had a pH of 2, according to the optimal pH for the extraction with these chelators, as determined by solvent extraction experiments [27–29]. The vials containing the aqueous solutions and PDMS beads were put on a Vortex-Genie 2 (Scientific Industries, Inc) at the highest speed for 1 hour to ensure equilibrium was reached. Afterwards, the aqueous solutions were pipet-

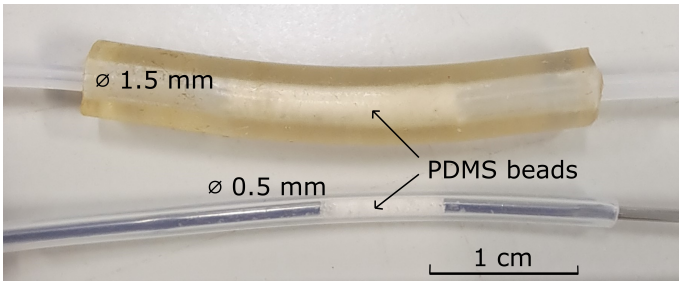

Figure 6.2: **Chromatography columns with chelator-impregnated PDMS beads used for the separation of radionuclides from their target.** D2EHPA-impregnated PDMS beads in a column with an inner diameter of 1.5 mm used for the in-flow separation of Y and La (top; loading 20 mg) and in a column with an inner diameter of 0.5 mm used for the in-flow separation of Ac-225 (bottom; loading 5 mg).

ted out of the vials, avoiding the PDMS beads. The concentration of Y, La, Cu, and Ga in the aqueous solutions was determined by measuring the radioactivity A of their corresponding radiotracers, which are representative of the total concentrations. The sorption capacity was calculated by subtracting the measured amount of Y-90, La-140, Cu-64, or Ga-68 after the adsorption ($n_{\text{aq, depleted}}$) from the initial amount ($n_{\text{aq, initial}}$), and dividing the adsorbed amount by the mass of the chelator-impregnated PDMS beads (m_{beads}), i.e.,

$$Sorption\ capacity\ [\frac{\text{mol}}{\text{g}}] = \frac{n_{\text{aq, initial}}\ [\text{mol}] - n_{\text{aq, depleted}}\ [\text{mol}]}{m_{\text{beads}}\ [\text{g}]}. \tag{6.1}$$

Experiments were done in triplicate and errors are given as one standard deviation of the mean.

In-flow separation

To test the in-flow separation of Y from Sr and La from Ba, 20 mg of D2EHPA-impregnated PDMS beads were loaded into a tubing with a diameter of 1.5 mm (Figure 6.2, top). The solutions consisted of 1 M $Sr(NO_3)_2$ with 100 μM [^{90}Y]$Y(NO_3)_2$ or 0.1 M $Ba(NO_3)_2$ with 10 μM [^{140}La]$La(NO_3)_2$, dissolved in Milli-Q water (nomenclature adapted from [53]). For the Ac-225 separation from [^{223}Ra]$Ba(NO_3)_2$, only 5 mg of D2EHPA-impregnated PDMS beads were loaded into a tubing with a diameter of 0.5 mm (Figure 6.2, bottom), because of the significantly lower Ac-225 concentration in the solution (in the picomolar range, compared to the micromolar range for Y and La). The solution consisted of 0.1 M $Ba(NO_3)_2$ with ~ 10 kBq/mL Ac-225 and ~ 10 kBq/mL of Ra-223. These model solutions were used for the experiments to collect results, upon which future experiments with irradiated targets can be designed. The aqueous solutions containing the radionuclides were filled into syringes and pushed through the column by a syringe pump (AL-1000 Programmable Syringe pump 941-371-1003 from World Precision Instruments Inc.) at various flow rates in the range of 0.1 - 6 mL/min. The adsorption efficiency (AE) was defined as the relative difference in measured radioactivity before (A_{initial}) and after

($A_{\text{after adsorption}}$) the in-flow separation, i.e.,

$$AE\ [\%] = \left(1 - \frac{A_{\text{after adsorption}}}{A_{\text{initial}}}\right) \times 100\%. \tag{6.2}$$

After the adsorption, the radionuclide of interest needs to be eluted from the beads into another aqueous solution. Herefore, different HCl concentrations were tested, ranging from 0.1 M to 4 M HCl, to see if a difference in acidity leads to a difference in elution speed. The flow rate was kept at 0.1 mL/min. 100 µL fractions were collected consecutively and their radioactivity was measured as described above.

Co-adsorption of Sr, Ba, and Ra-223, from 1 M $Sr(NO_3)_2$ for Sr, and 0.1 M $Ba(NO_3)_2$ for Ba and Ra-223, was also studied in-flow using the above procedure and the adsorption efficiency was determined according to Equation 6.2. Of note, for Sr and Ba, instead of the ratio of the radioactivities, we used the ratio of the concentrations before and after the in-flow separation as measured by inductively coupled plasma mass spectrometry (ICP-MS, Perkin Elmer, NexION 2000).

For the separation of Ac-225 from Ra-223 a separation factor (S) was calculated additionally, for the results at the optimal flowrate of 0.3 mL/min, according to Eq 6.3, where D is defined as the ratio of the adsorbed and not adsorbed radioactivity.

$$S = \frac{D_{\text{Ac}}}{D_{\text{Ra}}} \tag{6.3}$$

The co-adsorption of the potential metal contaminants Ni, Fe, Cu, Zn, Pb, Al, and Ca to the D2EHPA-impregnated PDMS beads was studied as well. These contaminations are commonly found in irradiated targets [54]. They are essential to study, since one important parameter for the use of the already separated radionuclides is the specific activity, which is the radioactivity per unit mass. A solution consisting of 100 µg/L of each metal contaminant was flown through the column as described above. We used a flow rate of 0.3 mL/min, which was identified as the optimal flow rate for Ac-225 adsorption as explained later. The initial concentrations and concentrations after the adsorption, as well as the elution into 0.1 M HCl (in which Ac-225 is collected), were measured by ICP-MS and the AE was calculated as described above. The total recovery of the contaminants was calculated as

$$Total\ recovery\ [\%] = \frac{c_{\text{elution}}}{c_{\text{initial}}} \times 100\%, \tag{6.4}$$

where c_{elution} is the measured concentration of the contaminant in the elution and c_{initial} is the initial concentration of the contaminant in the solution during the in-flow separation. All experiments were executed in triplicate and errors are given as one standard deviation of the mean.

6.2. Result and Discussion

6.2.1. PDMS beads impregnated with three different chelators

Figure 6.3 shows the FTIR spectra of bare PDMS beads and PDMS beads impregnated with three different chelators. These spectra confirm the presence of the chelators on

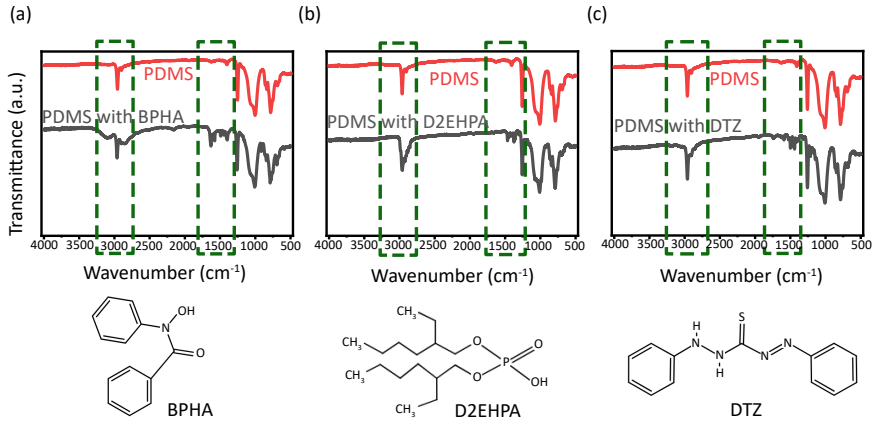

Figure 6.3: **Presence of the chelators on the impregnated PDMS beads by FTIR.** FTIR spectra of bare PDMS beads and PDMS beads impregnated with the chelators BPHA (a), D2EHPA (b), and DTZ (c), along with their corresponding chemical structure. The spectra of bare PDMS beads are in red, the spectra of the impregnated PDMS beads are in grey, and the peaks characteristic for the chelators are highlighted in the green boxes. The FTIR of the pure chelators can be found in the literature [36, 51, 55].

the impregnated beads, evident from peaks in the spectra specific to the specific bonds in the molecular structure of the different chelators. For BPHA, its presence is confirmed by the peak on the wavelength of 1622 cm^{-1} associated with the C=O bond of BPHA and on the wavelength of 3171 cm^{-1} associated with the O-H bond [51], see Figure 6.3(a). For D2EHPA, its presence is confirmed by the peak on 1230 cm^{-1} corresponding to the P=O bond of D2EHPA and by extra stretching in the 3000 - 2900 cm^{-1} region, see Figure 6.3(b). Although DTZ is harder to observe than the other two chelators as most of its characteristic peaks overlap with the peaks of PDMS, we confirm the presence of DTZ by the peaks in the 3000 - 2900 cm^{-1} region, see Figure 6.3(c).

Since the final application of the chelator-impregnated PDMS beads is to adsorb radionuclides, the chelators are preferably located at the outer surface, where most of the adsorption takes place. While FTIR spectra indicate the presence of the characteristic peaks corresponding to the chemical groups of the chelators, its penetration depth is relatively high (in µm range), and it does not reveal where the chelators are present. Therefore, we approached this hypothesis with additional FE-SEM and XPS measurements. The FE-SEM images show that the surface morphology changes with the impregnation, see Figure 6.10. More specifically, particle-like structures are seen on the surface of the PDMS beads impregnated with BPHA and DTZ, while a smoothening-like effect is observed on the surface of the PDMS beads impregnated with D2EHPA. This difference may arise from the fact that D2EHPA is in liquid form at room temperature, while DPHA and DTZ are in powder form when dissolved in chloroform. Furthermore, the XPS survey spectra show the presence of characteristic atomic peaks on the first few nanometers of the surface of the samples: a nitrogen peak on the PDMS impregnated with BPHA, a phosphorus peak on the PDMS impregnated with D2EHPA, and a nitrogen peak, and a sulfur peak on the PDMS impregnated with DTZ, see Figure 6.11. The XPS survey scans

on the surface thus agree with the visual FE-SEM inspections, which indicates that the chelators may be present on the surface of the PDMS beads. Interestingly, the depth profiling of the samples shows the characteristics peaks even after etching of 400 seconds, see Figure 6.11. This indicates infiltration of the chelators inside the PDMS beads. This infiltration is explained by the entrapment of the chelators in the matrix of PDMS during the chloroform swelling process [56]. This swelling process hence is important, increasing the loading capacity of the chelators in the PDMS beads.

To investigate further whether the chelators are chemically or physically sorbed, the XPS survey scans of Si2p are resolved. The Si2p peaks are chosen as they are exclusive peaks present in PDMS beads and not in the chelators. Figure 6.12 shows the scan of Si2p where both bare PDMS and PDMS impregnated with three different chelators have comparable peaks, indicating no chemical changes in the Si atomic bond. This result implies the absence of a chemical interaction between the chelators and the Si atoms of the PDMS beads. Additionally, we conducted and resolved XPS survey scans of C1S. From Figure 6.12, there are extra peaks visible in the C1s scans (at 288.1 eV) of the chelators-impregnated PDMS beads when compared with the C1s scans of bare PDMS beads. These peaks correspond to the presence of C-O bonds in the samples. However, this C-O bond is typically present in BPHA, D2EHPA, and DTZ. Thus, to infer the presence of chemical interaction between PDMS beads and the chelators from this bond is difficult. Furthermore, most C1s peaks (as well as the O1s peaks) also experience broadening and shifts, common occurrences in non-conductive samples such as PDMS beads. The broadening and the shifts of the peaks make the inferring of the resolve less reliable. From the resolves of Si2p, we hence argue that the impregnation process, as indicated by other works [22, 57], is a physisorption process, with a swelling-induced transport of chelators into the matrix of the PDMS beads.

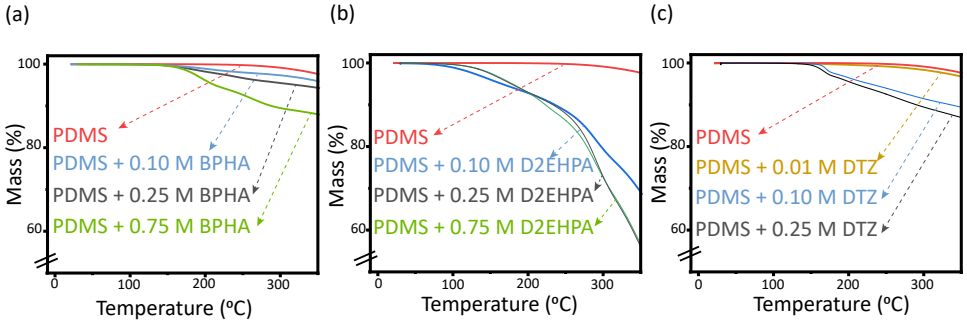

Figure 6.4: **Quantification of the amount of chelator impregnated in the PDMS beads using thermogravimetry.** Thermogravimetry of PDMS beads impregnated with BPHA (a), D2EHPA (b), and DTZ (c) at various concentrations of these chelators in chloroform.

Since the maximum sorption capacity is limited by the amount of chelators present, it is important to quantify the amount of impregnated chelators on the PDMS beads. We determined this amount based on thermogravimetry. We measured the mass of the beads at temperatures increasing from 25 °C to 800 °C and calculated the mass of the samples impregnated with the three types of chelators at various concentrations relative

to the initial mass of the samples at 100 °C. Following the common practice of assuming that the mass decline between 25 °C and 100 °C is due to sample dehydration, we consider the mass difference between bare PDMS beads and impregnated PDMS beads at 310 °C, where bare PDMS starts decreasing in mass, as an approximation of the total mass of the impregnated chelators. For BPHA-impregnated PDMS beads, the mass difference increases from 1.8 % ± 0.1 % for PDMS beads impregnated with 0.10 M BPHA in chloroform to 3.7 % ± 0.1 % and 9.7 % ± 0.2 % for PDMS beads impregnated with 0.25 M and 0.75 M BPHA in chloroform, respectively, see Figure 6.4(a). This indicates an increasing BPHA amount impregnated in the PDMS beads as the available BPHA in chloroform increases. Since the solubility of BPHA in chloroform is around 155 g L^{-1} (equivalent to 0.72 M [34]), we suspect that the impregnated BPHA amount does not increase further. This hypothesis is supported by the TGA results of DTZ-impregnated PDMS beads where the beads impregnated with 0.01 M DTZ in chloroform show a mass difference of 1.4 % ± 0.1 %, while the beads impregnated with DTZ solutions of 0.10 M and 0.25 M, above their saturation concentration (solubility of DTZ is 17 g L^{-1} or 0.075 M in chloroform [35]) show no significant difference in their mass difference (7.4 % ± 1.0 %, and 8.9 % ± 1.7 %, respectively), see Figure 6.4(c). For D2EHPA, liquid at room temperature, a similar trend of increasing mass difference between PDMS beads impregnated with 0.10 M and 0.25 M D2EHPA in chloroform is observed, from 21.0 % ± 0.9 % to 30.9 % ± 1.1 %, see Figure 6.4(b). The difference does not significantly increase when the beads are impregnated with 0.75 M (31.3 % ± 1.2 %), indicating the maximum capacity of the PDMS matrix in accommodating D2EHPA. To confirm this hypothesis about PDMS matrix capacity, we conduct an additional swelling test. We immerse bare PDMS bead samples in chloroform for 10 hours and measure a volumetric increase of 16.0 % ± 2.2 % and a mass increase of 23.4 % ± 3.1 %. This PDMS volumetric increase due to swelling corresponds well with the mass increase, as the density of chloroform is 1.489 g mL^{-1}, indicating the filling of the PDMS matrix with chloroform. However, when we apply a similar calculation to 0.25 M D2EHPA-impregnated PDMS beads samples, the expected mass increase (15.6%, the density of D2EHPA is 0.976 g mL^{-1}) due to D2EHPA impregnation is lower than the measured mass decrease by TGA (30.9 % ± 1.1 %). This difference could happen due to the adsorption of D2EHPA on the surface of the PDMS beads. To resolve this, we reduce the surface adsorption effect by immersing a PDMS block with a lower surface-to-volume ratio (1 cm x 1 cm x 1 cm) in a similar chloroform solution containing 0.25 M D2EHPA. We then conduct TGA measurements on the cut samples to approximate the amount of the impregnated D2EHPA. The result shows a much lower mass decrease (15.8%) compared to the bead samples. This measured mass decrease is closer to the calculated mass increase due to swelling. From both tests, we argue that the total impregnated chelator amount is the sum of the amount of D2EHPA accommodated inside the PDMS matrix and the amount of D2EHPA located on the surface. This result also emphasizes the importance of the PDMS beads' diameter, where a smaller diameter leads to an increase in surface area and subsequently an increase in the impregnation amount. While this study focuses on a fabrication method using simple kitchen equipment, there have been many studies on increasing the surface area of PDMS beads (e.g., PDMS beads with a median diameter of 1 µm obtained using droplet microfluidics [58] or porous PDMS using template moulding [59]). We note that Figure 6.4 also implies that

the chelator-impregnated PDMS beads are stable at temperatures below 120 °C.

6.2.2. Chemical stability of the chelator-impregnated PDMS beads

A known problem in the applications of chelator-impregnated resins is the low chemical stability, leading to leaching of the impregnated chelator over time, causing contamination during elution [23, 26]. To assess the chemical stability of the chelator-impregnated PDMS beads, we immerse the beads in three solutions of different acidity: Milli-Q water, 1 M HCl, and 12 M HCl. For D2EHPA-impregnated PDMS beads, the XPS spectra obtained after washing and drying are shown in Figure 6.5(a). P2p peaks are observed in all samples, indicating the presence of D2EHPA in all the samples. Furthermore, the phosphorus atom remains in a phosphate form (at 134 eV) with no significant chemical state change even after washing it with 12 M HCl. The Cl2p spectra show no chlorine sorbed

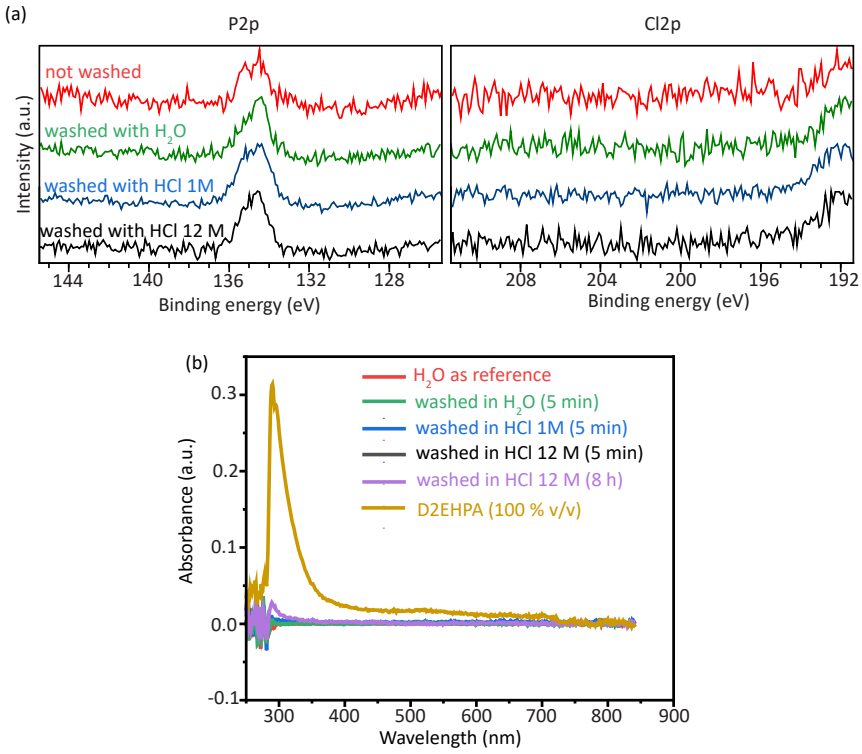

Figure 6.5: **Chemical stability of D2EHPA-impregnated PDMS beads against leaching measured with XPS and UV-Vis.** (a) XPS P2p scan and Cl2p scan of D2EHPA-impregnated PDMS beads before and after 5 minutes of immersion in solutions of different acidity (b) the corresponding UV-Vis spectra of the immersion solutions.

into the PDMS beads, reducing the possibility of contamination during the separation of the radionuclides. Complementing the XPS results, Figure 6.5(b) shows the UV-Vis spectra of the immersion solutions. Pure D2EHPA (100%(v/v)) shows a peak at 274 nm [60], while no peaks are observed in all liquid samples after 5 minutes of immersion,

indicating at least no detectable D2EHPA. The liquids remain visibly clear and no fluid separation after 24 hours is observed. On the other hand, the immersing liquid from D2EHPA-impregnated silica powder is opaque and cloudy, indicating the presence of dispersed D2EHPA. After decanting, these impregnated silica samples show a D2EHPA release of 220 mg/g ± 13 mg/g, 45 mg/g ± 11 mg/g, and 52 mg/g ± 12 mg/g in Milli-Q water, 1 M HCl, and 12 M HCl, respectively. When we challenge the stability of the D2EHPA-impregnated PDMS beads by immersing them in both 1 M HCl and 12 M HCl for a longer period (8 hours), as well as in a different acid (1 M HNO_3), we find no indication of leached D2EHPA aside from the samples immersed for 8 hours in 12 M HCl, see Figure 6.5(b).

To compare with the D2EHPA-impregnated PDMS beads, we carry out the stability tests for BPHA-impregnated PDMS beads and DTZ-impregnated PDMS beads along with BPHA- and DTZ-impregnated silica powder. As expected, all BPHA-impregnated PDMS samples (washed and non-washed) show the presence of N1s peaks in the XPS spectra, while no BPHA-indicative peaks are found in the immersing liquids around 200 nm (indicating the N-phenylhydroxamide group [61]) in the UV-Vis spectra, see Figure 6.13(a) and (c), respectively. Please note that the shape of the N1s peaks in the XPS spectra of non-washed BPHA-impregnated PDMS samples is different from those washed due to protonation of BPHA, as reported in previous work [62]. Similar behavior is observed for all DTZ-impregnated PDMS samples, with the presence of N1s XPS peaks for washed and non-washed beads, while no peaks are found in the immersing liquids around 450 nm and 618 nm (indicative for DTZ [63]), see Figure 6.13(b) and (d), respectively. In contrast, all immersion liquids of the impregnated silica powder samples show intense peaks in the UV-Vis spectra, see Figure 6.13(e) and (f). Please note that in Figure 6.13(f), the peaks shifted due to possible oxidization of DTZ [63].

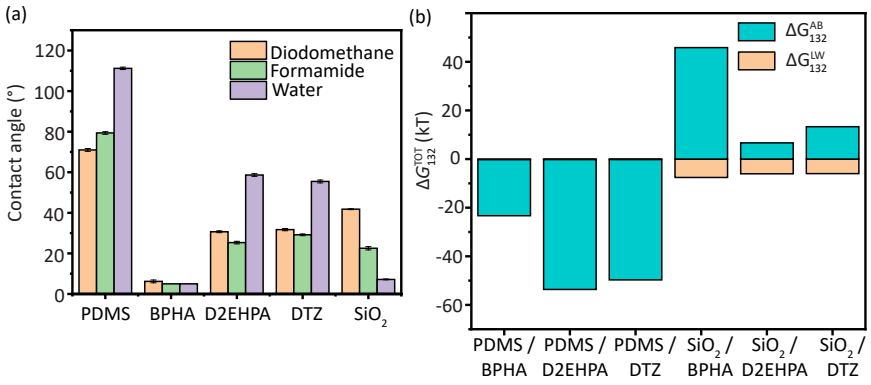

Figure 6.6: **Approximation of hydrophobic interaction between PDMS beads and chelators.** (a) The average measured static contact angle of non-polar liquid diiodomethane and polar liquid formamide and water on various substrates (the error bars represent 1 standard deviation from the average) and (b) Gibbs free energy calculated for estimating the interaction strength using the extended Derjaguin-Landau-Verwey-Overbeek approach.

To understand the reason behind the stability of the impregnated chelator on PDMS

Table 6.1: **Sorption capacity.** Sorption capacity of PDMS beads with different chelators, specific for Yttrium (Y), Lanthanum (La), Copper (Cu), and Gallium (Ga) (n=3).

Chelator	Element	Sorption Capacity
D2EHPA	Y	2.75 ± 0.53 mg/g
D2EHPA	La	4.03 ± 0.41 mg/g
DTZ	Cu	4.0 ± 1.1 ng/g
BPHA	Ga	0.329 ± 0.092 ng/g

beads, we evaluated the interactions between the chelator and PDMS in an aqueous medium using the extended Derjaguin-Landau-Verwey-Overbeek (EDLVO) theory [48, 52, 64]. We determined the Gibbs free energy using this theory, complemented by a series of contact angle measurements. The Gibbs free energy indicates the presence (or absence) of hydrophobic interactions, a common interaction found in polymeric materials, where a negative Gibbs free energy indicates the presence of hydrophobic interactions [47, 49, 65]. Figure 6.6(a) shows the measured contact angle of three different liquids on PDMS and the three different chelators. Additionally, reference measurements were performed on silica. Our reported contact angle values for PDMS and silica are comparable with previous works [66–69]. Figure 6.6(b) shows the subsequently calculated Gibbs free energy. The interaction between PDMS and all three chelators shows a negative Gibbs free energy, indicating the presence of hydrophobic interaction. This is consistent with previous works on PDMS [70–72]. From Figure 6.6(b), most of the negative Gibbs free energy for the PDMS-chelator combinations is contributed by the acid-base interaction (ranging from -20 kT to -60 kT), while the Lifshiftz-van der Waals interaction contributes much less (~-1 kT). This suggests that the resulting hydrophobic interaction is due to hydration repulsion towards the chelators instead of a direct attraction force of PDMS [73, 74]. Furthermore, while the interaction between PDMS and D2EHPA, and PDMS and DTZ show comparable negative values, the interaction between PDMS and BPHA shows a less negative Gibbs free energy, implying a relatively weaker hydrophobic interaction. This result is in line with the theoretical use of the octanol-water partition coefficient (K_{ow}) of the chelators to predict the sorption behavior (and sorption strength) of the chelators [75] on hydrophobic material. A positive K_{ow} indicates a partition preference of the chelators in octanol (as opposed to water), with higher K_{ow} indicating a higher octanol partition, and subsequently stronger hydrophobic interaction. Previous works indicate K_{ow} of 4 for D2EHPA [76]; 3-4 for DTZ [77] and 2-3 for BPHA [78].

In sharp contrast to the interaction between the chelators and PDMS, we find that all interactions between the chelators and silica show a positive Gibbs free energy, explaining the high release of the chelators when immersed in an aqueous medium (Figure 6.13). Please note that this approach neglects a plausible complementary phenomenon where the chelator molecules are physically trapped in the PDMS matrix and therefore become immobile. While this complimentary effect is not incorporated, the comparison to the silica samples already shows that chelators are more strongly bound to PDMS beads than to silica powders.

6.2.3. Sorption capacity of PDMS beads with different chelators

Table 6.1 shows the measured sorption capacity of D2EHPA-, DTZ-, and BPHA-impregnated PDMS beads, for Y, La, Cu, and Ga, respectively. The results show a much higher sorption capacity of the D2EHPA-impregnated PDMS beads over the DTZ- and BPHA-impregnated PDMS beads. More specifically, the D2EHPA-impregnated PDMS beads have a six orders of magnitude higher sorption capacity towards Y and La than the DTZ-impregnated PDMS beads have towards Cu, and a seven orders of magnitude higher sorption capacity than the BPHA-impregnated PDMS beads have towards Ga. This proves again the significantly higher integration of D2EHPA into the PDMS compared to BPHA and DTZ, with the underlying reasons discussed in the previous section.

In comparison to other commercial ion-exchange resins, the D2EHPA-impregnated beads show a lower sorption capacity. For example, the Dowex 50W-X8 resin has a sorption capacity towards rare earth elements between 191 and 294 mg/g [79], Ln resin has a sorption capacity of 30.67 mg/g for Eu [80], the Amberlite IR120H (AIR120H) resin has a sorption capacity of 8.2 mg/g for Ce [81], and HDEHP-loaded microcapsules (impregnated) have a sorption capacity of 58.07 mg/g for Eu [80]. While the primary focus of this work is on the development of a selective and stable resin, we note that optimizing the sorption capacity for the chelator-impregnated beads is outside the scope of the present work. We expect that higher sorption capacities can be obtained, for example by optimization of the diameter and the porosity of the beads for example as shown by [82] and [58].

6.2.4. In-flow separation with D2EHPA-impregnated PDMS beads

Given the high chemical stability and the higher sorption capacities of the D2EHPA-impregnated PDMS beads for Y and La, we continued with in-flow separation and elution studies using a chromatography column with these combinations of chelator and radionuclides. For the separation of La from its Ba target, we prepared an aqueous 10 μM La (and a La-140 radiotracer with 0.1 M $Ba(NO_3)_2$) solution and injected the mixture at various flow rates in the column to study the influence of the residence time on the adsorption efficiency. For the separation of Y from its Sr target, an aqueous solution containing 100 μM Y (and a Y-90 radiotracer) and 1 M $Sr(NO_3)_2$ was prepared, and injected in the column.

For the lowest range of flow rates studied, we observe that both Y and La are adsorbed to the D2EHPA-impregnated PDMS beads with almost 100 % adsorption efficiency, see Figure 6.7(a). For increasing flow rates, i.e., decreasing residence times, the adsorption efficiency declines. A notable decline is observed for flow rates above 1 mL/min and 4.5 mL/min for Y and La, respectively. Apart from this difference in onset, we also observe a clear difference in slope. While the adsorption efficiency already decreases from 99.89 % ± 0.14 % at 1 mL/min to 77.5 % ± 1.8 % at 2.6 mL/min for Y, it only decreases from 99.50 % ± 0.12 % at 4.5 mL/min to 91.1 % ± 1.4 % at 6 mL/min for La. The difference in onset and slope might be explained by (I) the concentration of Y being ten times higher than the concentration of La in their respective solutions and (II) the smaller ionic radius of Y.

For the application of the chelator-impregnated PDMS beads in the field of nuclear medicine, it is not only important that the adsorption efficiency of the radionuclide of

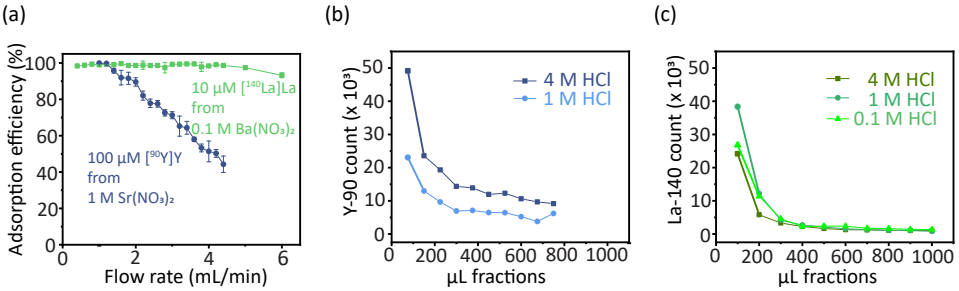

Figure 6.7: **Chromatography column separation and elution with D2EHPA-impregnated PDMS beads for Y and La.** (a) In-flow separation of 10 μM [^{140}La]La and 100 μM [^{90}Y]Y from their respective target solutions of 0.1 M $Ba(NO_3)_2$ and 1 M $Sr(NO_3)_2$ (n=3). (b) Elution profile of [^{90}Y]Y into 4 M and 1 M HCl at a flow rate of 0.1 mL/min (n=1). (c) Elution profile of [^{140}La]La into 4 M, 1 M and 0.1 M HCl at a flow rate of 0.1 mL/min (n=1).

interest is close to 100 %, but also that the adsorption efficiency of the corresponding target is as low as possible. We therefore also measured the co-adsorption of the Ba and Sr target solutions at the largest flow rates that still result in high adsorption efficiencies of La and Y. Ba co-adsorption was measured to be 1.28 % ± 0.45 % at a flow rate of 4 mL/min and Sr co-adsorption was 1.24 % ± 0.57 % at a flow rate of 1 mL/min. From these results, the co-adsorption of the corresponding target material is low, showing a promising application in the clinical field.

Elution of Y and La from the D2EHPA-impregnated PDMS beads was studied for elution solutions of different acidity. We observe that elution of Y is incomplete after 1 mL and only around 65 %, while the elution of La is about 85 % in the first 1 mL, see Figure 6.7(b) and (c). The difference in behavior might be due to the higher concentration of Y, necessitating higher volumes to increase the total elution. The acidity of the solutions does not significantly influence the elution profiles. Additionally, the smaller ionic size of Y leads to a more stable complex with D2EHPA. This trend of increasing complex stability with increasing charge density (i.e., decreasing ionic radius) is often found in chelate complexation [83] and was shown before for lanthanide and actinide complexes [84], making it more difficult to fully elute in small volumes.

A radionuclide that currently receives increasing attention for its potential in targeted alpha therapy is Ac-225. For this reason, we also studied the in-flow separation Ac-225 from its target Ra-223 and its subsequent elution in a chromatography column loaded with D2EHPA-impregnated PDMS beads. Since the total concentration of Ac-225 compared to Y and La was significantly lower by nine orders of magnitude, only 5 mg of PDMS beads was used. The results again show an adsorption efficiency close to 100 % for the lower range of flow rates, with a decline in adsorption efficiency for increasing flow rate, see Figure 6.8(a). At a flow rate of 0.3 mL/min, the adsorption efficiency of Ac-225 is 98.51 % ± 0.25 % , while the co-adsorption of its target Ra-223 is 0.94 % ± 0.57 %.

Elution of Ac-225 was achieved with 0.1 M HCl at a flow rate of 0.1 mL/min. 80.3 % ± 0.9 % of Ac-225 was eluted in the first 1 mL and 93.2 % ± 1.7 % in the first 2 mL, see Figure 6.8(b). The final eluted solution contains 0.053 % ± 0.014 % of the initial amount of

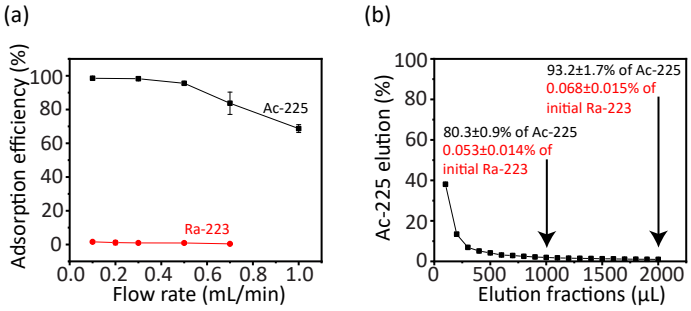

Figure 6.8: **Chromatography column separation and elution with D2EHPA-impregnated PDMS beads for Ac-225.** (a) In-flow separation of Ac-225 at different flow rates (n=3). (b) Elution profile of Ac-225 indicated by Fr-221 in 0.1 M HCl at a flow rate of 0.1 mL/min (n=2).

Table 6.2: **Adsorption of metal contaminants during the separation of Ac-225**. Adsorption efficiency (*AE*) and total recovery of the metal contaminants in the 0.1 M HCl elution. The concentrations of the metals were 100 µg/L. Experiments were done in triplicate and errors are given as one standard deviation of the mean.

	Ni	Fe	Cu	Zn	Pb	Al	Ca
AE [%]	0.99 ± 0.86	82.8 ± 4.6	0.95 ± 0.64	15.7 ± 7.1	14.5 ± 6.6	48.1 ± 1.8	11.78 ± 0.88
Recovery [%]	0.020 ± 0.003	1.38 ± 0.24	0.92 ± 0.06	15.1 ± 7.1	4.8 ± 1.5	0.13 ± 0.08	3.81 ± 0.97

Ra-223 in the first 1 mL and a total of 0.068 % ± 0.015 % in 2 mL, resulting in a separation factor that averages over 6000. We note that we washed the column before the elution of Ac-225 with the 0.1 M HCl solution with Milli-Q water, which reduced the amount of Ra-223 in the elution solution by 90.8 % ± 2.5 %.

A known problem that may arise during the production of Ac-225 is the contamination of the Ac-225 solution with metal contaminants during production as reported by Ramogida *et al.* [54]. For this reason, we studied the in-flow separation and elution of metals as well. Table 6.2 shows the adsorption efficiency and the total recovery. From all measured metal contaminants only Zn is co-adsorbed at 15.7 % ± 7.1 % and also fully eluted in 0.1 M HCl, resulting in a total recovery of 15.1 % ± 7.1 % in the elution fraction. While Fe shows a high *AE* of 82.8 % ± 4.6 %, it is not eluted in 0.1 M HCl and only 1.38 % ± 0.24 % of the initial amount is present in the elution solution, meaning that it is also cleared from the target solution. All other tested elements are neither co-adsorbed nor eluted in significant amounts. These results indicate a high decontamination during the Ac-225 separation with the presented D2EHPA-impregnated PDMS beads.

Overall, the D2EHPA-impregnated PDMS beads have proved successful in the separation of Ac-225 from [^{223}Ra]Ba$(NO_3)_2$ with around 93 % of Ac-225 and below 0.1 % of Ra-223 in the first 2 mL of elution. In comparison, multiple other methods have been investigated in the literature for the separation of Ac-225 from radium targets, including ion-exchange column chromatography (using AG50×8 [85] or AG50X4 [86], Ln- [87] or DGA resin [88]), microfluidic ion-exchange [86], as well as solvent impregnated resins [89]. While all of these methods achieve a good separation of Ac-225, they all show different drawbacks, such as the need for (i) large volumes of chemicals [85, 88, 89], (ii) highly acidic solutions for elution [85, 86, 89], (iii) slow processing [86, 89], or (iv) addi-

tional clean-up steps [87]. Furthermore, it has been reported that DGA resin is highly sensitive to radiolysis and extra washing steps are needed to reduce radiolytic degradation products [88], partially due to the characteristic water loading [90]. While it remains to be shown if the presented D2EHPA-impregnated PDMS beads have a higher radiation stability, D2EHPA and PDMS separately are reportedly highly resistant against radiation [91, 92]. Thus, in comparison with existing separation methods, the presented chelator-impregnated PDMS beads are promising to separate medical radionuclides in a commercial setting.

6.3. Conclusions

We presented chelator-impregnated PDMS beads that allow the selective and efficient separation of the medically-interesting radionuclides (Y-90, La-140, and Ac-225) from their liquid target ($Sr(NO_3)_2$, $Ba(NO_3)_2$, and $[^{223}Ra]Ba(NO_3)_2$), with minimal leaching of the chelator from the beads when contacted with the acidic solutions used for adsorption and subsequent elution of the radionuclides. This minimal leaching is beneficial for the purity of the radionuclide solution and at the same time offers the possibility of direct liquid target recycling. The simple fabrication of the chelator-impregnated PDMS beads together with the ability to impregnate PDMS with different types of chelators offers a versatile approach towards increasing the applicability of chelators for the simple, automatable separation of medical radionuclides.

6.4. Conflicts of interest and acknowledgements

There are no conflicts to declare. This publication is part of the Open Technology Programme (with project number 16913) financed by the Dutch Research Council (NWO). We would like to acknowledge Baukje Terpstra and Astrid van der Meer for their assistance with the irradiations at the HOR. We extend our gratitude to Bart van der Linden and Willie Rook for the technical support with TGA, to Bart Boshuizen for the fruitful discussion on the XPS results, and to Bijoy Bera for the fruitful discussion on the surface energy. We acknowledge the use of BioRender.com to partially make the figures.

6.5. Supplementary Information

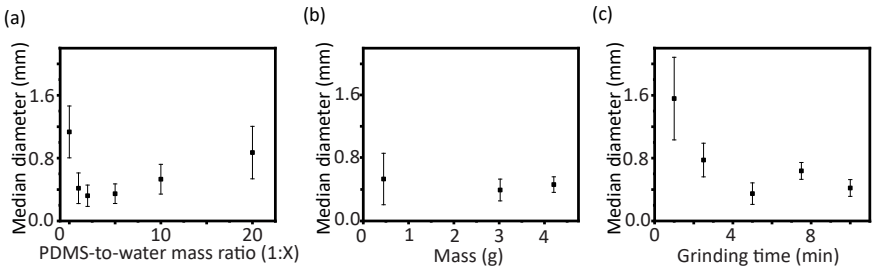

Figure 6.9: **Dependence of the diameter of the PDMS beads on operating conditions and preparation protocol.** Median diameter of bare PDMS beads fabricated with (a) different PDMS-to-water ratios (with 3 g of PDMS foam sheet and 5 min of grinding time), (b) different total weight (with 1:2 PDMS to water ratio and 5 min of grinding time) and (c) different grinding times (with 1:2 PDMS to water ratio and 3 g of PDMS foam sheet. In this paper, the beads are fabricated by grinding 3 g of PDMS foam sheet made out of 1:2 PDMS to water ratio for 5 min.

The calculation of the Gibbs free energy is given as follows

$$\Delta G_{132}^{TOT} = \Delta G_{132}^{LW} + \Delta G_{132}^{AB} + \Delta G_{132}^{EL}, \tag{6.5}$$

where ΔG_{132}^{TOT} refers to the total Gibbs free energy, ΔG_{132}^{LW} refers to the Lifshiftz-van der Waals (LW) contribution, ΔG_{132}^{AB} refers to the acid-base (AB) contribution and ΔG_{132}^{EL} refers to the electrostatic (El) contribution. The subscript 1 represents the chelator, 2 represents the substrate (PDMS), and 3 represents the aqueous medium (water). The notation ΔG_{132}^{TOT} represents the Gibbs free energy between the chelator and PDMS in water. Since the chelator and PDMS are assumed to be charge-neutral, the El contribution is neglected [47, 60].

The LW contribution is calculated as follows

$$\Delta G_{132}^{LW} = -2(\gamma_3^{LW} + \sqrt{\gamma_1^{LW}\gamma_2^{LW}} + \sqrt{\gamma_1^{LW}\gamma_3^{LW}} - \sqrt{\gamma_2^{LW}\gamma_3^{LW}}), \tag{6.6}$$

with the gammas representing the surface energies. The two surface energies of the chelator (γ_1^{LW}) and the PDMS (γ_2^{LW}) are unknown and follow from a set of contact angle measurements as described later, while the surface energy of water (γ_3^{LW}) is taken from literature, see the top row in Table 6.3.

The AB contribution is calculated as follows

$$\Delta G_{132}^{AB} = -2(\sqrt{\gamma_1^+\gamma_2^-} + \sqrt{\gamma_1^-\gamma_2^+} - \sqrt{\gamma_3^+}(\sqrt{\gamma_1^-} + \sqrt{\gamma_2^-} - \sqrt{\gamma_3^-}) - \sqrt{\gamma_3^-}(\sqrt{\gamma_1^+} + \sqrt{\gamma_2^+} - \sqrt{\gamma_3^+})). \tag{6.7}$$

where the superscripts + and - represent the positive and negative polar contribution (acid-base contribution) of the surface energies. The four surface energy contributions of the chelator (γ_1^+, γ_1^-) and the PDMS (γ_2^+, γ_2^-) are unknown and follow from a set of contact angle measurements as described later, while the surface energy contributions of water (γ_3^+, γ_3^-) are taken from literature, see again the top row in Table 6.3.

To determine the above-mentioned six unknown surface energies in Equations 6.6 and 6.7 for each combination of chelator and PDMS, we performed six types of contact

angle measurements. Since there are three types of contributions in Equations 6.6 and 6.7, Lifshiftz-van der Waals or non-polar, polar positive, and polar negative, the contact angle measurements (Krüss drop shape analyzer) were performed using three different liquids: One non-polar liquid (diiodomethane, > 98%, Merck Sigma) and two polar liquids (deionized water and formamide, > 99%, Merck Sigma). The unknowns γ_1^{LW}, γ_1^+, and γ_1^- in Equations 6.6 and 6.7 were determined by depositing a droplet of these three liquids on a PDMS surface in air, while the unknowns γ_2^{LW}, γ_2^+, and γ_2^- were determined by depositing a droplet of these three liquids on the chelator in air. More specifically, the Young -Dupre equation

$$(1+\cos\theta)\gamma_l^{TOT} = 2(\sqrt{\gamma_s^{LW}\gamma_l^{LW}} + \sqrt{\gamma_s^+\gamma_l^-} + \sqrt{\gamma_s^-\gamma_l^+}) \tag{6.8}$$

with

$$\gamma_l^{TOT} = \gamma_l^{LW} + 2\sqrt{\gamma_l^+\gamma_l^-} \tag{6.9}$$

was solved for the six measurements with the three liquids (l = diiodomethane, deionized water or formamide) and the two solid surfaces (s = PDMS or chelator). The surface energies for the three pure liquids, γ_l^{LW}, γ_l^+, γ_l^-, and γ_l^{TOT}, were obtained from literature [52, 60], see Table 6.3. For the contact angle measurements on the chelators BPHA and DTZ, their powder was placed on a glass slide and packed using a metal spoon. For the liquid chelator D2EHPA, it was pipetted on a glass slide. The reported contact angle was averaged out of 5 measurements. Once these contact angles were obtained, the Gibbs free energy was calculated by solving Equations 6.5 to 6.8. For reference, we also measured the Gibbs free energy for the interaction between the three chelators and silica.

Table 6.3: **Surface energies.** Surface energy of deionized water, diiodomethane, and formamide (in mN/m). The values were obtained from literature [52, 60].

Liquid	γ_l^{LW}	γ_l^+	γ_l^-	γ^{TOT}
Deionized water	21.8	25.5	25.5	72.8
Diiodomethane	50.8	0.0	0.0	50.8
Formamide	39.0	2.3	39.6	58.1

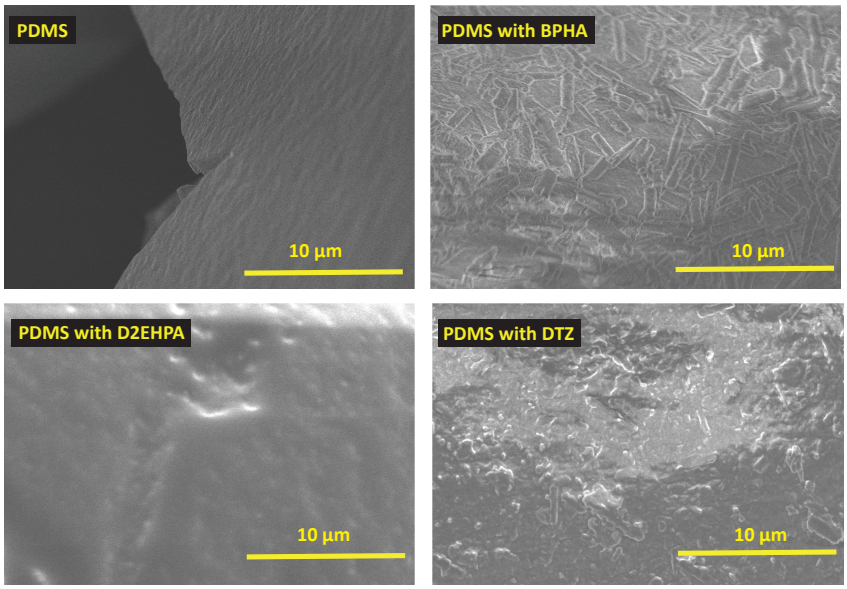

Figure 6.10: **Morphology of the beads' surface.** FE-SEM image of bare PDMS beads and PDMS beads impregnated with three different chelators (using chelator-containing chloroform solution, each with a concentration of 0.25 M).

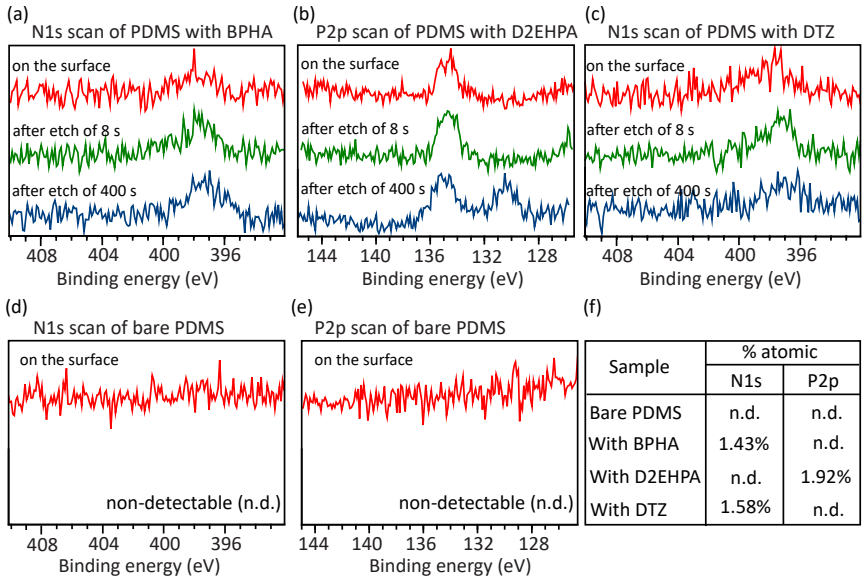

Sample	% atomic	
	N1s	P2p
Bare PDMS	n.d.	n.d.
With BPHA	1.43%	n.d.
With D2EHPA	n.d.	1.92%
With DTZ	1.58%	n.d.

Figure 6.11: **Presence of chelator on and inside the impregnated beads confirmed by XPS.** Overlay of XPS survey scans of (a) the N1s peak of BPHA-impregnated, (b) the P2p peak of D2EHPA-impregnated, and (c) the N1s peak of DTZ-impregnated PDMS coated flat silicon wafer. The survey scans were conducted at the surface (without ion-etching), after etching of 8 seconds (estimated to be ~1.6 nm, representing removal of possible surface contaminant groups), and after etching of 400 seconds (estimated to be ~80 nm, representing infiltration of the chelators inside the PDMS beads). (d) the N1s peak and (e) P2p peak of bare (not-impregnated) PDMS coated silicon wafer. (f) Comparison of N1s and P2p surface atomic percentage of bare PDMS and chelator-impregnated PDMS samples, where n.d. stands for non-detectable.

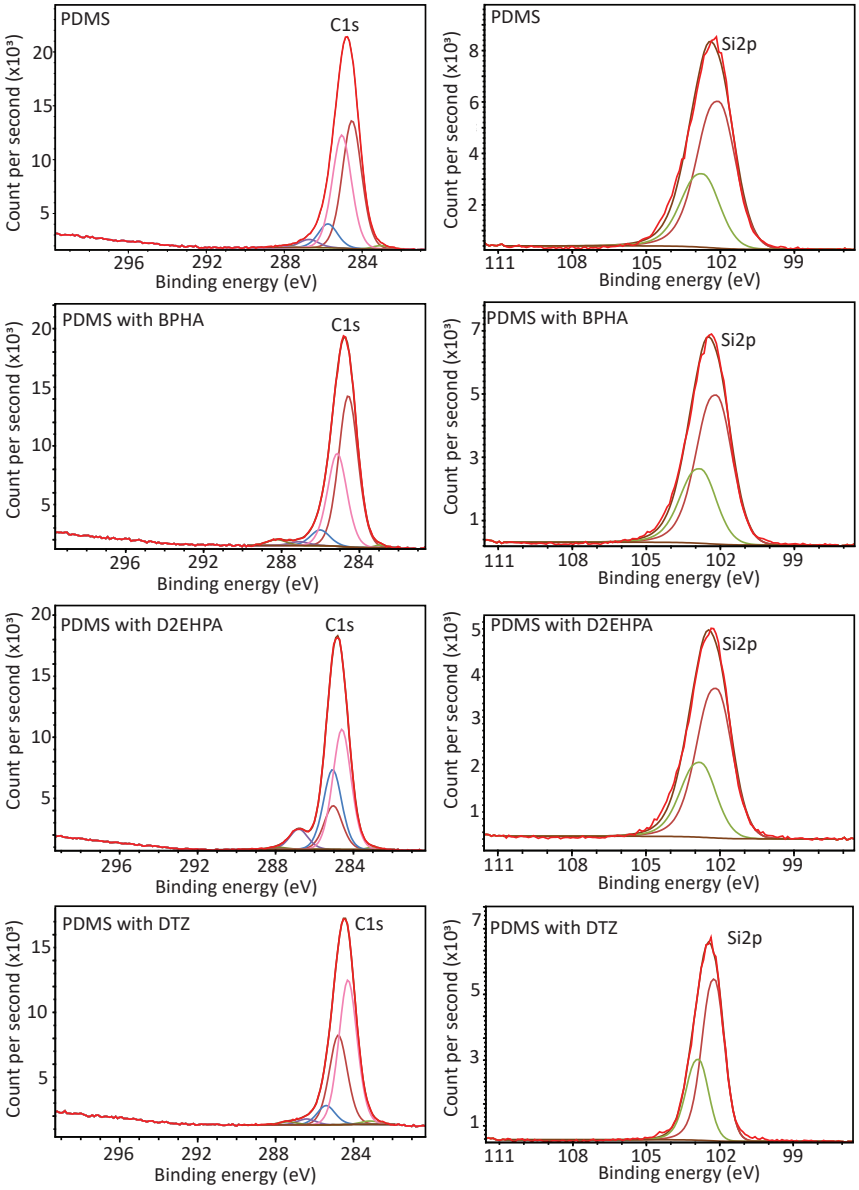

Figure 6.12: **Evaluation of the presence of chemical interaction between the chelators and PDMS.** XPS survey scans of C1s (left) and Si2p (right) for bare PDMS beads and chelator-impregnated PDMS beads. The lines inside the peaks are the XPS resolves.

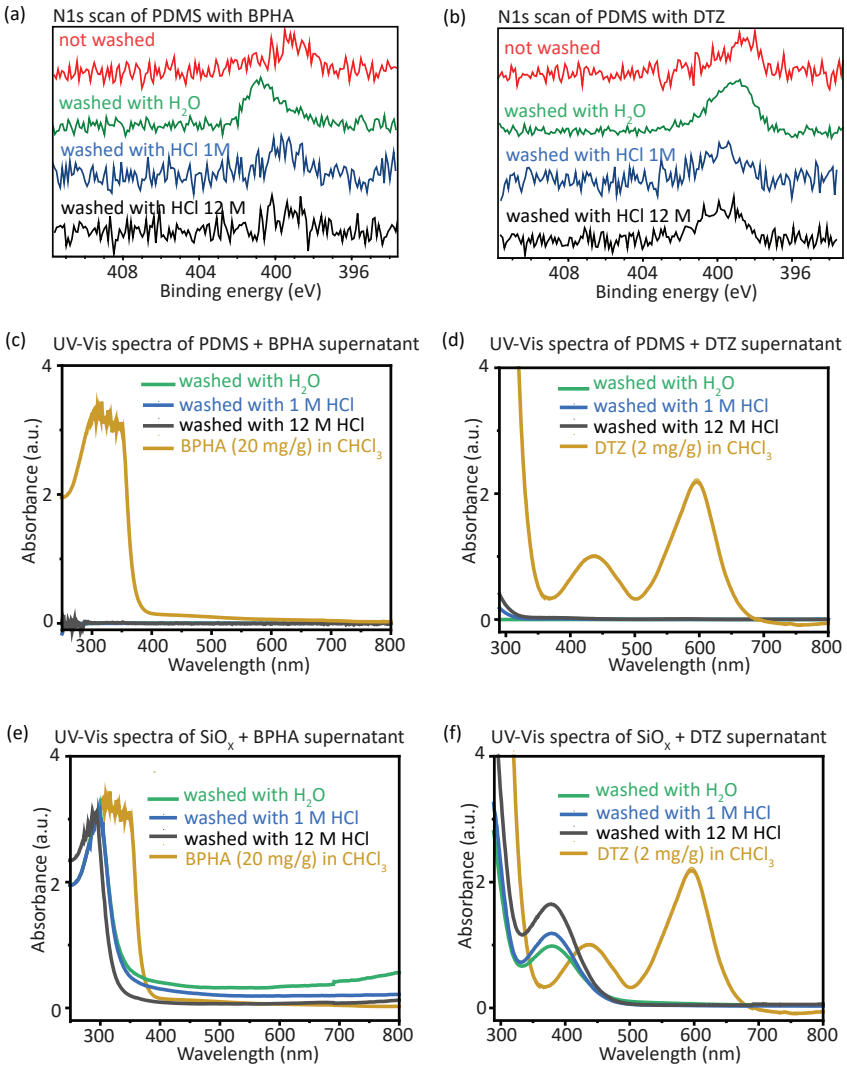

Figure 6.13: **Chemical stability of BPHA- and DTZ-impregnated PDMS beads and silicon oxide powder against leaching measured with XPS and UV-Vis.** (a-b) XPS N1s scan of (a) BPHA-impregnated and of (b) DTZ-impregnated PDMS beads before and after washing with the liquids for 5 minutes. (c-d) the corresponding UV-Vis spectra of their immersing liquid. (e-f) the UV-Vis spectra of immersing liquids used for washing (e) BPHA-impregnated and (f) DTZ-impregnated silicon oxide powder.

References

[1] A. Santoso, S. Trapp, V. van Steijn, R. M. de Kruijff, and J. R. van Ommen, *Method for preparing silicon elastomer beads loaded with chelating agents and their use for the separation of radionuclides,* Netherlands **Number: 2037212** (2024).

[2] A. Santoso, S. Trapp, I. Blommestein, S. Saedy, J. R. van Ommen, R. M. de Kruijff, and V. van Steijn, *Chelator-impregnated polydimethylsiloxane beads for the separation of medical radionuclides,* Separation and Purification Technology , 128865 (2024).

[3] W. Oyen, L. Bodei, F. Giammarile, H. Maecke, J. Tennvall, M. Luster, and B. Brans, *Targeted therapy in nuclear medicine—current status and future prospects,* Annals of Oncology **18**, 1782 (2007).

[4] W. A. Weber, J. Czernin, C. J. Anderson, R. D. Badawi, H. Barthel, F. Bengel, L. Bodei, I. Buvat, M. DiCarli, M. M. Graham, J. Grimm, K. Herrmann, L. Kostakoglu, J. S. Lewis, D. A. Mankoff, T. E. Peterson, H. Schelbert, H. Schöder, B. A. Siegel, and H. W. Strauss, *The future of nuclear medicine, molecular imaging, and theranostics,* Journal of Nuclear Medicine **61**, 263S (2020).

[5] A. Sanchez-Crespo, *Comparison of gallium-68 and fluorine-18 imaging characteristics in positron emission tomography,* Applied Radiation and Isotopes **76**, 55 (2013).

[6] G. Crișan, N. S. Moldovean-Cioroianu, D.-G. Timaru, G. Andrieș, C. Căinap, and V. Chiș, *Radiopharmaceuticals for PET and SPECT imaging: A literature review over the last decade,* International Journal of Molecular Sciences **23**, 5023 (2022).

[7] E. Deshayes, M. Roumiguie, C. Thibault, P. Beuzeboc, F. Cachin, C. Hennequin, D. Huglo, F. Rozet, D. Kassab-Chahmi, X. Rebillard, and N. Houédé, *Radium-223 dichloride for prostate cancer treatment,* Drug Design, Development and Therapy **11**, 2643 (2017).

[8] R. Eychenne, M. Chérel, F. Haddad, F. Guérard, and J.-F. Gestin, *Overview of the most promising radionuclides for targeted alpha therapy: The "hopeful eight",* Pharmaceutics **13**, 906 (2021).

[9] C. Decristoforo, O. Neels, and M. Patt, *Emerging radionuclides in a regulatory framework for medicinal products–how do they fit?* Frontiers in Medicine **8**, 678452 (2021).

[10] S. M. Qaim and I. Spahn, *Development of novel radionuclides for medical applications,* Journal of Labelled Compounds and Radiopharmaceuticals **61**, 126 (2018).

[11] D. R. McAlister and E. P. Horwitz, *Automated two column generator systems for medical radionuclides,* Applied Radiation and Isotopes **67**, 1985 (2009).

[12] M. A. Synowiecki, L. R. Perk, and J. F. W. Nijsen, *Production of novel diagnostic radionuclides in small medical cyclotrons,* EJNMMI radiopharmacy and chemistry **3**, 1 (2018).

[13] P. Martini, A. Adamo, N. Syna, A. Boschi, L. Uccelli, N. Weeranoppanant, J. Markham, and G. Pascali, *Perspectives on the use of liquid extraction for radioisotope purification,* Molecules **24**, 334 (2019).

[14] T. Mastren, V. Radchenko, A. Owens, R. Copping, R. Boll, J. R. Griswold, S. Mirzadeh, L. E. Wyant, M. Brugh, J. W. Engle, *et al.*, *Simultaneous separation of actinium and radium isotopes from a proton irradiated thorium matrix,* Scientific Reports **7**, 8216 (2017).

[15] V. Radchenko, J. W. Engle, J. J. Wilson, J. R. Maassen, F. M. Nortier, W. A. Taylor, E. R. Birnbaum, L. A. Hudston, K. D. John, and M. E. Fassbender, *Application of ion exchange and extraction chromatography to the separation of actinium from proton-irradiated thorium metal for analytical purposes,* Journal of Chromatography A **1380**, 55 (2015).

[16] A. Kotovskii, N. Nerozin, I. Prokof'ev, V. Shapovalov, Y. A. Yakovshchits, A. Bolonkin, and A. Dunin, *Isolation of actinium-225 for medical purposes,* Radiochemistry **57**, 285 (2015).

[17] C. Rébufa, A. Traboulsi, V. Labed, N. Dupuy, and M. Sergent, *Experimental design approach for identification of the factors influencing the γ-radiolysis of ion exchange resins,* Radiation Physics and Chemistry **106**, 223 (2015).

[18] P. Wang, J. Zu, A. Khayambashi, R. Liu, and Y. Wei, *Gamma radiolysis of anion exchange resins based on 4-vinylpyridine in aqueous solution,* Journal of Radioanalytical and Nuclear Chemistry **311**, 1619–1625 (2017).

[19] M. Aguilar and J. L. Cortina, *Solvent extraction and liquid membranes: Fundamentals and applications in new materials* (CRC Press, 2008).

[20] H. Itabashi and T. Nakahara, *Chelation solvent extraction for separation of metal ions,* Comprehensive Analytical Chemistry **41**, 459 (2003).

[21] M. F. Alam, Z. A. Begum, Y. Furusho, H. Hasegawa, and I. M. Rahman, *Selective separation of radionuclides from environmental matrices using proprietary solid-phase extraction systems: A review,* Microchemical Journal **181**, 107637 (2022).

[22] N. Kabay, J. L. Cortina, A. Trochimczuk, and M. Streat, *Solvent-impregnated resins (SIRs)– Methods of preparation and their applications,* Reactive and Functional Polymers **70**, 484 (2010).

[23] A. M. Tamang, N. Singh, S. K. Chandraker, and M. K. Ghosh, *Solvent impregnated resin a potential alternative material for separation dyes, metal and phenolic compounds: A review,* Current Research in Green and Sustainable Chemistry **5**, 100232 (2021).

[24] J. N. Lee, C. Park, and G. M. Whitesides, *Solvent compatibility of poly (dimethylsiloxane)-based microfluidic devices,* Analytical Chemistry **75**, 6544 (2003).

[25] C. Rumens, M. Ziai, K. Belsey, J. Batchelor, and S. Holder, *Swelling of PDMS networks in solvent vapours; applications for passive RFID wireless sensors,* Journal of Materials Chemistry C **3**, 10091 (2015).

[26] A. Trochimczuk, N. Kabay, M. Arda, and M. Streat, *Stabilization of solvent impregnated resins (sirs) by coating with water soluble polymers and chemical crosslinking,* Reactive and Functional Polymers **59**, 1 (2004).

[27] S. Trapp, T. Lammers, E. Paulssen, and R. M. de Kruijff, *Rapid, automated radionuclide separation with high yield - towards microfluidic solvent extraction for ^{61,64,67}cu production,* European Research Reactor Conference (Antwerp) , 177 (2023).

[28] R. Chakravarty, N. Sen, S. Patra, A. Rajeswari, P. Shetty, K. K. Singh, and S. Chakraborty, *Microfluidic solvent extraction of no-carrier-added 64cu from irradiated zn target for radiopharmaceutical preparation,* Chemical Engineering Journal Advances **13**, 100433 (2023).

[29] S. Trapp, T. Lammers, G. Engudar, C. Hoehr, A. G. Denkova, E. Paulssen, and R. M. de Kruijff, *Membrane-based microfluidic solvent extraction of ga-68 from aqueous zn solutions: towards an automated cyclotron production loop,* EJNMMI Radiopharmacy and Chemistry **8**, 9 (2023).

[30] E. Oehlke, C. Hoehr, X. Hou, V. Hanemaayer, S. Zeisler, M. J. Adam, T. J. Ruth, A. Celler, K. Buckley, F. Benard, and P. Schaffer, *Production of Y-86 and other radiometals for research purposes using a solution target system,* Nuclear Medicine and Biology **42**, 842 (2015).

[31] R. Chakravarty, S. Patra, K. Jagadeesan, S. Thakare, and S. Chakraborty, *Electrochemical separation of 132/135-La theranostic pair from proton irradiated Ba target,* Separation and Purification Technology **280**, 119908 (2022).

[32] C. Kratochwil, F. Bruchertseifer, F. L. Giesel, M. Weis, F. A. Verburg, F. Mottaghy, K. Kopka, C. Apostolidis, U. Haberkorn, and A. Morgenstern, *^{225}Ac-PSMA-617 for PSMA-targeted alpha-radiation therapy of metastatic castration-resistant prostate cancer,* Journal of Nuclear Medicine **57**, 1941 (2016).

[33] J. W. Engle, *The production of Ac-225,* Current Radiopharmaceuticals **11**, 173 (2018).

[34] U. Priyadarshini and S. Tandon, *Spectrophotometric determination of vanadium (v) with n-benzoyl-n-phenylhydroxylamine,* Analytical Chemistry **33**, 435 (1961).

[35] R. J. Aguado, A. Mazega, N. Fiol, Q. Tarrés, P. Mutjé, and M. Delgado-Aguilar, *Durable nanocellulose-stabilized emulsions of dithizone/chloroform in water for Hg^{2+} detection: A novel approach for a classical problem,* ACS Applied Materials & Interfaces **15**, 12580 (2023).

[36] K. K. Singh, S. K. Pathak, M. Kumar, A. Mahtele, S. Tripathi, and P. N. Bajaj, *Study of uranium sorption using D2EHPA-impregnated polymeric beads,* Journal of Applied Polymer Science **130**, 3355 (2013).

[37] M. D. Abràmoff, P. J. Magalhães, and S. J. Ram, *Image processing with ImageJ,* Biophotonics International **11**, 36 (2004).

[38] T. Church, *Problems associated with the use of the ratio of Martin's diameter to Feret's diameter as a profile shape factor,* Powder Technology **2**, 27 (1968).

[39] J. P. Lewicki, J. J. Liggat, and M. Patel, *The thermal degradation behaviour of polydimethylsiloxane/montmorillonite nanocomposites,* Polymer Degradation and Stability **94**, 1548 (2009).

[40] R. A. Meyer, J. F. Hazel, and W. M. McNabb, *Thermal analysis of some metal n-benzoyl-n-phenylhydroxylamine chelates,* Analytica Chimica Acta **31**, 419 (1964).

[41] C. F. Croft, M. I. G. Almeida, and S. D. Kolev, *Characterisation of micro polymer inclusion beads by thermogravimetric analysis,* Polymer **283**, 126203 (2023).

[42] N. H. Aprilita, M. Luqman, and A. Suratman, *Removal of cobalt (II) by dithizone-immobilized nickel slag,* Results in Chemistry **5**, 100698 (2023).

[43] J. Cai, D. Xu, Z. Dong, X. Yu, Y. Yang, S. W. Banks, and A. V. Bridgwater, *Processing thermogravimetric analysis data for isoconversional kinetic analysis of lignocellulosic biomass pyrolysis: Case study of corn stalk,* Renewable and Sustainable Energy Reviews **82**, 2705 (2018).

[44] A. Santoso, A. Damen, J. R. van Ommen, and V. van Steijn, *Atmospheric pressure atomic layer deposition to increase organic solvent resistance of pdms,* Chemical Communications **58**, 10805 (2022).

[45] Y. Zhang, Z. Chen, Y. Shi, Q. Ma, H. Mao, Y. Li, H. Wang, and Y. Zhang, *Revealing the sorption mechanisms of carbamazepine on pristine and aged microplastics with extended DLVO theory,* Science of the Total Environment **874**, 162480 (2023).

[46] S.-L. Badea, S. Lundstedt, P. Liljelind, and M. Tysklind, *The influence of soil composition on the leachability of selected hydrophobic organic compounds (HOCs) from soils using a batch leaching test,* Journal of Hazardous Materials **254**, 26 (2013).

[47] Y. Suo and Y. Ren, *Research on the mechanism of nanofiltration membrane fouling in zero discharge process of high salty wastewater from coal chemical industry,* Chemical Engineering Science **245**, 116810 (2021).

[48] J. N. Israelachvili, *Surface forces,* in *The Handbook of Surface Imaging and Visualization* (CRC Press, 2022) pp. 793–816.

[49] N. A. Mishchuk, *The model of hydrophobic attraction in the framework of classical DLVO forces,* Advances in Colloid and Interface Science **168**, 149 (2011).

[50] X. Liu, J. Xu, Y. Zhao, H. Shi, and C.-H. Huang, *Hydrophobic sorption behaviors of 17β-estradiol on environmental microplastics,* Chemosphere **226**, 726 (2019).

[51] O. Artiushenko, E. P. Avila, M. Nazarkovsky, and V. Zaitsev, *Reusable hydroxamate immobilized silica adsorbent for dispersive solid phase extraction and separation of rare earth metal ions,* Separation and Purification Technology **231**, 115934 (2020).

[52] P. Sharma and K. H. Rao, *Adhesion of paenibacillus polymyxa on chalcopyrite and pyrite: surface thermodynamics and extended DLVO theory,* Colloids and Surfaces B: Biointerfaces **29**, 21 (2003).

[53] H. H. Coenen, A. D. Gee, M. Adam, G. Antoni, C. S. Cutler, Y. Fujibayashi, J. M. Jeong, R. H. Mach, T. L. Mindt, V. W. Pike, and A. D. Windhorst, *Consensus nomenclature rules for radiopharmaceutical chemistry — setting the record straight,* Nuclear Medicine and Biology **55**, v (2017).

[54] C. F. Ramogida, A. K. Robertson, U. Jermilova, C. Zhang, H. Yang, P. Kunz, J. Lassen, I. Bratanovic, V. Brown, L. Southcott, C. Rodríguez-Rodríguez, V. Radchenko, F. Bénard, C. Orvig, and P. Schaffer, *Evaluation of polydentate picolinic acid chelating ligands and an α-melanocyte-stimulating hormone derivative for targeted alpha therapy using ISOL-produced ^{225}Ac,* EJNMMI Radiopharmacy and Chemistry **4** (2019), 10.1186/s41181-019-0072-5.

[55] M. Mudasir, R. A. Baskara, A. Suratman, K. S. Yunita, R. Perdana, and W. Puspitasari, *Simultaneous adsorption of Zn (II) and Hg (II) ions on selective adsorbent of dithizone-immobilized bentonite in the presence of Mg (II) ion,* Journal of Environmental Chemical Engineering **8**, 104002 (2020).

[56] H. B. Soltane, D. Roizard, and E. Favre, *Effect of pressure on the swelling and fluxes of dense PDMS membranes in nanofiltration: An experimental study,* Journal of Membrane Science **435**, 110 (2013).

[57] S. Batra, A. Awasthi, M. Iqbal, and D. Datta, *Solvent impregnated resins for the treatment of aqueous solutions containing different compounds: a review,* Reviews in Chemical Engineering **38**, 209 (2022).

[58] Y. H. Choi, K. H. Chung, H. B. Hong, and W. S. Lee, *Production of PDMS microparticles by emulsification of two phases and their potential biological application,* International Journal of Polymeric Materials and Polymeric Biomaterials **67**, 686 (2018).

[59] O. Dufaud, E. Favre, and V. Sadtler, *Porous elastomeric beads from crosslinked emulsions,* Journal of Applied Polymer Science **83**, 967 (2002).

[60] G. Zhang, D. Chen, W. Zhao, H. Zhao, L. Wang, W. Wang, and T. Qi, *A novel D2EHPA-based synergistic extraction system for the recovery of chromium(III),* Chemical Engineering Journal **302**, 233 (2016).

[61] B. Saha, K. Venkatesan, R. Natarajan, M. Antony, and P. Vasudeva Rao, *Studies on the extraction of uranium by n-octanoyl-n-phenylhydroxamic acid,* Radiochimica Acta **90**, 455 (2002).

[62] X. Guo, B. Hurley, F. Yang, and R. Buchheit, *A novel organic conversion coating based on n-benzoyl-n-phenylhydroxylamine chemistry for the corrosion protection of AA2024-T3,* Electrochimica Acta **246**, 197 (2017).

[63] H. Tavallali, G. Deilamy-Rad, A. Parhami, and S. Kiyani, *Dithizone as novel and efficient chromogenic probe for cyanide detection in aqueous media through nucleophilic addition into diazenylthione moiety,* Spectrochimica Acta Part A: Molecular and Biomolecular Spectroscopy **121**, 139 (2014).

[64] C. J. Van Oss, *Interfacial forces in aqueous media* (CRC press, 2006).

[65] A. M. Smith, M. Borkovec, and G. Trefalt, *Forces between solid surfaces in aqueous electrolyte solutions,* Advances in Colloid and Interface Science **275**, 102078 (2020).

[66] B. Mustin and B. Stoeber, *Single layer deposition of polystyrene particles onto planar polydimethylsiloxane substrates,* Langmuir **32**, 88 (2016).

[67] M. J. Bower, T. L. Bank, R. F. Giese, and C. J. van Oss, *Nanoscale forces of interaction between glass in aqueous and non-aqueous media: A theoretical and empirical study,* Colloids and Surfaces A: Physicochemical and Engineering Aspects **362**, 90 (2010).

[68] K. Fazle Rabbi, J. Y. Ho, X. Yan, J. Ma, M. J. Hoque, S. Sett, and N. Miljkovic, *Polydimethylsiloxane-silane synergy enables dropwise condensation of low surface tension liquids,* Advanced Functional Materials **32**, 2112837 (2022).

[69] S. Vlassov, S. Oras, M. Antsov, I. Sosnin, B. Polyakov, A. Shutka, M. Y. Krauchanka, and L. M. Dorogin, *Adhesion and mechanical properties of PDMS-based materials probed with AFM: A review,* Reviews on Advanced Materials Science **56**, 62 (2018).

[70] S. H. Donaldson Jr, J. P. Jahnke, R. J. Messinger, Å. Ostlund, D. Uhrig, J. N. Israelachvili, and B. F. Chmelka, *Correlated diffusivities, solubilities, and hydrophobic interactions in ternary polydimethylsiloxane–water–tetrahydrofuran mixtures,* Macromolecules **49**, 6910 (2016).

[71] S. H. Donaldson Jr, A. Røyne, K. Kristiansen, M. V. Rapp, S. Das, M. A. Gebbie, D. W. Lee, P. Stock, M. Valtiner, and J. Israelachvili, *Developing a general interaction potential for hydrophobic and hydrophilic interactions,* Langmuir **31**, 2051 (2015).

[72] J. Chen, Q. Peng, X. Peng, H. Zhang, and H. Zeng, *Probing and manipulating noncovalent interactions in functional polymeric systems,* Chemical Reviews **122**, 14594 (2022).

[73] B. W. Ninham, *On progress in forces since the DLVO theory,* Advances in Colloid and Interface Science **83**, 1 (1999).

[74] Y. Fu, F. Hu, H. Li, L. Cui, G. Qian, D. Zhang, and Y. Xu, *Application and mechanisms of microalgae harvesting by magnetic nanoparticles (MNPs),* Separation and Purification Technology **265**, 118519 (2021).

[75] J. Xu, L. Wang, and H. Sun, *Adsorption of neutral organic compounds on polar and nonpolar microplastics: Prediction and insight into mechanisms based on pp-LFERs,* Journal of Hazardous Materials **408**, 124857 (2021).

[76] M. C. Bridoux, H. Malandain, F. Leprince, F. Progent, and X. Machuron-Mandard, *Quantitative analysis of phosphoric acid esters in aqueous samples by isotope dilution stir-bar sorptive extraction combined with direct analysis in real time (DART)-Orbitrap mass spectrometry,* Analytica Chimica Acta **869**, 1 (2015).

[77] H. Akaiwa and H. Kawamoto, *The partition of dithizone between carbon tetrachloride and aqueous sulphuric acid,* Journal of Inorganic and Nuclear Chemistry **29**, 541 (1967).

[78] I. P. Alimarin, F. P. Sudakov, and B. Golovkin, *Use of n-benzoyl-n-phenylhydroxylamine in analytical chemistry,* Russian Chemical Reviews **31**, 466 (1962).

[79] E. Monazam, R. Siriwardane, D. Miller, and D. McIntyre, *Rate analysis of sorption of Ce^{3+}, Sm^{3+}, and Yb^{3+} ions from aqueous solution using Dowex 50W-X8 as a sorbent in a continuous flow reactor,* Journal of Rare Earths **36**, 648 (2018).

[80] M. A. Momen and M. L. Dietz, *High-capacity extraction chromatographic materials based on polysulfone microcapsules for the separation and preconcentration of lanthanides from aqueous solution,* Talanta **197**, 612 (2019).

[81] A. M. S. El-Din, H. E. Rizk, E. H. Borai, and E. S. M. E. Afifi, *Selective separation and purification of cerium (iii) from concentrate liquor associated with monazite processing by cationic exchange resin as adsorbent,* Chemical Papers **77**, 2525 (2023).

[82] W. Liu, Y. Zhang, S. Wang, L. Bai, Y. Deng, and J. Tao, *Effect of pore size distribution and amination on adsorption capacities of polymeric adsorbents.* Molecules **26**, 5267 (2021).

[83] D. Chapman, *Electronegativity and the stability of metal complexes,* Nature **174**, 887–888 (1954).

[84] A. Mishustin, *Estimate of the stability constants of trivalent actinide and lanthanide complexes with o-donor ligands in aqueous solutions.* Russian Journal of Inorganic Chemistry **55**, 746–752 (2010).

[85] J. Fitzsimmons, B. Foley, B. Torre, M. Wilken, C. S. Cutler, L. Mausner, and D. Medvedev, *Optimization of cation exchange for the separation of actinium-225 from radioactive thorium, radium-223 and other metals,* Molecules **24**, 1921 (2019).

[86] S. Davern, D. O'Neil, H. Hallikainen, K. O'Neil, S. Allman, L. Millet, S. Retterer, M. Doktycz, R. Standaert, R. Boll, S. V. Cleve, D. DePaoli, and S. Mirzadeh, *Microfluidics-based separation of actinium-225 from radium-225 for medical applications,* Separation Science and Technology **54**, 1994 (2019).

[87] A. K. H. Robertson, C. F. Ramogida, P. Schaffer, and V. Radchenko, *Development of Ac-225 radiopharmaceuticals: Triumf perspectives and experiences,* Current Radiopharmaceuticals **11**, 156 (2018).

[88] B. Zielinska, C. Apostolidis, F. Bruchertseifer, and A. Morgenstern, *An improved method for the production of Ac-225/Bi-213 from Th-229 for targeted alpha therapy,* Solvent Extraction and Ion Exchange **25**, 339 (2007).

[89] M. T. Friend, T. G. Parker, T. Mastren, V. Mocko, M. Brugh, E. R. Birnbaum, and M. E. Fassbender, *Extraction chromatography of ^{225}Ac and lanthanides on n, n-dioctyldiglycolamic acid/1-butyl-3-methylimidazolium bis (trifluoromethylsulfonyl) imide solvent impregnated resin,* Journal of Chromatography A **1624**, 461219 (2020).

[90] A. Baidak and J. A. LaVerne, *Radiation-induced decomposition of anion exchange resins,* Journal of Nuclear Materials **407**, 211 (2010).

[91] C. Venkateswara Rao, A. Rout, S. Mishra, and K. Venkatesan, *Thermophysical properties of neat and radiolytically degraded acidic extractants present in room temperature ionic liquid,* Journal of Radioanalytical and Nuclear Chemistry **321**, 907–916 (2019).

[92] I. Pucić, I. Cetina, and A. Šantić, *Component compatibility influences radiation stability of low temperature cured gels based on PDMS,* Radiation Physics and Chemistry **185**, 109493 (2021).

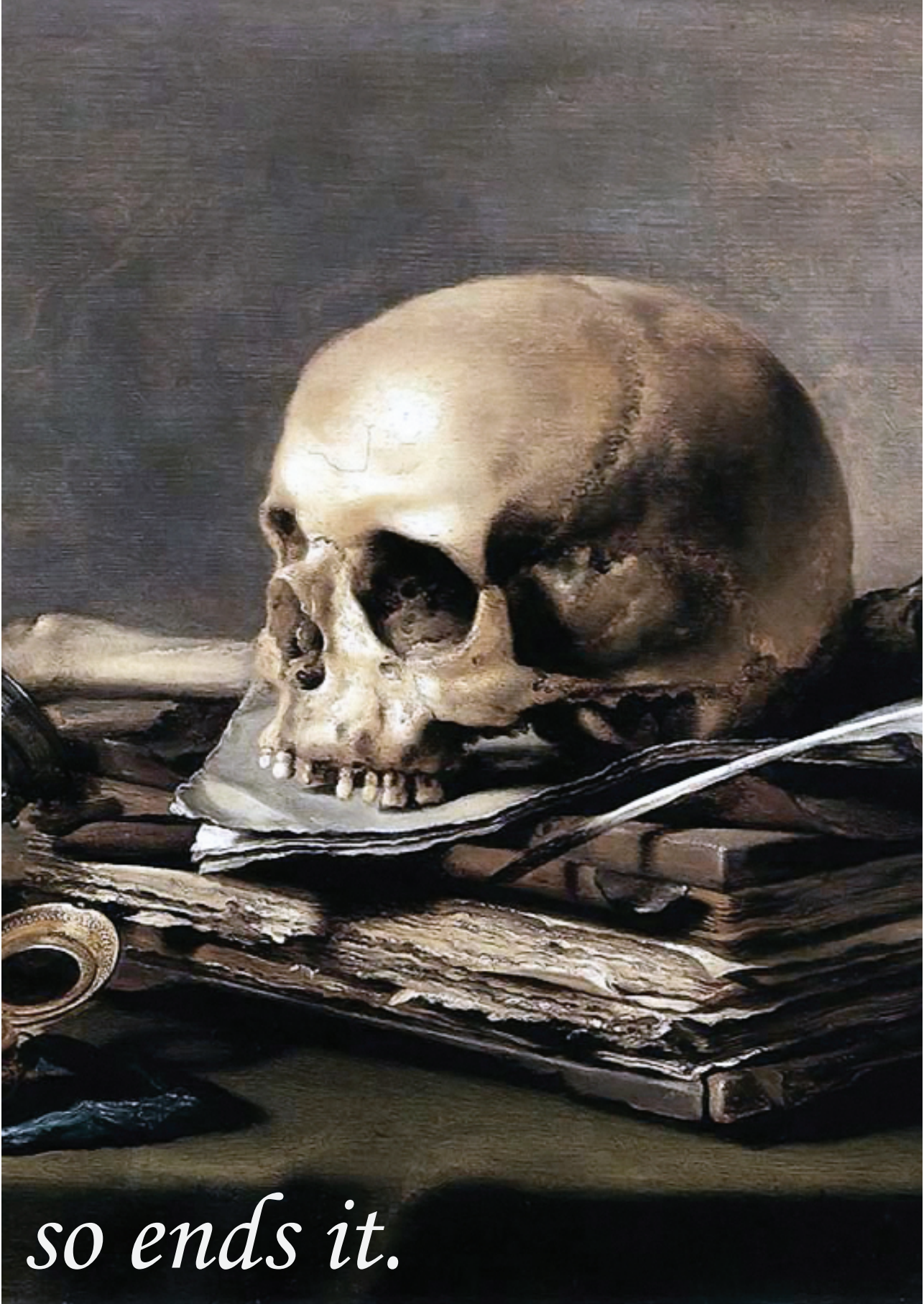
so ends it.

Vanitas still life
Pieter Claesz, 1630

7

Conclusion and outlook

In this chapter, there are four sections. Section 7.1 and Section 7.2 summarize the findings from the thesis and their corresponding outlook while Section 7.3 and Section 7.4 explore two relevant side-projects.

Section 7.1 discusses the findings with regard to the role of atomic layer deposition (ALD) in modifying polymeric substrates (Chapter 2, Chapter 3 and Chapter 4) and their potential applications. Section 7.2 discusses the findings concerning medical radionuclide separation (Chapter 5 and Chapter 6) and a perspective regarding their outlook. Section 7.3 discusses a new study exploring the use of ALD in increasing polymeric material tolerance against radiation damage, a topic relevant to the potential use of polymeric microfluidic devices in medical radionuclide processing. Section 7.4 discusses another new study using an ALD-treated microfluidic chip as a continuous biosensor device, an example of valorisation from the developed concept in this dissertation.

7.1. Atomic layer deposition on polymeric substrates

One of the main objectives of this thesis is to modify the surface of polymer to obtain certain surface properties (e.g. resistance against organic solvents). In this thesis, metal oxide nano-layers are deposited on polymeric substrates, mainly polydimethylsiloxane (PDMS) using atomic layer deposition. During the deposition, both surface and subsurface growth can take place, resulting in different forms of deposited nano-layers. The morphology and the chemical compositions of the deposited layers depend on the type of ALD reactants, the operating pressure and temperature, and the number of ALD cycles. While commercial ALD reactants such as silicon tetrachloride and tetrakis(dimethyl amido) titanium can become metal precursors during the deposition, the role of ozone, plasma or other highly energetic co-reactants is found to be of importance in becoming the oxygen precursor. The energetic co-reactant helps to increase the reactivity of the PDMS surface, favoring surface deposition, especially during the first few cycles. Similarly, exposing PDMS samples to plasma chambers before deposition also helps make the surface more reactive. Subsequently, surface deposition can also take place.

Secondly, the operating temperature and pressure are important. When exposed to high temperatures (e.g. 120°C), the flexible PDMS expands. It then contracts when being taken out of the reactor, leading to the formation of cracks due to a difference in the thermal expansion coefficient of the deposited nano-layer and the PDMS. Therefore, ALD on PDMS should be done at lower temperatures (e.g. <100°C). A low temperature might result in condensation of precursors and slower surface reaction, leading to the presence of chemical vapor deposition (CVD) during the deposition process. Furthermore, in this dissertation, the resulting surface morphology due to the conventional vacuum ALD and the atmospheric pressure ALD (AP-ALD) is compared. As discussed in Chapter 2 and Chapter 3, AP-ALD leads to simultaneous surface and subsurface layer growth. The extent of the layer growth, though, is determined by the number of the ALD cycles. This gives a high degree of control in tuning the layer morphology and their subsequent properties.

The deposited metal oxide nano-layers offer interesting surface properties while remaining transparent and flexible. The introduced surface properties help overcome the disadvantages of PDMS substrates such as low organic solvent resistance and the absence of functional groups. When exposed to common organic solvents, PDMS swells and becomes rendered useless. As nano-layers are deposited on the surface of the PDMS, the layers become a diffusion barrier, reducing the direct exposure of PDMS towards the organic solvents. Consequently, the PDMS stays intact and can be used without being swollen, as described in Chapter 2 (see Figure 7.1). Furthermore, the deposited nano-layers also have several surface groups (e.g. hydroxyl) that are ready to be functionalized further with other groups. This allows PDMS to be functionalized, as discussed in Chapter 3. Uniquely, the use of AP-ALD in the deposition results in more durable, robust nano-layers, a characteristic desirable in commercial practice. The obtained robust nano-layers can be extended to other applications, such as the development of high-performance nano-coatings, polymeric optical films, dielectric films, packaging films, and separation membranes [1–3].

This dissertation goes further in developing a novel ALD method inside PDMS mi-

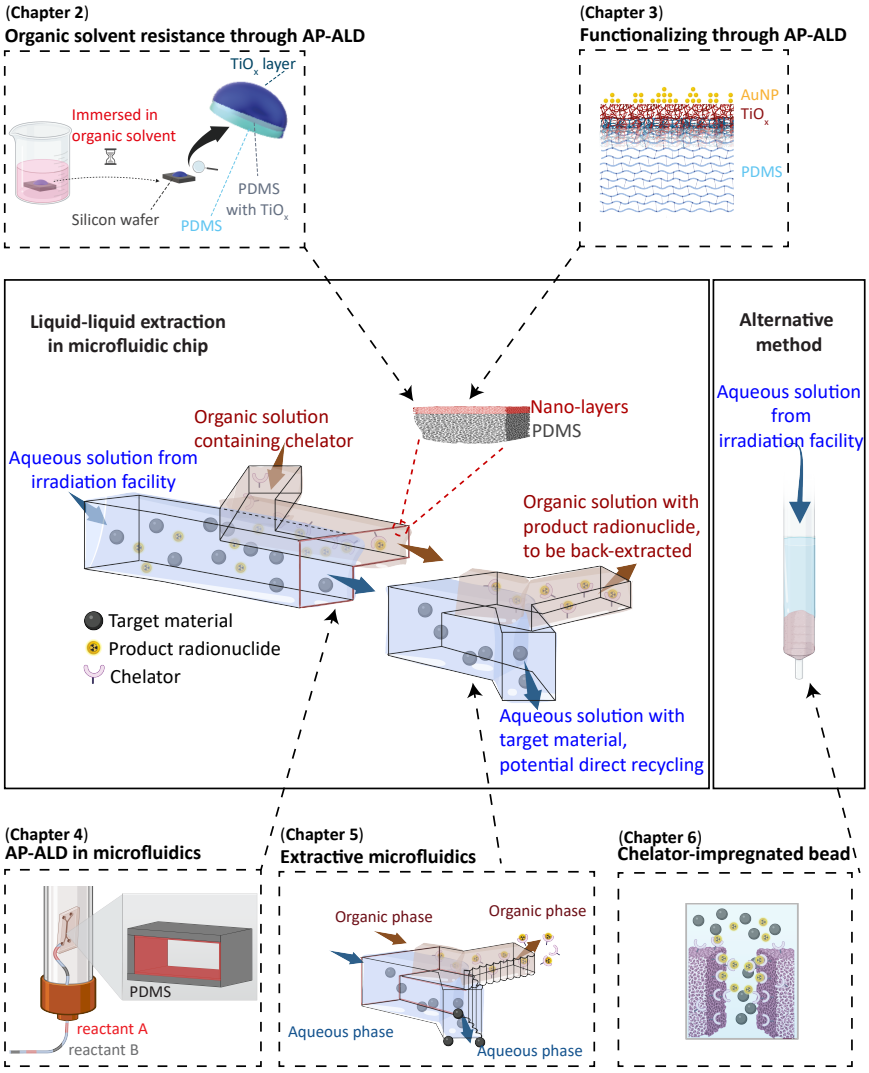

Figure 7.1: Illustration of the topics described in the chapters of this thesis and their relation.

crofluidic channels. Making use of the convective flow, the ALD reactants are brought into the channels, leading to high coverage coating throughout the channels within a reasonable processing time, even in networks of microchannels. The treated PDMS channels retain the advantageous PDMS bulk properties while obtaining interesting surface properties. This proof-of-concept is demonstrated through three case studies in Chapter 4, where otherwise non-existent surface properties such as the discussed organic solvent resistance and functionality can be present. Hence, this AP-ALD widens the use of PDMS microfluidics in many fields, including but not limited to cell biology

and precision chemistry.

While this dissertation focuses on silicon oxide and titanium oxide nano-layers in a PDMS microfluidic channel, the developed methods can easily be expanded to other types of nano-layers and other systems with confined geometry. For example, depositing copper, platinum, and palladium using ALD in a microfluidic channel may be of interest to elucidate the transport and kinetic parameters in the rising carbon dioxide management technologies [4, 5]. Gold, titanium-based and silver nanoparticles can also be deposited inside the microfluidic channels to study light-based kinetic parameters in photocatalysis, or to evaluate biological responses [6–10]. The insight can also be adapted for fine-tuning nano-layer deposition in microelectromechanical systems (MEMS) and semiconductor developments [11]. In conclusion, combining nano-layer deposition with microfluidics enables studies and applications, that are promising to advance cutting-edge technologies.

7.2. Separation of medical radionuclides

One of the main objectives of this dissertation is to separate product radionuclides from their target material for medical applications. To reach the objective, this dissertation draws inspiration from the literature [12, 13] and designs microfluidic chips with a height difference, where two fluids are guided and then in contact with each other to allow the extraction to take place (see Figure 7.1). As expected, a stable laminar parallel flow and perfect phase disengagement with minimum leakage is obtained over a considerably wide range of flow rate combinations. Unique to this dissertation, the PDMS chips are first coated with silicon oxide nano-layers using AP-ALD. As a result, the chips can be tested using relevant solvents used in the extraction of medical radionuclides (HCl, HNO_3, and chloroform). Without the presence of the nano-layers, the PDMS chips swell due to the employed solvents. Using these AP-ALD-treated PDMS chips, efficient chelation-based extraction of several elements including beta-emitter Y-90 and alpha-emitter Ac-225 is demonstrated in a relatively short time and simple manner. These two advantages address the concern in the field of medical radionuclide production since the half-life of the nuclides is rather short and there is great interest in having less personnel involvement. This microfluidic extraction also opens the possibility of producing medical radionuclides with less amount of radioactive waste, fewer post-processing steps, and direct recycling of the valuable target material. Hence, the developed chips are promising, especially in the context of on-demand productions in hospitals where short and simple separations are needed.

To adopt the developed microfluidic chips in the clinical setting, there are two points to consider: the ease of use and the type of radionuclides to be separated. While in this dissertation, a microfluidic chip with stable laminar flow and perfect disengagement has been fabricated, the presence of knowledgeable experts is needed to operate the chips. Several factors such as introducing the fluids inside the chips (priming), connecting the chips with the auxiliaries (e.g. pumps), and constant monitoring are important to ensure outgoing fluids with no phase contaminations. Disturbances such as changing flow rates abruptly, accidental mishandling of the systems, or even banging the doors might create small, momentary disturbances of the flow resulting in possible toxic chloroform con-

tamination in the final aqueous phase. While some of the concerns can be addressed by providing manuals, training the operators, and adding a chloroform-evaporation step after the extraction, a foolproof, plug-and-play, and reliable microfluidic module is important. Several researchers have been looking into developing a plug-and-play microfluidic module [14–16]. In the context of medical radionuclide extraction, an integrated forward and backward extraction channel can be of interest. This module can also be connected to post-processing steps, including radiolabelling [17]. Depending on the capacity demand, numbering-up could also be included in this "factory-on-a-chip" [18]. By having a plug-and-play module, the integrated separation platform can be placed inside an isolated "hot cell", where the exposure risks towards personnel are lowered while efficient radiopharmaceutical production with cost-effective use of target materials is possible.

The second consideration point is the type of radionuclides to be separated and their relevant chelation chemistry. In this dissertation, four model radionuclide systems were tested, namely extracting Sc-46 from Ca-45, Y-90 from Sr-85, La-140 from Ba-139, and Ac-225 from Ra-223 using D2EHPA as discussed in Chapter 5. While the microfluidic forward extraction of all four product radionuclides from their respective target can be done in seconds, Sc-46 is found to be difficult to be back-extracted, reducing the applicability. Attempts have also been made to extract Ga-68 from other possibly present nuclides (Ge-68, Zn-68) using BPHA as the chelators. However, both the forward and backward extractions of Ga-68 in the tested system require a considerably long contact time, making it impractical given the half-life of Ga-68 is only 68 minutes. Furthermore, the chelator, BPHA, can precipitate, leading to clogging and pressure imbalances inside the microfluidic chips. The BPHA is also slightly miscible in the aqueous phase, resulting in a plausible chelator contamination that exceeds the legal limit. Moreover, the model extraction systems discussed in Chapter 5 are ideal models, with controlled concentrations of contaminants (e.g. aluminum) and relatively low radioactivity. Whether the developed extraction systems can withstand commercial radionuclide production and whether chelators are stable against radiation damage remain a question. Thus proper selection of the extraction system and tailoring the microfluidic chips to the system are also of importance.

Among many factors to consider in selecting the right extraction system, the first factor is that the product radionuclides themselves are interesting. This means that the radionuclides either have been approved and should be more available, can become a theranostic pair (therapy and diagnostic), or have the potential for certain therapy/imaging. Some radionuclides have already been (or are ongoing to be) approved by the authority for their radiopharmaceutical purposes, including but not limited to F-18, Ga-68, Y-90, Lu-177, Ra-223, and Ac-225 [19–23]. The separation of these radionuclides from their respective target materials or contaminants is definitely of interest for future study. However, not all the production routes of these radionuclides are suitable for microfluidic extraction, and therefore have to also be carefully screened. Other radionuclides such as Cu-64 and Zr-89 have also seen the most growth in basic, translational and clinical tests [19]. Copper, for example, also has the potential to become a theranostic pair (Cu-64/Cu-67), along with yttrium (Y-86/Y-90), and iodine (I-124/I-131). On the other hand, several radionuclides have been researched for their specific diagnos-

tic/therapeutic potentials such as Sm-153, Re-188, At-211, Pb-212, Bi-212, and Th-227 [24–26], and some in the combination with nanomaterials [27]. While microfluidic extraction can be loosely adapted to separate many of the mentioned radionuclides, the full benefit of microfluidic extraction can be seen in the radionuclides that require short processing time (e.g. in the order of tens of minutes or hours), contain elements/compounds with distinct solubility factors, and have efficient extraction (chelation) kinetics.

As a side note, the development of this microfluidic platform for radionuclide separation could also be extended to other radionuclide handling or radionuclide-related processing. Several interesting examples include the use of microfluidics as microreactors to accommodate radiochemistry and radiolabelling [17, 28]. Microfluidics can also be used in the processing of spent radioactive waste with extremely long half-life [29, 30]. Other interesting applications include the use of microfluidic chips as a sensor for radioactive analytes [31] and the use of microfluidic chips to study radionuclide interaction with biological systems [32].

Additionally, this dissertation explores an alternative to microfluidic extraction by developing chelator-impregnated PDMS beads. These impregnated beads are fabricated by making use of the swelling phenomenon of PDMS when exposed to organic solvents. On the other hand, the organic solvents are used to dissolve many interesting chelators. By dissolving the chelators first in the organic solvent and exposing this solution to a PDMS substrate, the impregnation process takes place, as discussed in Chapter 6. These chelator-impregnated PDMS beads are used to adsorb the product radionuclides specifically while letting the target materials and contaminants flow out. Consequently, the beads are expected to receive less radioactive doses. Further tests on the beads show that the chelators are physically trapped inside the PDMS matrix and highly stable against leaching. Additionally, this complementary alternative system results in a solution with target material and an eluent containing pure product radionuclides without the involvement of toxic organic solvents. The resulting target material solution can still be suitable to be re-irradiated, allowing direct recycling of the target materials with fewer processing steps. Moreover, there is the possibility of reducing the eluent pH, easing the post-labelling processes. While this dissertation introduces this alternative separation method, it can be further optimized, from the production of the monodisperse beads to the types of impregnated chelators and the adsorption process operation.

7.3. Increasing radiation damage tolerance through metal oxide nano-layers

One challenge in the separation of the medical radionuclides is material degradation due to radiation damage [33–36]. This damage can come from direct interaction (e.g. with neutrons, ions, or electrons [37]) as well as from indirect interaction (e.g. water radiolysis leading to radical formation [38]). As a result, separation platforms have to be replaced frequently, often leading to more radioactive waste and longer downtime [39]. Subsequently, an approach to increase the material tolerance towards radiation damage is an interesting outlook.

Current researches focus on the development of composites [39]. As composites lead

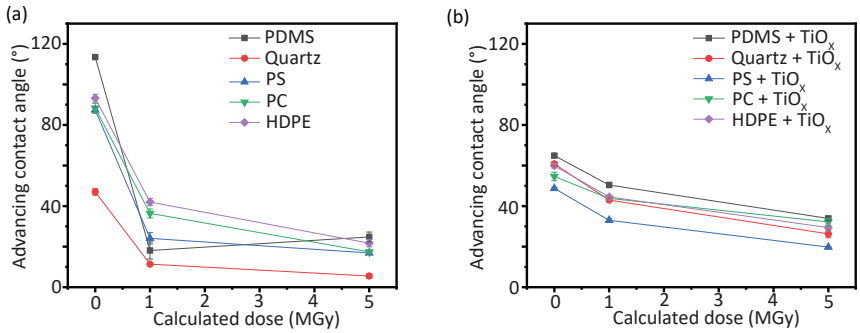

Figure 7.2: Advancing contact angle of several bare (a) and ALD-treated (b) polymeric samples after being exposed to different gamma radiation doses.

to undesirable changes in bulk properties, this dissertation explores the use of metal oxide nano-layers to enhance the material tolerance towards radiation damage without changing much of the convenient bulk properties. A small study was conducted on several microfluidic material candidates such as polydimethylsiloxane (PDMS), quartz, polystyrene (PS), polycarbonate (PC), and high-density polyethylene (HDPE). On these materials (flat substrates), nano-layers of titanium oxide were deposited using vacuum ALD (Veeco Fiji G2). Tetrakis(dimethylamino)titanium and oxygen plasma were used as the ALD reactants, introduced alternatingly under a constant argon flow of 60 sccm at a pulse time of 0.06 seconds and 0.25 seconds respectively, and with a purge of 5 seconds in between for 700 cycles. Both the bare and ALD-treated samples were placed on a table, where a Van der Graaf electron accelerator was used to irradiate the samples with a beam current of 208.5 μA and a voltage of 1 MeV, resulting in an average dose of 48.0 kGy/cm^2 in 80 seconds. During the irradiation, the table temperature was monitored to not exceed 40°C. After receiving an estimated dose of 1 MGy and 5 MGy, the surface energy was approached using advancing contact angle measurement, as described

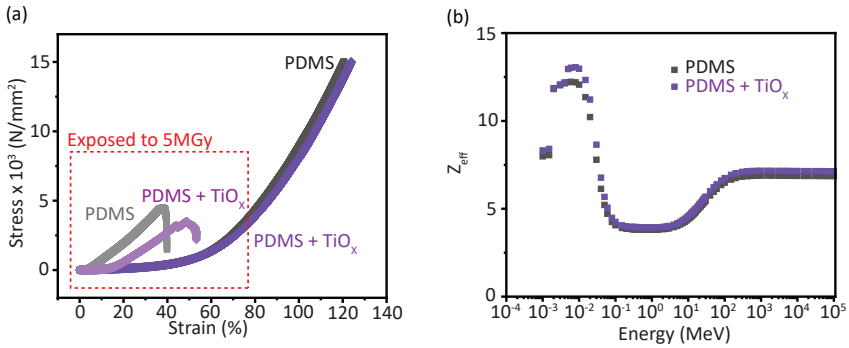

Figure 7.3: (a) Stress versus strain curve of bare and ALD-treated PDMS, unexposed and exposed to 5 MGy. (b) Effective nuclear charge of bare PDMS and ALD-treated PDMS over different exposure energies, estimated using an online software Phy-X/PSD.

in Chapter 3. Figure 7.2 shows the advancing contact angle of the bare and ALD-treated samples. The bare samples show a sharp drop in the advancing contact angle, indicating an increase in hydrophilicity, and subsequently changes in surface energy. On the contrary, the ALD-treated samples also show a decrease in the advancing contact angle, albeit milder. This milder change indicates the potential of titanium oxide nano-layers to increase the radiation damage tolerance of the material's surface.

In this study, the irradiation was performed in a dry environment with electron accelerators. Conducting the experiment in a wet environment to evaluate the radiation damage due to indirect mechanisms and using other irradiation sources (e.g. alpha particles, electron, positron, gamma, or x-rays) are more complex, yet important to obtain a thorough understanding. In this dissertation, an attempt was made to irradiate different microfluidic chip material candidates individually placed in a vial containing 1 M HNO_3 in a chamber (Gammacell 220 Excel). The chamber was equipped with multiple, well-positioned gamma sources (Co-60) with a relatively low dose rate of 0.566 kGy/hour. The result, however, was inconclusive indicating a complex interplay between various factors such as dose rates, ability of some polymeric structures to recover, and many others.

From the irradiation using an electron accelerator, PDMS is found to be among the promising materials. Since material exposure to radiation doses also leads to changes in the material structures, the study then evaluated the mechanical changes. The changes are usually classified into chain scission (ruptures of bonds) and crosslinking (chain branching) [40]. Both bare and ALD-treated PDMS were exposed to 5 MGy using the Van der Graaf electron accelerator and their compression behaviour was tested using a Zwick 20kN compression bench with a speed of 1 mm/second up to 15 kN or until the sample fractured. Figure 7.3(a) shows the stress-strain curve of the samples. As expected, the deposition of titanium oxide nano-layers does not change the compression behaviour of PDMS samples. On the other hand, when exposed to 5 MGy, both bare and ALD-treated PDMS samples fractured, indicating the effect of radiation damages, where crosslinking dominates over chain scission, in line with reported phenomena [41, 42]. However, the bare PDMS samples fractured at an earlier strain (the Young's modulus is calculated to be higher) than ALD-treated PDMS samples, indicating that the bare PDMS samples are slightly stiffer compared with ALD-treated samples and highlighting the potential of nano-layers to increase the radiation damage tolerance.

To understand the role of titanium oxide in increasing the tolerance, several radiation attenuation parameters can be estimated using publicly available models. In this simple study, an online Phy-X/PSD software was used to estimate one of the parameters, the effective nuclear charges (Z_{eff}) of bare PDMS and ALD-treated PDMS from 10^{-4}MeV to 10^{5}MeV [43]. Changes in Z_{eff} indicate different attenuation responses of the materials. Using the PDMS and titanium dioxide molecular formula, Figure 7.3(b) shows small yet distinctive differences between the estimated Z_{eff} of bare PDMS and ALD-treated PDMS, especially at the lower energy range. This difference is apparent, despite the small percentage of titanium oxide (assumed to be 0.5% of total molecular weight). While this dissertation only conducted a simple study using rough estimates, publicly available simulation models such as GEANT4 (based on Monte-Carlo method) [44] or fundamental molecular dynamic models can also be used to predict the suitable nano-layers in increasing tolerance towards specific radiation damage sources.

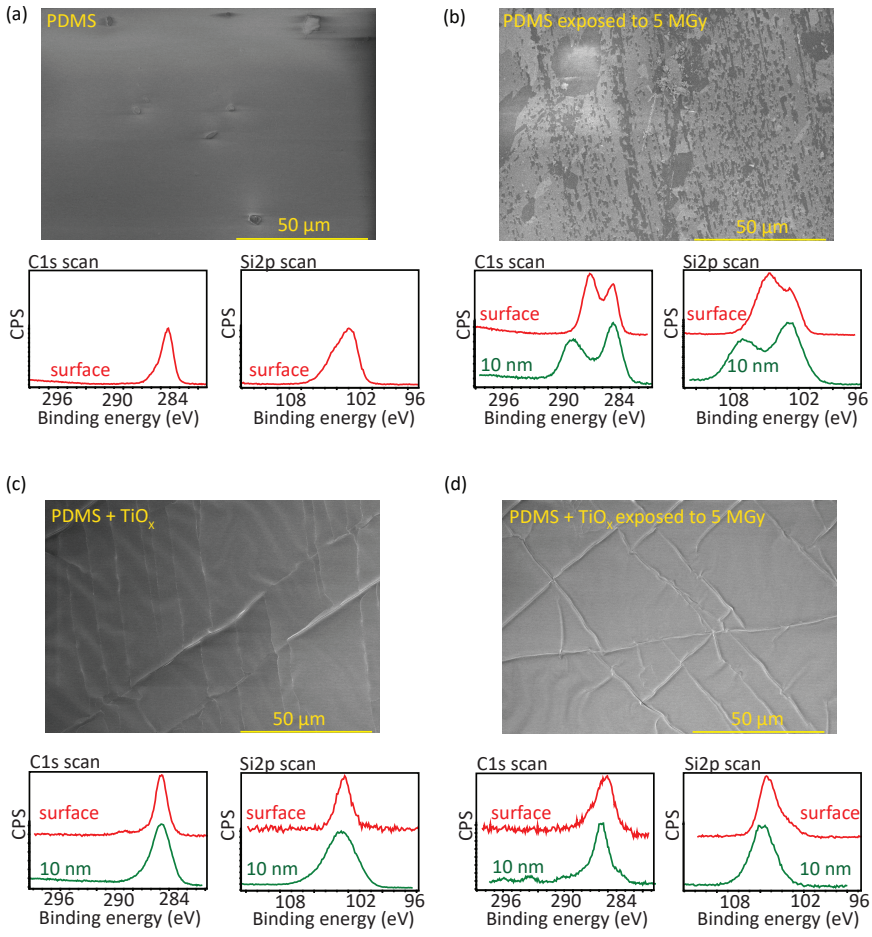

Figure 7.4: FE-SEM figures and the corresponding XPS C1s and Si2p spectra of bare PDMS samples, (a) unexposed and (b) exposed to 5 MGy; and of ALD-treated PDMS samples, (c) unexposed and (d) exposed to 5 MGy. The red lines in the XPS graphs represent the spectra on the surface of the samples, while the green lines represent the reading after etching the samples for ~10 nm.

Lastly, to confirm the importance of titanium oxide nano-layers, both bare and ALD-treated PDMS samples, unexposed and exposed to 5 MGy were visualized using Field Emission Scanning Electron Microscopy (FE-SEM, Hitachi S-4800) at a beam current of 1 μA and an accelerating voltage of 1 KeV. Figure 7.4(a) and 7.4(b) show a stark visual difference between the surface of unexposed bare PDMS and bare PDMS exposed to 5 MGy. On the contrary, the ALD-treated PDMS samples show comparable visuals before and after exposure to 5 MGy. The chemical state of the samples was then evaluated using X-ray photoelectron spectroscopy (XPS, ThermoFisher Scientific Nexsa). The spectra were

charge-corrected with the adventitious carbon peak at 284.8 eV. Figure 7.4(a) and 7.4(c) show C1s scans and Si2p scans for bare PDMS and ALD-treated PDMS samples (with cracks), comparable with previous results (see Chapter 2). To evaluate the effect of the radiation damage, similar XPS scans were conducted on the samples exposed to 5 MGy. Figure 7.4(b) shows C1s and Si2p spectra of the bare PDMS samples after exposure to 5 MGy (see Figure 7.4(b)). Different peak shapes are observed on the spectra, where the C1s scans show double peaks, associated with C=O bonds, typical to radiation-induced crosslinking expected to take place inside PDMS matrix [41, 42]. The Si2p scans also show an extra broad peak at higher binding energy, possibly indicating silicate or other bonds that are not present in unexposed PDMS. On the contrary, while there were shifts, Figure 7.4(d) shows C1s and Si2p scans that are more comparable to the unexposed samples, indicating less radiation-induced chemical changes are observed.

This initial study showcases the potential of metal oxide nano-layers to improve the tolerance towards radiation damage. While the improvement seems not to be suitable for an extreme dose environment (e.g. shielding material for uranium fission reactor), it might be of importance in portioned environments such as disposable microfluidic chips, resin, and phase separation membranes. Further tests using different materials and different nano-layers can be explored, especially nano-layers with promising radiation attenuation parameters such as zirconium-based materials [45]. On the other hand, several ALD processes have been shown to be capable of depositing zirconium-based nano-layers, suggesting a feasible outlook. Furthermore, the addition of other metals or ceramics has been shown also improve the properties of the zirconium-based materials [46], which can easily be achieved using ALD.

We acknowledge the thesis work of Rémy de Jong and the help of Lennart van de Hengel with the van der Graff accelerator (Delft Reactor Institute). We also extend our gratitude to Dave Ruijtenbeek for the use of their mechanical testing facility at Aerospace Engineering (Delft University of Technology) and to Joost Middelkoop for the ALD facility.

7.4. Gold nanoparticle in microfluidic chips for biosensor

In this dissertation, microfluidic chips with nano-layer coating throughout the channels have been developed. One of the most interesting materials to deposit on transparent PDMS substrates is gold nanoparticles (AuNPs). AuNPs have two attractive characteristics: their unique optical plasmonic resonance and their bond with thiol, a group that can easily be introduced to many biomolecules [47, 48]. An initial study was performed by treating PDMS slabs with 100 AP-ALD cycles of titanium oxide layers (TiO_x) and 5 AP-ALD cycles of gold nanoparticles (AuNPs), using the parameters described in Chapter 3. The gold nanoparticles are then functionalized by modified aptamer RD1 dissolved in phosphate-buffered saline (0.67 μM). The aptamer is chosen for its specific affinity against endotoxin [49, 50]. This endotoxin is an indicator of gram-negative bacteria presence, one cause of sepsis and food poisoning [49]. To be able to respond to the endotoxin as well as to be bound to the gold nanoparticles, the aptamers were modified to have an amine group at the 5'-end and a thiol group at the 3'-end[49]. To test the performance, the aptamer-incubated ALD-treated PDMS slabs were exposed to a stock

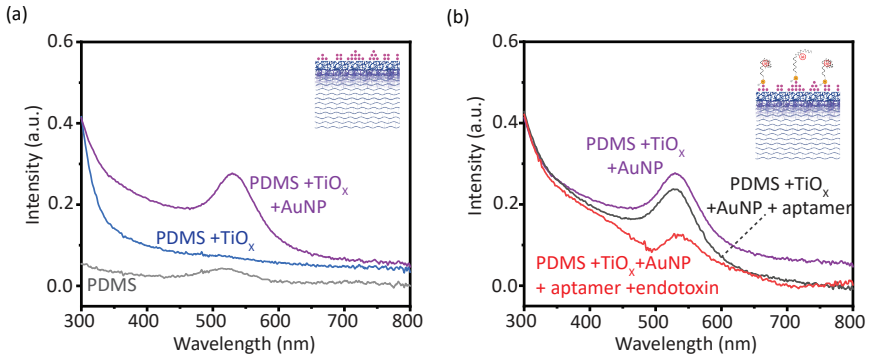

Figure 7.5: (a) UV-Vis spectra of PDMS, PDMS treated with TiO_x, and PDMS treated with TiO_x and AuNPs. and (b) UV-Vis spectra of PDMS treated with TiO_x and AuNPs, along with aptamer-bound samples and endotoxin-measured samples.

solution containing endotoxin (500 ng/ml; LPSs from Escherichia coli O111:B4; L2630, Sigma-Aldrich) prepared according to the protocol from its supplier [49]. The optical responses of the bare PDMS, ALD-treated PDMS, and PDMS samples incubated with aptamer and endotoxin were measured using a UV-visible spectrophotometer (NanoDrop™ 2000/2000c Spectrophotometer, wide scan reading, which wavelength 300 -800 nm).

Figure 7.5(a) shows the UV-vis spectra of bare PDMS, PDMS treated with TiO_x and PDMS treated with both TiO_x nano-layers and AuNPs. As expected, both PDMS and PDMS with TiO_x were considerably transparent. On the other hand, the PDMS samples treated with TiO_x and AuNPs show a peak at 530 nm. When incubated with aptamer, the peak was slightly attenuated yet not shifted (see Figure 7.5(b)). Only when incubated with endotoxin, there was a clear shift to 535 nm. This shift was probably the result of AuNPs' plasmonic response.

To gain an understanding, fresh ALD-treated PDMS samples and the samples incu-

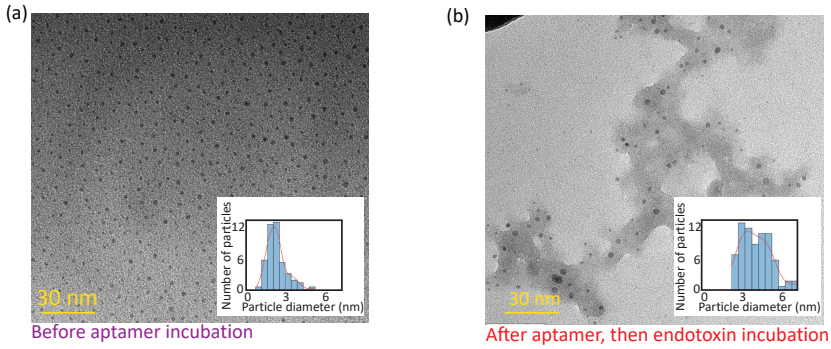

Figure 7.6: Transmission electron microscopy (TEM) photo of (a) AuNPs after AP-ALD deposition (in-channel, Chapter 4) and (b) AuNPs after incubation with aptamer and endotoxin (on a slab). In both cases, the AuNPs were detached from the ALD-treated PDMS samples prior to the TEM analysis by dissolving the underneath TiO_x layers with acid and sonicating the samples.

bated with aptamer and endotoxin were sonicated in 1 M HNO_3 solution for 15 minutes, before being left immersed for 48 hours to dissolve the underneath TiO_x layers and disperse the AuNPs. The immersing liquid was then centrifuged (MicroCL 21/21R, Thermoscientific) at 14800 rpm for 10 min, before being decanted, washed with ethanol and transferred onto a Quantifoil copper TEM grids (refer to Chapter 3). Transmission electron microscopy (TEM, JEOL JEM1400) was performed with a voltage of 120 kV and the particle size was analyzed using ImageJ. Figure 7.6 shows an increase of the mean particle diameter from 2 nm before being incubated with aptamer and endotoxin to 4 nm after incubations. This increase indicates the movement, and subsequent aggregation of AuNPs on the surface of the samples, probably due to endotoxin, as indicated by the shift in the UV-vis spectra. Despite the potential, there is a big room for improvement. For example, the fabricated PDMS samples could not be reused. An attempt was made in this study where the samples were reused after being stored for 6 months after the ALD treatments at ambient conditions. However, no UV-vis peak shifts were observed, indicating the non-reusability of the samples.

Furthermore, a comparative study was also conducted where the AuNPs were synthesized using liquid techniques. Nonetheless, most of the AuNPs were synthesized subsurface, resulting in them not being able to be exposed to endotoxin. While the study implied potential approaches to increase the sensing sensitivity, e.g. post-treatment thermal annealing, it also highlighted the importance of ALD to deposit AuNPs on the surface. This study could also be extended to a microfluidic system, where continuous monitoring of endotoxin is of importance. Other types of aptamers and plasmonic response manipulations could also be studied to expand the applicability of this technology. Thus, depositing nano-layers inside microfluidic chips could help in developing a commercial biosensor with high specificity, on top of other potentials discussed in the case studies of Chapter 4. Therefore, performing ALD in microfluidics enables many applications that could help advance the overall technology, especially those involving valuable, small volumes.

We thank Alina Rwei, Zhu Pancheng, and Lena Fasching (Chemical Engineering, Delft University of Technology) for their collaboration. We also extend the gratitude to Saeed Saedy and Wiel Evers (Chemical Engineering, Delft University of Technology) for the TEM and we acknowledge the thesis works of Martin Meijer and Maarten Klumperman in this initial study.

References

[1] A. K. Singh, K. Adstedt, B. Brown, P. M. Singh, and S. Graham, *Development of ALD coatings for harsh environment applications,* ACS applied materials & interfaces **11**, 7498 (2018).

[2] P. Paul, K. Pfeiffer, and A. Szeghalmi, *Antireflection coating on PMMA substrates by atomic layer deposition,* Coatings **10**, 64 (2020).

[3] G. Song and D. Q. Tan, *Atomic layer deposition for polypropylene film engineering—a review,* Macromolecular Materials and Engineering **305**, 2000127 (2020).

[4] J. Ma, N. Sun, X. Zhang, N. Zhao, F. Xiao, W. Wei, and Y. Sun, *A short review of catalysis for CO_2 conversion,* Catalysis Today **148**, 221 (2009).

[5] Y. Lu, Z. Zhang, H. Wang, and Y. Wang, *Toward efficient single-atom catalysts for renewable fuels and chemicals production from biomass and CO_2,* Applied Catalysis B: Environmental **292**, 120162 (2021).

[6] A. Primo, A. Corma, and H. García, *Titania supported gold nanoparticles as photocatalyst,* Physical Chemistry Chemical Physics **13**, 886 (2011).

[7] M. Endo-Kimura and E. Kowalska, *Plasmonic photocatalysts for microbiological applications,* Catalysts **10**, 824 (2020).

[8] A. Kumar, P. Choudhary, A. Kumar, P. H. Camargo, and V. Krishnan, *Recent advances in plasmonic photocatalysis based on TiO_2 and noble metal nanoparticles for energy conversion, environmental remediation, and organic synthesis,* Small **18**, 2101638 (2022).

[9] K. B. Patil, N. B. Patil, S. V. Patil, V. K. Patil, and P. C. Shirsath, *Metal based nanomaterial's (silver and gold): Synthesis and biomedical application,* Asian Journal of Pharmacy and Technology **10**, 97 (2020).

[10] L. Zhao, P. K. Chu, Y. Zhang, and Z. Wu, *Antibacterial coatings on titanium implants,* Journal of Biomedical Materials Research Part B: Applied Biomaterials **91**, 470 (2009).

[11] M. Fraga and R. Pessoa, *Progresses in synthesis and application of SiC films: From CVD to ALD and from MEMS to NEMS,* Micromachines **11**, 799 (2020).

[12] P. Vulto, S. Podszun, P. Meyer, C. Hermann, A. Manz, and G. A. Urban, *Phaseguides: a paradigm shift in microfluidic priming and emptying,* Lab on a Chip **11**, 1596 (2011).

[13] A. Hibara, S. Iwayama, S. Matsuoka, M. Ueno, Y. Kikutani, M. Tokeshi, and T. Kitamori, *Surface modification method of microchannels for gas-liquid two-phase flow in microchips,* Analytical Chemistry **77**, 943 (2005).

[14] Z.-J. Meng, W. Wang, X. Liang, W.-C. Zheng, N.-N. Deng, R. Xie, X.-J. Ju, Z. Liu, and L.-Y. Chu, *Plug-n-play microfluidic systems from flexible assembly of glass-based flow-control modules,* Lab on a Chip **15**, 1869 (2015).

[15] T. Fujii, Y. Sando, K. Higashino, and Y. Fujii, *A plug and play microfluidic device,* Lab on a Chip **3**, 193 (2003).

[16] H. Herman, G. Flores, K. Quinn, M. Eddings, S. Olma, M. D. Moore, H. Ding, K. P. Bobinski, M. Wang, D. Williams, *et al.*, *Plug-and-play modules for flexible radiosynthesis,* Applied Radiation and Isotopes **78**, 113 (2013).

[17] G. Pascali, P. Watts, and P. A. Salvadori, *Microfluidics in radiopharmaceutical chemistry,* Nuclear medicine and biology **40**, 776 (2013).

[18] R. M. Van Dam, N. S. Ha, J. Jones, J. Ly, S. Liu, and S. Cheung, *Microscale device and method for purification of radiopharmaceuticals,* (2023), uS Patent 11,660,571.

[19] W. A. Weber, J. Czernin, C. J. Anderson, R. D. Badawi, H. Barthel, F. Bengel, L. Bodei, I. Buvat, M. DiCarli, M. M. Graham, *et al.*, *The future of nuclear medicine, molecular imaging, and theranostics,* Journal of Nuclear Medicine **61**, 263S (2020).

[20] ^{225}*Ac-PSMA-617 for PSMA-targeted a-radiation therapy of metastatic castration-resistant prostate cancer,* Journal of Nuclear Medicine **57**, 1941 (2016).

[21] P. M. Anderson, V. Subbiah, and M. M. Trucco, *Current and future targeted alpha particle therapies for osteosarcoma: Radium-223, actinium-225, and thorium-227,* Frontiers in Medicine **9**, 1030094 (2022).

[22] Ø. S. Bruland, S. Nilsson, D. R. Fisher, and R. H. Larsen, *High-linear energy transfer irradiation targeted to skeletal metastases by the α-emitter ^{223}Ra: adjuvant or alternative to conventional modalities?* Clinical cancer research **12**, 6250s (2006).

[23] P. Shende and S. Gandhi, *Current strategies of radiopharmaceuticals in theranostic applications,* Journal of Drug Delivery Science and Technology **64**, 102594 (2021).

[24] R. C. Mease, C. M. Kang, V. Kumar, S. R. Banerjee, I. Minn, M. Brummet, K. L. Gabrielson, Y. Feng, A. Park, A. P. Kiess, *et al.*, *An improved ^{211}At-labeled agent for PSMA-targeted α-therapy,* Journal of Nuclear Medicine **63**, 259 (2022).

[25] J. L. Hatcher-Lamarre, V. A. Sanders, M. Rahman, C. S. Cutler, and L. C. Francesconi, *Alpha emitting nuclides for targeted therapy,* Nuclear medicine and biology **92**, 228 (2021).

[26] E. O. Aboagye, T. D. Barwick, and U. Haberkorn, *Radiotheranostics in oncology: making precision medicine possible,* CA: A Cancer Journal for Clinicians **73**, 255 (2023).

[27] E.-K. Lim, T. Kim, S. Paik, S. Haam, Y.-M. Huh, and K. Lee, *Nanomaterials for theranostics: recent advances and future challenges,* Chemical reviews **115**, 327 (2015).

[28] A. D. Gee, M. M. Herth, M. L. James, A. Korde, P. J. Scott, and N. Vasdev, *Radionuclide imaging for neuroscience: Current opinion and future directions,* Molecular Imaging **19**, 1536012120936397 (2020).

[29] G. Hellé, C. Mariet, and G. Cote, *Liquid–liquid extraction of uranium (VI) with aliquat® 336 from HCl media in microfluidic devices: Combination of micro-unit operations and online ICP-MS determination,* Talanta **139**, 123 (2015).

[30] A. Bruchet, V. Taniga, S. Descroix, L. Malaquin, F. Goutelard, and C. Mariet, *Centrifugal microfluidic platform for radiochemistry: Potentialities for the chemical analysis of nuclear spent fuels,* Talanta **116**, 488 (2013).

[31] Z. Liu and X. Lan, *Microfluidic radiobioassays: a radiometric detection tool for understanding cellular physiology and pharmacokinetics,* Lab on a Chip **19**, 2315 (2019).

[32] J. Lacombe, S. L. Phillips, and F. Zenhausern, *Microfluidics as a new tool in radiation biology,* Cancer letters **371**, 292 (2016).

[33] K. S. Pedersen, K. M. Nielsen, J. Fonslet, M. Jensen, and F. Zhuravlev, *Separation of radiogallium from zinc using membrane-based liquid-liquid extraction in flow: experimental and COSMO-RS studies,* Solvent Extraction and Ion Exchange **37**, 376 (2019).

[34] S. Trapp, T. Lammers, G. Engudar, C. Hoehr, A. G. Denkova, E. Paulssen, and R. M. de Kruijff, *Membrane-based microfluidic solvent extraction of Ga-68 from aqueous Zn solutions: towards an automated cyclotron production loop,* EJNMMI Radiopharmacy and Chemistry **8**, 9 (2023).

[35] P. Martini, L. Uccelli, A. Duatti, L. Marvelli, J. Esposito, and A. Boschi, *Highly efficient micro-scale liquid-liquid in-flow extraction of ^{99m}Tc from molybdenum,* Molecules **26**, 5699 (2021).

[36] H. Zhu, S. Heinitz, S. Eyley, W. Thielemans, E. Derveaux, P. Adriaensens, K. Binnemans, S. Mullens, and T. Cardinaels, *Gamma radiation effects on AG MP-50 cation exchange resin and sulfonated activated carbon for bismuth-213 separation,* RSC advances **13**, 30990 (2023).

[37] K. Nordlund, S. J. Zinkle, A. E. Sand, F. Granberg, R. S. Averback, R. E. Stoller, T. Suzudo, L. Malerba, F. Banhart, W. J. Weber, F. Willaime, D. S. L., and D. Simone, *Primary radiation damage: A review of current understanding and models,* Journal of Nuclear Materials **512**, 450 (2018).

[38] M. M. Chaudhry, *Comparison of the direct and indirect mechanisms for the production of radiation damage* (University of London, Chelsea College (United Kingdom), 1963).

[39] S. Nambiar and J. T. Yeow, *Polymer-composite materials for radiation protection,* ACS applied materials & interfaces **4**, 5717 (2012).

[40] J. Davenas, I. Stevenson, N. Celette, S. Cambon, J. Gardette, A. Rivaton, and L. Vignoud, *Stability of polymers under ionising radiation: the many faces of radiation interactions with polymers,* Nuclear instruments and methods in physics research section B: Beam Interactions with Materials and Atoms **191**, 653 (2002).

[41] Q. Liu, W. Huang, B. Liu, P.-C. Wang, and H.-B. Chen, *Gamma radiation chemistry of polydimethylsiloxane foam in radiation-thermal environments: experiments and simulations,* ACS Applied Materials & Interfaces **13**, 41287 (2021).

[42] I. Kamal, M. K. A. Karim, H. H. Harun, H. R. A. Razak, L. Y. Jian, J. L. Y. Chyi, and M. M. A. Kechik, *Evaluation of radiation attenuation properties on a various composition of polydimethylsiloxane (PDMS) for fabrication of kidney phantom,* Radiation Physics and Chemistry **189**, 109661 (2021).

[43] E. Şakar, Ö. F. Özpolat, B. Alım, M. Sayyed, and M. Kurudirek, *Phy-X/PSD: development of a user friendly online software for calculation of parameters relevant to radiation shielding and dosimetry,* Radiation Physics and Chemistry **166**, 108496 (2020).

[44] S. Agostinelli, J. Allison, K. a. Amako, J. Apostolakis, H. Araujo, P. Arce, M. Asai, D. Axen, S. Banerjee, G. Barrand, *et al.*, *GEANT4—a simulation toolkit,* Nuclear instruments and methods in physics research section A: Accelerators, Spectrometers, Detectors and Associated Equipment **506**, 250 (2003).

[45] H. Akyildirim, E. Kavaz, F. El-Agawany, E. Yousef, and Y. Rammah, *Radiation shielding features of zirconolite silicate glasses using XCOM and FLUKA simulation code,* Journal of Non-Crystalline Solids **545**, 120245 (2020).

[46] T. Ghrib, M. Mhareb, M. Sayyed, Y. Alajerami, N. Dwaikat, A. B. Ali, and M. Gondal, *Structural, optical and radiation shielding properties of zirconium–titanium–thallium ternary oxide (0.5 ZrO_2-(0.5-x) TiO_2-xTl_2O_3),* Ceramics International **47**, 21837 (2021).

[47] Y. Luan, N. Wang, C. Li, X. Guo, and A. Lu, *Advances in the application of aptamer biosensors to the detection of aminoglycoside antibiotics,* Antibiotics **9**, 787 (2020).

[48] K. Saha, S. S. Agasti, C. Kim, X. Li, and V. M. Rotello, *Gold nanoparticles in chemical and biological sensing,* Chemical reviews **112**, 2739 (2012).

[49] P. Zhu, V. A. Papadimitriou, J. E. van Dongen, J. Cordeiro, Y. Neeleman, A. Santoso, S. Chen, J. C. Eijkel, H. Peng, L. I. Segerink, *et al.*, *An optical aptasensor for real-time quantification of endotoxin: From ensemble to single-molecule resolution,* Science advances **9**, eadf5509 (2023).

[50] P. Xie, L. Zhu, X. Shao, K. Huang, J. Tian, and W. Xu, *Highly sensitive detection of lipopolysaccharides using an aptasensor based on hybridization chain reaction,* Scientific Reports **6**, 29524 (2016).

Acknowledgements

A night, a sleeping night

There has been night
where I can't sleep
The night where they weep
The night where they seep

Seeping deep, deep into me
As in gleaming, gleaming in the bin
In the bin, in the sin, in the fin
Or beaming thin, with mirth all in

There has been night
where I do see
The night seething fit
The night glaring bit

And it glares bit and bit
bits and pieces and another bit
With me here beating, and my heart beats

There has been night
And fight
And light

Yes, there has been night
I sleep

Just like any other ordinary acknowledgement page, let me start with a disclaimer. A disclaimer for the peace of my mind, since this book is written with a thumping heart, a perspiring forehead, and a heart filled with relief. That without the continual support of many, and the blessing of the Above, accomplishing this feat unscathed was but a dream of a fool. And here is the disclaimer, after that long-winding sidetrack. I am writing this section, overwhelmed with thankfulness, in a manner I am used to and not I have been, in the last four years, trained for. But there is this part of me that's insecure. Insecure that I didn't attribute the right gratitude, or even worse to forget one or two names. Such a people pleaser, my insecurity has been. But please be noted that my gratitude has been genuine and well, it is written. So here your humble servant is, a most notable coward, an infinite and endless liar, an hourly promise breaker, the owner of no one good quality (William Shakespeare, First Folio, All's Well That Ends Well act 3 scene 6, 1623).

The ones without whom, I would open a toko

No amount of words can express my gratitude to the amazing promotors **Ruud** and **Volkert**, for all the learning, the discussions, and the chats. I have to say, it was really a privilege to have both of you as my supervisors. You both are experts in your field, easily saying no to my stupid ideas, and reminding me to take care of myself, and you both are very supportive and encouraging, despite all the stormy messy projects and collaborations I had. From the beginning of the PhD where you both were concerned with my number of students, to her end where you both came to terms with my digging-my-own-grave-habit, thank you for bearing with me while I was a child. Thank you for having meetings at 7 in the morning, continuously checking-in my sanity and well-being, and sacrificing your Saturday and Sunday, so that not only this book is completed on time, but also with a smile. **Ruud**, despite the silent moments we had at 3 o'clock in the morning in front of the coffee machines, despite hundreds of secret PhD students and projects that you had, I was so grateful that we could still meet biweekly, and I still remembered your comment in one of the meetings: you don't have bad time management, you just made your life more difficult with all your projects. And **Volkert**, thank you for all the nice chats we had. You listened to my whining, my break-down with students, and my broken Dutch, and yet still accommodating and attentive. I learned a lot to be a good teacher, to be a good researcher, and to speak Dutch with expressions and sayings. Sitting down in a bar to celebrate IPT, or the end of the project, while talking about the students, and many others, it was very heartfelt.

Secondly, this dissertation would be nothing without you **Svenja**. We complained to each other, complained about each other, and cried together. Without you, the whole 4 years would have been a nightmare or even would have not been four years. Your enthusiasm is contagious, and moments where we went for writing retreats together, or just chilling with beers with **Gerrit** and **Zila** and **Johnny**, or exchanging Harry Potter's stories and geology stories, it was amazing. You all made me not feel bad as a nerd, as a scientist, and as a stupid guy. And within four years, we changed a lot. You are now with each other (yeay, the wedding party was dope), and I am with a double belly. Thank you for the crash courses, for the Friday evening bar time at the cool bar, and for teaching me to be authentic. You are amazing.

And **Gabrie**, thank you for being such a mentor, even since my EngD life. Thank you

for being there during my good and bad moments, difficult and whatnot. It was very reassuring to have you around, to hear your stories from all over the world, and to teach me how to be a person, to say no, to hightlight where I am good at and to improve where I lack.

The life I had once, only now to look back

I would like to also thank **Robin**. Thanks for being there, for being an anchor, for making my students cry (yes, all my students who had defence with you cried, it is NOT my fault), but above all, thanks for being a friend. Thank you for keep reminding me that there is life outside the students (well that life, is called, work, as you have been showing). Hope your rabbits are always jumping, and please bring them over once.

To the best support, without them, I might as well go outside AS buildings and sell some chicken satays, to the technician team. **Kristen** thank you for being more than just a colleague, for all the chats and the nice eat-out together, for all the "I-don't-know-what-happens" in the cleanroom, the "I-thought-you-are-not-going-to-have-students-anymore" and the "I-dont-understand-what-your-project-is-actually", I can't be more thankful that you were there during the PBVs. **Mojgan** thank you for going through the tough times with ALD, the crazy panic moments, the you-are-doing-okay moments, thank you for being a mama in the team, your leave was heartfelt. **Stefan** I would love to thank you as well, for all the mechanics that I have no idea, to be a role model that screwdriver and nuts and bolts are not there to screw me up and drive me nuts. **Bart Boshuizen** thank you for all the nice chats, and the XPS lessons, so that I can grow from a crawling babe to a babbling babe in the XPS. **Duco, Cas** thank you for all the nice lessons, the way to wear gloves since my samples destroy the microscope, and the resurrection of the ALD. While in this topic, I would love to also thank the great team in Kavli Cleanroom, especially to **Pauline, Roald** (good luck with your PhD!) **Eugene, Hozanna** (thank you for being there and allow me to train in all the SEMs!) and the rest of the teams. Thank you for all the support, and for making me feel part of the group. And of course the RID people. I am proud to say that I have never been contaminated, nor have I called the SBD (though I have made some foolish mistakes haha). A super duper special thank to the secretary team **Leslie, Sandra**, without you being lenient on my request to find a timeslot at Ruud's and Volkert's agenda, what would I become. And of course, the best lady in the corridor **Maria**.

Another important core of my gratitude would definitely go to **the students**! While there has been an extensive list written in my portfolio, I would like to thank all of them personally here. You guys have been amazing companions, and even more, bright minds with so much potential, so much curiosity, and so many colours! Thank you for pulling your project through, for all the nice personal chats, and for making my PhD journey more adventurous. Since I have a squad of them, here it is!

I remember **Okker** came on my second day after starting the PhD, saying to me I am the student. From that point onward, we had a lot of ride, and I was so thankful to have you around, along with **Amy** who taught me to be merry and danceful. **Arden** broke so many wafers! His quest to be sustainable ended up in a bloody tear, and thanks for being around. The energy you gave, the enthusiasm, I wish you all the luck for the new jobs. Another student to remember is **Bart**, the one I always had to look up when having

meeting. Very bright and fun, and I know how traumatized you have been with the ALD. Good times. **Sulaika** was also equally amazing, with all the spirit you managed to pull it through!

Apparently, having students from Chemical Engineering is not enough, **Remy** came from a complete different background. I was so impressed with his proactiveness, his managerial skill, and of course, his beer brewing skill! **Afke** also came around the same time, inspiring me to be the dead weight in a competitive rowing tournament (which I self-awaredly decided not to do), and it was amazing how you kept your schedule. Then **David**, how you were so eager, it was so innocent yet reminding me the passion a researcher should have! I hope the leaked chips did not bring too much nightmares to you.

Yassine came after, along with **Walter** and **Friso**. Completely three different fields, one was working with microfluidics, another with ALD and another with modelling. It was so admirable to see your perseverance, your dedication, your neat work Yassine! While I was also impressed with how Walter, despite of your convenient life, still wanted to hold the commitment to finish your bachelor. It was extremely well-executed, and I could not forget how I got an emergency (unexpected) wisdom tooth extraction in the morning, and continued working with ALD with you. Your brewing skill was also top-notch! And **Friso**, you did very well, even during the parts when your LateX crashed an hour before the deadline and all the panic modes we had in the call.

Maud, Jessey, Nick were three inseparable students! It was so, again and I would not stop saying this to all the students I got the privilege to supervise, amazing that you pulled it off Maud, despite you were still recovering from a concussion. In that regards, the cooperation with Jessey was also amazing, despite of different background, you managed to catch up so fast. And Nick, I am impressed on how you managed to finish such a complex project, despite the time limitation and the always-amazing ALD.

Fabrice, the ability of you comprehending four different subjects (microfluidic, electrowetting, rheology, coacervate chemistry) and defending the thesis in front of 6 professors is beyond my comprehension. You were very cheerful, very proactive, and very motivated. That was an amazing pull in my PhD journey. And **Julia**, it was great to have you around, shopping all the polymers in the world, placing it in the weirdest machine, and still managed to come with that jars. I hope you could judge who won the fights, me or Rens. And of course, **Martijn** and **Maarten**, the ones working with gold nanoparticles. Thanks for sticking around and did not kick me for my stupidity, and I am looking forward to your stories and adventures. Furthermore, while **Iris** came to me due to broken ALD, you were proven to be amazing in your way. You found a lot of things during the project, and the amount of workload you had during the thesis, I could only attach superlative adjectives here. It was fun to work with you, with your analytical mindset, and friendly approach.

Lubna, I was so happy when you managed to pull it through and I wish you good luck for your future endeavours! Along with this, **Vera**, **Enver** and **Didier** it was nice to know you in the last part of my PhD. Despite of the less supervisions you got, you all performed amazing! Good luck for the future as well. And of course, for the currently still running students **Xanne** along with **Anna**, good luck! Life is still ahead.

I would like to also extend my gratitude to the many collaborators that I got to meet.

I learned a lot, and it has been such a pleasure to be acquainted. **Anand** thank you for all the nice discussions on the physics of the fluid, and good luck with your PhD. **Saeed** thanks for being such a mentor, **Pan Cheng** for the nice chats, I really missed you! **Jingjing** good luck with the PhD and special thanks to many others. Thank you as well for the opportunity to work with you, and get to know a lot **Pouyan, Antonia**. And special thanks to **Alina** and **Bijoy** for letting me in your project, and I can't thank you both more for the opportunities. I got to learn a lot from you both. I would like to also extend my gratitude to other collaborators (**Sean Barry, Eden Goodwin, Lars Bannenberg, Jan-Willem Hurksman, Santiago** and many others!)

The laugh, the merry, and the tears

To the one, friendship I earned before and during my PhD journey. **Ruben, Maud** Thank you for being there during good and bad moments. Thank you for allowing me to buy and bring flowers to the theatre, for the first time in my life, and thank you for being such a great laugh, be it from our first competition ever in Delft to our continuous check-in and update. Thank you as well for a memorable bet in the first year, or the birthday parties I got invited. The backstabbing is a thing I will always remember to repent in my life. And good luck with your life! **Christian and Bente**, what a great pleasure to know you (FYI, Gabrie told me a lot about you, even before you came), to finally have someone who shares my passion for Indonesian food, the one who stays true to fish and meat despite the dominance of the veggies! **Rensie and Saskia**, thank you for being such a good friend, checking in with me during the lonely New Year Eve, saving me from the terror of the cockroach in Naples, and the nice evening with Meg. Hope your routine stays the same, and nothing random ever befalls you! In this case, I would like to also thank **Kosta, Stef, Christel**. The dancing on the rainy new year's eve, the terrible king's cup, and the saving from the abominable cockcroach and GC, thank you. I would also like to thank **Meg, Edo, Zaid** for so many things, the great noona's cantuccini, the inspiration to go to the gym (though my laziness trumps), the laugh, and the merry!

I would like to also congratulate **Lena, Riccardo, Ignasi** and the rest of the new batches **Bhavesh, Athina, Katherine**, good luck with all the craziness and **Marc, Nasim, Peter, Mingliang the PSE gangs, Lukas, Gao, Dominik, Max, many others** good luck with your PhD/Postdocs. Good luck with the ALD as well, hope they stay tame till the end. Also, it was such a pleasure to get acquainted and to know you **Emma** I wish the best for your professorship! **Abtin** Thank you for all the nice chats, and the personal invite, hope your PhD is doing you well. And of course **Pranav**, though our trip to Azores didn't turn out as expected, I hope you manage to manage in your life. Along with this, to the supermom officemates **Isabell, Ida, Mahdiyeh**, you all have my unending admiration. Dealing with kids at home and another kid at the office, along with other kids doing a thesis with you, and your PhD/Postdoc. How did you manage to do them? Hope Cleo, Anuar, Soorena, and I don't know if there is any other, can stay as your source of inspiration, that in turn also inspires others around you.

To the debating club members **Enrique**, my twin, **Romme, Jelmer** (congrats again for your baptism!), **Rebecca, Namo, Charles** (how is your HSK now?), **Sherrie, Reeti, Lars, Fons, Lucia, Tanya** thanks for hanging around. Also to **Boby, Odi**, may you both rest in peace there, and **Bram, Omar** it was such a pleasure.

To many new friendships made along the way. **Ninad, Tanvi** thanks for being around and for all the amazing invites, to the better life in the future. **June**, good luck with your professorship at WUR! **Romme, Jelmer** what a privilege to know you, from birthday party all the way to the new year's eve! Thanks for sticking around. **Lieke**, semoga tetap menakjubkan! Du kannst es. **Dias**, please keanehan, kegalauan, kepintaran, pilih satu aja. **Irene**, dari 2 hari di Jakarta, drama-drama telepon, sampai 10 hari iceland dengan mobil terjebak salju, thanks udah ga kick gue out. Dan juga **Intan**, untuk semua kemenakjubkannya dan jalan2nya.

One who have seen me without coffee

Tzu Han, Yilin, Mia I can't be more happier than to hear your news about the little one. It was such a privilege to have you around, to attend your wedding during Covid, to go diving together to spend the post-bachelor commemoration, and to be such a brother. Meine wie wie jetzt nicht schlecht lor aber meine dulam walao, encore gros (Nous devons reprendre notre français). Also thanks to **Tongtong** for the being there, for the lovely trip in the Baltics, for the help in KL, for many! Thanks for pulling me to the light, that at least I didn't become that bad **Fermi, Winnie, Ivan, Melissa, Naomi, Josef, Brian, Abby, Jerry, Vickie, Fei Ling, Benjamin, Flori, Clemens, Andreas, all the workers** and I wish that your service may be true to Him. Add oil!

Kepada **Abram, Novia**, walaupun kita baru bertemu sebentar, sudahlah kita menjadi teman yang baik. Sungguh mengherankan. Semoga kalian tetap mau berteman denganku, walaupun kita tidak menggunakan bahasa Indonesia yang baku. Tolong jangan aneh-aneh banget. Semoga semangat One Piece tetap bersama dan semoga Kratos dan poin poin Hilton serta semangat juang 45 nya tidak dikalahkan oleh zaman. Dan juga teruntuk **Gita**, makasih udah ada di good and bad moments git, udah ke US bareng juga dan menemani gue, udah mau berdoa saat gue nyetir, semoga lo selalu bahagia ya. Demi hidup 2040 yang bersinar nih. Makasih udah pada mau membuat trip ke US demi menemani diriku yang kesepian, hingga bisa ketemu mas Bruce, makan tombstone yang berlimpah ruah, ketemu Karen dan bapak2 bawa pistol di Wendy's, makan lucu2, menerima bahasa Indonesia yang hancur.

Sian Tee dan Maria, dari les bahasa belanda sampai Belitung Bali bersama, makasih banget udah ada dan mau datang ke rumah gue, udah undang makan. Panjang cerita bisa sampai kenalan, dan lebih panjang lagi cerita yang ada di depan. Makasih juga udah being there, dan mau mendengar cerita. Makasih udah mau dorongin motor yang terjebak kubangan lumpur, mau menerima keanehan2 dan kebodohan2 ini, udah mau nyamperin dari Ubud-Canggu, kasih saran makanan2 enak foodie grade. Untuk kehidupan belanda yang lebih baik.

Mbak Nelly makasih mbak udah mau share story, dan jadi sumber inspirasi, cepet lulus ya mbak! Juga **Bella and Frank**, thanks for being around Bel, kamu semoga juga cepat lulus. Juga kepada geng Bosboom **Atin, Kristi, Edgar, mas Wicak, mbak Desy, Tara, mas Aga, mbak Kitty, Aira, Antra dan geng PPI Delft lainnya** dan geng mamacan **Ceu Meut, Ceu Karmen** makasih yah udah stick around dan mengobati keinginan ku makan indo.

Luis, Clara, David thank you for reminding me, that life is more than only a PhD. And I would like to congratulate you on David and your wedding! And in this part, **Tomtom**

Vila de Conde's did bring us quite far, and I would like to thank you for all the spirits you shared. Good luck to all of you! Special thanks as well to **Marco, Pablo** for going through the COVID period with me.

Thousand miles apart and yet seconds away

Untuk **Cepret**, plis lah dikurangi keanehannya haha. Makasih udah stick around for so long. Semoga misa bersama Paus, juga hidup hidup lucunya bersama Nikki selalu berbahagia ya. Untuk **Stacey** makasih udah jadi teman yang baik, dan udah menularkan semangat hidup lebih dari laya. Semoga ga galau2 banget ya dan semoga selalu berkelimpahan dan gelimangan! **Iim** dari ketemu di UI, sampai Litbang bersama, sampai Tebet rasa Kemang. Tinggal kurang madiun bersama nih. Makasih ya iim udah jadi sumber inspirasi, menakjubkan sekali ini. Dan untuk **Jessica** been a while, tapi always happy untuk keep in contact dengan lo. Untuk semua trip trip lucu nya, dari Oslo dengan taksi berdarah, sampai Portugal Selatan penyebab putus, makasih untuk cerita taritari seprainya. Aku padamu. Juga untuk **Teph**, thanks for sticking around! good luck buat anak2 bocilnya, untuk **Andre** semoga selalu menakjubkan dengan Rosy, Sera, dan hidupnya, serta untuk **Gani** good luck PhD nya di Canada. Serta untuk geng friendship **Ivone ketua geng, Adri, Hendi, Nelly, Vanila** serta geng Jalan2 **Beto, Fanda, Hans, Leo**.

Papa, mama, terima kasih sudah mendukung Albert, baik dalam doa, dalam cerita, dalam semua-semuanya. Mohon maaf Albert jarang pulang ke rumah, semoga papa mama selalu sehat, selalu bahagia, dan juga udah bisa berbulan madu. **Johan, Nando,** ayo kapan kita nyelam lagi (biar koko Johan iri hehe). Semoga sukses dalam kehidupan dan dalam semua pilihannya.

Ad maiorem Dei gloria

PhD Portfolio

Name of PhD candidate:	Albert SANTOSO
Department:	Chemical Engineering
Research group:	Product and Process Engineering
Research school:	TU Delft graduate school; J.M. Burgerscentrum for fluid mechanics
PhD period:	January 2020 - May 2024
Promotor:	Prof. Dr. ir. J. Ruud van Ommen
Promotor:	Dr. ir. Volkert van Steijn

PhD Training

General Courses, TU Delft graduate school

PhD start-up	2020
Advanced Dutch for foreigners	2020
Creative tools for scientific writing	2022
Looking for a career in the Netherlands	2023
Marketing tools to position yourself confidently in the job market	2023
How to effectively communicate your research online	2024
Writing for a broader audience	2024
Effective negotiation	2024

Specific courses

RPO Dispersible Radioactive Material level-D (TMS VRS-D)	2020
Nuclear Chemistry	2020
Thin Film Materials	2020
Product Safety Training Metal Alkyl	2020
Capillarity-driven flows in microfluidic	2020
COMSOL Multiphysics	2020
Computational Multiphase Flow	2023

Supervision and Co-supervision/support

Amy Rijsdijk	BSc	MST	ALD modelling inside PDMS matrix	2020
Okker van Batenburg	MSc	CE	Microfluidic experiment and modelling	2021
Arden J. Timmermans	MSc	CE	Wettability manipulation on PDMS	2021
Bart J. van den Berg	MSc	CE	ALD for robust wettable PDMS	2021
Sulaika S.M. Khedoe	MSc	CE	ALD for organic barrier on PDMS	2022
Rémy de Jong	MSc	BME	Radiation damage in polymer	2022
Afke G.M. Damen	BSc	MST	ALD for organic barrier on PDMS	2022
Runjie Zheng	MSc	CE	ALD and PDMS channel deformation	2022
Yassine Hounat	BSc	MST	Flow profile in ALD-treated PDMS chips	2022
Walter Starmans	BSc	MST	SiO_x ALD nucleation study on polymer	2022
Friso Vodegel	BSc	MST	Modelling of ALD deposition in structures	2022
Nick T.Y. Wijers	BSc	MST	ALD in microfluidic channel	2022
Jessey W.B. de Roeck	BSc	AP	Microfluidic extraction of Ga-68	2022
Maud C.E. Appel	BSc	MST	Microfluidic extraction of Y and La	2022
Fabrice C.G. de Cocq	MSc	CE	Complex coacervate in electric field	2023
Julia A.M. Everard	MSc	CE	ALD as a moisture barrier	2023
Maarten Klumperman	BSc	MST	Liquid synthesis of gold nanosensor	2023
Martijn Meijer	BSc	MST	Robustness study of ALD biosensor	2023
Iris Blommestein	BSc	MST	Adsorbent to separate radionuclides	2023
Lubna Ghabbash	BSc	MST	Salt concentration effect on coacervates	2023
Vera Aarts	BSc	MST	Microrheometry of complex coacervate	2024
Enver Akif Özbey	BSc	MST	Nanoliposome - drug carrier production	2024
Didier Ehlert	BSc	MST	COMSOL model in microfluidic	2024
Xanne van Meijbeek	MSc	CE	Coacervate and microfluidic study	2024
Vincent Eschauzier	MSc	CE	Solute drying in microfluidics	2020
Rebecca Baijens	MSc	CE	Gold ALD for catalytic purposes	2021
Justin Schat	MSc	CE	Characterization of bentonites	2021
Floris Hoekman	BSc	MST	Nanocatalyst for Haber-Bosch	2023
Tim Groeneveld	MSc	CE	Enzymatic deposition of metal oxide	2023
Loulotte Waling	MSc	LST	Micromixer for microbioreactor	2023
Vishnupriya Subburasu	MSc	CE	Surface roughness and electrowetting	2023
Marc Scholtens	MSc	CE	Diffusion study of rhodamine dyes	2023
Na Dong Hyuk	MSc	AE	Corrosion control substrate manipulation	2023
Joey Meidam	MSc	CE	Coacervate and microfluidic study	2024
Anna Verdouw	MSc	AP	Chelator-impregnated PDMS	2024

List of Publications

Journal publications related to this dissertation

5. **A. Santoso**, S. Trapp, I. Blommestein, S. Saedy, J.R. van Ommen, R.M. de Kruijff, and V. van Steijn, *Chelator-impregnated polydimethylsiloxane beads for the separation of medical radionuclides*,Separation and Purification Technology **354**, 12885 (2025).

4. S. Trapp, **A. Santoso**, Y. Hounat, E. Paulssen, J.R. van Ommen, V. van Steijn and R.M. de Kruijff, *Microfluidic chip solvent extraction of medical radionuclides*, in preparation.

3. **A. Santoso**, M.K. David, P.E. Boukany, V. van Steijn and J.R. van Ommen, *Atmospheric pressure atomic layer deposition for in-situ surface modification of PDMS microfluidic channels*, Chemical Engineering Journal **498**, 155269 (2024).

2. **A. Santoso**, B.J. van den Berg, S. Saedy, E. Goodwin, V. van Steijn and J.R. van Ommen, *Robust surface functionalization of PDMS through atmospheric pressure atomic layer deposition*, Atomic Layer Deposition Journal**1**, 1-13 (2023).

1. **A. Santoso**, A.J.G. Damen, J.R. van Ommen, and V. van Steijn, *Atmospheric pressure atomic layer deposition to increase organic solvent resistance of PDMS*, Chemical Communications **77**, 10805-10808 (2022).

Patent

1. **A. Santoso**, S. Trapp, R.M. de Kruijff, V. van Steijn and J.R. van Ommen, *Method for preparing silicon elastomer beads loaded with chelating agents and their use for the separation of radionuclides*, filed on 11th of March 2024.

Other journal publications

7. I. Baghemihl, N. Girichandran, J. Bleeker, **A. Santoso**, S. Saedy, R. Kortlever, J.R. van Ommen and V. van Steijn *Exploring the Viability of a Taylor Flow Electrolyser for Enhanced CO2 Electrolysis*, under review, Chemical Engineering Journal.

6. S. Trapp, B. Giling, E. Spuijbroek, **A. Santoso**, R.M. de Kruijff and E. Oehlke *Microfluidic purification of Ga-68 solution after solvent extraction from liquid targets*, in preparation.

5. A. Sudha, **A. Santoso**, and M. Rohde *Parallel flow stability in a microfluidic system: experiment and simulation investigation*, in preparation.

4. **A. Santoso**, S. Trapp, R.M. de Kruijff, V. van Steijn and J.R. van Ommen *Extraction of* ^{68}*Ga medical radioisotopes from Zn nitrate liquid target using atomic layer deposited microfluidics*, Nuclear Medicine and Biology **126**, 108756 (2023), conference proceeding of ISRS 2023, US.

3. K.V. Petrov, M. Mao, **A. Santoso**, I. Ryzhkov, and D.A. Vermaas *Design criteria for selective nanofluidic ion-exchange membranes*, Journal of Membrane Science **688**, 122156 (2023).

2. J. Zhao, **A. Santoso**, and S.J. Garcia *Small concentrations of NaCl help building stable inhibiting layers from 2,5-dimercapto-1,3,4-thiadiazole (DMTD) on AA2024-T3*, Corrosion Science **225**, 5111562 (2023).

1. P. Zhu, V.A. Papadimitriou, J.E. van Dongen, J. Cordeiro, Y. Neeleman **A. Santoso**, S. Chen, J.C.T. Eijkel, L.I. Segerink, and A. Rwei, *An optical Aptasensor for real-time quantification of endotoxin: From ensemble to single-molecule resolution*, Science Advances **9**, 6 (2023).

External outreach

7. S. Trapp, **A. Santoso**, J.R. van Ommen, V. van Steijn, C. Hoehr, A.G. Denkova, E. Oehlke, and R.M. de Kruijff, Workshop on Targetry and Target Chemistry, Heidelberg, Germany (2024). Oral presentation

6. **A. Santoso**, S. Trapp, R.M. de Kruijff, E. Oehlke, V. van Steijn and J.R. van Ommen, National Process Technology Symposium 18, Enschede, The Netherlands (2023). Oral presentation

5. **A. Santoso**, Y. Hounat, R. Zheng, N.T.Y. Wijers, J.W.B. de Roeck, M.K. David, V. van Steijn and J.R. van Ommen, 23rd International Conference on Atomic Layer Deposition and Atomic Layer Etching, AVS, Bellevue, The United States of America (2023). Oral presentation

4. **A. Santoso**, S. Trapp, R.M. de Kruijff, E. Oehlke, V. van Steijn and J.R. van Ommen, 25th International Symposium of Radiopharmaceutical Sciences, SRS, Honolulu, The United States of America (2023). Poster presentation.

3. **A. Santoso**, B.J. van den Berg, V. van Steijn and J.R. van Ommen, 22nd International Conference on Atomic Layer Deposition and Atomic Layer Etching, AVS, Ghent, Belgium (2022). Oral presentation

2. **A. Santoso**, A.G.M. Damen, S.S.M. Khedoe, V. van Steijn and J.R. van Ommen, 22nd International Conference on Atomic Layer Deposition and Atomic Layer Etching, AVS, Ghent, Belgium (2022). Poster presentation

1. **A. Santoso**, B.J. van den Berg, V. van Steijn and J.R. van Ommen, 21st International Conference on Atomic Layer Deposition and Atomic Layer Etching, AVS, Virtual (2021). Oral presentation

Curriculum Vitæ

Albert SANTOSO

Albert was born and raised in Jakarta, Indonesia. After completing his BSc in Bioprocess Engineering and MSc in Chemical Engineering at Universitas Indonesia (Cum Laude) with final project in utilization of microalgae for carbon capture and biofuel, he continued with his Professional Doctorate in Engineering at TU Delft where he conducted a one-year research in designing new infant formula at FrieslandCampina under ISPT. After obtaining his EngD degree, he became a tech-transfer engineer at Pfizer (BE), then an R&D manager at a start-up, Peelpioneers (NL), working in food/pharma-grade valorisation of citrus peels.

In 2020, right before the pandemic period, Albert started with his Ph.D. in Product and Process Engineering group of the Delft University of Technology group under the supervision of Prof.dr.ir. J. Ruud van Ommen and Dr.ir. Volkert van Steijn. During his time at the TU Delft, he helped with two bachelor courses (Introduction to Process Technology and Practicum Basisvaardigheden) in Dutch. He also supervised 24 students and consulted another 11 students from Chemical Engineering, Applied Physics, Bioprocess Engineering and Biomedical Engineering. During his stay at the group, he presented his works in Belgium, The Netherlands, and US, while being a member of American Vacuum Society and J.M. Burgerscentrum for Fluid Mechanics. He also earned certification for Radiation Protection Officer (level D), Safety Training with Metal Alkyl, and COMSOL Multiphysics. He managed to inititate cooperations ranging from the application in pharmaceuticals to sustainable energy and the presented dissertation is the result of his main works.